Co-evaporated perovskites and incorporation into tandem solar cells

Zur Erlangung des akademischen Grades eines

Doktors der Ingenieurwissenschaften (Dr.-Ing.)

von der KIT-Fakultät für Elektrotechnik und Informationstechnik
des Karlsruher Instituts für Technologie (KIT)

angenommene

Dissertation

von

M.Sc. Thomas James Feeney
geb. in Melbourne, Australia

Tag der mündlichen Prüfung: 08.05.2025
Erster Gutachter: Prof. Dr. Ulrich W. Paetzold
Zweiter Gutachter: Prof. Dr. Stefan Weber

Kurzfassung

Da der vom Menschen verursachte Klimawandel allmählich die sozioökonomische Politik bestimmt und vorausschauende Nationen angesichts des steigenden Energieverbrauchs Netto-Null-Emissionen anstreben, ist Solarenergie die billigste Quelle für erneuerbare Energie. Unter den Solartechnologien der nächsten Generation sind Perowskit-Solarzellen (PSC) ein aussichtsreicher Kandidat um den wachsenden Energiebedarf zu decken. Sie versprechen hohe Wirkungsgrade bei der Energieumwandlung, niedrige Materialkosten und das Potenzial, sich mit bestehenden Technologien zu Tandemsolarzellen zu kombinieren. Gasphasen-Perowskite sind besonders kompatibel mit den derzeitigen industriellen Fertigungstechnologien. Allerdings müssen grundlegende Herausforderungen bewältigt werden, damit ko-verdampfte Gasphasen-Perowskite für die Kommerzialisierung in Frage kommen. Erstens gibt es ein Wirkungsgrad-Defizit zwischen typischen ko-verdampften und lösungsgefertigten Perowskiten welches sich im Großen und Ganzen durch folgende Faktoren erklären lässt: minderwertige Materialeigenschaften, ein Mangel an kompatiblen Passivierungsmitteln und minderwertige vakuum-prozessierte Löchertransportschichten (HTLs) in der Gasphase. Darüber hinaus bedeutet das substratabhängige Wachstum von ko-verdampften Perowskiten, dass jede neue Entwicklung von Dampfphasen-HTLs auch die resultierende Perowskit/HTL-Grenzfläche verstehen muss. Schließlich ist das Verständnis der vergleichbaren optischen Eigenschaften von semitransparenten (ST) PSCs noch begrenzt, was für Tandemarchitekturen von großer Bedeutung ist. Die zweite große Herausforderung ist die Geschwindigkeit der Abscheidung. Die Ko-Verdampfung ist ein relativ langsamer Prozess mit Abscheidungsraten, die um Größenordnungen unter dem liegen, was für die Kommerzialisierung erforderlich ist. Dies ist zum Teil auf das mangelnde Verständnis des Sublimationsverhaltens organischer Kationen bei hohen Abscheidungsraten zurückzuführen. Diese Arbeit zielt darauf ab, diese Herausforderungen durch die Entwicklung effizienter ko-verdampfter PSCs zu bewältigen, einschließlich ihrer Einbindung in monolithische und mechanisch gestapelte Tandemarchitekturen, um ihre Machbarkeit zu demonstrieren.

Erstens trägt diese Arbeit durch die systematische Optimierung der optischen Eigenschaften von ST-PSC zur Entwicklung von vierpoligen Perowskit/CIGS-Tandembauelementen bei. Vorder- und rückseitig transparente leitfähige Oxide und antireflektierende Beschichtungen werden untersucht, um die NIR-Transmission zu maximieren. Dies wird durch eine Reihe von optischen Simulationen unterstützt, um das zukünftige Potenzial des optischen Managements zu bestimmen. Mit dieser Strategie lassen sich vierpolige Perowskit/CIGS-Tandemsolarzellen mit PCEs von 27,3 % für lösungsprozessierte und 23,8 % für co-verdampfte Perowskit-Absorber erzielen. Die Ergebnisse im Lösungsprozess stellen nahezu einen Weltrekord an Effizienz für 4T-Perowskit/CIGS-Tandemgeräte dar.

Zweitens wird in dieser Arbeit eine Dampfphasenabscheidungsmethode für SAM-HTLs auf Basis selbstorganisierter Monolagen entwickelt. Diese Schichten sind für die Entwicklung von *p-i-n*-PSCs von entscheidender Bedeutung, wurden bisher jedoch ausschließlich mit lösungsbasierten Methoden abgeschieden. Die Auswirkungen der Verdampfung auf die chemischen Eigenschaften dieser Materialien werden gründlich untersucht um sicherzustellen, dass sie sich während der Abscheidung nicht thermisch zersetzen. Anschließend werden die Grenzflächeneigenschaften zwischen aufgedampften und in Lösung hergestellten SAM-HTLs verglichen, wobei für alle untersuchten Materialien vergleichbare Grenzflächeneigenschaften sowohl mit in Lösung hergestellten als auch mit mitverdampften Perowskit-Absorbern festgestellt wurden. Die Dampfphasenabscheidung erhöht die Flexibilität dieser Materialien erheblich und ist eine inhärent konforme und skalierbare Methode.

Als nächstes werden in dieser Arbeit die Grenzflächenwechselwirkungen untersucht, die zwischen SAM-HTLs, einschließlich aufgedampfter SAM-HTLs, und ko-verdampften Perowskiten auftreten. Aufgrund des substratabhängigen Wachstums von ko-verdampften Perowskiten ist das Verständnis dieser Wechselwirkungen entscheidend für die Entwicklung aller Dampfphasen-PSCs mit SAM-HTLs. Mit Hilfe verschiedener Techniken wird die Form dieser Wechselwirkung als Wasserstoffbrückenbindung zwischen Phosphonsäuren und Grenzflächenhalogeniden bewertet, die sich in erster Linie auf den Einbau organischer Kationen in den Perowskit auswirkt. Darüber hinaus werden die Auswirkungen dieser Wechselwirkung auf das Wachstum des Perowskits und die photovoltaischen Eigenschaften untersucht. Diese Wechselwirkung stellt eine bisher unbekannte Form der Substratwechselwirkung bei ko-verdampften Perowskiten dar und erweitert das Verständnis dieses wichtigen Parameters erheblich.

Schließlich werden in dieser Arbeit die Auswirkungen einer erhöhten Abscheidungsrate auf co-verdampfte Perowskite auf Formamidinium (FA)-Basis untersucht. Die potenzielle Zersetzung des FA-Kations ist für die Erzielung kommerziell nutzbarer Abscheidungsraten von Perowskiten von großer Bedeutung. Wir stellen fest, dass thermische Schwankungen innerhalb des Tiegels zu einer selektiven Zersetzung des Materials führen, der sich bei hohen Raten auf die Eigenschaften der Bauteile auswirkt. Es werden drei Methoden vorgeschlagen und bewertet, um diese Einschränkung zu verringern. Dazu gehören die Verwendung zusätzlicher organischer Quellen, die Vorkonditionierung des organischen Materials und das Design des Tiegels. Darüber hinaus werden durch den Einbau von Perowskiten mit niedriger und hoher Abscheidungsrate in monolithische Tandems weitere potenzielle Probleme mit hohen Abscheidungsraten untersucht. Diese Arbeit liefert wichtige Erkenntnisse darüber, was erforderlich ist, um die Abscheidungsraten von ko-verdampften Perowskiten sinnvoll zu erhöhen.

Abstract

As human-caused climate change begins to shape socioeconomic policy, and forward thinking nations strive towards net-zero emissions in the face of increasing energy consumption, solar power is the cheapest source of renewable energy. Among next generation solar technologies, perovskite solar cells (PSCs) are a strong candidate to meet evolving energy needs, promising high power conversion efficiencies (PCEs), low material costs and the potential to combine with existing technologies to form tandem solar cells,. Vapour-phase perovskites are especially compatible with current industrial manufacturing technologies. However, fundamental challenges must be addressed specifically for vapour-phase co-evaporated perovskites to be considered suitable for commercialisation. First, there is a PCE deficit between typical co-evaporated and solution-processed perovskites. This can be broadly explained by: inferior bulk material properties, a lack of compatible vapour-based passivants and inferior vapour-phase hole transport layers (HTLs). Furthermore, the substrate dependent growth of co-evaporated perovskites means any new development in vapour-phase HTLs must also understand the resultant perovskite/HTL interface. There also remains limited understanding on the comparative optical properties of semitransparent (ST) PSCs, which is of extreme importance for tandem devices. The second key challenge is their deposition speed. Co-evaporation is a relatively slow process, with deposition rates orders of magnitude lower than what is required for commercialization. Part of this is due to a lack of understanding into the sublimation behaviour of organic cations at high deposition rates. This thesis aims to address these challenges by developing efficient co-evaporated PSCs, including incorporating them into monolithic and mechanically stacked tandem architectures to demonstrate their feasibility.

First, this thesis contributes to the development of four-terminal perovskite/CIGS tandem devices by systematic optimization of the ST-PSC optical properties. Front-and rear-transparent conductive oxides and antireflective coatings are studied to maximise NIR transmission. This is boosted further through a series of optical simulations, aimed at determining future potential of optical management. This strategy is able to achieve four-terminal perovskite/CIGS tandem solar cells with PCEs of 27.3% for solution-processed and 23.8% for co-evaporated perovskite absorbers. The solution-processed results represent near world-record efficiency for 4T perovskite/CIGS tandem devices.

Second, this thesis develops a vapour-phase deposition method for self-assembled monolayer based SAM-HTLs. These layers are critical to the development of *p-i-n* PSCs but historically have exclusively been deposited using solution-based methods. The impact of evaporation on the chemical properties of these materials is thoroughly investigated to ensure they do not undergo thermal decomposition during deposition. Following this, interfacial properties are compared between evaporated and solution-processed SAM-HTLs, finding comparable interfacial properties for all studied materials with both solution-processed and co-evaporated perovskite absorbers. Vapour-phase deposition greatly enhances the flexibility of these materials, and is an inherently conformal and scalable method.

Next, this thesis investigates the interfacial interactions that arise between SAM-HTLs, including vapour-phase SAM-HTLs, and co-evaporated perovskites. Due to the substrate dependent growth of co-evaporated perovskites, understanding these interactions is crucial to developing all vapour-phase PSCs with SAM-HTLs. Through a variety of techniques, the form of this interaction is evaluated as being hydrogen bonding between phosphonic acids and interfacial halides, which primarily impacts organic cation incorporation into the perovskite. Furthermore, the impact of this interaction on perovskite growth and photovoltaic properties is evaluated. This interaction represents a previously unknown form of substrate interaction for co-evaporated perovskites, greatly expanding understanding of this important parameter.

Finally, this thesis analyses the impact of increased deposition rate on formamidinium (FA)-based co-evaporated perovskites. The potential degradation of the FA cation is of great concern for achieving commercially viable perovskite deposition rates. Thermal variations within the crucible will lead to selective degradation of the material, impacting device properties at elevated rates. Three methods are proposed and evaluated to alleviate this constraint. These entail: utilising additional organic sources, preconditioning the organic material and crucible design. Furthermore, by incorporating baseline and elevated deposition rate perovskites into monolithic tandems, other potential issues with high deposition rates are explored. This work represents an important insight into what is required to meaningfully increase co-evaporated perovskite deposition rates.

Table of Contents

1 Introduction

According to the Intergovernmental Panel on Climate Change (IPCC), in the 2011 – 2020 period, the average surface temperature of the Earth has increased by 1.1 °C compared to 1850 – 1900 preindustrial baseline levels.[1] As recently as 2024, this increase in temperatures has spiked to 1.6 °C.[2] The global scientific consensus on climate change is clear on two aspects. Human-driven activity has changed the Earth's climate, and that if decade-scale temperature increase exceed 1.5 °C of pre-industrial levels, then advanced society may no longer be sustainable in the new climate of Earth.[3–5] Fossil fuel consumption, especially in the production of electricity, is a significant driver of global warming by producing 34% of greenhouse gases.[6] Transitioning to renewable energy sources, such as hydro, solar and wind power, is crucial to prevent catastrophic climate change. Further, the practice of electrification, transitioning other sectors to utilise electricity, is considered vital to combat climate change,[7,8] placing ever increasing requirements on renewable energy.

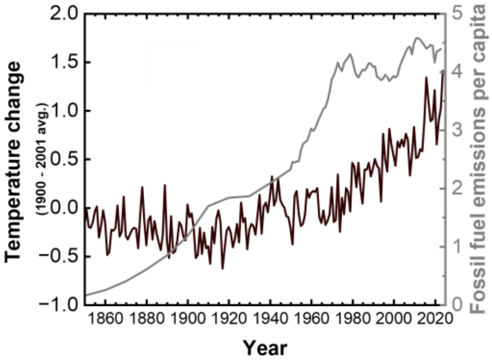

Figure 1-1 Change in average surface temperature (compared to the 1900 – 2001 average temperature) and annual per capita emissions due to the burning of fossil fuels. Data taken from refs.[9,10]

A powerful technology to produce renewable energy is solar power. Approximately $1.08\cdot10^{17}$ W of solar energy strikes the Earth's surface every second, roughly 7000 times the current global electricity consumption.[11] Solar power employs photovoltaic materials to convert this sunlight into usable electricity, and is predicted to be the most common form of renewable energy production by 2029.[8] Solar power also benefits from an incredibly low levelised cost of electricity (LCoE), and is currently the most cost effective electricity source per installed GW, with low estimates in Germany of 4.1 €$_{\text{cent}}$/kWh, compared to similar estimates of 14 €$_{\text{cent}}$/kWh for coal.[12] The current greatest limitation in the transition to solar power is production capacity.[13,14] Installed solar capacity will need to exceed ~75 direct current terawatts (TW$_{\text{DC}}$) by 2050 to meet predicted energy requirements, compared to a capacity of merely 1 TW$_{\text{DC}}$ in 2022.[13,14] While installed capacity continues to surge year-on-year, with approximately 600 GW$_{\text{DC}}$ of production installed in 2024,[15] matching the expected production demand requires constantly increasing power conversion efficiencies (PCE) as well as industrial output. Conservative calculations indicate commercial module PCEs will need to reach 24.1% by 2030, and 27.8% by 2050.[13] The theoretical efficiency limits of single-junction silicon, the largest market share technology, is 29.4%,[16] but approaching theoretical limits is exceedingly difficult in practice.[17] Commercial and laboratory silicon modules have achieved ~22% and 24.9% respectively as of 2024.[18] Hence, reliably achieving the required PCE goals will require tandem devices comprised of multiple junctions.[13,19]

Metal-halide perovskite semiconductors are a prime candidate to create high performance multi-junction photovoltaics.[20–22] Their excellent optoelectronic properties and tuneable bandgap make them efficient and versatile as single-junction perovskite solar cells (PSCs).[23–25] They are also suitable to form multi-junction tandems with established solar technologies such as silicon,[26–32] copper indium gallium selenide (CIGS),[26,33–35] and can even form perovskites-perovskite multi-junction tandems.[36–39] Furthermore, while precise calculations vary based on theoretical stabilities, perovskite-based tandems are predicted to be highly cost effective, further driving down LCoE for solar power.[32,40–42] Two-junction tandem devices are commonly fabricated in two architectures with independently tracked champion PCEs,[43] and independent processing cost considerations.[40,41] These architectures are the monolithic 2T and the mechanically stacked 4T, and will be discussed in more detail in **Chapter 2**.

While laboratory-scale research has achieved impressive PCEs for single-junction and tandem PSCs, commercialisation of perovskites remains in the exploratory phase. Three remaining issues are key. The first can be generally termed the process scalability, which refers to achieving production-scale absorber fabrication speeds and uniform deposition over commercial wafer areas. Next is device stability, achieving a comparable solar cell lifetime to established technologies. While perovskite stability has improved, it is still well below the 25 years expected from silicon solar cells.[44–46] The final challenge can be broadly described as manufacturing compatibility, utilising exclusively industrially relevant deposition methods to meet the previous two challenges. Vapour-phase deposition of perovskite absorbers is a promising route to simultaneously overcome these three challenges. Vapour-phase deposition methods have demonstrated a high degree of uniformity over large areas,[47–50] and are well established in industry, with many other commercial thin-film solar cells extensively utilising vapour-phase methods.[51] Furthermore, these methods have a lower number of parameters that need to be controlled compared to solution-based deposition methods,[51–53] which is also desirable for industrial manufacturing. Finally, while decisive results are currently lacking, vapour-phase methods have exhibited promising stability compared to comparable solution-based methods under light or temperature stressors that mimic operational conditions.[54,55]

However, numerous challenges remain when using vapour-based perovskites, and especially for co-evaporation, the most common deposition method. First is that typical PCEs of vapour-phase PSCs lag compared to solution-based methods for several reasons,[56–58] only recently achieving parity for single-junction sequentially evaporated perovskites, as shown in **Figure 1-2**.[59] This can be partially attributed to a disparity in volume of literature. Comparing all pure vapour-phase and all spin-coating publications from 2009 to 2020, vapour-phase publications average less than 4% of publications.[60] Spin-coating is chosen for comparison as it is the most common solution-based technique and is almost exclusively the method used to achieve champion PSC PCEs. Due to the similarly lower volume of vapour-phase tandem literature,[51,60] tandem devices are also both less commonly reported and achieve lower champion PCE.[43,60]

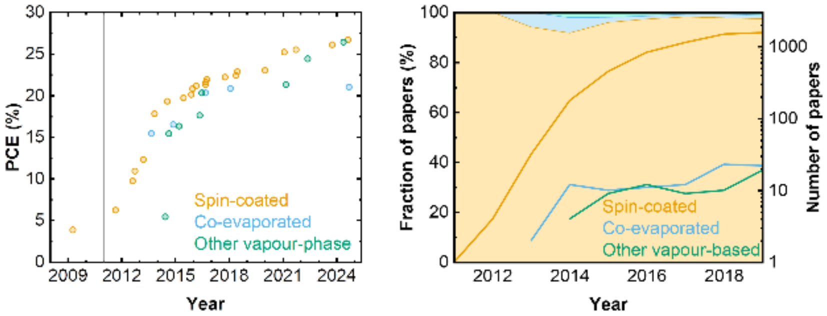

Figure 1-2 A comparison of vapour-phase deposition methods with spin-coating, the dominant solution-based deposition method. (*Left*) Evolution of maximum reported PCE for spin-coating, co-evaporation and other pure vapour-phase deposition techniques. Data taken from ref.[51,59–63] (*Right*) Comparing volume of literature, both as an absolute number (line) and a fraction of the combined papers (area) for each class of deposition method, data taken from ref.[60] Due to the large number of solution processed papers, only years with full reporting in the Perovskite Database are shown.

Furthermore, most research into perovskite-based tandems typically considers gains from perovskite PCE, and not on how systematically optimizing optical properties can improve the underlying subcell without a change in the perovskite absorber (**Challenge 1**). This is a potential niche for vapour-phase perovskites. As vapour-phase perovskites are able to exploit textured surfaces more effectively, tandems focussing more on light management may be able to achieve parity even with reduced perovskite performance.[31,54,64] Comparing optically optimized vapour-based and solution-based perovskites would allow a meaningful identification of the optical and device level challenges for each deposition method (**Challenge 2**), which are not directly related to the established lower co-evaporated bulk film quality.

Another challenge is that, to simplify process transfer to industry, fabricating PSCs with all functional layers deposited in the vapour-phase is desirable, but not currently simple. Perovskites require numerous functional layers for charge transportation and extraction. While vapour-phase methods are common for many of these layers, especially in the readily tandem compatible *p-i-n* architecture, vapour-phase hole transport layers (HTLs) are relatively rare.[65,66] The options that currently exist typically require an interlayer to minimize interfacial losses,[67–69] and HTLs that naturally exhibit low interfacial losses, such as self-assembled monolayers (SAM-HTLs), are not deposited in the vapour-phase (**Challenge 3**).[67,70] Furthermore, co-evaporated perovskites show a strong substrate dependence,[69,71–73] necessitating an understanding of potential interactions between any vapour-phase SAM-HTLs and co-evaporated absorbers (**Challenge 4**), including the impact on bulk perovskite properties (**Challenge 5**).

Finally, while the large area uniformity of vapour phase perovskites is well proven, production-scale absorber fabrication remains well below the industrially relevant ~1000 nm.min^{-1}.[51] Attempts to increase the deposition rates of co-evaporated methylammonium-based perovskites are promising, with maximum rates of 28 nm.min^{-1},[74] but no such attempt has been made for formamidinium (FA)-based perovskites. FA$^+$ can decompose at high sublimation rates,[75] and the impact of potential decomposition at high sublimation rates is not well understood (**Challenge 6**), stifling development in this research field.

The outline of this thesis is as follows:

Chapter 2 describes the fundamental working principles that govern solar cells and how their photovoltaic characteristics and limitations are determined from the associated physics. This chapter goes on to describe metal halide perovskite semiconductors and fabrication methods for single-junction and tandem PSCs. Finally, the particulars of atomic layer deposition in the context of the functional layer SnO_x and thermal sublimation from a crucible in the context of vapour-phase deposition of perovskites are described, including considerations for fabrication of co-evaporated PSCs.

Chapter 3 presents the materials and deposition methods utilised in this thesis to fabricate perovskite absorbers and solar cells. It goes on to discuss the theoretical principles underpinning the characterisation techniques employed to analyse the aforementioned devices and half-stacks.

Chapter 4 addressed **Challenge 1** and **Challenge 2**. It presents the application of high-efficiency wide-bandgap PSCs in mechanically-stacked 4T tandem solar cells. First, we provide a robust series of optical optimizations, describing how transparent conductive electrodes and antireflective layers can impact the near infrared transmission of semitransparent (ST) perovskite absorbers. The resultant optically optimized ST-PSCs are applied as a top cell to 4T perovskite/CIGS tandem solar cells, and the optical and device differences between spin-coated and co-evaporated PSCs are considered. Finally, we outline the potential of further optical optimizations to further improve 4T tandem PCE.

Chapter 5 considers **Challenge 3**. In this chapter we develop and optimize evaporated self-assembled monolayers as a potential vapour-phase HTL. We first demonstrate that the material does not experience degradation at the utilised deposition temperature, and continues to bind to the substrate as a monolayer. Comparing the interfacial and crystal characteristics of spin-coated and co-evaporated perovskites deposited on these layers to spin-coated references reveals that the superior interfacial properties remain unchanged and solution-processed perovskite growth is unchanged.

Chapter 6 addresses **Challenge 4** and **Challenge 5** by investigating the interface between SAM-HTLs and co-evaporated perovskite absorbers. We compare crystallographic and photovoltaic properties of absorbers deposited on HTLs with exposed phosphonic acid functional groups to a true monolayer to understand this additional substrate interaction. Continuing, we determine the precise nature of said interaction as to gain further understanding into the substrate dependence of co-evaporated absorbers, and demonstrate that our results can be replicated using rationally designed monolayers.

Chapter 7 will consider **Challenge 6** by investigating the current potential for increasing the deposition speed of co-evaporated FA-based perovskites. We investigate the relation between perovskite deposition speed and perovskite material and photovoltaic properties. Once we identify the cause of performance loss at high deposition speeds, we provide two methods to overcome this limitation and apply our variant deposition speeds to monolithically stacked 2T perovskite/silicon tandem solar cells with textured silicon bottom cells.

Chapter 8 provides a summary of the key results presented in this thesis and finishes with an outlook for further development of co-evaporated perovskite photovoltaics.

2 Theoretical background

This chapter discusses the fundamental physics principles that govern solar cells. It provides specific descriptions of metal halide perovskite semiconductors, the absorber material which is the focus of this thesis, and outlines their incorporations into solar cells. The chapter concludes with a discussion on two key deposition techniques that were required for this thesis, thermal co-evaporation of perovskites and atomic layer deposition of SnO_x.

2.1 Fundamentals of *p-i-n* solar cells

Solar cell (or photovoltaic cell) is a general term applying to optoelectronic devices which employ the photovoltaic effect to produce electricity. Under illumination, solar cells in an electrical circuit spontaneously and simultaneously generate current and voltage, resuting in an electrical power output.

Most solar cells utilise semiconductor materials, typically silicon, to absorb sunlight. The discussion in this chapter will occur in the context of *p-i-n* semiconductor junctions. In *p-i-n* junctions, an intrinsic semiconductor is contacted to a p-type semiconducting material (either a p-doped or a hole selective layer), and an n-type semiconducting material (either an n-doped or an electron selective layer). These layers are then connected to electrical contacts which extract charge carriers. P-type and n-type layers can be inorganic semiconductors, with valence and conduction bands, or organic semiconductors, with highest occupied and lowest unoccupied molecular orbitals. For simplicity, the following discussion will refer to valence and conduction bands. Alternative architectures which are related to *p-i-n* exist and a selection of these will be discussed briefly at the end of this section.

The basic working principle of a solar cell involves the formation of an electron-hole pair through absorption of incident photons, the generation and separation of free charge carriers and their extraction using selective contacts. The following subsections will expand upon these steps.

2.1.1 Generation of free charge carriers

In a system with two energy levels separated by a bandgap E_g, as outlined in **Figure 2-1**, an incident photon can be absorbed if its frequency v and resultant energy hv follows:[76]

$$h\nu \geq E_g \tag{2.1}$$

If a photon has energy below this value it is not absorbed. Photons with energies equal to or above E_g can be absorbed, promoting an electron from the valence band to the conduction band and leaving a hole in the valence band. If the energy exceeds E_g then the charge carrier will subsequently relax to the band edge, generating heat in the process.

However, it is not guaranteed that incident photons will be absorbed. The actual fraction of light absorbed for a material is governed by a material specific property termed optical absorption coefficient $\alpha(h\nu)$, which can vary substantially based on the optoelectronic properties of the material.

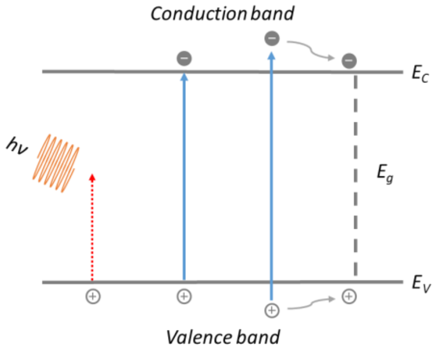

Figure 2-1 Absorption process in semiconductor materials. Simplified visualization of photon absorption in a two-band model, where an electron in the valence band can be promoted to the conduction band upon absorption of a photon $h\nu \geq Eg$.

Importantly for photovoltaic materials, indirect bandgap materials exhibit a significantly reduced $\alpha(h\nu)$ near the band edge as they require lattice vibrations to conserve the momentum of near E_g photons.[78] Using $\alpha(h\nu)$, a term called absorptance $A(h\nu)$ can be calculated for a slab of material with finite thickness d. Neglecting reflectance gives a general function for absorptance as:

$$A(h\nu)=1-e^{-\alpha(h\nu)d} \qquad 2.2$$

When considering realistic $A(h\nu)$, reflectance and scattering must also be considered, and a more general expression considers reflectivity at both the front and back surfaces.[79–85] A full discussion is beyond the scope of this section, but can be found in ref.[86] If it is assumed that the reflection at the rear is unity, and perfect Lambertian scattering occurs at the front surface, $A(h\nu)$ for a textured surface can be given by:

$$A(h\nu)=\frac{1-R_f}{1+\frac{1-R_f}{4n^2 d\alpha(h\nu)}} \qquad 2.3$$

Here, n is the refractive index of the material and R_f is the reflectance of the incident surface.

In semiconductors, optical bandgap, which is the bandgap derived from optical absorption measurements, can differ slightly from electrical bandgap, which is the difference in energy between the conduction band and the valence band. This is due to the potential for the formation of the quasi-particle known as an exciton.[87–90] Excitons allow absorption of photons with energies slightly below the electrical bandgap, and significantly increase the near bandgap absorption of photons.[87,91] The presence of sufficient free carriers, which is commonly found in heavily-doped materials, screens Coulomb interactions and impedes the formation of excitons, and such materials are considered to be free carrier materials.[87,90,92] In excitonic materials, dissociation of the exciton into free charger carriers is necessary for current generation, but specific exciton dissociation mechanisms differ substantially in form and required energy between materials.[87,93,94] For materials with sufficiently low exciton binding energies, this dissociation can occur spontaneously.

Either spontaneous in free carrier materials, or post-dissociation in excitonic materials, an electron hole pair is formed, with electrons in the conduction band and holes in the valence band. These charge carriers must be extracted to generate photocurrent.

2.1.2 Extraction of charge carriers

The separation and extraction of charge carriers and the emergence of a device voltage in *p-i-n* devices can be explained using the band diagram, as shown in **Figure 2-2**. The difference in work function between the contacting p-type and n-type layers (the difference between their Fermi levels (E_{F0}) and the vacuum level) results results in a built-in potential across the device. When the space charge region (w) is sufficiently small compared to the intrinsic semiconductor thickness (d), there is essentially no built-in potential across the device, and this junction can instead be approximated by a flatband solar cell.[87,95,96]

For typical *p-i-n* junction devices, the change in charge carrier concentrations of the valence and conduction bands upon illumination results in new Fermi levels, E_{Fp} and E_{Fn} respectively, a phenomena termed quasi-fermi level splitting (QFLS). This splitting persists under steady state illumination and charge extraction, even under short-circuit conditions. Free charges generated from incident photons will flow along the respective QFL gradients and are extracted at their respective contacts, leading to a diffusion current *via* electrical drift. However, drift is not the dominant charge carrier separation mechanism for *p-i-n* junctions,[97,98] where charge carrier separation and extraction is best described by the drift-diffusion model.

Under no illumination, the occupancy of electrons is strongly dependent on temperature and is given by the Fermi-Dirac function:

$$F(E)=\frac{1}{1+e^{\left(\frac{E\text{-}E_F}{k_BT}\right)}} \qquad 2.4$$

Here E is the energy of the system and E_F is the Fermi level, which can be calculated from the charge-neutral condition.[96] Another term can be introduced, N_C, which is called the effective density of states for the conduction band. For a direct semiconductor, N_C is calculated as:[87,96,99,100]

$$N_C(E) = \frac{\left(2{m_{de}}^3(E\text{-}E_C)\right)^{\frac{1}{2}}}{\pi^2\hbar^3} \tag{2.5}$$

Here m_{de} is the effective mass of an electron in the conduction band and $\hbar = \frac{h}{2\pi}$, which is Planck's constant. Under dark conditions the electron density in the conduction band can now be calculated by combining **Equation 2.4** and **Equation 2.5**:

$$n = \int_{E_C}^{\infty} N_C(E)F(E)dE \tag{2.6}$$

Upon illumination, charge carriers are promoted to the conduction band and separate, which results in a mobile population of free charges. These particles will undergo natural diffusion process. The p-type (n-type) layers have high hole (electron) mobility, coupled with low electron (hole) mobility. This suppression of the hole (electron) current, results in a chemical potential gradient, which drives charge carrier diffusion.[97] This diffusion is sufficient as to overcome small electrical fields generated at high charge carrier currents.[97] Furthermore, by aligning the valence (conduction) bands of the p-type (n-type) layer with the intrinsic semiconductor, they can be highly selective for the relevant charge carrier, blocking the opposing charge carrier and minimizing interfacial recombination.[101,102] Hence, selection of charge transport layers is crucial for efficient charge separation of *p-i-n* devices.[97,102–104] With sufficiently selective contacts, charge carrier diffusion is even able to overcome a small potential field opposing their movement,[97,100] resulting in the simultaneous production of current and voltage.

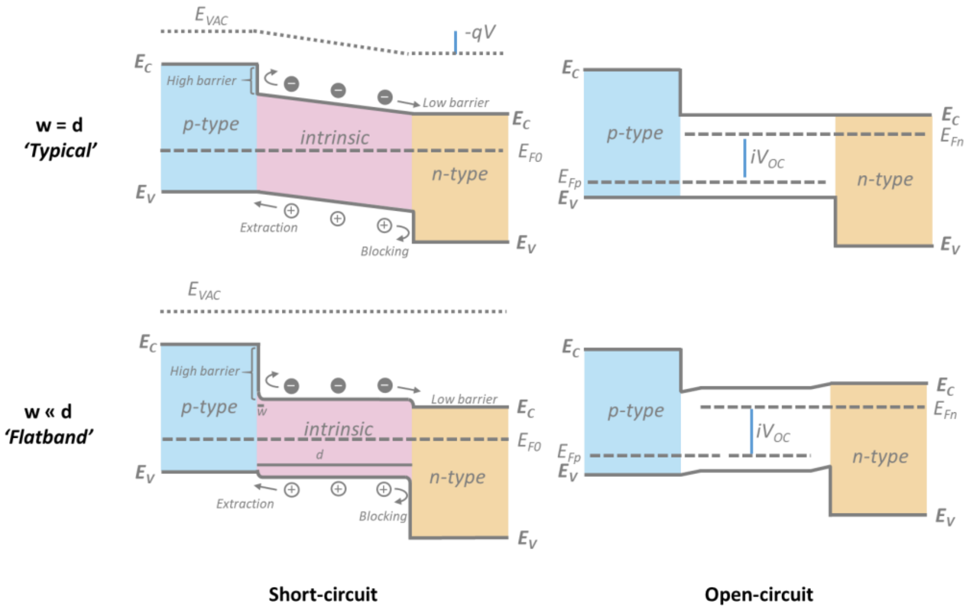

Figure 2-2 Band diagrams of a two potential *p-i-n* junctions. The first junction exhibits a large space-charge region (typical) and the other a comparatively small space charge region (flatband). Both are shown under short-circuit (*left*) and open-circuit (*right*) conditions, demonstrating the splitting of energy levels and typical direction of charge carrier flow in valence and conduction bands.

2.1.3 Implied potential across the *p-i-n* junction

For an illuminated *p-i-n* junction, assuming that the change in relative charge carrier densities is not too extreme, then it can also be assumed that they will form a new QFL equilibrium. We can express the magnitude of the QFLS as a function of the of electron density (n) and hole density (p) by applying **Equation 2.6**:[87,99]

$$n = n_0 e^{\left(\frac{E_{Fn}-E_{F0}}{k_B T}\right)} = N_c e^{-\left(\frac{E_C-E_{Fn}}{k_B T}\right)} \tag{2.7.1}$$

$$p = p_0 e^{\left(\frac{E_{F0}-E_{Fp}}{k_B T}\right)} = N_V e^{-\left(\frac{E_{Fp}-E_V}{k_B T}\right)} \tag{2.7.2}$$

$$np = N_c N_V e^{-\left(\frac{E_C-E_V}{k_B T}\right)} e^{\left(\frac{E_{Fn}-E_{Fp}}{k_B T}\right)} = N_c N_V e^{-\left(\frac{E_g-QFLS}{k_B T}\right)} \tag{2.7.3}$$

Here n_0 and p_0 are the initial densities of electrons and holes, while E_{F0} is the fermi level under short-circuit conditions. n and p are dependent upon charge generation, but also upon the radiative recombination rate R_{rad} according to the radiative recombination constant k_{rad}:[105]

$$R_{rad} = k_{rad} np \tag{2.8}$$

The gradient of charge carriers that were mentioned in **Section 2.1.2** will lead to an electric potential (*V*) acting in the opposite direction as the drift-diffusion current. This implied potential while under current flow is reflected in the QFLS of E_{Fn} and E_{Fp}, with the magnitude of the QFLS directly proportional to *V* by:

$$E_{Fn}-E_{Fp} = QFLS = qV \tag{2.9}$$

If there is no current extraction, i.e at the open-circuit condition, then the absorption of incoming photons will be matched by the radiative recombination of charge carriers, leading to a stable population of charge carriers in the conduction and valence bands and a stable separation of fermi levels.[106] It is possible to use **Equations 2.7 – 2.9** to obtain the equation for the implied open-circuit voltage (iV_{OC}):

$$q \times iV_{OC} = QFLS = E_g - k_B T ln\left(\frac{N_C N_V}{np}\right) = E_g - k_B T ln\left(\frac{k_{rad} N_C N_V}{R_{rad}}\right) \tag{2.10}$$

Short-circuit and open-circuit conditions are extreme situations. Under continuous illumination and standard operational conditions, there will exist a steady-state balance between charge generation, recombination and extraction. The resultant QFLS and extraction of charge carriers results electrical potential across the device and a concurrent photocurrent. The simultaneous generation of voltage and current is key to the practical functioning of solar cells, and the production of electrical power.

2.1.4 Related semiconductor junctions

There exist several related forms of semiconductor junctions, which will be briefly discussed here.

A *p-n* homojunction is comprised of two layer of one material, which are doped to increase the relative density of electrons (n-doped) or holes (p-doped). It resembles a typical *p-i-n* junction in overall form without the intrinsic inner semiconductor, and with the semiconductor material itself comprising the p-doped and n-doped regions.

Meanwhile *n-i-p* (or *n-p*) junctions are comparable to a mirrored *p-i-n* (or *p--n*) junction in band structure. However, charge carrier transport *via* the drift-diffusion model occurs in the opposite direction due to the changed order of the p-doped and n-doped regions. Practical fabrication differences may emerge, and will be discussed in a later section.

2.2 Electrical representation of a solar cell

In this section we will discuss a simple representation of a solar cell called the one diode model. Using this model, we will outline how various photovoltaic parameters can be calculated. Finally, we will describe a method to quantify open-circuit voltage losses.

2.2.1 One diode model of a solar cell

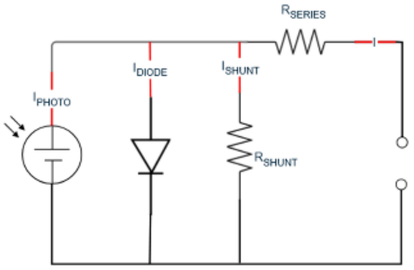

Figure 2-3 Electrical representation of a solar cell using the one diode model.

A solar cell can be represented as a basic equivalent circuit, as shown in **Figure 2-3**, with a source of photocurrent, a single diode and resistors providing series (R_{Series}) and shunt (R_{Shunt}) resistance. More complex models exist, including multiple diode model, which also measures charge carrier recombination. Series resistance represents the net electrical resistance of the solar cell, while shunt resistance represents alternative current pathways. Output current density can be represented as:

$$J(V)=J_{photo}-J_{diode}-J_{shunt} \tag{2.11}$$

Here J_{photo} represents photo-generated current density, J_{diode} represents current density flow across the diode, which is proportional to the dark current density, and J_{shunt} represents leakage current density due to shunt resistance. The current density flowing across a real diode is given by:

$$J(V)=J_0\left(e^{\left(\frac{qV}{n_{id}k_BT}\right)}\text{-}1\right) \qquad 2.12$$

Where J_0 is the dark current density, q the elemental charge, V the voltage, n_{id} the ideality factor, k_B the Boltzmann constant and T the temperature. Taking into account R_S and R_{SH}, **Equation 2.12** can be rewritten as:

$$J(V)=J_{photo}\text{-}J_0\left(e^{\left(\frac{q(V+J(V)R_{Series})}{n_{id}k_BT}\right)}\text{-}1\right)\text{-}\frac{V+J(V)R_{Series}}{R_{Shunt}} \qquad 2.13$$

The solving of this equation is non-trivial. It is easier to consider an ideal solar cell where $R_S = 0$ and $R_{SH} = \infty$. In that case:

$$J(V)=J_{photo}\text{-}J_0\left(e^{\left(\frac{qV}{n_{id}k_BT}\right)}\text{-}1\right) \qquad 2.14$$

2.2.2 Deriving solar cell efficiency from the one diode model

When $V = 0$ the short-circuit current condition J_{SC} is obtained:

$$J_{SC}=J(0)=J_{photo}\text{-}J_0(1\text{-}1)=J_{photo} \qquad 2.15$$

Conversely, when $J(V) = 0$, and considering that $J_{photo} >> J_0$, the open-circuit voltage V_{OC} condition is obtained:

$$V_{OC}=\frac{n_{id}k_BT}{q}ln\left(\frac{J_{photo}}{J_0}+1\right) \approx \frac{n_{id}k_BT}{q}ln\left(\frac{J_{photo}}{J_0}\right) \qquad 2.16$$

Hence, V_{OC} is dependent on the photo-generated current density and the dark current density. Photogenerated current is typically material dependent, and does not vary significantly. J_0 can vary by orders of magnitude depending on the recombination within the cell, making V_{OC} representative of overall recombination within the device.

A typical *J-V* curve without series or shunt resistance losses is shown in **Figure 2-4**, along with the impact of reintroducing R_{Series} and R_{Shunt}. When plotting output power P:

$$P=JV \qquad 2.17$$

Then a new term can be defined, maximum power point (MPP). MPP can be defined as:

$$P_{MPP}=J_{MPP}V_{MPP} \qquad 2.18$$

The variable called fill factor (FF), gives the ratio of the measured P_{MPP} to a theoretical P_{MPP} where J_{MPP} = J_{SC} and V_{MPP} = V_{OC}. Fill factor can serve as a measure for imperfections within a solar cell, and is defined by:

$$FF = \frac{P_{MPP}}{P_{MAX}} = \frac{J_{MPP}V_{MPP}}{J_{SC}V_{OC}} \tag{2.19}$$

By assuming an exponential *J-V* curve, FF can be approximated directly from the V_{OC} using the equation:[100]

$$FF = \frac{\frac{qV_{OC}}{k_BT} - ln\left(1 + \frac{qV_{OC}}{k_BT}\right)}{1 + \frac{qV_{OC}}{k_BT}} \tag{2.20}$$

Finally, combining **Equation 2.18** and **Equation 2.19** defines the power conversion efficiency (PCE) of a solar cell based on the ratio of generated to incident power, which can be given by the absorbed flux (φ_{absorb}):

$$PCE = \frac{FF \times J_{SC} \times V_{OC}}{\varphi_{absorb}} \tag{2.21}$$

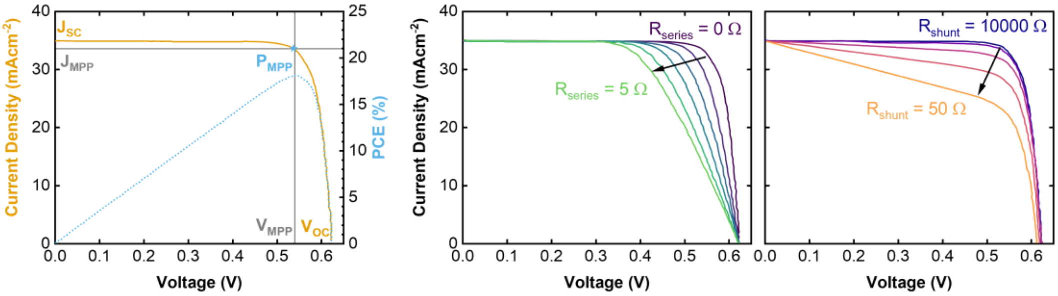

Figure 2-4 Parameters of a representative *J-V* curve and the impact of resistance on these curves. (*Left*) *J-V* curve of a silicon cell, with the photovoltaic parameters (J_{SC}, J_{MPP}, P_{MPP}, V_{OC} and V_{MPP}) marked and a visualization of the PCE at each point in the curve. (*Middle, Right*) Visualisation of the impact series and shunt resistance will have on a *J-V* curve as they deviate from ideal values of R_{series} = 0 and R_{shunt} = ∞. Data adapted with permission from ref.[107]

2.2.3 Recombination mechanisms

The difference between iV_{OC} and V_{OC} (externally measured open-circuit voltage) can be broadly considered as the difference of (E_{Fn}-E_{Fp}) in the bulk absorber, and ($E_{Fn}{}^{cathode}$-$E_{Fp}{}^{anode}$), which can be primarily attributed to non-radiative interfacial recombination.[108] This difference is easiest to quantify under V_{OC} conditions, where directional charge carrier motion is driven purely by recombination,[108,109] which results in a spatial non-uniformity of the electron and hole QFLs near the contacts. The classical interpretation of this bending is that it can be attributed to non-ideal charge transport, such as the relative mobilities of majority and minority charge carriers.[100,106] However, there exist various other non-radiative recombination mechanisms which can also impact this bending.[103,108–112] Quantifying the relative contribtuions of these loss pathways is non-trivial due to the myriad of potential origins for non-radiative recombination. These mechanisms can be roughly designated into three categories, which are visualised in **Figure 2-5**:

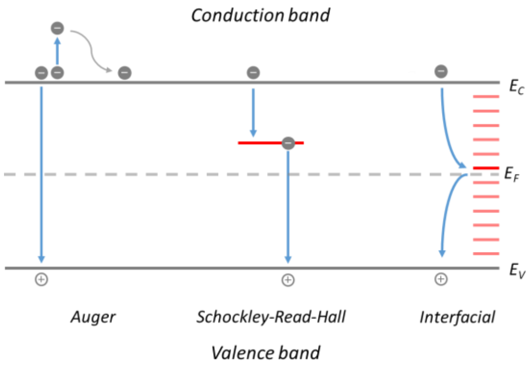

Figure 2-5 Basic schematic illustration of non-radiative recombination in semiconductors. Blue arrows indicate the movement of electrons. Holes will move in the opposite direction to the arrow. Red lines indicate trap states. The provided schematic of interfacial recombination is through a gap state, although other mechanisms exist for interfacial recombination.

Auger recombination is a trimolecular process when excess energy from an electron and hole recombination is transferred to another electron or hole, which will then thermalize back to the band edge without emitting a photon.[113,114] As Auger recombination relies on three charge carriers, it is proportional to charge carrier density to the power of three, either $n_e^2 n_p$ or $n_e n_p^2$, and is important in materials with high charge carrier density, such as silicon.[114,115] Auger recombination is an intrinsic process.

Shockley-Read-Hall recombination occurs when defect induced trap energy states form within the bandgap, and can capture electrons or holes in a form of non-radiative recombination.[116–119] Trap states can originate from crystallographic defects or dopants, either intentionally or from contamination.[109,120–122] Crystallographic defects can be categorised as point defects (atomic vacancies, interstitials, anti-site substitutions), or higher-dimensional defects (dislocations, grain boundaries, precipitates).[118] For multicrystalline devices, these crystallographic defects are particularly common at grain boundaries.[121–125] This recombination process dominates at low charge carrier densities. Shockley-Read-Hall recombination is extrinsic, meaning strategies to prevent or mitigate defects and grain boundaries can effectively reduce it.

The final class is interfacial recombination, which is a broad term to associate all non-radiative recombination at layer interfaces. Interfaces recombination orginates from: i) crystallographic defect induced trap states, ii) induced deep trap states at the CTL, iii) energy level misalignment between the intrinsic semiconductor and the CTL causing band bending,[102,126] iv) back transfer recombination and contact resistances.[109,117,123,124,127–129] Interfacial recombination is also extrinsic, meaning that selection of proper CTLs and minimising contact resistances can reduce its impact.

2.2.4 PLQY to quantify non-radiative voltage losses

To determine the impact of non-radiative recombination, assumeing all emitted photons stem from radiative recombination of free charges measurements of the photoluminescence quantum yield (PLQY) can be perfomed. . PLQY is defined by the ratio of the absorbed φ_{absorb} and the emitted φ_{emit} photon flux. Under steady-state illumination, a PLQY of unity indicates that all recombination is radiative, while lower values reveals the presence of non-radiative pathways as described in **Section 2.1.3**. For simplicity, it will be assumed in this section that $n_{id} = 1$. For realistic devices, n_{id} must also be considered. Under open-circuit conditions:[103,110,130,131]

$$PLQY=\frac{\varphi_{emit}}{\varphi_{absorb}}=\frac{J_{rad}}{J_{total}}=\frac{J_{rad}}{J_{non\text{-}rad}+J_{rad}}=\frac{J_{rad}}{J_G} \qquad 2.22$$

Here, J_{rad} and $J_{non\text{-}rad}$ refer to the radiative and non-radiative current densities, and J_G refers to the generation current density. If recombination goes through the same channels independent of QFLS,[132] then applying **Equation 2.12** gives:

$$J_{rad}=J_{0,rad}\left(e^{\left(\frac{qV}{k_BT}\right)}\text{-}1\right) \approx J_{0,rad}\left(e^{\left(\frac{qV}{k_BT}\right)}\right) \qquad 2.23$$

$J_{0,rad}$ is obtained by integrating the external quantum efficiency over the blackbody spectrum. By applying **Equation 2.9 and 2.22**:

$$QFLS=k_BTln\left(\frac{J_{rad}}{J_{0,rad}}\right)=k_BTln\left(PLQY*\frac{J_G}{J_{0,rad}}\right) \qquad 2.24.1$$

$$QFLS=k_BTln(PLQY)+k_BTln\left(\frac{J_G}{J_{0,rad}}\right) \qquad 2.24.2$$

Finally, this equation can be converted into an implied voltage and written as:

$$iV_{OC}=V_{OC\text{-}rad}+\frac{k_BT}{q}ln(PLQY) \qquad 2.25$$

$V_{OC\text{-}rad}$ is the radiative limit of the open circuit voltage, given by:

$$qV_{OC\text{-}rad}=k_BTln\left(\frac{J_{SC}}{J_{0,rad}}\right) \qquad 2.25$$

2.3 Theoretical limits of single-junciton and tandem solar cells

In this section we shall discuss the Shockley-Queisser limit for single-junction devices and how they can be applied to obtain detailed balance limit calculations. We shall also briefly discuss how the limits are higher for multiple-junction tandem devices.

2.3.1 Assumptions for utilised detailed balance limit calculations

Here we will address the assumptions used for the provided detailed balance limit calculations. Real solar cells are unable to convert all incident sunlight into electrical energy with 100% efficiency. As mentioned in **Figure 2-2**, when a photon strikes the absorber layer (assuming reflection is zero and absorptance is infinite), one of three things will happen:

- $hv < E_g$: The photon will not be absorbed, transmission losses occur
- $hv = E_g$: The photon will be absorbed
- $hv > E_g$: The photon will be absorbed, thermalisation losses of excess energy occur

Only absorbed photons contributed to the photocurrent, with the excess energy of photons in the $hv > E_g$ case transformed into phonons, which are not extracted and do not contribute to electricity, as discussed in **Section 2.1**.[133] Hence, only in the $hv = E_g$ case will losses not occur. Fundamental recombination losses from radiative recombination will further decrease the maximum extracted voltage. Calculations of the maximum achievable PCE for a solar cell, also known as the Shockley-Queisser detailed balance limit,[134,135] must make several assumptions:

- 100% of photons with $hv \geq E_g$ are absorbed (no transmission or reflection losses)
- 0% of photons with $hv < E_g$ are absorbed
- 100% of absorbed photons generate electron-hole pairs
- Infinite mobility of charge carriers, leading to 100% extraction
- Only radiative recombination occurs
- No preceding layers result in parasitic absorption

2.3.2 Schockley-Queisser detailed balance limit calculations

These calculations involve using determining the absorption and emission flux to determine the *J-V* characteristics of the solar cell under these conditions.

$$J=-q(\varphi_{absorb}-\varphi_{emit}) \tag{2.27}$$

For a given black body, φ(E) is determined using Planck's equation for black body radiation:

$$\varphi(E)=\frac{2\pi}{h^3c^2}\frac{E^2}{e^{\frac{E}{kT}}\text{-}1}\approx\frac{2\pi}{h^3c^2}\frac{E^2}{e^{\frac{E}{kT}}} \qquad 2.28$$

Here E is the energy of a photon, given by $E = hv$ and T is assumed to be constant for the emitting surface. For the following calculations, assume the temperature of the solar cell to be equal to the temperature of the Earth. For emission of a solar cell, which can be under applied voltage V, this equation becomes:[106]

$$\varphi_{cell}(V,E)\approx\frac{2\pi}{h^3c^2}\frac{E^2}{e^{\frac{E\text{-}qV}{kT}}}=\frac{2\pi}{h^3c^2}\frac{E^2}{e^{\frac{E}{kT}}}e^{\frac{qV}{kT}}=\varphi_{earth}(E)e^{\frac{qV}{kT}} \qquad 2.29$$

Thus, when applying the above assumptions it is possible to obtain the equation:

$$J(V)=q\left(\int_{E_g}^{\infty}\varphi_{cell}(E)\,dE\text{-}\int_{E_g}^{\infty}\varphi_{sun}(E)\,dE\text{-}\int_{E_g}^{\infty}\varphi_{earth}(E)\,dE\right) \qquad 2.30.1$$

$$J(V)=q\left(\int_{E_g}^{\infty}\varphi_{earth}(E)e^{\frac{qV}{kT}}\,dE\text{-}\int_{E_g}^{\infty}\varphi_{earth}(E)\,dE\text{-}\int_{E_g}^{\infty}\varphi_{sun}(E)\,dE\right) \qquad 2.30.2$$

$$J(V)=q\left(\int_{E_g}^{\infty}(e^{\frac{qV}{kT}}\text{-}1)\varphi_{earth}(E)\,dE\text{-}\int_{E_g}^{\infty}\varphi_{sun}(E)\,dE\right) \qquad 2.30.3$$

The solar spectrum arriving on Earth is not a perfect black body spectrum, primarily due to and reflection absorption in the atmosphere. It is possible to quantify the change in solar blackbody radiation by the length of the atmosphere it must pass through, called the air mass (AM). AM0 represents the solar radiation outside Earth's atmosphere. The standard spectrum used for detailed balance limit calculations and photovoltaic testing assumes an incident angle of 48.2°,[87] leading to a net irradiance of $\int_0^{\infty}\varphi_{sun}^{AM\ 1.5G}dE$ = 100 mW.cm^{-2}.

By solving **Equation 2.29**, then using these calculations to obtain V_{OC} from **Equation 2.14**, FF from **Equation 2.18** and PCE from **Equation 2.19**, it is possible to determine the theoretically achievable solar cell parameters as a function of E_g.[136,137] The results of these calculations are shown in **Figure 2-6.** These indicate that, for a single-junction device, the maximum achievable PCE corresponds to a bandgap of 1.337 eV and a PCE of 33.7%.

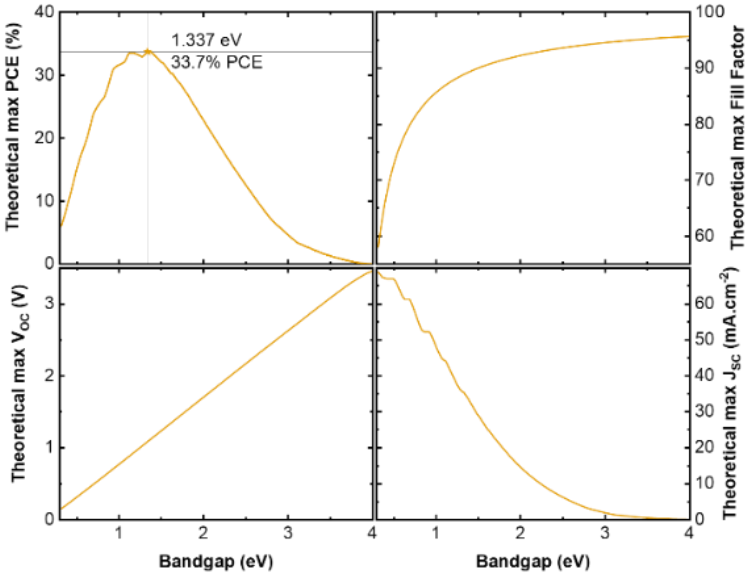

Figure 2-6 Theoretical evolution of solar cell parameters based on bandgap. Theoretical maximum PCE (*top-left*), fill factor (*top-right*), V_{OC} (*bottom-left*) and J_{SC} (*bottom-right*) based on Shockley-Queisser detailed balance limit calculation of a device illuminated by an AM1-5G spectrum. Data adapted from ref.[136]

2.3.3 Multi-junction detailed balance limits

Detailed balance limit calculations can also be applied to multi-junction devices by combining a series of absorbers with decreasing E_g, which increases the theoretical achievable limit.[138] These calculations indicate that multi-junction devices utilising stacked absorbers can surpass the theoretical limits of maximum PCE of single-junction solar cells.[138–140] By stacking multiple absorbers a gradient is formed, ensuring low energy photons are transmitted while higher energy photons are absorbed. This strategy reduces thermalisation and extraction losses by ensuring a greater proportion of incident photons satisfy $h\nu \approx E_g$. **Figure 2-7** demonstrates how the double-junction tandem devices increase their utilisation of the solar spectrum compared to single-junction devices.

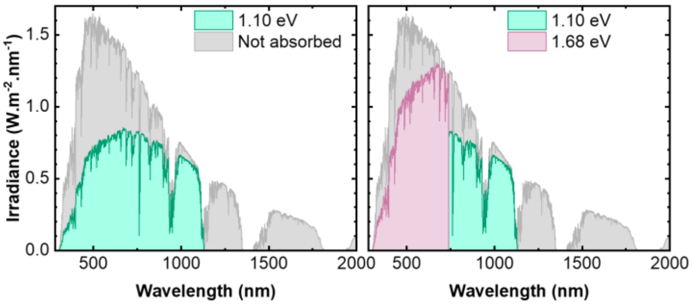

Figure 2-7 Effectively utilized portion of the AM1.5G solar spectrum, subcell bandgap and resultant maximum PCEs for various junction solar cells. Shown are sample single-junction devices with an absorber bandgap of 1.10 eV (*left*) and double-junction tandems withabsorber bandgaps of 1.10 eV and 1.68 eV (*right*). Data adapted from ref.[136]

2.4 Metal halide perovskite semiconductors

Perovskites refer to a family of compounds of the general formula ABX_3. Here A is a monovalent cation, B a divalent metal cation and X are anions. This section will focus on organic-inorganic halide perovskites, where X is a halide material, and A can be an organic cation. They are highly promising photovoltaic materials with outstanding optoelectronic properties, and are the utilised absorber material for this thesis.

2.4.1 Structure of organic-inorganic perovskites

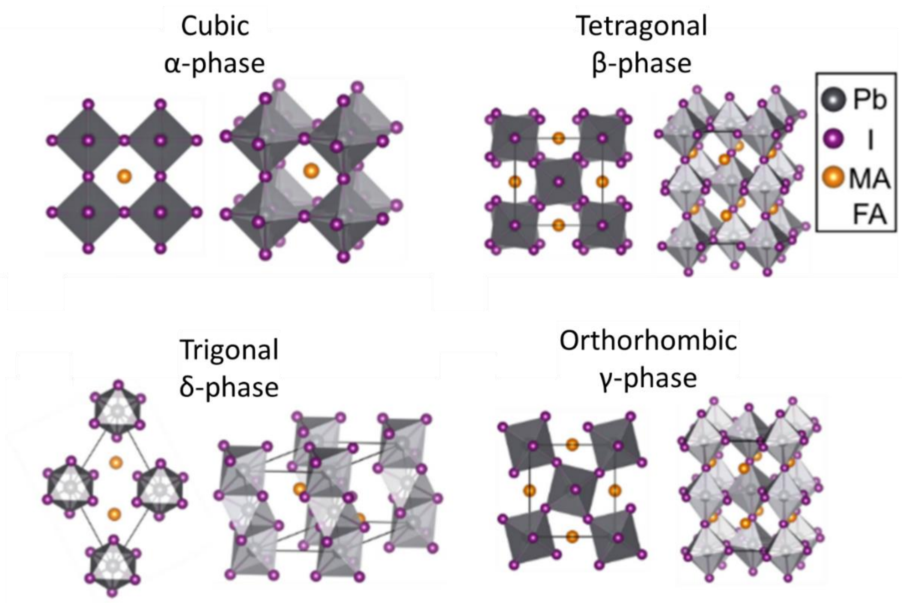

Figure 2-8 Crystal structure of a typical organic-inorganic halide perovskite. The γ-phase and β-phase occur for perovskites with methylammonium or formamidinium cations respectively, but require temperatures well below 200 K. Figure reproduced with permission from Springer Nature Limited, ©2020.[141]

An idealised perovskite takes a cubic structure, with the A site surrounded by corner-sharing $[BX_6]^{4-}$ octahedral clusters. In photovoltaic applications, cation A is typically methylammonium (MA^+), formamidinium (FA^+) or Cs (Cs^+). Cation B is typically either lead (Pb^{2+}) or tin (Sn^{2+}). Finally the anion X is a halide, typically iodine (I^-), bromine (Br^-) or chlorine (Cl^-). Real perovskites can form in multiple phases, as outlined in **Figure 2-8**, with the stable phase defined by the chemical composition and operating temperature.[141] The expected stable phase can typically be determined using the Goldschmidt tolerance factor:[142]

$$t=\frac{r_A+r_X}{\sqrt{2}(r_B+r_X)} \tag{2.31}$$

Here, r_A, r_B and r_X are the ionic radii of each corresponding ion. When $0.8 < t < 1$, a perovskite can form in the ideal cubic phase, with slight distortions for $t < 1$.[94,143–145] For $t < 0.8$, non-ideal perovskite phases will be more stable at room temperature. Meanwhile for $t > 1$, the A cation will disrupt the typical lattice, leading to the formation of lower dimensional perovskites.[146,147] This effect restricts the possible stable perovskite compositions. A second figure of merit for perovskite formation is known as the octahedral factor (μ), which governs the ability to form a BX_6 octahedral in the perovskite structure. This factor is given by:

$$\mu = \frac{r_B}{r_X} \qquad 2.32$$

An ideal perovskite requires $0.8 < t < 1.0$ and $0.414 < \mu < 0.732$.[145]

2.4.2 Optoelectronic properties of organic-inorganic perovskites

Organic-inorganic perovskites possess a high absorption coefficient ($\alpha > 10^4$ cm^{-1})[23,148,149] and sharp band edge, which is commonly attributed to their direct bandgap and excitonic properties.[150–153] As mentioned in **Section 2.1**, exciton formation improves near bandgap absorption. However, due to their low binding energies,[152,154,155] excitons in perovskites can readily dissociate into free charge carriers at room temperature, and free charges comprise the majority charge carrier.[83,93,150,151,156,157]

Free carriers in perovskites demonstrate high mobilities (6 - 10 $cm^2.V^{-1}.s^{-1}$),[158–162] low levels of bimolecular recombination,[160,163] and long diffusion lengths.[24,164–167] The high absorption coefficient also enables perovskites to efficiently absorb light with sub-μm absorber thicknesses.[23,148,149] Coupling low thickness with high carrier mobility enables perovskites to achieve high PCEs even in the flatband model.

What makes perovskites even more valuable is their tunable bandgap, which can be varied from 1.5 – 3.1 eV for lead based perovskites, with the inclusion of tin allowing bandgaps as low as 1.1 eV.[168,169] Bandgap tuning is achieved through compositional engineering. Replacing I^- halides with Br^- or Cl^-, and the organic cations with Cs^+ increases the absorber bandgap.[170–175] However, selection of stable compositions must also consider tolerance factor.[143,144,146,147,176,177] Pairing excellent optoelectronic properties with the flexibility offered by the potential to vary bandgap make perovskite absorber materials an excellent choice for a wide range of optoelectronics.[23,34,178–182]

2.5 Perovskite solar cells

In this section we will outline the possible architectures used in perovskite solar cells (PSCs) along with the requirements for electrodes and charge transport layers. We will finish with a discussion of common absorber fabrication techniques.

2.5.1 Perovskite single-junction solar cell architectures

Single-junction PSCs are typically fabricated onto a glass substrate, coated with transparent conductive oxide (TCO) to form a transparent electrode. The typical architecture is one of the following (shown in **Figure 2-9**):[102,183,184]

- *p-i-n*: TCO/HTL/perovskite/ETL/rear electrode
- *n-i-p*: TCO/ETL/perovskite/HTL/rear electrode

These architectures are also known as planar (*n-i-p*) and inverted planar (*p-i-n*). This thesis will exclusively report on perovskite solar cells using the *p-i-n* architecture. The choice of rear electrode is dependent on the requirements for the device. Opaque devices typically utilise a metallic rear electrode with high reflectivity to double the optical path of incident lights. For semitransparent devices or monolithic tandems, as discussed in **Chapter 4** and **Chapter 7** respectively, the electrode is often comprised of a second TCO, as light needs to be transmitted through the entire device, with metal deposited outside the active area to improve the effective sheet resistance, as shown in **Figure 2-9**. Monolithic tandems also differ in that the substrate will be another solar cell instead of glass, and a recombination junction or tunnel junction will replace the TCO, as mentioned in **Section 2.1.3**.

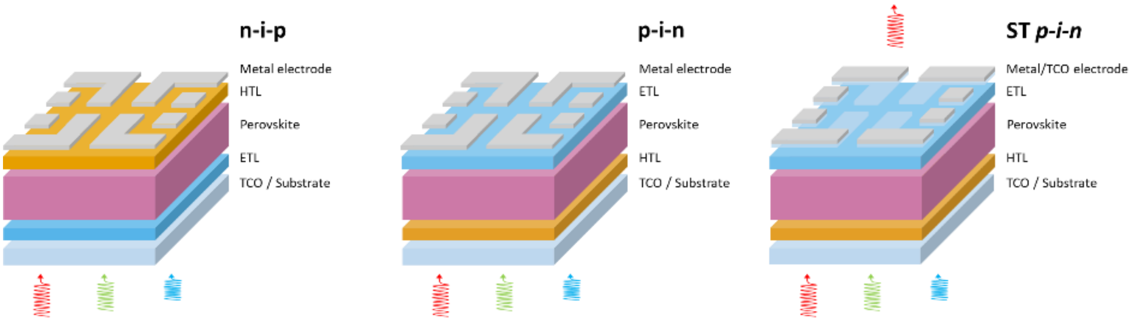

Figure 2-9 Schematic illustrations of possible perovskite solar cell architectures. Shown are planar *n-i-p* (*left*) and inverted planar *p-i-n* (*middle*) perovskite architectures, and a semitransparent form of the *p-i-n* architecture (*right*). The electrode (and TCO) pattern shown is what is used for single-junction devices in this thesis.

There are a large number of compatible materials for each layer charge transport and extraction layers (ETL, HTL, TCO, electrode), with the optimum layers dependent on architecture and specifics of the perovskite absorber. Ideal HTLs and ETLs will match the perovskite valence and conduction bands respectively in order to minimize band bending.[102,112,126] Due to the primarily flatband nature of perovskites, band matching, low interfacial losses and high carrier selectivity is crucial.[102,126]

Preceding layers must also be suitable for perovskite growth, as will be discussed in the next section. Layers following the perovskite cannot use temperatures that lead to thermal degradation of the perovskite and must use orthogonal solvents and low energy deposition processes, or must incorporate dense buffer layers to protect the perovskite.[37] Alternative fabrication routes such as lamination can relax this specific requirement, but are not commonly used at time of writing.[185,186]

2.5.2 Multi-junction tandem solar cell architectures

Perovskite double junction tandem devices, hereafter referred to as tandems, are commonly fabricated in one of two architectures. These architectures are comprised of the monolithically integrated two-terminal (2T), and the mechanically integrated four-terminal (4T). There exist another potential architecture, termed three-terminal, but it will not be discussed in this section.[187,188] **Figure 2-10** outlines the electrical connections and optical paths of 4T- and 2T-tandem devices. Typically in 4T tandems, an index matching interlayer can be inserted between the top (wide E_g) and bottom (narrow E_g) subcells to minimize reflections.

Each architecture possesses unique advantages and disadvantages. The monolithic integration of 2T means it is connected in series, with both optical and electrical coupling, as shown in **Figure 2-10**. 2T tandems can also preserve the underlying substrate texturing, enabling enhanced light in-coupling in the top subcell.[29,31,54,64,189–194] However, this integration produces additional challenges, such as the requirement for compatible processing and the need to minimize losses from recombination layers or tunnelling junctions.[21,195,196] 2T tandems are typically assumed to require current matching in both subcells for optimal devices,[197] leading to a relatively narrow range of suitable combinations of bandgap for the top and bottom subcell compared to 4T tandems.[22,198] In reality, small levels of current mismatch can be beneficial for tandem device FF and stability,[199] leading to a range of acceptable bandgaps.

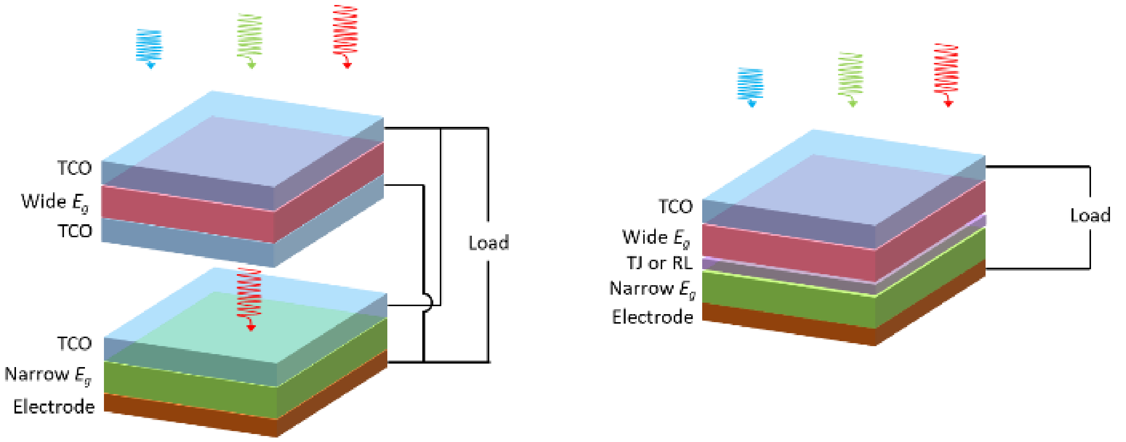

Figure 2-10 Representative illustration of the two most common tandem architectures for tandem devices incorporating perovskites. Shown are 4T (*left*) and 2T (*right*) tandem architectures. TCO refers to transparent conductive oxide, typically paired with a metallic electrode on non-active areas to reduce sheet resistance. TJ and RL refer to tunnel junction or recombination layer, which facilitates charge carrier recombination to prevent build-up of charge from the currents in the top and bottom sub cells.

4T tandems are fabricated independently, and hence do not suffer from these requirements. Despite the lack of current matching, energy yield calculations do not report on a significantly higher potential PCE.[38,200–202] This is due to their enhanced optical losses stemming from additional parasitic absorption which arises from additional TCOs and increased reflection losses.[21,198] In addition, the need for an additional TCO and substrate makes the perovskite subcell more costly for 4T tandems.[42] The industrial module fabrication processes also requires either inverters or complicated module interconnection.

2.5.3 Processing of perovskite absorbers

There exist two basic fabrication classes for perovskite solar cells, solution-based deposition methods and vacuum based deposition methods. This thesis utilises both basic fabrication class. **Chapter 4 and 5** will focus on solution-processed perovskites deposited *via* spin coating, while **Chapter 6 and 7** will focus on vacuum-based perovskites deposited via co-evaporation. Hybrid processes, where precursors are deposited by different methods, also exist but will not be discussed here as they are not used in this thesis

Solution-processing encompasses spin-coating, inkjet printing, blade coating, slot-die coating and spray coating. Precursors are dissolved in a solution and film formation typically follows from super-saturation, either from solvent extraction / evaporation or from applying an anti-solvent.[37,207–209] Solution processing offers simple process optimization and rapid absorber deposition.[210] However, solution-processed methods are prone to higher upscaling losses,[211] and typically require toxic solvents, although some recent work has involved investigation of green solvent alternatives.[212,213] Furthermore, certain substrates are incompatible for solution processed perovskites due to poor precursor wetting,[214] which can significantly impact device yield, and will form part of the discussion in **Chapter 5**.

Vacuum-based vapour-phase deposition is a broad term for methods occurring under vacuum conditions. It includes thermal sublimation from a crucible, close space sublimation (currently used for MA^+, FA^+ and Cs^+), flash sublimation of perovskite powders and chemical vapour deposition.[215–217] Vacuum methods are well suited for rough or textured surfaces, such as those found in high efficiency Si bottom cells, due to their conformal coating properties and easy thickness control, and exhibit reduced upscaling losses for industrially relevant active areas.[31,211,218,219] However, the typically reported device performance of *p-i-n* architectures is reduced compared to solution-based processes, with only some recent work on sequential evaporation achieving comparable PCEs for the same composition.[220] Much of the device performance deficit is attributed to the limited options for bulk and surface passivation while retaining all-evaporated layers.[221–223] Vapour-phase processes are also slower than solution-processed methods.[51] While flash sublimation has demonstrated deposition rates above 1000 $nm.min^{-1}$,[215,224–226] the more common co-evaporation remains a comparatively slow process, with only recent studies achieving rates of ~26 $nm.min^{-1}$.[75,227] Vacuum processed perovskites are unaffected by poor wetting, but many vacuum deposited layers show a strong influence of substrate dependent growth,[70,73,228,229] which limits the choice of suitable under layers, and will be discussed further in **Chapter 5** and **Chapter 6**.

2.6 Vapour-phase deposition of buffer and absorber layers

In the following section we will outline some considerations and descriptions of two deposition methods that are heavily featured in this thesis: atomic layer deposition of SnO_x and vapour-phase thermal sublimation of perovskites.

2.6.1 Atomic layer deposition

Atomic layer deposition (ALD) is an adaptation of chemical vapour deposition,[223] producing layers with increased uniformity, conformality and control over film thickness.[224] The principle of ALD involves a series of self-limiting surface reactions to afford monolayer growth. A full layer is known as a cycle, which proceeds in two half cycles. The first half cycle exposes a heated surface to a gaseous precursor, which is adsorbed and reacts with surface sites. Excess reactant is removed from the reactor through a purging step, involving an influx of inert gas. Next the coated surface is exposed to an oxidizing reactant, which reacts to form the first layer of the new material before excess reactant is purged. Exposed surface sites will allow binding of a new precursor layer, continuing the growth of the film.

2.6.1.1 Substrate dependence of ALD growth

As ALD is initiated by the reaction of a precursor with substrate surface groups (such as hydroxyls), initial layer formation is highly substrate dependent. ALD on non-ideal surfaces leads to a nucleation delay period before isolated reaction sites eventually coalesce into a continuous layer.[225] This is especially important for *p–i-n* perovskite solar cells, as the common preceding layer is C_{60}-fullerene or [6,6] phenyl-C61-butyric acid methyl ester (PCBM), which are considered non-reactive mediums for ALD growth.[226] When depositing on non-reactive surfaces, typical precursors do not react with the underlayer.[227] Growth occurs from precursor diffusion into the organic layer, if some precursor remains during the subsequent purge cycle it can react with water to form a permeable layer with poor interfacial quality, that itself provides a reactive surface.[36,226,228] The extent of this sub-surface diffusion is dependent on the functional groups of the precursor.[225] Precursor chemical properties can also influence nucleation delay, with tetramethyl aluminium (TMA) acting as a Lewis acid to enhance reactivity in unreactive compounds.[229] This diffusion increases the importance of deposition parameters to minimise the nucleation delay, or necessitates the use of layers such as Al_2O_3 or AZnO to reduce nucleation delay.[226,230]

2.6.2 ALD of tin oxide (SnO_x)

ALD-SnO_x, grown from the precursor TDMASn with H_2O as an oxidiser, is the primary ALD material deposited in this work due to its high density and suitability as a buffer layer, the lack of required post-deposition annealing and relatively fast growth rate.[226,230–233] ALD-SnO_x is widely used in *p-i-n* architectures as both an electron selective layer, and as a buffer layer for semitransparent or monolithic tandem devices to protect the perovskite from sputter damage from transparent conductive oxide deposition. Density functional theory modelling shows that ALD-SnO_x growth follows the reaction pathway:[232]

$$(OH)^*_x + Sn(DMA)_4 \rightarrow O_2Sn(DMA)_{4\text{-}x}{}^* + xHDMA$$

$$O_2Sn(DMA)_{4\text{-}x}{}^* + 2H_2O \rightarrow (OH)^*_x + SnO_2 + (4\text{-}x)HDMA \qquad 2.33$$

Here * refers to the surface species, while the extent of the conversion 'x' determines the number of residual DMA ligands during the water half reaction, with *in-situ* measurements indicating an x distribution between 2 and 3.[232,234] TDMASn is adsorbed *via* hydrogen bonds between amine group N atoms and surface OH* species, followed by an H transfer from OH* to DMA, the formation of an S-O bond and concomitant release of gaseous HDMA. Steric hindrances make additional HDMA bonding less energetically favourable. The water half cycle reaction pathway proceeds with water forming a hydrogen bond with an amine nitrogen of $O_2Sn(DMA)_{4\text{-}x}$, followed by H transfer to form physio-adsorbed HDMA and chemisorbed $O_2Sn(DMA)OH^*$. The second water molecule reacts with $O_2Sn(DMA)OH^*$ in a much more energetically favourable reaction to form $O_xSn(OH)_2$. At sub 100 °C deposition temperatures, HDMA remains adsorbed to the initial surface during the precursor purge following reactant deposition, however XPS measurements confirm this residual HDMA will be released during the H_2O half reaction.[232]

2.6.2.1 Bulk perovskite degradation from ALD-SnO_x

As mentioned in Section 2.6.1.1, the poor reactivity of common underlayers results in diffusion of ALD precursors. Fortunately, despite the ready degradation of most perovskites on exposure to H_2O, the exposure is low (equivalent to ~30 ppm),[235] and water exposure during ALD has not been found to lead to perovskite degradation.[236] Studies into degradation mechanisms during the ALD process observed that vacuum heating at typical ALD temperatures (~100 °C) and heating under exposure to H_2O pulses display nearly identical XRD to untreated samples, with only slight degradation to PbI_2.[237]

TDMASn is a source of potential degradation, removing organic cations *via* a ligand exchange reaction with underlying perovskites, with the potential to disrupt bulk properties for certain perovskites.[54,236,238,239] Reactor temperature is crucial, with observations of emerging bulk degradation, identified *via* crystalline PbI_2 formation, when raising reactor temperature from 100 °C to 150 °C.[237,240] Vacuum annealing of films with a completed ALD-SnO_x layer showed high degrees of stability and no degradation, indicating the active TDMASn was responsible for the degradation, rather than a reaction with interfacial SnO_x.[237] This also means that perovskite degradation from TDMASn exposure occurs in the initial deposition stage, before the formation of a continuous layer. If a perovskite is vulnerable to bulk degradation, care must be taken of reactor conditions or supplemental nucleation layers must be employed to prevent sub surface diffusion.

2.6.3 Vacuum-based evaporation and sublimation

In this section we will discuss the mechanisms behind vapour-phase deposition methods utilising sublimation of materials in a vacuum. This is the deposition mechanism used for co-evaporated perovskites in this thesis. For a solid or liquid undergoing evaporation or sublimation, the saturation vapour pressure *P* can be obtained via the Clausius Clapeyron equation:

$$\frac{dP}{dT}=\frac{\Delta Q_D}{T\Delta V} \tag{2.34}$$

Here, *T* is the material temperature, Q_D is the heat of vaporisation and *ΔV* is the change in molar volume between the gaseous and solid/liquid material. Taking the ideal gas law and assuming $\Delta V \approx V_{gas}$ (as the molar volume in gas form is much larger than in solid/liquid form),[241,242] this equation can be rewritten as:

$$\Delta V \approx V=\frac{RT}{P_D} \tag{2.35.1}$$

$$\frac{1}{P_D}\frac{dP}{dT}=\frac{dlnP}{dT}=\frac{\Delta Q_D}{RT^2} \tag{2.35.2}$$

$$dlnP=\frac{-\Delta Q_D}{R}d\frac{1}{T} \tag{2.35.3}$$

$$P=A_x e^{\frac{-\Delta Q_D}{RT}} \tag{2.35.4}$$

Here, A_x is an integration constant and *R* is the gas constant. Below 1 mbar, this is considered a good approximation of vapour pressures. The exponential dependence on *T* means small changes in temperature can have relatively large impacts on evaporation / sublimation rate.[241,243] Assuming the system is under the equilibrium condition, then the kinetic gas laws can be used to show that the maximum number of particles leaving the surface for size A can be given by:[242,244]

$$\frac{dN}{Adt}=\sqrt{\frac{N_A}{2\pi k_B}}\times\frac{P_D}{\sqrt{MT}} \tag{2.36}$$

Here, *M* is the molar mass of the evaporating species, N_A is Avogadro's number and k_B is the Boltzmann constant. However, real evaporation rates do not typically reach this value. This is due to the potential for backscattering molecules and hydrostatic pressure, which contribute to pressure but do not lead to a flux of evaporating molecules. This is solved by modifying **Equation 2.34** with a term for hydrostatic pressure (*p*) and another term to account for backscattering,[245] called the evaporation constant α_v:

$$\frac{dN}{Adt}=\alpha_v\sqrt{\frac{N_A}{2\pi k_B}}\times\frac{P_D\text{-}p}{\sqrt{MT}} \qquad 2.37$$

This equation is termed the Hertz-Knudsen equation and describes the general evaporation / sublimation rate from a source.

2.6.4 Vapour transport in a vacuum

Except in specific cases, which do not apply to vacuum deposition methods in this thesis,[243] not all material evaporating from a source will be deposited onto the substrate. This is due to the behaviour of sublimated material from an effusive source, and due to mechanisms which impact vapour transport under vacuum conditions, which will be discussed in the following section.

2.6.4.1 Mean free path

One important consideration to maintain effusive deposition is maintaining a high mean free path (λ) for all precursor materials. Calculations of mean free path for a simple gas with partial pressure P and molecular diameter d follows the formula:[243]

$$\lambda=\frac{k_BT}{\sqrt{2}\pi Pd^2} \qquad 2.38$$

The cross sectional area Q for the gas scattering of any two molecules (diameter d_1 and d_2), assuming the can be approximated as circular, follows the relation:

$$Q=\pi\left(\frac{d_1}{2}+\frac{d_2}{2}\right)^2 \qquad 2.39$$

Then the λ_{mean} of a gas mixture containing two gases can be rewritten as:

$$\lambda=\frac{4k_BT}{\sqrt{1+\frac{M_1}{M_2}}(d_1+d_2)^2\pi P_2} \qquad 2.40$$

Here, P_2 is the partial pressure of gas 2, and $M_{1/2}$ are the molar masses of gas 1 and 2 respectively. Assuming the chamber pressure is predominantly due to a single gas, it is possible to substitute the chamber pressure for p_2, and use the relevant d_2 and M_2 by using calculated values to determine the mean free path of M_2.[72,144,246] The Beer-Lambert law can be used to calculate the flux Γ reaching a surface without experiencing a collision at arbitrary distance r from a source with a flux of Γ_0:[247,248]

$$\Gamma=\Gamma_0e^{-\frac{r}{\lambda}} \qquad 2.41$$

Mean free path calculations have been performed for MAI / PbI_2 systems, which found a suitable process pressure range to maintain good quality deposition.[72] However, FA-based systems are more complex, due to its dissociation and decomposition into multiple possible elements, including 1,3,5-sym-triazine, ammonia, hydrogen cyanide and formamide. Kroll *et al* assumed a background pressure was due exclusively due to 1,3,5-sym-triazine in their calculation of mean free path.[75] Utilizing a similar methodology and set of assumptions as in previous calculations of λ,[72,75,246] and calculated effective radii for formamidinium,[177,249] we can estimate the impact of chamber pressure on λ and Γ for all materials typically used as precursors in this thesis. As shown in **Figure 2-11**, depending on which gas is chosen as g_2 during FA-based co-evaporation, the calculated λ can differ by a factor of ~4. This inherently causes a degree of uncertainty in any calculations.

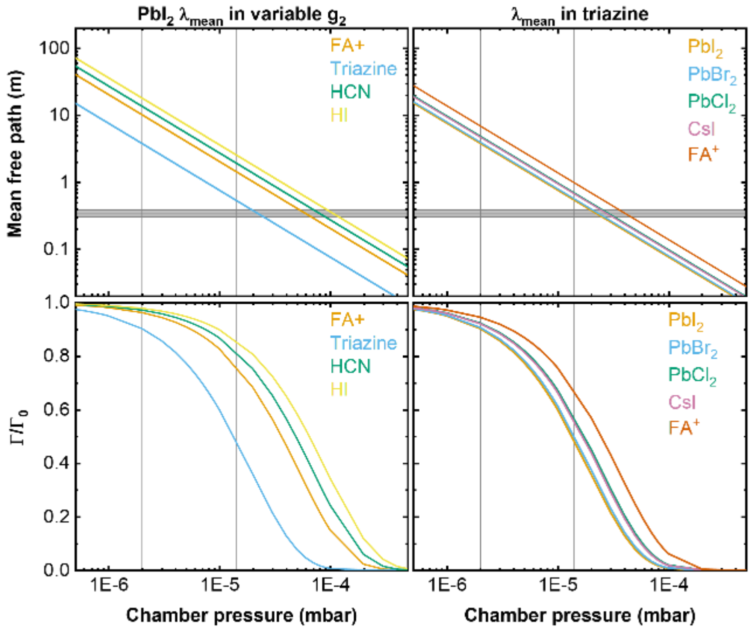

Figure 2-11 Influence of reactor pressure and g_2 on molecular flux. Impact of mean free path (*top*) and flux (*bottom*) with various (*left*) primary gas, (*right*) material. The grey horizontal section shows the range of distances for our substrate from the typical source. Grey vertical lines represents the lowest and highest measured pressure seen in this thesis. Inorganic materials are typically not considered to dissociate during sublimation, but FAI is known to dissociate into FA^+. Calculations of Γ assume r to be the distance to the middle of the substrate, meaning Γ is expected to vary slightly over the substrate.

A number of assumptions were made in applying these calculations. First, due to the layout of our evaporation chamber, mentioned in **Chapter 3**, the measured pressure is not guaranteed to be equivalent to the process pressure.[243] Kroll *et al.* made similar observations, including that effective partial pressures near crucibles are expected to be three orders of magnitude higher than measured pressure.[75] Hence, it must be assumed that measurd pressure is comparable to process pressure. Next, these equation assume a basic dissociation of FAI, which is slightly idealistic due to the myriad potential decomposition and dissociation pathways. However, mass spectroscopy measurements in **Chapter 7** indicate this assumption is mostly accurate for equivalent systems. Assumptions regarding Γ typically assume that molecules undergoing collisions do not reach the surface, but the large surface area of our substrate means this is not nescessarily true. Finally, it was assumed that each process acts as an ideal gas, although the positive charge of FA^+ makes coulomb interactions possible, which further complicate λ.[247] Hence, while the present current calculations λ give a good approximation of general changes in evaporation and sublimation dynamics, they cannot perfectly describe the reality within our evaporation system.

2.6.4.2 Evaporation cone shape

The next section discusses the evaporation of a typical effusion source. For evaporation of a source, when the λ is sufficiently higher than the distance to the surface such that collisions are negligible, and assuming no localised vapour pressure at the source, Knudsen's $\cos^n$ law for evaporation on a parallel plane can be applied. [243,250] At an arbitrary point, this law gives for gives the ratio of deposition flux $\Gamma_{substrate}$ source flux Γ_0 as follows:

$$M = \frac{\Gamma_{substrate}}{\Gamma_0} = \frac{(n+1)}{2\pi}\frac{(cos\theta)^n}{r^2} \qquad 2.46$$

Here r is the distance to the point, θ is the angle between the source and the point, and n is dependent on the source geometry. n roughly describes the linearity of the source, and for a theoretical Knudsen cell n = 1. **Figure 2-12** provides a number of possible evaporation cones, for n = 1 to 8, along with a visualisation of the discussed geometry.

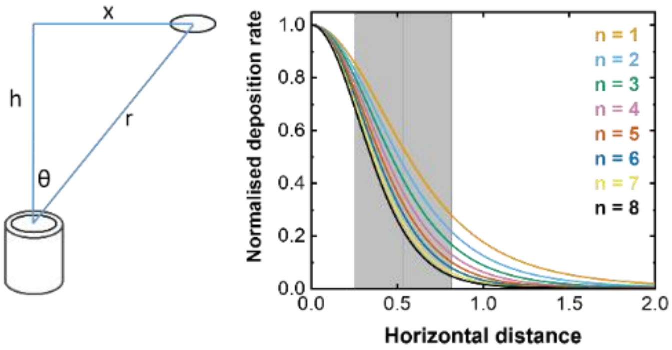

Figure 2-12 Visualization of source / point geometry outlined in **Equation 2.46** and plotting of normalized associated evaporation cones (*right*) with n varied from 1 to 8. Horizontal distance is plotted as a function of sample height, at a value of 1.0 the horizontal distance (x) is the same as the sample height (h). The grey region represents the area our substrates occupy.

Differences exist between the theoretical and practical evaporation cones. As discussed above, at high pressures λ is not sufficiently high for collisions to be negligible. Furthermore, potential higher localised vapour pressure at the source can distort practical evaporation behaviour.[75] However, plotting these curves can give us reasonable estimates on the evaporation cone of our sources and, more importantly, the possible limitations. The evaporation cones for our conical crucibles can be approximated as n ≈ 6.22 to n ≈ 8.46 depending on the source material,[521] which shows the relatively high degree of variation between sources over our substrate.

2.6.5 Condensation and film formation

2.6.5.1 Surface interactions

Molecules in vapour form are attracted to the substrate through Van der Waals forces. Assuming scattering does not occur, which occurs if the molecular-surface interaction is sufficiently weak, then the molecule is adsorbed to the surface and becomes known as an adatom. The ratio of adhering incident molecules to total incident molecules is known as the sticking coefficient (δ):

$$\delta = \frac{\Gamma_{sticking}}{\Gamma_{incident}} \qquad 2.47$$

This can be used to create a function for the number of absorbing molecules per unit of time and surface area, which follows the same form as **Equation 2.33**:

$$u = \delta\frac{dN}{Adt} = \delta\sqrt{\frac{N_A}{2\pi k_B}} \times \frac{P_D}{\sqrt{MT}} \qquad 2.48$$

The sticking coefficient is dependent on numerous factors, and is generally a function of surface properties, such as surface temperature, adsorption energy, absorbed molecule coverage, and surface structure.[243] Once a molecule is physisorbed, they remain mobile until they either re-evaporate, nucleate with existing bond or undergo non-dissociative adsorption by forming a more covalent or ionic bond with a surface bonding site, termed chemisorption.[251] The kinetics of this process is complicated, and may require an activation energy if it involves the breaking of bonds. Furthermore, inhomogeneities in the surface structure have increased binding energy, resulting in different diffusion and chemisorption properties. Desorption and re-evaporation of chemisorbed adatoms is possible but less likely than for physisorbed adatoms. Subsequent adatoms can themselves become individually chemisorbed, or form clusters via nucleation.[252] Further, more complex interactions are possible, but are not relevant for this thesis. A representation of the discussed surface interaction mechanisms is shown in **Figure 2-13**.

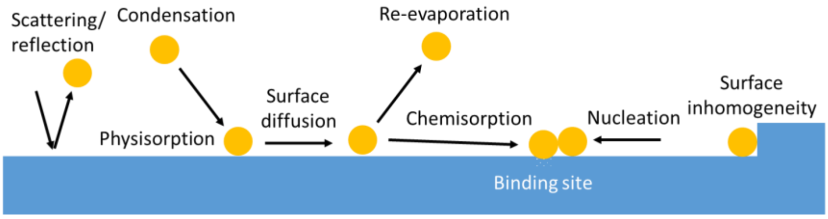

Figure 2-13 Different potential processes occurring to gas molecules impinging upon a surface.

2.6.5.2 Film formation

As molecules coalesce on the surface, they begin to form more complete films. This is an incredibly complex process dependent on the precise interactions between the surface and the impinging molecules, as well as the molecular flux and lattice mismatch between substrate and film.[245] There are three primary growth modes, and one common variant, that are generally accepted, outlined in **Figure 2-14**.

In Volmer-Weber mode, which occurs when interactions between impinging molecules are stronger than interactions with the substrate,[251,253] smaller clusters nucleate directly on the substrate and grow as independent islands until they merge into a complete film.[245,251,252] A variation of Volmer-Weber growth, which occurs when atomic mobility is sufficiently low,[245] is called columnar growth mode, where the islands grow as columns and do not merge.

Stranski-Krastanov is an intermediary case. An initial monolayer forms as a continuous layer and islands emerge on top of this layer. The reasons for the emergence of this growth mode are complex. [251,254] The most common cause is when the monolayer lattice parameters are mismatched from the bulk lattice parameters.[255] Under sufficient strain, the high free energy of the interface will eventually favour island formation.[245,251,255] Even intrinsic surface stress can strain films with minimal mismatch, meaning eventual Stranski-Krastanov growth is expected, except for cases with an epitaxial relationship and no lattice mismatch between the film and substrate.[255,256] In these cases, the final form of growth is expected, known as the Frank-van der Merwe mode, where flat monolayers form.[243,245,257,258]

Vacuum co-evaporated perovskites are typically found to grow following the Volmer-Weber model.[72] Independent nucleation sites undergo Oswald ripening, before coalescing into a complete film. Due to the dependence of this behaviour on surface interactions and substrate temperature, control of both parameters is crucial for co-evaporated film growth.[72,259]

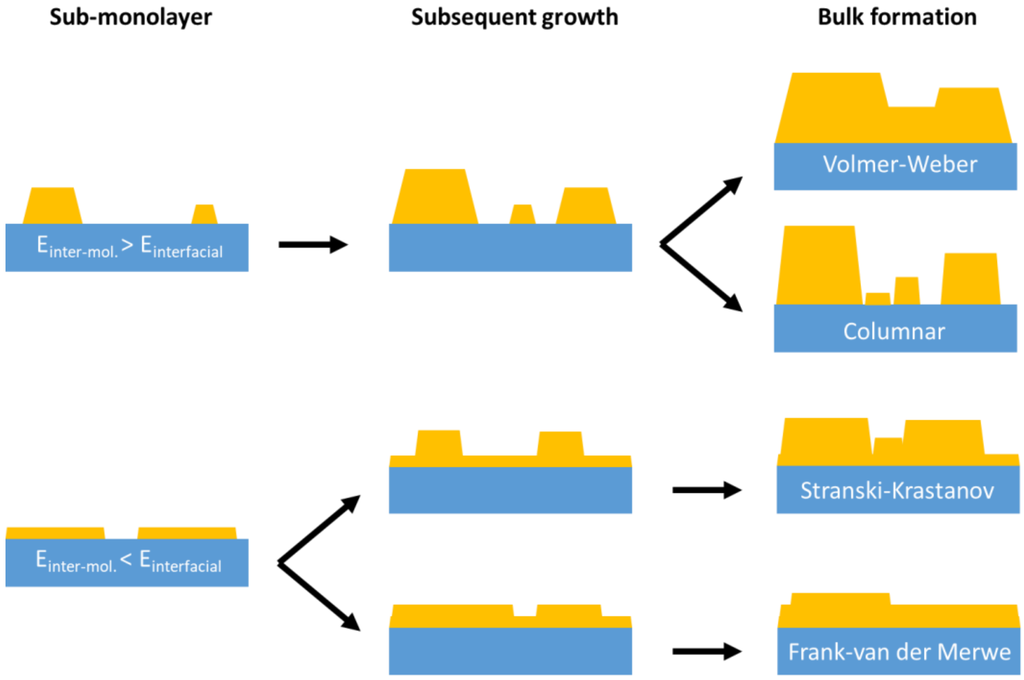

Figure 2-14 Visualization of the different classes of growth modes. The initial growth is determined by the relative intermolecular- and interfacial- interaction strengths. Subsequent growth is decided by other factors, such as film strain.

3 Materials, fabrication and characterisation methods

This chapter will outline the fabrication and characterization processes employed for the perovskite solar cells (PSCs) that will be reported in this thesis. The majority of reported perovskite thin films are fabricated by thermal evaporation in a vacuum, with all precursor materials sublimed simultaneously, which will be henceforth referred to as co-evaporated. Some samples, including the majority of samples presented in **Chapter 4** and **Chapter 5**, are solution-processed via spin coating. Remaining active layers have been deposited by various methods, including thermal s and spin-coating, but extending to also include magnetron sputtering and atomic layer deposition (ALD).

After discussing the utilized fabrication methods, we introduce and discuss the characterization methods that were used for analysis of the chemical and optical properties of various active layers, with a focus on the perovskite absorber. Finally, we introduce characterization tools for analysing completed PSCs in terms of photovoltaic (PV) device performance (PCE), and supplemental analysis of completed devices.

3.1 Materials

3.1.1 Perovskite precursor materials

Solution-processed: formamidinium iodide (FAI, *Dyenamo*); cesium iodide (CsI, *Alfa Aesar*); lead iodide (PbI_2, *TCI Chemicals*); lead bromide ($PbBr_2$, *TCI Chemicals*); lead chloride ($PbCl_2$, *TCI Chemicals*); methylammonium chloride (MACl, *Dyenamo*); methylammonium bromide (MABr, *Greatcell Solar Materials*).

Co-evaporation: PbI_2 (*TCI Chemicals*); $PbBr_2$ (*TCI Chemicals*); $PbCl_2$ (*TCI Chemicals*); CsI (*TCI Chemicals*); cesium chloride (CsCl, *TCI Chemicals*); FAI (*Greatcell Solar Materials*); methylammonium iodide (MAI, *Lumtec*).

3.1.2 Charge transport layers

2,2′,7,7′- Tetrakis(N,N′-di-p-methylphenylamino)-9,9′-spirobifluorene (SPIRO-TTB, *Sigma Aldrich*); [2-(9H-carbazol-9-yl)ethyl]phosphonic acid (2PACz, *TCI Chemicals*)**;** [2-(3,6-dimethoxy-9H-carbazol-9-yl)ethyl]phosphonic acid (MeO-2PACz, *TCI Chemicals*), [4-(3,6-dimethyl-9H-carbazol-9-yl)butyl]phosphonic acid (Me-4PACz, *TCI Chemicals*); 2,9-Dimethyl-4,7-diphenyl-1,10-phenanthrolin (BCP, *Sigma Aldrich*); fullerene-C_{60} (C_{60}, *Sigma Aldrich*).

3.1.3 Solvents and other materials

Isopropanol (IPA, *VWR Chemicals*); acetone (*VWR Chemicals*); N,N-dimethylformamide (DMF, *Sigma Aldrich*); anhydrous dimethyl sulfoxide (DMSO, *Sigma Aldrich*); dimethyl sulfoxide-d_6 (d_6-DMSO, *Sigma Aldrich*); anyhdrous chlorobenzene (CB, *Sigma Aldrich*); γ-butyrolactone (GBL, *Merck*).

Phenethylammonium chloride (PEACl, *Greatcell Solar Materials*) lithium fluoride (LiF, *Sigma Aldrich*); Magnesium fluoride (MgF_2, *Sigma Aldrich*); tetramethyl aluminium (TMA, *Strem*); tetrakis dimethyamido tin (IV) (TDMASn, *Strem*); indium oxide/tin oxide wafer 90%/10% weight (ITO, *Kurt J. Lesker Company*); indium oxide/zinc oxide wafer 90%/10% weight (IZO, *Kurt J. Lesker Company*); ITO coated glass substrate (*Lumtec*).

3.2 Fabrication methods

All PSCs reported in this thesis were fabricated in the inverted *p-i-n* architecture, with either planar glass or silicon solar cells. The *p-i-n* architecture classically is comprised of the substrate coated with transparent conductive oxide (TCO) as a front electrode, followed by the hole transport layer (HTL), perovskite absorber, electron transport layer (ETL) before finishing with the rear electrode. Devices are fabricated in opaque stacks, which employ a pure metallic rear electrode, or as semitransparent stacks, which utilise a hybrid layer comprised of a TCO deposited over the active area with a further metallic layer deposited on the non-active area to reduce sheet resistance. Additional active layers, such as passivation, buffer or antireflective layers may also be included in this stack and will be discussed last.

3.2.1 Substrate preparation

Most semitransparent and opaque perovskite solar cells in this work utilized a commercial 64 x 64 mm^2 substrate with 1.1 mm glass coated with ~135 nm ITO with a sheet resistance of ~15 Ω/sq. ITO substrates were cut to 16 x 16 mm^2 and labelled prior to cleaning. Cleaning was comprised of immersion in solutions of first acetone, then isopropanol for ~20 minutes each in an ultrasonic bath. Samples were dried with N_2 before immersion to remove potential glass shards from the cutting and labelling process, between solutions to reduce cross contamination and immediately following isopropanol cleaning to prevent formation of a residual material film. Samples were treated with oxygen plasma at 100% power for 3 minutes unless otherwise stated immediately prior to HTL deposition. When large numbers of samples were fabricated at one time, at most 12 samples were plasma treated in each batch to minimize time between treatment and HTL deposition.

Silicon substrates for tandem devices were prepared in different methods depending on the source of the silicon substrate. For substrates without a rear metallic electrode, first a 300 nm Ag metallic electrode was deposited on the rear of the substrate. Then substrates were cleaned by spin coating acetone and isopropanol in ambient conditions after N_2 drying to remove potential dust. Spin-coating cleaning utilized two 1 mL pipettes of each solution while samples rotate at 4000 rpm for 25 s. Plasma treatment was identical to glass/ITO samples.

3.2.2 Hole transport and selective layers (HTLs)

This work entails use of two classes of HTLs, fabricated using multiple deposition techniques. They include thermal evaporation of SPIRO-TTB, and various self-assembled monolayer based HTLs (SAM-HTLs), fabricated by either thermal evaporation or spin coating. We will discuss the various deposition processes in the following section.

3.2.2.1 SPIRO-TTB (thermal evaporation)

For co-evaporated samples presented in **Chapter 4**, 5 nm of SPIRO-TTB was evaporated in a thermal evaporation system (OPTIvap, Creaphys). 2 tips from a small spatula was placed in a cleaned (IPA and N_2) 8 ccm Al_2O_x crucible for each evaporation. Prior to deposition the chamber was evacuated to ~$1 \cdot 10^{-6}$ mbar. Evaporation occurred at a deposition rate of 0.1 – 0.3 As^{-1}. Typically temperatures varied based on crucible filling and thermocouple placement, but was in the range of 180 °C to 220 °C.

3.2.2.2 SAM-HTLs (spin-coating)

The precise precursor concentration and spin-coating parameters for SAM-HTLs varied between each chapter. All solutions were prepared by dissolving the requisite mass of powder in anhydrous ethanol in a nitrogen atmosphere glovebox. All solutions were also deposited and annealed at 100 °C for 10 min in a nitrogen atmosphere glovebox immediately after deposition. The precise deposition parameters for each chapter will be independently outlined in the following.

In **Chapter 4** and **Chapter 5**, a 1 mM 2PACz solution was prepared, while in **Chapter 5**, 1 mM MeO-2PACz and Me-4PACz solutions were also prepared. Prepared solutions were placed in an ultrasonic bath for 15 min before use. 70 µL of 2PACz was deposited on the substrate by 1-step spin-coating at 3000 rpm for 30 s. Select samples were washed as outlined below.

In **Chapter 6**, 2.98 mM 2PACz, MeO-2PACz and Me-4PACz solutions were prepared. The prepared solution was put in an ultrasonic bath for 30 min before use. 70 µL of the SAM solution was deposited on the substrate by 1-step spin-coating at 3000 rpm for 30 sec with sitting time of 5 sec. Select samples were washed as outlined below.

In **Chapter 7**, a 4 mM MeO-2PACz precursor solution was prepared. The prepared solution was put in an ultrasonic bath for 60 min before use. 70 µL of the SAM solution was deposited on the substrate by 1-step spin-coating at 4000 rpm for 30 s with sitting time of 5 s. These samples were not washed.

3.2.2.3 SAM-HTLs (thermal evaporation)

For relevant samples presented in **Chapter 5** and **Chapter 6**, 2PACz, MeO-2PACz and Me-4PACz were evaporated in a thermal evaporation system (OPTIvap, Creaphys). 3 tips from a small spatula was placed in a cleaned (IPA and N_2) 8 ccm Al_2O_x crucible for each evaporation. Evaporated SAM-HTLs did not display a noticeable change in device performance if the crucible was not cleaned, but for consistency it was freshly cleaned each deposition. Prior to deposition the chamber was evacuated to $\sim 1 \cdot 10^{-6}$ mbar. Evaporation occurred at a deposition rate of 0.1 – 0.5 As^{-1}. Typically temperatures varied based on crucible filling and thermocouple placement, but was in the range of 140 °C to 180 °C.

3.2.2.4 SAM-HTLs (washing)

For relevant samples presented in **Chapter 5** and **Chapter 6**, some SAM-HTLs utilised a washing step to remove weakly bound bulk molecules. Washing was performed by static deposition of 150 µL anhydrous ethanol, followed by dynamic spin coating of a further 150 µL anhydrous ethanol on the substrate at 3000 rpm for 30 sec. Samples were subsequently annealed at 100 °C for 10 min in a nitrogen atmosphere.

3.2.3 Perovskite absorbers (spin-coating)

Dr. Saba Gharibzadeh prepared the perovskite precursor solution utilised in **Chapter 4** by forming a 1 M precursor solution of the perovskite $Cs_{0.17}FA_{0.83}Pb(I_{0.92}Br_{0.08})_3$ with a 10% PbI_2 excess. FAI, CsI, PbI_2, and $PbBr_2$ were dissolved in a DMF:DMSO solvent mixture with a 4:1 volume ratio. Afterward, 35 µL of a $PbCl_2$:MACl solution with a 1:1 molar ratio in DMSO was added as a bulk passivation additive. The solution was deposited onto the SAM-HTL by a two-step spin coating process. The first step was 1000 rpm (2000 $rpm.s^{-1}$ acceleration) for 10 s, the second was 5000 rpm (2000 $rpm.s^{-1}$ acceleration) for 40 s. Anti-solvent quenching with 150 µL CB was performed 20 s before the end of the second step. Samples were annealed at 100 °C for 30 min in an inert atmosphere.

Dr Ahmed Farag prepared the perovskite precursor solution utilised in **Chapter 5** by forming a 1.6 M precursor solution of the perovskite $Cs_{0.17}FA_{0.83}Pb(I_{0.92}Br_{0.08})_3$. PbI_2 was dissolved in a DMF:DMSO solvent mixture with a 4:1 volume ratio. The prepared solution was heated for 25 min at 120 °C, then allowed to cool for ~10 min. Next, $PbBr_2$, CsI, MABr, and FAI was added to the solution and agitated until dissolved. The solution was deposited onto the SAM-HTL by a two-step spin coating program. The first step was 2000 rpm (1000 $rpm.s^{-1}$ acceleration) for 10 s, the second was 5000 rpm (2000 $rpm.s^{-1}$ acceleration) for 30 s. Anti-solvent quenching with 150 µL CB was performed 15 s before the end of the second step. Samples were annealed at 100 °C for 30 min in an inert atmosphere.

3.2.4 Perovskite absorbers (co-evaporation)

In the following, we will discuss general fabrication and processing parameters for the various co-evaporated PSCs employed in this work, before going into specifics for each composition used in this thesis. For perovskite deposition, a nitrogen glovebox integrated thermal evaporation system designed specifically for perovskite deposition (PEROvap, CreaPhys) was typically employed. The system was comprised of five sources with 8 ccm conical Al_2O_x crucibles and molybdenum heating wires arranged equidistant to the substrate with independent quartz-crystal monitors (QCMs). A description of the various reactor components is shown in **Figure 3-1**. A cooling surface surrounding all sources was set to -20 °C. This surface is designed to condense volatiles and hence reduce the overall chamber pressure. Conversely, the exterior walls of the reactor were kept at 40 °C to reduce volatile condensation. The reactor utilised a turbopump to obtain high vacuum (~10^{-8} mbar base pressure), with a nitrogen coldtrap (operational temperature: -192 °C - -129 °C) used to condense escaping volatiles and achieve a lower base pressure.

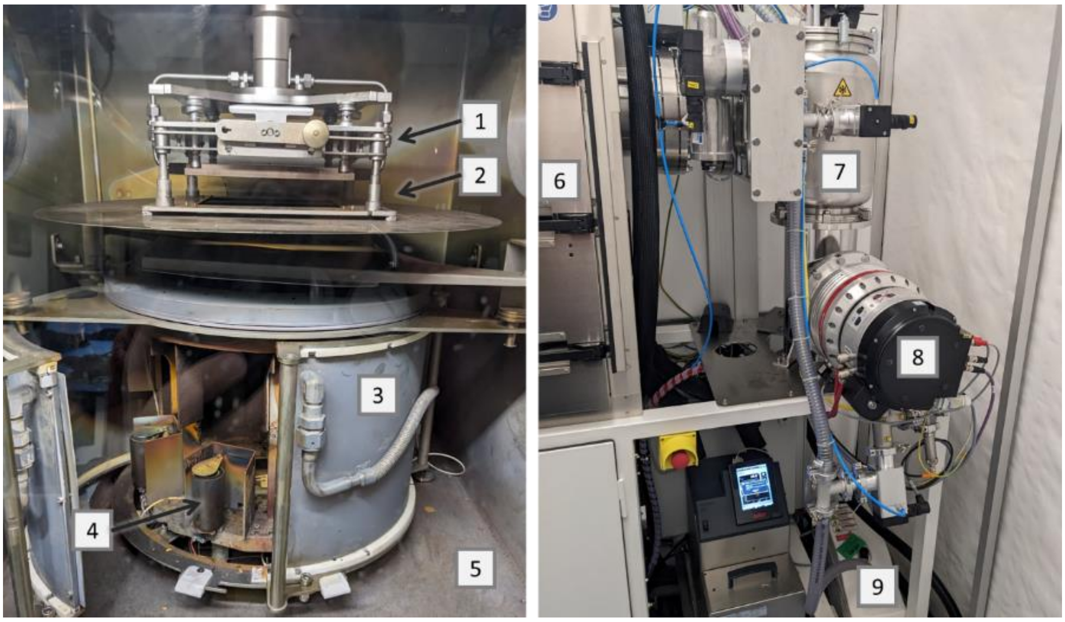

Figure 3-1 Overview of reactor used for co-evaporated perovskites presented in this thesis. [1] Substrate heating mechanism (typically 18 °C); [2] Substrate holder; [3] Cooling shield (-20 °C); [4] Source 3 crucible (PbI_2); [5] Chamber wall (40 °C); [6] Chamber (rear); [7] Coldtrap (~-192°C); [8] Turbopump; [9] Roughing pump.

Prior to deposition, the system was evacuated for ~60 min, with a standard base pressure at start of heating of $3 \cdot 10^{-6}$ mbar. Substrate temperature was varied where specified, but substrate rotation speed (10 rpm) was held constant. Inorganic sources were first heated to the desired rate, with organic source heating starting when inorganics began to show deposition. For every process, the evaporation rate of each material was kept constant by manually adjusting the source temperature.

Inorganic materials (PbI_2, $PbBr_2$, $PbCl_2$, CsI, CsCl) were not replaced between depositions. When an inorganic source was empty, ~4 – 6 ccm of fresh material was added to the crucible. Organic materials (FAI and MAI) were replaced between depositions. Smaller FAI grains at the bottom of each bottle lead to a slight change in optimum FAI rate. For that reason, FAI was sieved to isolate grain sizes from 200 – 500 µm to minimise material-based fluctuations. This was found to improve process repeatability. Before each deposition ~1.1 grams of FAI was placed in the crucible. Organic and PbI_2 QCMs were replaced between each deposition in order to prevent QCM fluctuations. Other QCMs were replaced when their lifetimes fell below 92%.

Often a series of perovskite depositions were performed with varied organic deposition rates in order to obtain an optimum corresponding to the highest PCE. It was assumed that this optimum lead to a roughly stoichiometric perovskite, with composition calculated by assuming complete incorporation of all inorganic rates, with organic cations balancing Pb. This was because small shifts in crucible position can lead to large changes in the effective evaporation rate due to the evaporation cone shape of the utilised crucibles. Organic sources were particularly vulnerable to this effect due to their frequent replacement.

3.2.4.1 MA-based perovskites

In the **Chapter 4** optimization of the SnO_x layer, a co-evaporated $MAPbI_3$ layer was employed. This layer was the only perovskite not deposited in the PEROvap system. Instead a modified three chamber evaporation system (Amocon) was employed. Base PbI_2 evaporation rates were 0.5 $A.s^{-1}$ and MAI was controlled via chamber pressure, with a base pressure of $5{\cdot}10^{-6}$ mbar. Substrates and materials were outgassed overnight.

Dr. Tobias Abzieher prepared the double-cation perovskite of the composition $Cs_{0.17}MA_{0.83}Pb(I_{0.91}Br_{0.09})_3$ used in 4T tandems in **Chapter 4**. Substrate temperature was held constant at 25 °C. Inorganic rates during evaporation were: $PbI_2 = 1.30$ $Å.s^{-1}$, $CsI = 0.20$ $Å.s^{-1}$, and $PbBr_2 = 0.15$ $Å.s^{-1}$. Measured MAI rate was 2.00 $Å.s^{-1}$ but, due to its unstable and difficult to measure nature, the rate is somewhat arbitrary. All samples were annealed in nitrogen atmosphere at ambient pressure immediately after evaporation.

3.2.4.2 FA-based perovskites with $PbCl_2$

In **Chapter 5** and **Chapter 6**, an FA-based double cation perovskite of the composition $Cs_{0.13}FA_{0.87}Pb(I_{0.95}Cl_{0.05})_3$ was employed. Substrate temperature was held constant at 18 °C for all experiments. Inorganic rates during evaporation were: $PbI_2 = 0.23$ $Å.s^{-1}$, $CsI = 0.025$ $Å.s^{-1}$, and $PbCl_2 = 0.01$ $Å.s^{-1}$. Due to its unstable and difficult to measure nature, the tooling factor and rates of FAI were somewhat arbitrary. Instead, the required FAI rate was set to 1.0 $Å.s^{-1}$, which was the rate corresponding to the highest photovoltaic performance for perovskites on a washed 2PACz HTL. For a standard co-evaporation of a 550 nm perovskite layer, deposition time was approximately 180 min. All samples were annealed at 140 °C for 10 min in nitrogen atmosphere at ambient pressure immediately after evaporation. Before each deposition FAI was left under vacuum for 2 hours to allow outgassing of potential contaminants.

3.2.4.3 FA-based perovskites (1.68 eV)

In **Chapter 7**, an FA-based wide bandgap (1.68 eV) double cation perovskite of the composition $Cs_{0.13}FA_{0.87}Pb(I_{0.95}Cl_{0.05})_3$ was employed. Substrate temperature was held constant at 18 °C for all experiments. Baseline evaporation rates for initial devices were: PbI_2 = 0.26 A.s^{-1}, CsI = 0.055 A.s^{-1} and $PbBr_2$ = 0.115 A.s^{-1}. The required FAI rate was set to 1.0 Å.s^{-1}, which was the rate corresponding to the highest photovoltaic performance for perovskites on an unwashed MeO-2PACz HTL. This work included varying overall perovskite deposition, which was achieved by linearly increasing inorganic evaporation rates by integer factors and optimizing FAI rate for each series. In this manner, deposition rate was varied from ~5 nm.min^{-1} to ~ 19 nm.min^{-1}. All samples were annealed at 110 °C for 30 min in nitrogen atmosphere at ambient pressure. Before each deposition FAI was left under vacuum overnight to allow outgassing of potential contaminants. For select depositions, a 10 ccm cylindrical Al_2O_x crucible was used for FAI.

3.2.5 Electron transport or selective layers (ETL)

3.2.5.1 Thermally evaporated ETLs

Two systems were utilised for ETLs, with slightly different optimums. 20 nm fullerene (C_{60}, Alfa Aesar) was evaporated in a thermal evaporation system (OPTIvap, Creaphys). 3 tips from a small spatula was placed in an empty 8 ccm Al_2O_x crucible for each evaporation. Prior to deposition the chamber was evacuated to ~$1\cdot10^{-6}$ mbar. Evaporation occurred at a deposition rate of 0.1 – 0.3 Å.s^{-1}. Typically temperatures varied over the course of deposition across the range of 300 °C to 440 °C. Alternatively, 25 nm C_{60} (Alfa Aesar) was evaporated in another available thermal evaporation system (Angstrom). Deposition pressure was typically ~$5\cdot10^{-6}$ mbar, with a rate of ~0.2 Å.s^{-1}. Typically temperatures varied over the course of deposition across the range of 370 °C to 480 °C.

Samples were either finished with BCP or ALD-SnO_x (which will be discussed in the following section). Typically opaque samples were finished using BCP, except for the co-evaporated perovskites presented in **Chapter 5 and 6**, and opaque references in **Chapter 7**, which utilised ALD-SnO_x. 7 nm BCP was deposited in the OPTIvap at ~$1\cdot10^{-6}$ mbar with a rate of 0.2 – 0.4 Å.s^{-1}. Alternatively, 7 nm BCP was deposited in the Angstrom at ~$5\cdot10^{-6}$ mbar with a rate of 0.1 – 0.2 A.s^{-1}.

3.2.5.2 ALD of SnO_x as a simultaneous ETL / buffer layer

For ST or tandem samples in **Chapter 4** and **Chapter 7**, and select other samples, following the following the deposition of a C_{60} layer, a SnO_x layer was deposited via ALD to act as a buffer layer to prevent sputter damage, and as an alternative to BCP. Due to the diffusion of ALD precursors into non-reactive substrates, the quoted thicknesses were measured on a crystalline silicon substrate but do not correspond exactly to SnO_x thickness.

For ST samples in **Chapter 4** and opaque samples in **Chapter 6**, 35 nm of ALD was deposited via a glovebox-integrated showerhead ALD system (R-200 Advanced, Picosun). N_2 was used as a carrier and purge gas, with TDMASn and H_2O (in-house, Milli-Q) as precursor and oxidiser respectively. Due to its low vapour pressure, the TDMASn source was heated to 70 °C and allowed to equilibrate for a minimum of 60 min before deposition. To prevent condensation, the carrier line for TDMASn was kept at 125 °C during deposition. The reactor contains an intermediary space to prevent source leakage, which was cleaned by a 200 standard cubic centimetre (sccm) continual flow of N_2 during deposition. TDMASn and H_2O lines were kept at 150 sccm when not pulsing to prevent cross-contamination. Due to system layout, a boosting system was utilized instead of a conventional bubbler for TDMASn. Under boosting, line flow was increased to 500 sccm immediately prior to pulsing to increase precursor concentration. Prior to deposition, the chamber was pumped to ~10 mbar and allowed to remain at the desired temperature for 10 minutes to equilibrate sample temperatures. SnO_x was deposited over 300 cycles using the following parameters: 1.6 s TDMASn pulse (with 1.0 s boosting, 0.5 s pulse, 0.1 s relax) with 12 s purge at 50 sccm, then 0.1 s H_2O pulse with 16 s purge at 100 sccm. Chamber temperature was 90 °C and 80 °C for solution-process and for co-evaporated samples respectively.

Co-evaporated samples in **Chapter 4** included an Al_2O_3 layer deposited at 80 °C with an unheated TMA source, all parameters were consistent with SnO_x, except the precursor was a 0.5 s TMA pulse (no boosting).

For ST and tandem samples in **Chapter 7**, 20 nm of ALD was deposited via a glovebox-integrated ALD system (GEMStar XT, Arradiance). N_2 was used as a carrier and purge gas, with TDMASn and H_2O (in-house) as precursor and oxidiser respectively. Due to its low vapour pressure, the TDMASn source was heated to 70 °C and allowed to equilibrate for 60 min before deposition. To prevent condensation, the carrier line for TDMASn was kept at 130 °C during deposition. Prior to deposition, the chamber with loaded samples was pumped to ~0.07 mbar and allowed to remain at the desired temperature for 10 minutes to equilibrate samples. SnO_x was deposited over 200 cycles using the following parameters: 0.5 s TDMASn pulse 12 s purge at 50 sccm, then a 1.0 s H_2O pulse with 12 s purge at 50 sccm. For all samples the chamber temperature was 80 °C.

3.2.6 TCO and metallic electrodes

3.2.6.1 Hydrogenated indium oxide (IO:H) as a front TCO electrode

For select samples presented in **Chapter 4**, a front TCO of IO:H was obtained from a collaboration partner, Zentrum für Sonnenenergie (ZSW), instead of the commercially available ITO. IO:H was deposited onto clean glass via an inline sputtering system (Leybold Z600i). Samples were sputtered at a pressure of ~10 mbar, with DC power = 1.4 W.cm^{-2}, and gas flow ratios of 1.7% O_2 and 3.4% H_2 in Ar. No intentional heating was applied during the deposition. Post-deposition substrates were annealed for 20 min at 250 °C in vacuum.

3.2.6.2 Preparation of samples for rear electrodes

After deposition of the ETL, the underlying TCO was exposed by either physical scratching using a stainless steel scalpel, dissolved using GBL, or a combination of both methods. This combination was most required for samples with ALD-SnO_x as the relative impermeability of the layer made GBL swiping less effective.

3.2.6.3 Rear TCO electrodes

For ST samples in **Chapter 4**, a rear TCO of ITO was deposited *via* a thin-film deposition system (Kurt J. Lesker, PVD-75) using a 4 inch^2 ITO wafer with a direct-current (DC) sputtering power supply. 160 nm of ITO was deposited at a process pressure of ~$1 \cdot 10^{-3}$ mbar without heating. DC power was set to 50 W with a deposition time of 2310 s and an O_2 to Ar ratio of 2.5%.

For ST samples in **Chapter 4**, and monolithic 2T tandem samples in **Chapter 7**, a rear TCO of IZO was deposited *via* a magnetron sputtering system (Kurt J. Lesker, PVD-75) using a 4 inch^2 IZO wafer with a radio-frequency (RF) sputtering power supply. For sputtered samples in **Chapter 4**, 165 nm of IZO was deposited at a process pressure of ~$2.0 \cdot 10^{-3}$ mbar without heating. RF power was set to 100 W with a deposition time of 2550 s and an O_2 to Ar ratio of 1%. For tandem samples in **Chapter 7**, 65 nm of IZO was deposited at a process pressure of ~$1.5 \cdot 10^{-3}$ mbar without heating. RF power was set to 190 W with a deposition time of 341 s and an O_2 to Ar ratio of 0.25%.

3.2.6.4 Rear metallic electrodes

All samples were finished with a metallic rear electrode of either 75 nm Au, 100 nm Ag or 300 nm Ag (for tandem devices) using a bell jar evaporation system (Vactec Coat 320), with evaporation rates of 0.5 – 2.0 Å.s^{-1} and chamber pressures of ~ $1 \cdot 10^{-6}$ mar. Cell active area was defined by a shadow mask. For most samples this resulted in a 10.5 mm^2 active area, for tandem devices the active area was 50 mm^2. ST and tandem devices did not evaporate the metallic electrode on the active area, expect for metallic fingers of 150 µm width, used to improve effective TCO sheet resistance.

3.2.7 Other function layers

3.2.7.1 Surface passivation (solution-processed perovskites)

Passivation layers were deposited by Dr. Saba Gharibzadeh and Dr. Ahmed Farag.

In **Chapter 4**, the solution-processed double cation perovskite also employed a solution-processed passivation layer. PEACl was dissolved in IPA at a concentration of 0.95 mM. The solution was deposited on top of bulk passivated perovskite film as a surface passivation interlayer at a speed of 5000 rpm (acceleration 2000 rpm.s^{-1}) for 30 s, followed by annealing at 100 °C for 5 min in a nitrogen atmosphere.

In **Chapter 4** and **Chapter 5**, a thermally evaporated passivation layer was employed. 1 nm of LiF was evaporated directly onto the perovskite in a thermal evaporation system (Lesker, Spectros PVD system) at a pressure of ~10^{-6} mbar and deposition rate of 0.1 - 0.2 Å.s^{-1}. **Chapter 4** employed this layer with the previously mentioned PEACl.

3.2.7.2 Antireflection coatings (ARCs)

For select devices a thermally evaporated ARC was employed to minimize reflection losses at the rear TCO and/or on the glass substrate. MgF_2 was deposited in a thermal evaporator (Angstrom). Films were deposited at a base pressure of ~$1{\cdot}10^{-6}$ mbar at a rate of 0.2 Å.s^{-1}, with a final thickness of 100 - 175 nm.

3.3 Characterization methods

In this section we will introduce and explain the characterization techniques employed to investigate thin films, half stacks and complete PSCs shown in this thesis.

3.3.1 Optical characterization techniques

3.3.1.1 Ultraviolet-visible (UV-vic) spectrophotometry

UV-vis spectrophotometry is a method to determine the wavelength dependent optical properties of thin films. By measuring transmittance (T) and reflectance (R) of a sample by illumination with monochromated white light, the absorptance (A) can be calculated via the equation:

$$A = 1 - T - R \qquad 3.1$$

To capture diffuse T and R, an integrating sphere coated with a reflective surface is typically incorporated into the measurement setup.

UV-vis spectrophotometry measurements were performed using two setups. The first was a benchtop spectrophotometer (PerkinElmerm, Lambda 1050) with an integrating sphere and a monochromator with a 930 Hz chopping frequency. Measurements used the largest possible aperture to prevent inhomogeneities from impacting results. For samples with stability concerns under exposure to air, a glovebox integrated characterization system (Bentham, PVE300) with an integrating sphere was used instead. This system also utilised a monochromator, with a chopping frequency of ~ 575 Hz, filtered with a lock-in-amplifier to distinguish the signal from background noises such as ambient light. Typically, a 1.5x1.5 mm^2 aperture was used for optical filters, and a 0.74x0.74 mm^2 aperture for complete devices.

3.3.1.2 Ellipsometry

Ellipsometry is a non-invasive technique to determine thin film dielectric properties by comparing the polarization of reflected light to incident light. Furthermore, the real and complex components of the refractive index can be calculated, which is useful to determine expected absorption and reflection behaviour of materials.

In this work, the ellipsometry data was measured by Dr. Adrian Mertens from Institute of Photonics and Quantum Electronics at KIT using an ellipsometer (Woollam, VASE), with analysis performed by the inbuilt software.

3.3.2 Photoluminescence (PL) spectrophotometry

PL is a versatile and non-destructive technique for characterizing the electronic structure of semiconductors by illuminating the material with photons of higher energy than the bandgap. Absorbed photons excite an electron from the valence to the conduction band, with the excess energy imparted into the material as heat before spontaneously recombining with holes in the conduction band. For direct semiconductors, such as perovskites, this process emits light of a characteristic energy. By analysing the wavelength and intensity of the emitted light, information on bandgap energy, defect nature and density, and electrical structure can be obtained.[260]

3.3.2.1 PL imaging

PL imaging is a rapid tool to evaluate sample homogeneity. By illuminating the sample with a fixed wavelength, and measuring the PL response of the entire sample, a spatially resolved image of relative PL intensity can be obtained.

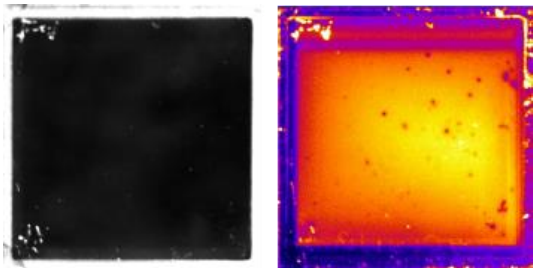

Figure 3-2 Representative PL map image. (*Left*) shows on image taken with a neutral density filter, which resembles the visible (to the naked eye) appearance of a sample with a few scratches and dots visible. (*Right*) shows an image taken with a 725 nm long pass filter, revealing the presence of many more inhomogeneous areas. A colour filter was applied to accentuate spectral differences.

The PL imaging system in this work is an in-house setup, introduced in previous literature.[205] A monochrome sCMOS camera (CS2100M-USB Quantalux, Thorlabs) was equipped with a lens (MVL25M23, Thorlabs) mounted above a sample holder, which was illuminated using two LED bars (LDL2, 146X30BL2-WD, CCS Inc.) with a centre wavelength of 467 nm and intensity of ~0.08 suns. One of three filters were used to isolate specific portions of the emitted PL signal: a 725 nm long pass (Edmund Optics), a 775 nm short pass (Edmund Optics), and a neutral density filter comprised of two stacked linear polarizers (LPVISE200-A, Thorlabs). Acquisition time varied greatly depending on the sample PL intensity, but was typically 1000 – 4000 ms for the short or long pass filters, the neutral density filter always used 10 ms to prevent damaging the camera. The image of a representative sample is provided in **Figure 3-2**.

3.3.2.2 PL quantum yield (PLQY)

PLQY is a technique that quantify the ratio of emitted photons to absorbed photons based on the PL of then thin film material. PLQY is often used to quantify maximum possible open-circuit voltage of a film, known as the implied open-circuit voltage iV_{OC}, which is given by the formula outlined in **Section 2.2.4**:

$$iV_{OC} = V_{OC-rad} + \frac{k_B T}{q} \ln(PLQY) \qquad 3.2$$

Here, k_B is the Boltzmann constant, T the system temperature, q the elemental charge. Corresponding internal ideality factors n_{id} can also be applied from PLQY measurements by varying the illumination intensity and applying a fit to the calculated iV_{OC} by plotting the formula:

$$iV_{OC}(I) = V_0 - n_{id} \frac{q}{k_B T} \ln \frac{J_R(I)}{J_0} \qquad 3.3$$

Here, V_0 is the iV_{OC} at 1 sun illumination intensity and $J_R(I)/J_0$ is the ratio of intensity dependent recombination to dark saturation current density. A representative PLQY spectra, and a calculation of ideality factor, are provided in **Figure 3-3**.

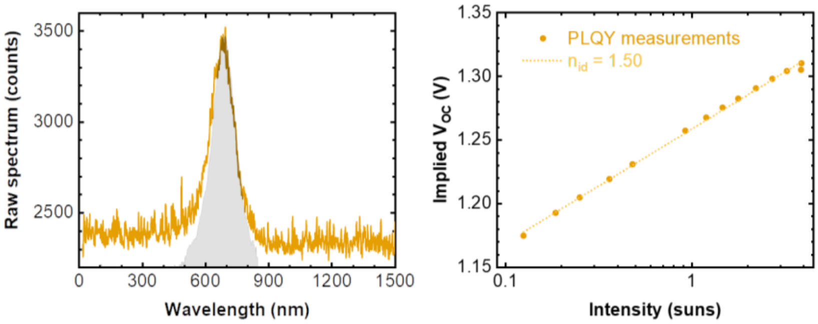

Figure 3-3 Representative PLQY spectrum and calculation of n_{id} from PLQY. (*Left*) Raw PQY spectrum from a measurement in **Chapter 5**, in grey is the baseline subtracted spectrum. (*Right*) Intensity dependent PLQY from a measurement in **Chapter 4** and the fit used to calculate n_{id}. Data adapted with permission from Wiley-VCH GmbH ©2023 and Elsevier Inc ©2024.[35,261]

In **Chapter 5**, PLQY measurements were performed by Dr. Paul Faßl on perovskite half stacks using an in-house setup in ambient atmosphere. Samples were placed in an integrating sphere (LabSphere) with a 15 cm diameter. A green laser (Coherent or LD-515-10MG, Roithner Lasertechnik) was used to irradiate the sample. Emission spectra was guided via optical fibre to two spectrophotometers (QE65 Pro, Ocean Optics and AvaSpec-ULS2048x64TEC, Avantes). Prior to measurements the spectral response was calibrated with a calibration lamp (HL-3plus-INT-Cal, Ocean Optics). To prevent perpendicular spectra reflectance of the laser, samples were oriented at a 15° angle.

In **Chapter 6** and **Chapter 7**, PLQY measurements were performed on perovskite half stacks using an in-house setup in ambient atmosphere. A benchtop radiative efficiency meter (LP 20-32 LuQY Pro, QYB GmBH) was used instead of the previous benchtop system. PLQY measurements were performed at an intensity of 1 sun with a 0.1 cm^2 laser spot size. 5 - 7 measurements were averaged to obtain an average PLQY value and five spots on each sample were measured to prevent local inhomogeneities from impacting results.

3.3.2.3 Time-resolved PL spectrophotometry (TrPL)

TrPL is a method to analyse the dynamics of PL emission in order to analyse charge carrier dynamics of the material. The typical method used in this work is termed time-correlated single photon counting. The sample is excited by a short light pulse, typically in the picosecond range, and the photon emission over time is plotted with an exponential fit to produce a decay curve that is governed by competing recombination processes outlined in **Section 2.2.3**.

$$I_{TrPL}(t) = \sum_{i}^{n} A_i e^{-\frac{t}{\tau_i}} \tag{3.4}$$

Here, A_i and τ_i are the respective amplitude and lifetime of the component i. A bi-exponential fit is typically performed for perovskites, with τ_1 typically associated with trap-mediated recombination and τ_2 associated with radiative recombination.[260] For samples with a strong value for A_1, it may be more accurate to fit a reduced section of the curve to obtain an accurate value to τ_2. A typical curve with an associated bi-exponential and truncated mono-exponential fits are provided in **Figure 3-4**.

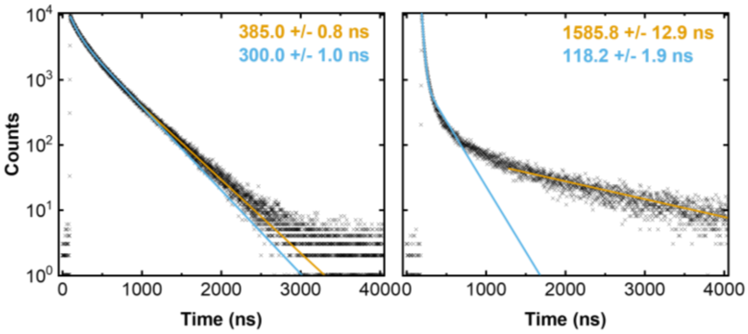

Figure 3-4 Representative TrPL spectrum and calculation of τ_2 using a standard bi-exponential (blue) and truncated mono-exponential (orange). (*Left*) TrPL spectrum from a measurement in **Chapter 6**, where the values are in good agreement. (*Right*) TrPL spectrum from a measurement in **Chapter 6**, where the truncated mono-exponential is required to accurately determine τ_2. Reproduced from Elsevier Inc ©2024 with permission.[221]

In **Chapter 4** and **Chapter 5**, TrPL was acquired by Dr. Yang Li and Benjamin Hacene using a fluorescence spectrometer (Edinburgh Instruments Ltd., FLSP920) using the TCSPC technique. Excitation occurred via a 635 nm picosecond pulsed laser diode (PicoQuant) triggered by a delay generator with a repetition rate of 150 kHz for Chapter 4 and 5, and 100 kHz for **Chapter 6**. Emission was collected using a photomultiplier tube (Hamamatsu R928P). Measurements were conducted in air.

3.3.3 Other material charactization techniques

3.3.3.1 X-ray diffractometry (XRD)

XRD is a reliable characterization technique for crystalline material microstructures through elastic scattering of x-rays with material electrons. Bragg's law is the basis of x-ray diffraction. For a crystalline material with interplanar distance of d, incident x-rays with wavelength λ and incident angle θ (also known as the Bragg angle) form constructive and destructive interference patterns following the relation:

$$2d\sin\theta = n\lambda \tag{3.5}$$

When the diffracted patterns are shifted by an integer multiple of the wavelength (i.e when *n* is an integer), constructive interference occurs and the Bragg condition is fulfilled. By scanning over a wide range of incident angles, a diffractogram with material dependent characteristic x-ray diffraction peaks can be formed and used to analyse the material. Each peak is indexed to a (h k l) Miller index to represent a corresponding crystal plane, with the possible Miller indices defined by the crystal phase. Peak position, are and full-width at half maximum (FWHM) can provide crystallographic and microstructure information about the materials, including the phase and presence of defects or strain.

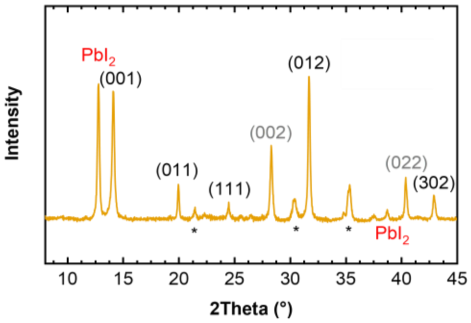

Figure 3-5 Representative XRD of a perovskite thin film. Relevant Miller indices are labelled, with higher order reflections labelled in grey and crystalline PbI_2 in red. * represents ITO peaks from the underlying substrate.

In this work, analysis of perovskite layer crystal structures was carried out utilizing an XRD system (Bruker, D2Phaser) with Cu-Kα radiation (λ = 1.5405 Å) in the Bragg–Brentano configuration using a LynxEye detector. Due to the substrate dependence of perovskite crystal growth, XRD spectra were measured on perovskite half stacks with unpatterned ITO and the relevant HTL. Samples were measured in air.

3.3.3.2 X-ray photoelectron spectroscopy (XPS)

XPS is a surface sensitive technique that can provide important information into the chemical composition of a material, as well as relevant electronic and chemical environments. XPS measures the kinetic energy of surface electrons, typically within the first ~10 nm of material depending on the element, upon irradiation with an x-ray beam. Electron binding energies (E_B) is calculated using the formula:

$$E_B = h\nu - E_K - WF \tag{3.6}$$

Here, $h\nu$ is the incident x-ray energy, WF is the spectrometer work function and E_K is the measured kinetic energy of ejected electrons. E_B is distinct for different elements and is impacted by the local chemical environment. Hence, shifted energies of expelled electrons is indicative of a change in the corresponding chemical state. Correct device calibration, especially of E_B, is crucial to avoid incorrect interpretation of XPS spectra.

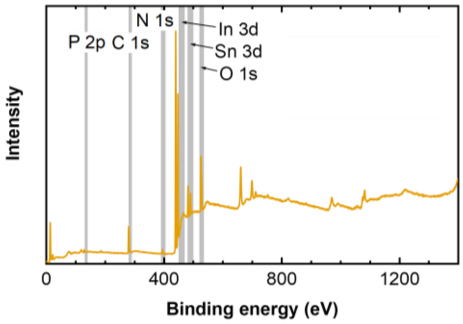

Figure 3-6 Representative raw XPS spectrum of MeO-2PACz on ITO. Grey regions indicate the areas that undergo further processing for investigation in **Chapter 5**. Adapted from Wiley-VCH GmbH ©2023 with permission.[261]

In **Chapter 5**, XPS was performed by Dr. Kathrin Kuster and Dr. Ulrich Starke from Max Planck Institute for Solid State Research under high vacuum conditions using an x-ray photoelectron spectrometer (Kratos, Axis Ultra) equipped with a monochromatic Al k_α x-ray source (1486.6 eV). Survey spectra and high resolution data were acquired with pass energies of 20 and 80 eV respectively with a charge-neutralizer in use. The binding energy was calibrated to the Sn $3d_{5/2}$ peak of ITO at 486.5 eV.[262] CasaXPS was used to analyse the resultant spectrum. Spectral deconvolution in the software utilised Gaussian / Lorentzian functions after subtraction of a Shirley background. P $2p_{3/2}$ and P $2p_{1/2}$ peak binding energy splitting and area ratios were constrained to 0.84 eV and 2:1 respectively. Samples were stored in Argon atmosphere until immediately before measurement.

In **Chapter 7**, XPS was performed by Dr. Suresh Maniyarasu from Helmholtz Zentrum Berlin under ultra-high vacuum (UHV, $<10^{-10}$ mbar) using an x-ray photoelectron spectrometer (Specs GmbH) with a monochromatic Al k_α x-ray source (1.49 keV, 14 kV emission at 300 W) and a 100/150 PHOIBOS hemispherical electron energy analyser. Survey spectra and high resolution data were acquired with pass energies of 30 and 60 eV respectively. CasaXPS was used to analyse the resultant spectrum. Spectral deconvolution in the software utilised Gaussian / Lorentzian functions after subtraction of a Shirley background for Pb 4f, I 3d and N 1s regions, or a Linear background for Cs 3d, Br 3d and C 1s regions. Samples were stored in a nitrogen environment during transport, storage and mounting.

3.3.3.3 X-ray emission spectroscopy (XES)

When a sample is irradiated by an x-ray source, the high energy photons ionise electrons from the inner shells. Outer shell electrons emit characteristic x-rays as they transition into the resultant holes, forming the XES spectrum. XES spectra reflect both the chemical and spin state of the target atoms, allowing chemical state analysis

In this work XES was performed and analysed by Dr. Dirk Hauschild, Dr. Lothar Weinhardt and Prof. Dr. Clemens Heske from Karlsruhe Institute of Technology and University of Nevada, along with Dr. Constantin Wansorra from Karlsruhe Institute of Technology. It was undertaken in the Beamline 8.0.1 at the Advanced Light Source (ALS), Lawrence Berkeley National Laboratory (LBNL) at the SALSA endstation.[263] N K emission spectra were recorded with a high-transmission soft x-ray spectrometer,[264] and the energy axis was calibrated using BN and CaSO4.[265] To mitigate x-ray beam-induced damage, all samples were scanned with a speed of 600 $\mu m.s^{-1}$, which corresponds to an exposure time of 50 ms for each spot. The studies performed to ensure that beam-induced changes were absent in the data with this scan rate are outlined in **Chapter 6**. Samples were transported in a nitrogen atmosphere and loaded without air exposure.

3.3.3.4 Scanning electron microscopy (SEM)

SEM allows for high resolution topographical mapping of electrically conductive samples using a beam of high-energy electrons, with an energy typically ranging from 0.1 to 40 keV and a possible resolution of below 5 nm. SEM topographical mapping typically uses secondary electrons, with typical energies below 50 eV, emitted from the sample surface by the ionising electron beam.

In this work, field emission top-view and cross-cross sectional SEM images were taken by Alexander Diercks using a scanning electron microscope (ZEISS, LEO Gemini 1530). Aperture size was 20 µm and an accelerating voltage of 5 kV.

Some samples in **Chapter 7** were obtained by Aleksandra Miaskiewicz from Helmholtz Zentrum Berlin using an alternate scanning electron-microscope (ZEISS, MERLIN FESEM) with a GEMINI II optical column. A current of 50 pA and acceleration voltage of 10 kV was used.

3.3.3.5 Energy dispersive x-ray spectroscopy (EDX)

EDX is a tool that is closely linked to the previously mentioned SEM, allowing further elemental analysis of samples through the addition of an energy-dispersive spectrometer. As inner shell electrons are ionised by the SEM electron beam, electrons from outer shells fill the resultant vacancies, emitting element specific characteristic x-rays which are collected by the spectrometer. Collecting an EDX spectrum therefore provides information on the relative concentration of specific elements in a sample. By combining this information with the topographical information of the SEM measurement, an elemental distribution map can be created. A sample SEM with corresponding EDX elemental maps are provided in **Figure 3-4**.

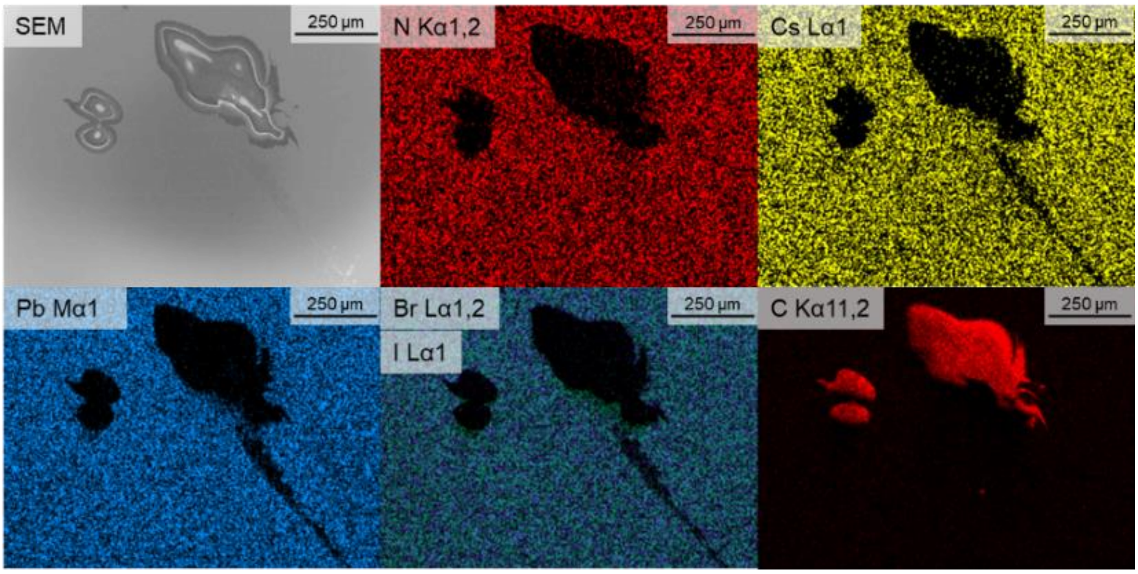

Figure 3-7 Representative SEM measurement of a perovskite with associated EDX. (*Top-left*) Top-down SEM of a perovskite surface with an unidentified particulate. (*Remainder*) Corresponding EDX measurements, filtered to show specific elements. EDX measurements are able to demonstrate the unidentified particle is carbon-rich. Care must be taken when interpreting EDX measurements. The remainder of the carbon spectrum, which appears black, also contains carbon, but the carbon-rich particulate distorts the image due to the much higher concentration.

EDX measurements were performed in conjunction with the SEM measurements obtained using the Zeiss MERLIN FESEM, as outlined above. An EDX detector (Oxford Instruments, Ultim Extreme) was used to collect characteristic x-rays. EDX mapping was performed using the AZtecLive Software from Oxford Instruments. As with the SEM, a current of 50 pA and acceleration voltage of 10 kV was used.

3.3.3.6 Reflection-absorption infrared spectrometry (RAIRS)

Infrared spectroscopy enables the gathering of information regarding vibrational transitions in a wide range of materials and phases. In RAIRS, an infrared photon beam illuminates the sample at a grazing angle and the reflected beam is collected. Absorption can be assigned to vibrational modes and dipoles that are perpendicular to the surface. RAIRS is especially valuable to identify carbon functional groups, as their XPS spectra, as discussed above, are typically difficult to deconvolute.

The presented RAIRS data was recorded by Dr. Rainer Bäuerle from InnovationLab GmBH and Dr. Mario Hentschel from the 4th Physics Institute and Research Center using a fourier-transformed infrared spectrometer (Bruker, Vertex 80v) with a liquid nitrogen cooled narrow-band MCT detector. Spectra were taken with p-polarized incident light after incubation of samples in low vacuum (~3 mbar) for 180 s. Spectral resolution was set to 4 cm^{-1}, aperture size 4 mm, and spectra were acquired by averaging 256 scans.

3.3.3.7 Liquid-phase nuclear magnetic resonance (NMR)

Liquid-phase NMR spectroscopy exploits inherent magnetic properties of certain atomic nuclei (typically those with spin ½), perturbing their spin state in order to induce a current at characteristic resonant frequencies. This information provides information on their immediate environment, which can be interpreted to reveal the structure and concentration of molecules in a solution. While equivalent nuclei form a coherent peak, with a chemical shift governed by surrounding electrons, non-equivalent nearby (typically one or two bonds) nuclei will undergo coupling to split the peak. Analysing the specific form of the split peak provides information on the number of nearby non-equivalent peaks. Chemical shifts are typically calibrated to a deuterated solvent.

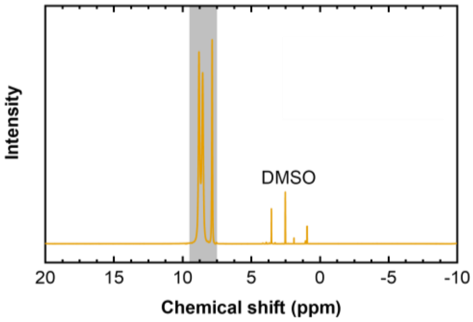

Figure 3-8 Representative raw NMR spectrum of FAI powder. The Grey region indicates the typical region of interest in this work and the residual DMSO peak used to calibrate chemical shift is labelled. Reproduced from Elsevier Inc ©2024 with permission.[221]

Liquid phase NMR spectra (^1H and ^{13}C) were recorded and analysed by Julian Petry in deuterated d_6-DMSO at 400 MHz with a Bruker spectrometer at 298 K. Chemical shifts are reported in parts per million (ppm) relative to residual d_5-DMSO (δ_H= 2.50 ppm) in the corresponding fully deuterated solvent. Powders were weighed in a nitrogen atmosphere and dissolved under ambient conditions.

3.3.3.8 Contact angle

Measuring contact angles of liquids on a solid surface can be used to assess the wetting qualities of said liquid. Furthermore, measuring multiple liquids with different polarities on the same surface can be used to calculate dispersive and polar surface free energies. Care must be taken, as liquid-surface interactions occur relatively quickly, which precludes exact surface energetic calculations. [266]

Contact angle measurements used an optical contact angle and drop contour analyser (DataPhysics Instruments GmbH, OCA 200). Polar and dispersive portions of the surface free energy were calculated using the OWRK model.[267] We utilize a high-speed camera (2450 fps) for our measurements to minimize measurement time.

3.3.4 Electrical charactization techniques

3.3.4.1 Current-density (*J-V*) characteristics

Typically two methods are used to characterize device performance of PSCs, a voltage sweep under illumination in a solar simulator and a constant measurement under maximum power point (MPP) conditions, as outlined in **Chapter 2**.

In this work we primarily utilised a xenon lamp class AAA (Newport, Oriel Sol3A), calibrated using a reference silicon solar cell (Newport, calibrated 2018) equipped with a KG5 bandpass filter. This setup simulates the air-mass (AM) 1.5G solar spectrum with an intensity of 100 mW.cm^{-2}. Scan rate during measurement was set to 0.6 V.s^{-1} using a digital source meter (Keithley, 2400 A). The stabilized PCE of PSCs was determined by tracking the MPP under continuous AM 1.5G illumination for 300 s. Device temperature was actively regulated during measurements by an in-house designed Peltier element connected to a microcontroller set to 25 °C. Opaque devices are typically measured without a mask, as the active area is defined by the overlap of front and rear electrodes. Semi-transparent devices utilised a variety of shadow masks, with the most common being 5.6 mm^2, in order to define a ST aperture area.

Tandem devices were typically characterized using a class AAA 21-channel LED solar simulator (Wavelabs Solar Metrology Systems, Sinus-70) along with a source meter (Keithley 2400). This setup simulates the air-mass (AM) 1.5G solar spectrum with an intensity of 100 mW.cm^{-2}. Scan rate during measurement was set to 0.6 V.s^{-1} using a digital source meter (Keithley, 2400 A). 4T tandems were measured under ST filters prepared alongside the ST-PSCs with an identical layer stack, but a 256 mm^2 area. Final power conversion efficiencies of 4T tandems were obtained by the sum of the top ST-PSC PCE and bottom cell PCE. Monolithic tandems were measured with a 100 mm^2 shadow mask to isolate the active area.

3.3.4.2 External quantum efficiency (EQE)

EQE is a method to characterise to define the spectral response of photovoltaic devices. It can be defined as the ratio of charge carrier flux to that of photon flux. EQE is general considered as a function of wavelength (λ) and can be used to calculate device current density (J_{SC}) by integrating over the relevant spectrum:

$$J_{SC} = \int q \times EQE(\lambda) \times S(\lambda) d\lambda \qquad 3.7$$

Here *q* is the electric charge and *S(λ)* is the incident solar intensity (AM 1.5G). EQE derived J_{SC} often is less than J_{SC} observed in current density measurements. This has been theorised by Saliba et al. to be due to numerous factors,[268] including but not limited to: measurement conditions such as incident light intensity, applied bias or preconditioning, and perovskite material properties such as ion migration.[269–271] EQE can also be used to estimate device bandgap by calculating the highest energy inflection point of the EQE curve. A representative EQE spectrum, along with an associated calculation of the bandgap, is provided in **Figure 3-11**.

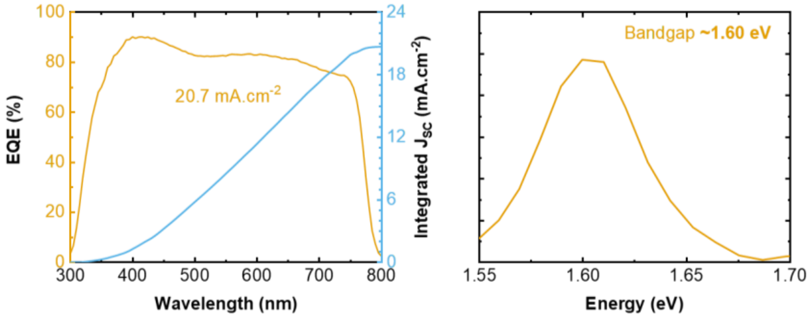

Figure 3-11 Representative EQE and associated derived photovoltaic properties. (*Left*) Representative EQE and corresponding calculation of J_{SC}. (*Right*) Bandgap determined by taking the derivative of the EQE near the bandgap.

In this work, EQE was characterised using a Bentham PVE300 system. The system uses a lock-in amplifier and monochromator the reference signal chopping frequency of ~580 Hz to improve signal-to noise ratio and filter ambient slight. Typical measurements employed a step size of 4 or 5 nm, and an integration time of 500 ms. Illumination area was typically restricted using a 0.74x0.74 mm^2 aperture coated with non-reflective substances. Prior to any measurement, the EQE response was calibrated using a certified Si cell. For tandem devices, the Si was used for the wavelength range of 300 to 1100 nm and a supplemental germanium (Ge) reference was used for 900 to 1300 nm. Monolithic tandem devices measured each subcell independently by applying bias light from light emitting diodes with wavelengths of 465 nm or 940 nm to saturate the non-measured subcell.

3.3.4.3 Electrical impedance spectroscopy (EIS)

EIS is a method used for the characterization of charge-carrier dynamics in photovoltaic devices. It is typically measured by applying a small sinusoidal AC voltage with frequency ω to the device, accompanied by a DC offset voltage. For a sufficiently small applied potential, the current response signal should have the same frequency as the sinusoidal potential with a phase shift (ϕ). Impedance can be expressed as a function of the magnitude (Z_0) and the phase shift:

$$Z = \frac{V\sin(\omega t)}{I\sin(\omega t + \phi)} = Z_0 \frac{\sin(\omega t)}{\sin(\omega t + \phi)} \qquad 3.8$$

Here *V* and *I* represent the amplitudes of the voltage and current. By applying Euler's formula, the impedance can be expressed as a complex function, then separated into real (*Re(Z)*) and imaginary (*Im(Z)*) components as follows:

$$Z(\omega) = \frac{V}{I} = Z_0 e^{i\phi} = Z_0(\cos\phi + i\sin\phi) \qquad 3.9$$

$$Re(Z) = Z_0(\cos\phi)$$

$$Im(Z) = Z_0(\sin\phi)$$

Plotting the relationship between these components, with *Re(Z)* on the x-axis and *Im(Z)* on the Y-axis gives the Nyquist plot used to represent impedance in this thesis.

In this work, impedance was characterised by Roja Singh using a general electrical characterization system (PAIOS, Fluxim). An amplitude of 70 mV was applied in EIS, with a sweep frequency from 1 Hz to 1 MHz. Bias was employed depending on relevant perovskite open-circuit voltage. The devices were measured while exposed to light.

3.3.5 Simulation techniques

3.3.5.1 Optical simulations

Optical simulations of 4T tandem modules were obtained by Fabrizio Gota using the open-source modeling platform EYcalc.[202,272] First the optics module was used to fit an experimental EQE to a simulated equivalent stack. The optics module is able to calculate absorptance through multiple thin-film stacks via the transfer matrix method,[273] and employed geometrical ray-tracing to simulate non-planar interfaces.[189] Integrating the EQE over the AM 1.5G spectrum gave a short-circuit current for each subcell. PCE was finally calculated using the electrical module, which can determine *J-V* characteristics *via* a model based on the Shockley diode equation, assuming a consistent temperature, ideality factor (*n_{id}*), R_{series} and R_{shunt} between the initial and simulated JV measurements:

$$J(V) = J_{SC} - J_0 \left(e^{\left(\frac{V + JR_{series}}{n_{id} k_B T} - 1\right)} \right) - \frac{V + JR_{series}}{R_{shunt}} \qquad 3.10$$

3.3.5.2 Density functional theory (DFT) calculations

DFT is a powerful modelling method to determine spatially dependent electron density of complex systems. In this thesis Dr. Abderrezak Torche, Dr. Michelle Ernst and Dr. Ganna Gryn’ova from Heidelberg University used DFT to determine interaction modes of 2PACz with perovskite surfaces. DFT computations were implemented in the quantum espresso package software using the PBE exchange-correlation functional with the dispersion correction included at the DFT-D3 level,[274,275] which is known to be accurate for calculating perovskite phase transitions.[276] Core electrons were modelled *via* ultrasoft pseudopotentials and a plane wave basis set cutoff of 55 Ry (748 eV) was used. Relaxations of these structures were performed using the conjugate gradient method. For this, the convergence threshold on forces was set to 10^{-3} atomic units.

4 Optical optimizations of 4T perovskite/CIGS solar cells with varied absorber materials

Abstract

In this chapter we investigate the potential of 4T perovskite/CIGS tandem solar cells through optical optimization applied to a variety of perovskite absorbers. We perform extensive optimization of the front and rear transparent conductive oxides (TCOs), comparing various combinations of common materials, and pairing with optimized magnesium fluoride (MgF_2) antireflective layers. These optimizations improve the weighted near-infrared (NIR) transmittance, an important figure of merit for tandem devices, from 62.0% for baseline devices to 88.8% for the best solution-processed devices. When optimized devices are employed in a 4T architecture with a CIGS bottom solar cell, our optimizations result in a PCE of 27.3% for solution processed and 24.2% for co-evaporated absorbers. From this baseline, we develop a detailed loss analysis that outlines a path towards achieving a 29.5% possible PCE for 4T perovskite/CIGS tandem devices exclusively through improved light management.

The work in this chapter resulted in the publication: **'Four-terminal Perovskite/CIGS Tandem Solar Cells: Unveiling the Path to >27% in Power Conversion Efficiency'**, published in **Solar RRL** by Thomas Feeney, Dr. Ihteaz M. Hossain, Dr. Saba Gharibzadehas shared first authors.[35] This work also includes additional contributions by Dr. Tobias Abzieher.[277]

This work is the result of collaborative research between Karlsruhe Institute of Technology and Zentrum für Sonnenenergie- und Wasserstoff-Forschung Baden-Württemberg (ZSW).

Thomas Feeney as a first author of this study designed the experiments and developed the original concept in tandem with Dr. Ihteaz M. Hossain and Dr. Saba Gharibzadeh. Thomas Feeney also developed the ALD-SnO_x *deposition method used in this work, deposited all co-evaporated perovskites for ALD-*SnO_x *optimization, optimized and deposited all layers post-*C_{60}*, performed all UV-vis, JV and EQE characterizations and analysed all relevant data. Dr. Saba Gharibzadeh produced and optimized all shown spin-coated perovskites to the* C_{60} *layer. Dr. Tobias Abzieher produced all wide bandgap co-evaporated perovskites to the* C_{60} *layer. Fabrizio Gota carried out optical simulations, Dr. Adrian Mertens measured and analysed ellipsometry data. Dr. Jan-Philipp Becker developed the IO:H processes on glass with support by Dr. Erik Ahlswedle, who was also involved in tandem optimization, Dr. Stefan Paetel optimized the CIGS bottom cell. The project was under the supervision of Prof. Dr. Ulrich Wilhelm Paetzold.*

4.1 Motivation

Development of thin film perovskite solar cells (PSCs) has been rapid and impressive, with power conversion efficiencies (PCEs) reaching over 26% in single-junction devices.[43] With this, they approach the PCEs of the industrially dominant thin film technology of silicon (at 27.6%),[43] and have long surpassed other thin film options, such as CIGS (at 23.6%).[43] Further advances in single-junction devices require perfect ideality factors coupled with lossless contacts and defect free materials to further improve their PCE.[137,278,279] An alternative method to further improve PCE is to utilise tandem device architectures, where two or more photovoltaic absorbers are employed in sequence to effectively harvest a greater portion of the solar spectrum. Lead based perovskites are uniquely suitable to be employed as the top subcell for tandem devices due to their wide and tunable bandgap, enabling them to match calculated optimal bandgaps of various bottom subcells.[198,280–282]

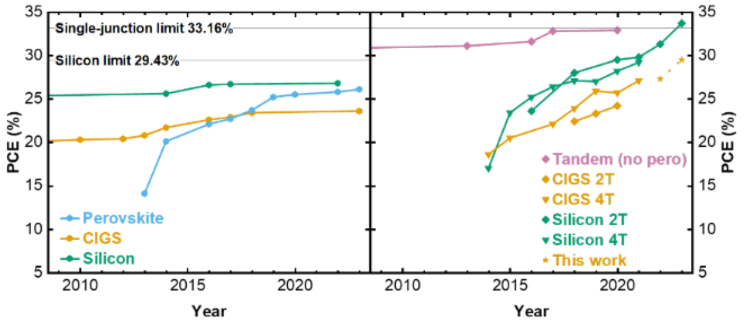

Figure 4-1 Maximum reported PCEs of various single-junction photovoltaic technologies (*left*) and tandem solar cells (*right*) in each calendar year at time of original publication. Stars represent the performance of the prototype device developed in this work (27.3%) and predicted after adopting the outlined recommendations derived from our optical simulations (29.5%). Figure adapted from Wiley-VCH GmbH ©2022 with permission.[35]

Detailed-balance calculations, as discussed in **Section 2.3**, yield theoretically achievable PCEs of up to ~45% for two-junction tandem solar cells, irrespective of architecture.[22,138,139] However, such calculations require multiple assumptions, including no losses from parasitic absorption. More recent calculations, which incorporate material property considerations of perovskite/CIGS tandems under realistic irradiance, predict feasible PCEs of ~32%.[283] Over the past decade, 4T tandems have demonstrated impressive PCE growth,[24,26,43,284–293] with the most recent record achieved by *Huang et al.* and *Xingxing et al*, who reported PCEs of 30.0% and 28.4% for perovskite/Si and perovskite/CIGS respectively.[280,294] This achievement for perovskite/CIGS 4T tandems represents an impressive jump from 2021 performances, which were steady at ~27%.[295] While perovskites based on silicon bottom solar cells consistently outperform CIGS due to the superior near infrared response of silicon, the bandgap tunability (~1.0–1.7 eV),[296] radiation hardness,[297] and the possibility for lightweight flexible tandem devices make CIGS an alternative worth additional research.[298]

This chapter will be based on perovskite/CIGS 4T tandem devices, with a focus on managing optical losses in response to **Challenge 1**. Optical losses in 4T tandem solar cells primarily arise from parasitic absorption and reflection losses, which reduce top subcell semitransparent (ST) PCE and limit sub-bandgap transmission of the photons to the bottom subcell.[27,64,299–301] Minimization of optical losses without sacrificing device performance is paramount for achieving high PCE 4T tandem devices.

First, **Section 4.2** will outline the optimization performed for the atomic layer deposited (ALD)-SnO_x used in this chapter. ALD-SnO_x is crucial to protect the perovskite layer during TCO deposition and, due to the specifics of the utilised system, differs slightly from common recipes.

The primary contributors to parasitic absorption in a 4T perovskite tandem device are the TCOs at the front and rear side of the top ST perovskite subcell, where front is defined as the first TCO exposed to incident light.[299,301] Hence, **Section 4.3** will address the initial optimization, and will focus on the minimization of optical losses arising from these TCOs. Reflection losses are more complex, stemming from numerous interfaces in the tandem stack, for instance, air/glass, perovskite/charge transport layers, TCO/air, etc.[302] The largest contributor to reflections losses are the air/TCO and air/glass interfaces in the top ST perovskite subcell, which will be the second focus of this optimization, utilizing the common antireflective coating (ARC) of magnesium fluoride (MgF_2). This systematic optimization of the top ST perovskite subcell layer stack, focusing on enhancing its optical properties, leads to the creation of ST perovskites with a weighted NIR transmission of 88.8%.

We incorporate these ST-PSCs into 4T perovskite/CIGS tandem solar cells in **Section 4.4** and achieve a record (at time of initial publication) PCE for 4T perovskite/CIGS tandem solar cells of 27.3%. This section will also explore a WBG co-evaporated perovskite in response to **Challenge 2**, witah a 4T perovskite/CIGS tandem PCE of 24.2%.

Based on optical simulations of champion devices, **Section 4.5** will develop a detailed loss analysis to outline how to improve these 4T perovskite/CIGS results to a theoretical 29.5%, exclusively *via* optical management. This chapter therefore highlights the need for optical management in high performance tandem devices.

4.2 ALD-SnO_x for ST devices

In this section we report on an optimized ALD-SnO_x buffer layer used to protect ST-PSCs during sputtering of the TCO. For the purposes of this optimization we utilized the layer stack glass/ITO/Spiro:TTB/perovskite/C_{60}/ALD layer/IZO/Au for co-evaporated ST-PSCs and glass/ITO/2PACz/perovskite/C_{60}/ALD layer/IZO/Ag for solution-processed. Dr. Saba Gharibzadeh produced solution-processed perovskites until the C_{60} layer. Device statistics of ST-PSCs produced during this optimization are found in **Figure 4-2**, with an additional set of optimizations using co-evaporated and solution-processed perovskites shown in **Figure S4-1**. A thickness of 300 cycles, corresponding to 35 nm on Si, was chosen as standard due to reduced yield at lower thicknesses for ST-PSCs.

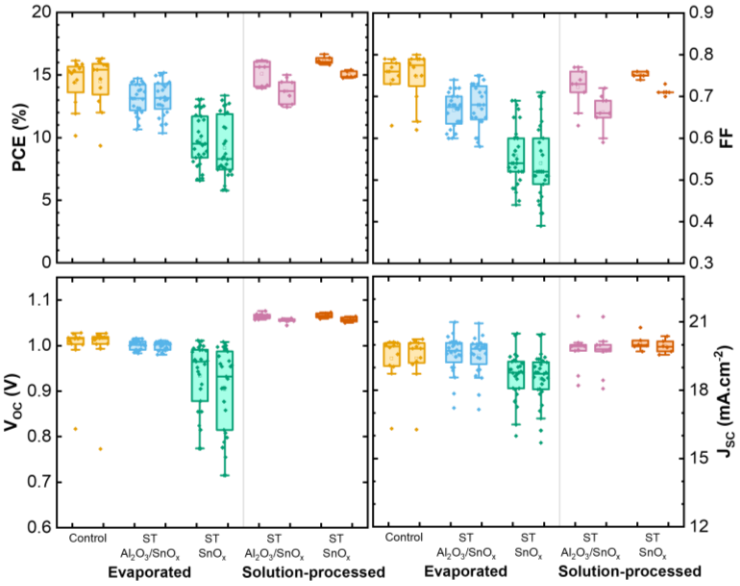

Figure 4-2 Statistics for forward and reverse scans of ST co-evaporated and solution-processed PSCs using ALD buffer layers. The control is an opaque co-evaporated reference with BCP instead of Al_2O_3/SnO_x.

Based on these results, a nucleating Al_2O_3 layer (20 cycles) was added to all co-evaporated ST-PSCs, due to the substantial increase in ST-PSC PCE. This layer is thicker than typical 10 cycle ALD-Al_2O_3 tunnel junctions,[303] but the expected thickness is lower due to poor ALD growth on non-reactive surfaces such as C_{60}.[225,227–229] The device improvement in co-evaporated perovskites is attributed to a mitigation of interfacial degradation they would otherwise experience during exposure to TDMASn.[54,236,239] The solution-processed perovskites used in this work are more robust,[236] meaning they do not benefit from this additional protection. Co-evaporated devices were also deposited at a lower temperature of 80 °C instead of 90 °C for similar reasons.[236]

ALD-SnO_x displays remarkable optical properties, outlined in **Figure 4-3.** Refractive index (*n*) aligns with the indium-doped tin oxide (ITO) or indium-doped zinc oxide (IZO) rear TCOs, meaning low reflections are expected at this interface. Furthermore, ALD-SnO_x exhibits an incredibly low extinction coefficient (*k*). The absorption coefficient α is given by the equation:

$$\alpha = \frac{4\pi k}{\lambda_0} \qquad 4.1$$

Here λ_0 is the vacuum wavelength and *k* the extinction coefficient. The incredibly low value of *k* across the measured spectrum means significant parasitic absorptance from the ALD-SnO_x layer is not expected, despite a higher thickness (35 nm on Si compared to 20 nm on Si) than typically used.

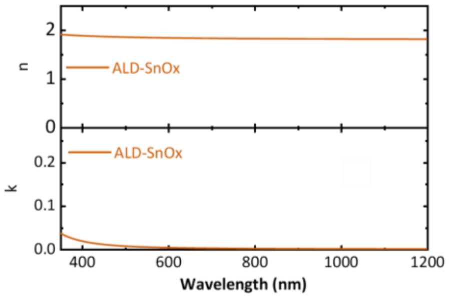

Figure 4-3 (*Top*) Refractive index and (*bottom*) extinction coefficient for ALD-SnO$_x$ developed for this work.

4.3 Minimization of ST device optical losses

In this section we consider the impact of various TCOs, and a MgF$_2$ ARC, on the near infrared transmission spectra of ST-PSCs and provide a brief explanation as to the cause of these impacts.

4.3.1 Selection and optimization of TCOs

TCOs are the largest source of parasitic absorption in ST-PSCs. Various combinations of three common TCOs are considered: commercially available or in-house sputtered ITO, in-house sputtered IZO and collaborator (ZSW) sputtered hydrogenated indium oxide (IO:H). ITO is considered the standard for front and rear TCOs, with a commercial front ITO and an in-house sputtered rear TCO.

When optimizing TCOs, three factors must be considered for each material. In terms of optical properties, reflectance and parasitic absorption losses must be kept at a minimum to maximize light transmission. However, this must be balanced against electrical properties, most importantly sheet resistance (R_{sheet}), with exact requirements differing between the front and rear TCOs. A final material consideration is the processing and post-processing steps. For in-house TCOs, IO:H requires post-deposition annealing of approximately 230 °C according to optimizations performed in previous literature.[301,304,305] Hence, it was not considered as a viable rear TCO for this work.

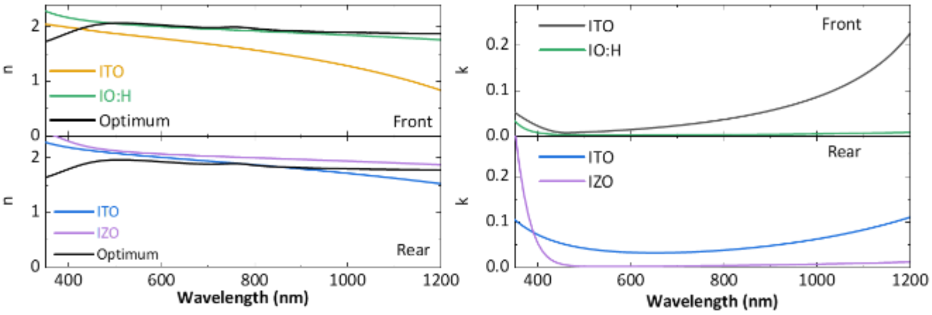

Figure 4-4 *(left)* Refractive indices and (*right*) extinction coefficients of front and rear TCOs. Reproduced from Wiley-VCH GmbH ©2022 with permission.[35]

Dr. Adrian Mertens from the Institute of Photonics and Quantum Electronics, KIT conducted analysis of TCOs deposited directly onto glass using ellipsometry to determine optical properties, with the results shown in **Figure 4-4**. In-house and commercial ITO (front) possess a high extinction coefficient, which is attributed to high free carrier concentration in ITO (~10^{21}/cm^3),[306] due to its low mobility.[307] Low mobility of ITO has been attributed to a hybridization of Sn 5s and In 5s orbitals causing a higher effective mass.[308] This non-ideal extinction coefficient is most prominent in the near-infrared (NIR) region of 500 – 1200 nm. An approximate perovskite bandgap of 800 nm, coupled with expected sub bandgap transmission in the 500 – 800 nm region, make maximising NIR transmission vitally important for current generation in CIGS subcells. IO:H and IZO outperform commercial or in-house sputtered ITO in terms of extinction coefficient over the NIR region. The reduced extinction coefficient of IO:H emerges from an exceptionally low charge carrier concentration (~10^{20}/cm^3),[306] even compared to IZO (~$5 \cdot 10^{20}$/cm^3).[309] Hence, replacing ITO with IO:H and IZO for the front and rear TCOs respectively is expected to reduce parasitic absorption in the NIR region. It is worth considering that IZO exhibits a higher extinction coefficient than in-house ITO below 400 nm, which would reduce perovskite performance if measured through the IZO. The lower extinction coefficient of IO:H compared to commercial ITO up to 800 nm indicates that an perovskite devices utilizing this material will benefit from reduced parasitic absorptance. UV-vis measurements of various TCOs is provided in **Figure S4-2**.

Next, we consider the more complicated characteristic of refractive index. For a perovskite on a glass substrate, the optimum refractive index of an ideal medium for the front TCO to minimize reflectance is determined from:

$$n_{optimum} = \sqrt{n_{glass} n_{perovskite}} \tag{4.2}$$

This would minimize reflectance between the glass substrate and the perovskite absorber. In a similar manner, minimizing the perovskite/air reflectance for the rear TCO is determined from:

$$n_{optimum} = \sqrt{n_{air} n_{perovskite}} \tag{4.3}$$

For air ($n \approx 1$), this corresponds to minimizing the refractive index of the TCO over all wavelengths. Ellipsometry measurements of *nk* values for perovskite and glass substrates are provided in **Figure S4-3**. These measurements allow the development of an optimum with respect to wavelength for the front and rear TCO. For the front TCO, the refractive index of ITO decreases compared to IO:H in visible wavelengths, which is the result of a blue-shifted ITO plasma frequency (due to a high charge carrier concentration of magnitude ~10^{21}/cm^3).[310,311] These results indicate that IO:H is superior to commercial ITO for minimizing reflections. However, the inferior matching of the refractive indices of IZO and in-house ITO indicate an expected increase in reflectance, which will limit the overall enhancement in transmittance when replacing ITO with IZO by causing increased Fresnel reflections at the air/IZO interface.

Parasitic absorption losses from IZO and IO:H can be reduced further by decreasing its thickness. However, a decrease in TCO thickness will lead to a corresponding increase in sheet resistance *R_{sheet}*, as shown in **Figure 4-5**, which is detrimental to device performance. However, IO:H sheet resistances of samples used in this work deviates from these values. Unlike other TCOs, chemisorption of H_2O and OH groups on the IO:H surface results in degradation of grain boundaries, decreasing Hall mobility.[312] As utilised IO:H samples were fabricated by an external partner and stored for an extended period, such degradation is expected.

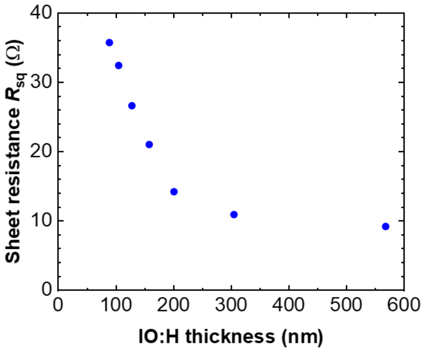

Figure 4-5 Manufacturer measured values of sheet resistances for IO:H with respect to thickness. Measured by collaborators from ZSW. Reproduced from Wiley-VCH GmbH ©2022 with permission.[35]

We opted for an optimized IZO front TCO that exhibits lower R_{sheet} (~45 $\Omega.sq^{-1}$) compared to the reference ITO in addition to the aforementioned lower parasitic absorption. Full R_{sheet} and thickness properties of the optimized TCOs used in this chapter are provided in **Table 4-1**. Also note the difference in R_{sheet} for front and rear ITO. This is attributed to the different processing allowed for commercial ITO in the absence of a perovskite under layer, which allows thermal annealing and higher plasma energies, both of which are attributed with a reduced series resistance.[311,313]

Table 4-1 Sheet resistance and thickness of the investigated TCOs at utilized thicknesses. Reproduced from Wiley-VCH GmbH ©2022 with permission.[35]

TCO/Parameters	Front TCO		Rear TCO	
	c-ITO	IO:H	ITO	IZO
R_{sheet} ($\Omega.sq^{-1}$)	~15	~22	~60	~45
Thickness (nm)	140	230	160	165

4.3.2 MgF_2 as an ARC

As a method to continue improving NIR transmittance and light incoupling we consider an MgF_2 based ARC. Since MgF_2 exhibits a comparatively constant refractive index of ~1.38 for a wide range of wavelengths,[314] a value below both the rear IZO and front glass, it can be exploited as a suitable ARC for visible and NIR wavelengths, given appropriate layer thickness. Theoretical optimum ARC thickness (d) for a given wavelength (λ) and ARC refractive index (*n*) is given by:

$$d = \frac{\lambda}{4n} \tag{4.4}$$

This leads to an expected optimum range of 144.9 - 217.4 nm for an ARC maximizing NIR. As the AM 1.5G spectrum is non-uniform, any optimization of transmission needs to be weighted to ensure the data accurately reflects reality. **Figure 4-6** outlines the results of these experiments.

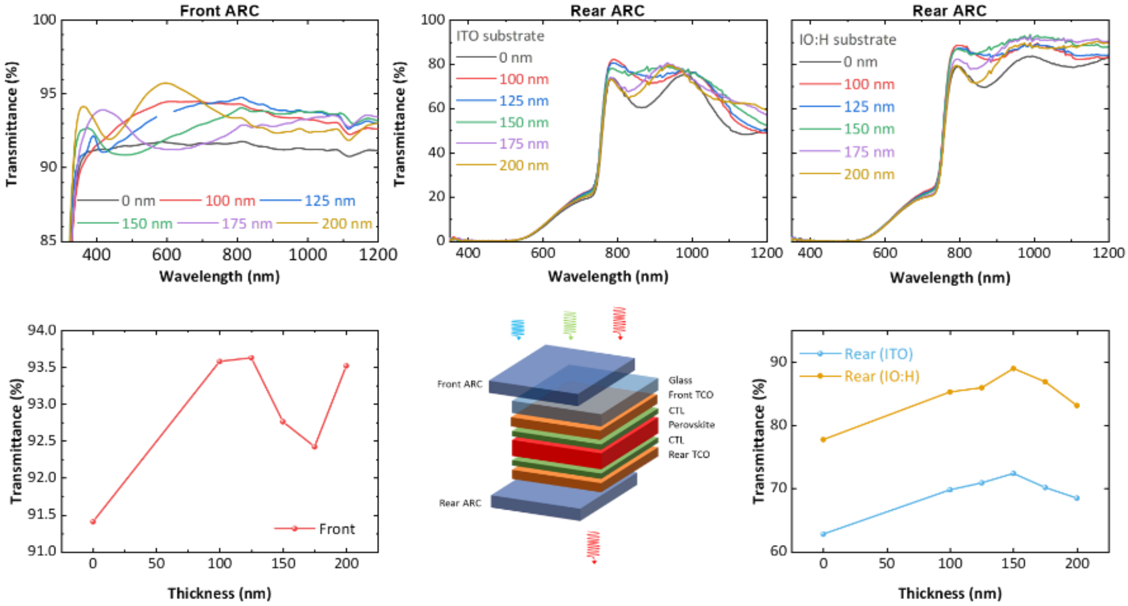

Figure 4-6 Optimizations of MgF_2 ARC. (*Top*) Transmittance spectra of MgF_2 deposited on glass (*left*) and MgF_2 deposited on perovskite filter rear IZO (*middle-left*) for various thicknesses. (*Bottom*) Weighted transmittance of MgF_2 deposited on glass (*left*) and MgF_2 deposited on perovskite filter rear IZO (*right*). (*Bottom-middle*) Outline of where in the device stack each MgF_2 is deposited. Adapted from Wiley-VCH GmbH ©2022 with permission.[35]

We considered two configurations during the ARC optimization. For MgF_2 deposited onto glass, it is sufficient to optimize transmission of this bare substrate. However, for MgF_2 deposited onto the IZO, reflections within the perovskite could be more complex. Optimization of the MgF_2 thickness on IZO was hence performed using the stack: MgF_2 (125 nm)/glass/TCO/2PACz/$Cs_{0.17}FA_{0.83}Pb(I_{0.92}Br_{0.08})_3$/$C_{60}$/$SnO_x$/IZO/$MgF_2$ (varied). For the initial variation, to demonstrate that the optimum is independent of the rear TCO, the MgF_2 thickness was optimised with both ITO and IO:H as front TCO. Perovskite half stacks utilising IO:H and an optimum MgF_2 thickness of 150 nm obtained a weighted NIR transmittance of 88.8%.

4.3.3 Iterative improvements in stack optical properties

With the impact of our two classes of optimization defined, we now consider the impact these variations have on a complete device. Dr. Saba Gharibzadeh produced solution-processed perovskites until the C_{60} layer. We performed a systematic investigation of an inverted ST-PSC stack, studying optics in a high-efficiency double-cation solution-processed perovskite *via* equivalent optical filters using an unpatterned front TCO. This optimization was undertaken with the aim of maximizing NIR transmission by simultaneous reduction in parasitic absorption and reflections. Stack breakdowns and accompanying broadband optical properties spectra are present in **Figure 4-7.** Stack A represents our baseline stack, which uses a commercial ITO for the front TCO with an in-house sputtered ITO as the rear TCO and no ARC.

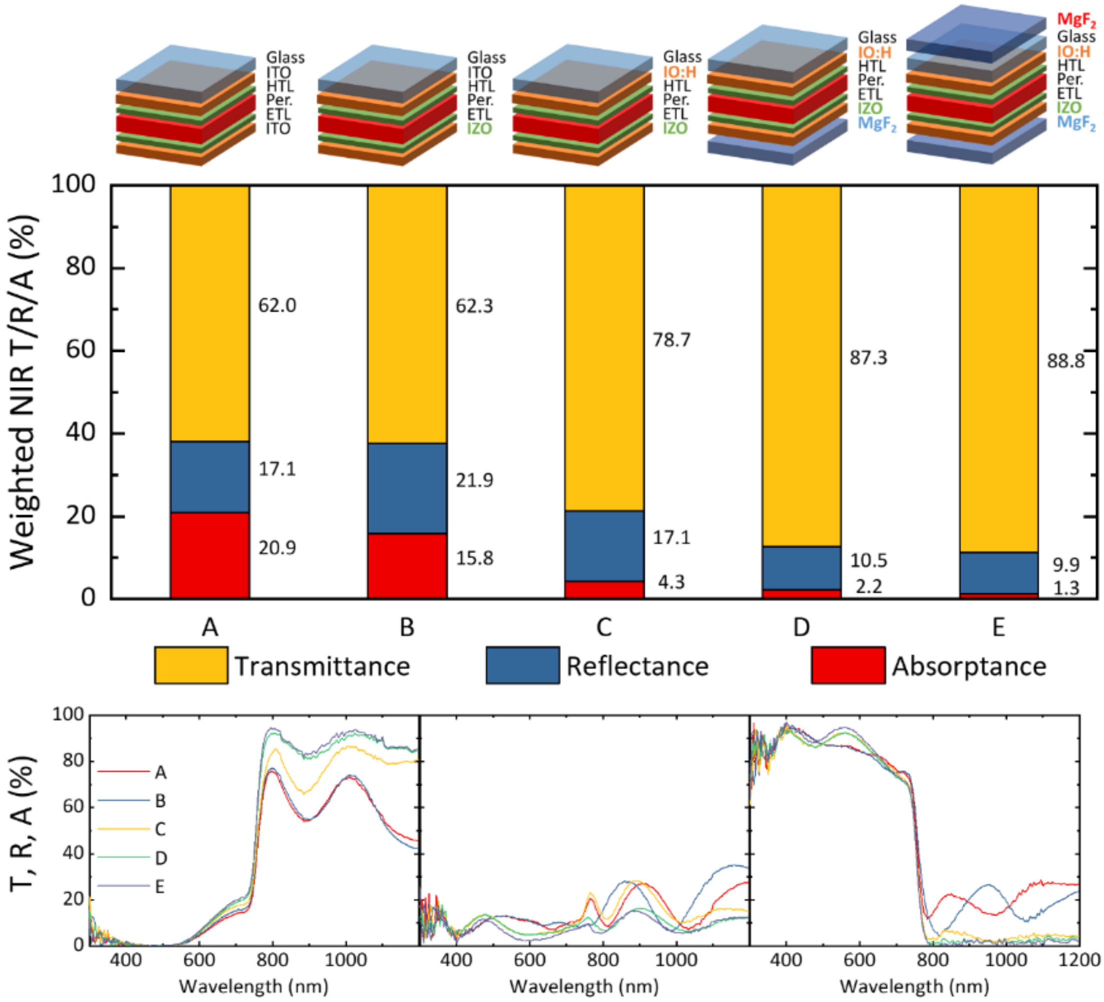

Figure 4-7 Outline of optical optimizations and the resultant impact on NIR optical properties. (*top*) Schematic illustration of ST-PSCs with various layer configurations as outlined in the above images. The accompanying bar chart (*middle*) represents the breakdown of absorptance, reflectance and transmittance in NIR wavelengths (800 – 1200 nm) for each respective stack. Values have been weighted against the relative portion AM 1.5G spectrum to obtain a practical effective value. In all optical stacks 2PACz is used as an HTL, while the ETL is C_{60}/SnO_x. Associated measurements are shown underneath. From left to right: transmittance, reflectance and absorptance spectra are shown. Reproduced from Wiley-VCH GmbH ©2022 with permission.[35]

To reduce parasitic absorption losses, the perovskite stack was first by using an optimized in-house sputtered IZO as a replacement for the rear ITO (Stack B). This was a clear first step in improving the NIR optical properties of our stack as, according to previous studies, a rear ITO layer contributes significant parasitic absorption that can be readily reduced by replacing it with IZO. Comparing Stack B with the reference Stack A results in an overall reduction in parasitic absorption of ~5%. Further comparison shows a notable increase in reflectance, due to the increased Fresnel reflections, which limits the overall enhancement in transmittance. Inclusion of an optimized ARC is crucial to minimize the impact of this effect.

In-house sputtered IO:H was next explored as an alternative to commercially available ITO as the front TCO to further reduce optical losses (Stack C). This replacement facilitates a substantial improvement in NIR transmittance of ~16.5%$_{abs}$, which can be attributed to a reduction of both parasitic absorption (~11.5%) and reflection losses (~5%) due to the more optimum *n* value of IO:H and reduced extinction coefficient.

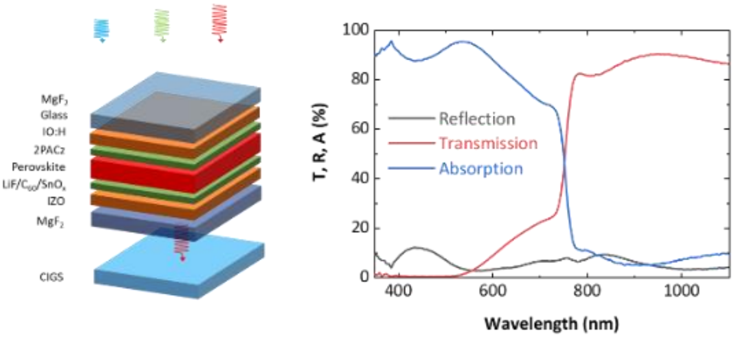

Figure 4-8 ST-PSC measurement stack. (*Left*) Schematic illustration of the layer stacks for perovskite/CIGS tandem device. (*Right*) Reflection (R), transmittance (T) and absorptance (A) spectra of the optical filter for the champion device. Reproduced from Wiley-VCH GmbH ©2022 with permission.[35]

In our third optimization series additional MgF_2 layers are incorporated to improve NIR transmittance and light in-coupling. One utilizes MgF_2 exclusively atop the rear IZO (Stack D), while the other has MgF_2 deposited on both sides of the ST-PSC (Stack E). Even a 150 nm thick layer of MgF_2 deposited only on the rear side significantly reduces IZO/air interfacial reflections, achieving an absolute improvement of ~8.6% in NIR transmittance. This improvement is essential for achieving high PCE in the bottom subcell of perovskite-based tandems. Employing a second MgF_2 layer with a thickness of 125 nm at the front glass side further reduces air/glass reflection losses by ~0.5%. The resultant overall transmittance averages 88.8% over the spectrally relevant NIR range, with minimized reflectance and parasitic absorptance losses of 9.9% and 1.3%, respectively. A summary of the final layer stack and associated UV-vis measurements is provided in **Figure 4-8**. These findings result in ST-PSCs with some of the highest average NIR transmission reported, highlighting the importance of implementing low loss TCOs in conjunction with ARCs to reduce parasitic absorption and reflection losses.

4.4 4T perovskite/CIGS tandem solar cells

In this section we consider the optoelectronic properties of solution-processed and co-evaporated ST-PSCs designed with optimized optical properties and the resultant 4T perovskite/CIGS PCE, allowing comparisons to be made between these deposition methods. CIGS bottom subcells were provided by ZSW)

4.4.1 Solution-processed WBG PSCs and champion 4T tandems

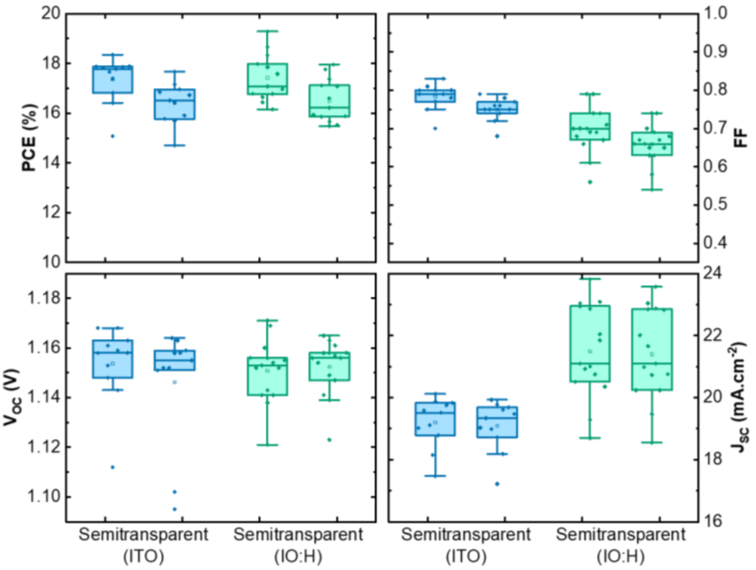

Figure 4-9 Photovoltaic parameter statistics derived from forward and reverse *J-V* scans for solution-processed ST-PSCs fabricated with ITO and IO:H as the front TCO. Reproduced from Wiley-VCH GmbH ©2022 with permission.[35]

To demonstrate the benefits of using top subcells optimized for low optical losses, on the performance of the perovskite/CIGS tandem solar cells, we fabricate top ST-PSCs with an active area of ~10.5 mm^2. Dr. Saba Gharibzadeh produced solution-processed perovskites until the C_{60} layer. The layer stack of our optimized top ST-PSC, along with the equivalent optical filter, is sufficiently similar to Stack E of **Figure 4-7** that any difference in overall optical properties can be disregarded. Two differences exist. First, a 1 nm thick LiF layer is employed between the perovskite and the C_{60} layer to reduce interfacial non-radiative recombination losses and improve open-circuit voltage (V_{OC}).[112,315] Second, the devices utilize metallic Ag fingers, which form a C shape to encircle the active area and thus reduce the series resistance in the rear contact of the device. These metallic fingers will not influence overall optical properties of the sample as they are not present in the defined active area. For calculation of the 4T tandem PCE, a CIGS solar cell was measured below a perovskite optical filter fabricated with the same layer sequence as the ST-PSC. Theoretically the optimum bandgap for CIGS can vary widely dependent on the utilized bandgap, but practically high efficiency CIGS devices are ~1.2 eV. 4T tandem devices exhibit a reduced dependence on top subcell bandgap due to a lack of current matching requirements.[30,316] Energy yield modelling of 4T perovskites coupled with ~1.2 eV CIGS in real world conditions find an optimal bandgap of ~1.70 - 1.80 eV,[283,316] while the optics focused simulations in **Section 4.5.2** find an optimum bandgap of 1.73 eV. However, due to complex factors that affect PSCs when increasing bandgap (such as voltage deficit and halide migration),[124,317–320] we elected to focus on a non-optimal bandgap of 1.68 eV, which was already known to enable stable and high efficiency devices.

The current density-voltage (*J-V*) characteristics and MPPs of champion ST-PSCs, along with corresponding statistics that highlight the high performance and reproducibility of the ST-PSCs are also presented in **Figure 4-9.** Here, the champion top ST-PSC demonstrates a PCE of 19.3%, a short-circuit current density (J_{SC}) of 20.7 mA.cm^{-2}, a V_{OC} of 1.17 V, and a fill factor (FF) of 0.79 in the backward scan. To demonstrate the benefit of using IO:H as a front TCO over ITO, ST-PSCs were fabricated using a commercially available ITO as the front TCO with similar MgF_2 and IZO. Resultant devices reflect the slightly higher R_{SQ} of IO:H (~22 Ω.sq^{-1}) compared to commercial ITO (~15 Ω.sq^{-1}), and the higher transmittance of IO:H in the perovskite region. Champion ITO top ST-PSCs demonstrate a PCE of 18.4%, a J_{SC} of 19.8 mA.cm^{-2}, a V_{OC} of 1.16 V, and a FF of 0.80 in the backward scan.

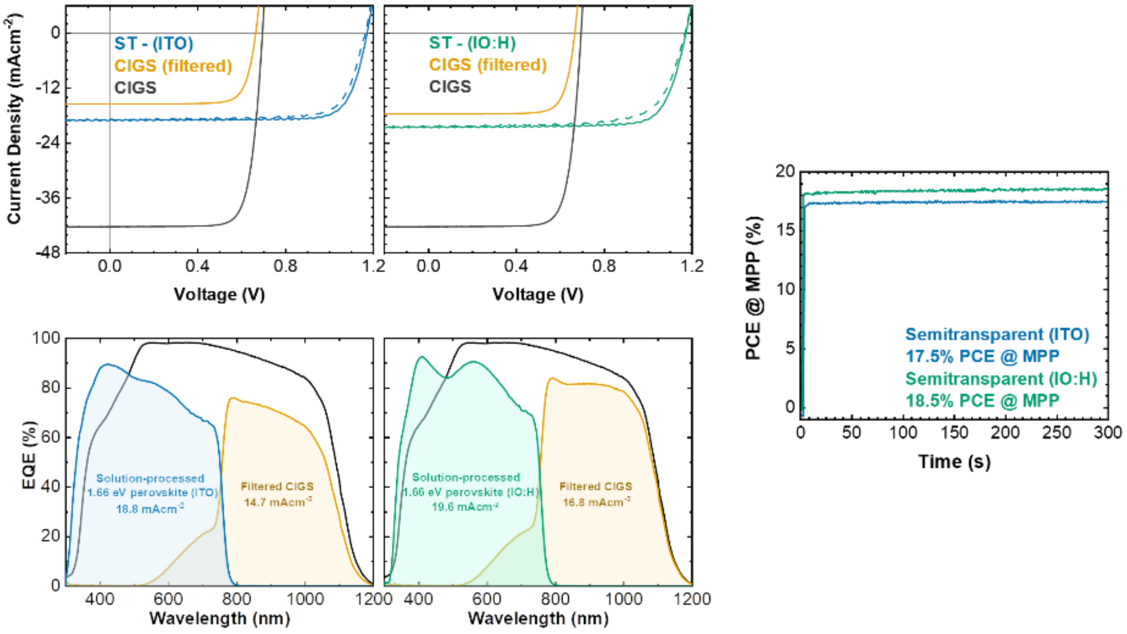

Figure S4-10 Measurements of 4T perovskite/CIGS tandems with a solution-processed absorber. (*Top) J-V* characteristics of solution-processed ST-PSC (ITO and IO:H substrates), with standalone and filtered CIGS solar cells. (*bottom*) External quantum efficiency of ST-PSC, standalone/filtered CIGS solar cell, as well as the corresponding integrated short-circuit current density (J_{SC}). (Right) MPP of associated ST-PSCs. Adapted from Wiley-VCH GmbH ©2022 with permission.[35]

In order to fabricate 4T perovskite/CIGS tandem solar cells, subcells are mechanically stacked. As the active area of our ST-PSC is smaller than the CIGS (active area 50 mm^2), the bottom cell performance was directly measured when filtered by an equivalent perovskite optical filter (active area 225 mm^2). The 4T perovskite/CIGS tandem is calculated by adding the PCE measured under MPP of the ST-PSC to the filtered CIGS PCE. The standalone and filtered *J-V* curves, along with corresponding external quantum efficiencies (EQEs) are shown in **Figure 4-10.**

The 4T perovskite/CIGS tandem solar cell with IO:H exhibits a calculated PCE of 27.3%, with 18.5% stemming from the top ST-PSC (obtained from MPP after 5 min under continuous AM1.5G illumination) and 8.8% derived from the filtered bottom CIGS device (20.95% unfiltered). Full PV characteristics of both subcells, along with those of the equivalent ITO based ST-PSC with optimized MgF_2 are presented in **Table 2**. The filtered CIGS bottom cell exhibits a J_{SC} of 16.8 mA.cm^{-2}, a V_{OC} of 0.66 V, and a FF of 0.786 This represents an absolute drop of 30 mV in the bottom cell's V_{OC} compared to the unfiltered variants, which is comparable to established literature.[26,284,286–292,321] The high PCE of the bottom CIGS solar cell is a result of high transmission achieved through the top ST-PSC due to our previous optimizations. EQE results indicate high photon-to-current conversion, with an integrated J_{SC} within 6% of the *J*-*V* measurement. An overall PCE of 25.8% is achieved using the ITO stack, slightly better than the values obtained in a previous study using an equivalent perovskite but without optical optimizations such as the use of MgF_2.

Table 4-2 Photovoltaic parameters of champion solution-processed ST-PSC, with both ITO and IO:H as a TCO, and standalone/filtered CIGS solar cell. Stabilized PCEs of the top perovskite and filtered bottom solar cells and the corresponding calculated four-terminal tandem PCE are given in bold. Average values for *J*-*V* parameters are presented in brackets. Due to the differing spectrum of the solar simulator used to measure CIGS devices, coupled with a lack of defined area, EQE values were used to calculate the performance of filtered CIGS devices. As perovskite devices were measured with a well defined area, stabilized PCE via MPP tracking is used to calculate their contribution to the 4T tandem

Solar cell	FF [%]	V_{OC} [V]	J_{SC} [mA.cm^{-2}]		PCE [%]	Stabilized PCE [%]
			Solar simulator	EQE		
Perovskite (ITO)	80 (79) 79 (75)	1.16 (1.15) 1.16 (1.15)	19.8 (19.2) 19.5 (19.1)	18.8	18.4 (17.4) 17.7 (16.4)	**17.5**
Perovskite (IO:H)	79 (70) 76 (66)	1.17 (1.15) 1.17 (1.15)	20.7 (21.5) 20.9 (21.4)	19.6	19.3 (17.1) 18.5 (16.2)	**18.5**
CIGS	78.2	0.69	42.3	38.8	20.95	
CIGS (ITO filter)	78.5	0.66	15.5	14.7	**7.7**	
CIGS (IO:H filter)	78.6	0.66	17.7	16.8	**8.8**	
Pero./CIGS (ITO)						**25.2**
Pero./CIGS (IO:H)						**27.3**

4.4.2 Co-evaporated WBG PSCs and champion 4T tandems

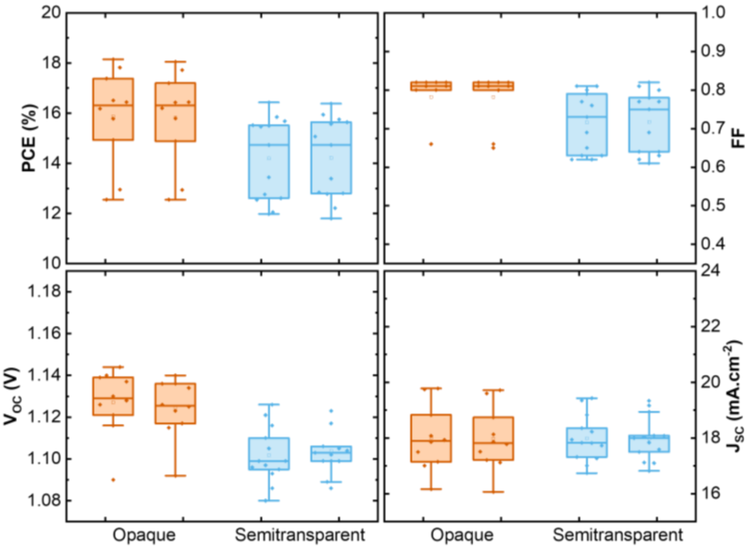

Figure 4-11 Photovoltaic parameter statistics derived from forward and reverse *J-V* scans for co-evaporated opaque and ST-PSCs fabricated with ITO as the front electrode. Part of figure adapted from ref.[277]

While the previously presented results represent our highest achieved 4T perovskite/CIGS PCE, we also repeated these optimizations with a co-evaporated perovskite to demonstrate the robustness of the optical optimizations presented in this chapter. Dr. Tobias Abzieher produced co-evaporated perovskites until the C_{60} layer. Active areas and layer stacks are equivalent to the previous section, however the co-evaporated perovskite excluded the LiF layer and utilized Spiro-TTB instead of 2PACz in order to maintain full vapour-phasec processing. The process of creating a vapour-phase 2PACz layer, and potential interactions between 2PACz and co-evaporated perovskites, are covered in **Chapter 5** and **Chapter 6**. MPPs of champion opaque and ST-PSCs, along with corresponding statistics are presented in **Figure 4-11 and 4-12**. Co-evaporated 1.66 eV bandgap devices on ITO demonstrated a champion PCE of 17.2%, J_{SC} of 21.7 mA.cm^{-2}, V_{OC} of 1.11 V, and FF of 0.82 in the backward scan. IO:H was not used, as device performance decreased drastically, see **Figure S2-4**, which is attributed to surface dependent growth observed for co-evaporated PSCs.[72] A re-optimization of the IO:H substrate for co-evaporated perovskites was beyond the scope of this work.

Co-evaporated ST-PSC subcells were incorporated into a series of 4T perovskite/CIGS tandem in a similar manner to **Section 4.4.1**, with the standalone and the filtered JV curves and EQEs shown in **Figure 4-12**. 4T perovskite/CIGS tandem solar cells with co-evaporated perovskites achieved a PCE of 23.8%. Full PV characteristics of all conditions, along are presented in **Table 4-3**. These results highlight the necessity of optical optimization in achieving high performance 4T tandem devices.

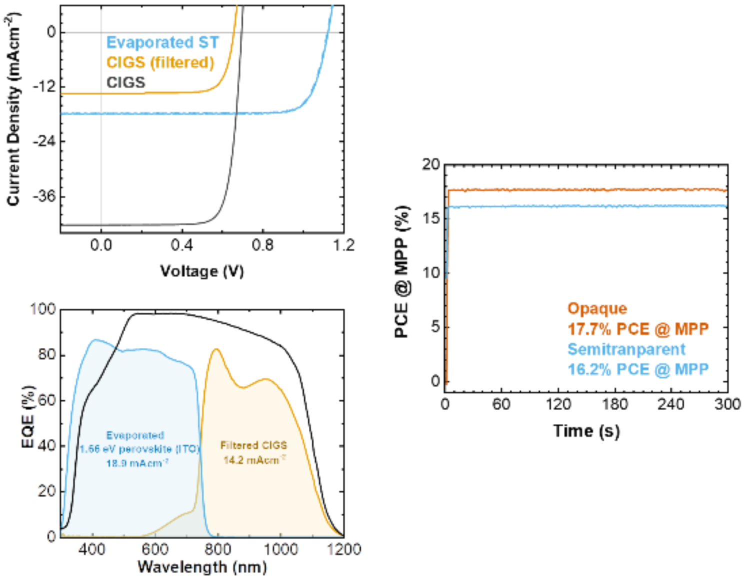

Figure 4-12 Measurements of 4T perovskite/CIGS tandems with a co-evaporated absorber. (Top) Current density–voltage characteristics of co-evaporated ST-PSC (ITO substrates), with standalone and filtered CIGS solar cells. (bottom) External quantum efficiency of ST-PSC, standalone/filtered CIGS solar cell, as well as the corresponding integrated short-circuit current density (J_{SC}). (Right) MPP of associated ST-PSCs. Part of figure adapted from ref.[277]

The co-evaporated perovskite with an ITO substrate achieved lost ~0.9%$_{abs}$ PCE compared to the equivalent solution processed, with a slightly larger ~1.4%$_{abs}$ drop in tandem PCE due to a simultaneous ~0.5%$_{abs}$ drop in CIGS PCE. Notably, the current in the CIGS subcell only experiences a drop of 0.5 mA.cm^{-2}. The remaining drop is in FF, which could be due to a relative red-shift in the CIGS spectra decreasing FF.[322,323] The presented optical optimization method can be considered reasonably resilient to perovskite fabrication method, highlighting the importance of NIR transmission in developing high performance 4T tandems.

Table 4-3 Photovoltaic parameters of champion co-evaporated ST-PSC, and standalone/filtered CIGS solar cell. Stabilized PCEs of the top perovskite and filtered bottom solar cells and the corresponding calculated four-terminal tandem PCE are given in bold. Average values for *J-V* parameters are presented in brackets. Due to the differing spectrum of the solar simulator used to measure CIGS devices, coupled with a lack of defined area, EQE values were used to calculate the performance of filtered CIGS devices. As perovskite devices were measured with a well-defined area, stabilized PCE *via* MPP tracking is used to calculate their contribution to the 4T tandem.

Solar cell	FF [%]	V_{OC} [V]	J_{SC} [mA/cm^2]		PCE [%]	Stabilized PCE [%]
			Solar simulator	EQE		
Perovskite (ITO)	82 (73) 81 (73)	1.11 (1.10) 1.11 (1.10)	21.7 (18.9) 21.7 (18.9)	19.0	17.2 (15.1) 17.1 (15.1)	**16.6**
CIGS	78.2	0.69	42.3	38.8	20.95	
CIGS (ITO)	77.2	0.66	13.4	14.2	7.2	
Perovskite/CIGS (ITO)						**23.8**

4.5 Simulations to determine the maximum potential of 4T perovskite/CIGS tandem solar cells

In this section we explore optical simulations as a method to evaluate the impact further improvements in optical properties has on PCE of 4T perovskite/CIGS tandem solar cells.

4.5.1 Recreation of best performing tandem devices

Our optical optimizations have highlighted how important optics management is to achieve high performance tandems devices. To elucidate the extent of this effect Fabrizio Gota performed optical simulations focusing on fine optimization of the relevant layers, without significantly altering the materials. Modelling was performed using EYcalc software based on measured refractive indices and EQEs.[324] The first step in optical modelling was to reproduce the experimental EQE data of our champion 4T perovskite/CIGS tandem (see **Figure 4-13**). There exists a slight discrepancy between simulated and experimental EQE data, which is attributed to minor variations of the actual thicknesses, refractive indices and extinction coefficients of the layers. However, the final PCEs of 4T tandem devices (simulated and experimental) are the same.

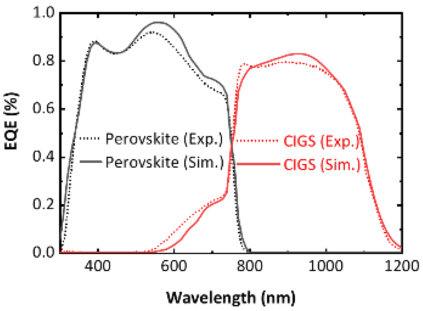

Figure 4-13 Measured and simulated external quantum efficiency of each subcell of the perovskite/CIGS tandem solar cell derived from optical simulations. Reproduced from Wiley-VCH GmbH ©2022 with permission.[35]

4.5.2 Simulated optical enhancements to achieve 29.5% 4T tandems

To determine the potential scope of optical optimizations, Fabrizio Gota performed simulations focusing on fine optimization of all relevant layers, without significantly altering the physical properties of the materials (i.e. the conductivity of transport layers). The considered improvement methods are outlined **Figure 4-14**. As optical properties were the primary motivator for these variations, calculations focused on the changes in expected J_{SC} of each subcell before calculating resultant 4T PCE.

The optimization series can be broken down into three subsections: thicknesses optimization of active layers, introduction of an encapsulation layer, and deployment of micro-textures to improve light in-coupling.[64] Combined, these optimizations are shown to lead to an increase in

PCE by a 2.7%$_{abs}$, enabling expected 4T perovskite/CIGS tandem solar cell of 29.5%. Significant gains are only obtained when any of the following are applied: (i) introduction of an encapsulation layer between the perovskite and CIGS subcells, (ii) employment of a thicker perovskite absorber, and (iii) deposition of micro-textures on the front glass substrate. Thickness optimization of various layers other than the perovskite absorber lead to a minor improvement of ~0.45%$_{abs}$. An example optimization is outlined in **Figure 4-15**, which details the tuning of the IO:H layer thickness. This variation also demonstrates the complexity of the simulation process, where modifications of the IO:H layer leads to shifts in interference patterns, and hence changes in the maximum absorption of the EQE: This result highlights the importance of high levels of control in film thickness to maximise optical properties.

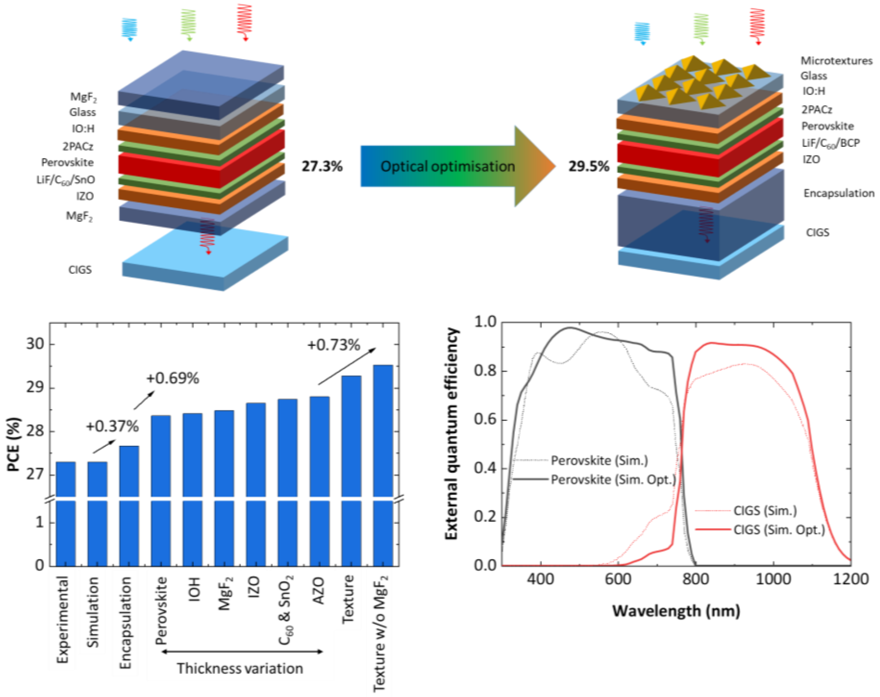

Figure 4-14 Simulated changes to optical layers. (*Top*) Simulated initial and final device stack. (*Bottom-left*) Simulated changes in PCE of resultant 4T tandem device with each modification. (*Bottom-right*) Initial and final simulated EQE spectrum corresponding to (top) stacks. Reproduced from Wiley-VCH GmbH ©2022 with permission.[35]

Considering the major influences on device performance, we first considered the inclusion of an encapsulant between the subcells. Although the use of an MgF_2 ARC substantially reduced reflection losses at the air/IZO interface for perovskite half stacks in **Section 4.2.2**, the air/MgF_2 interface continues to incur notable reflections. Inclusion of an encapsulation layer, in the form of an index matching liquid, with a near optimal refractive index of ~1.5 (optical data of ethylene-vinyl acetate was employed for simulations) would more effectively reduce interfacial reflections between the sub-cells. Simulations predict a net enhancement of 4T PCE by 0.37%$_{abs}$ with inclusion of this material.

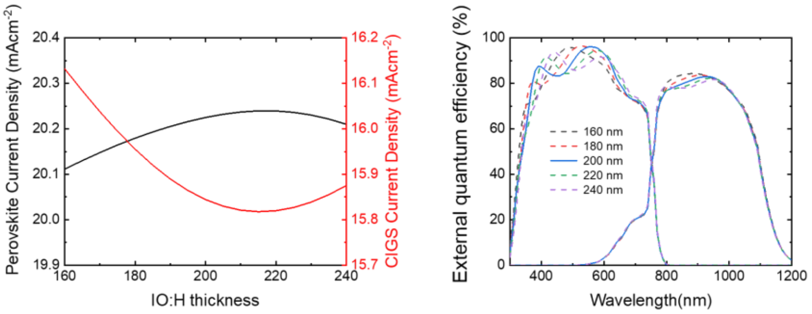

Figure 4-15 Representative simulation of IO:H thickness variation. (*Left*) Simulated variation in perovskite and CIGS current density and (*right*) select expected EQE for slight variations around the calculated maximum. While 200 nm showed best fit (see **Figure S10**), 230 nm was the expected average thickness in real world devices. Replicated from Wiley-VCH GmbH ©2022 with permission.[35]

The next aspect calculated to provide a significant enhancement, is the utilization of a thicker perovskite absorber, with ~800 nm estimated to improve PCE by 0.69%$_{abs}$. Transmission of near bandgap photons is typically expected for ST-PSCs compared to their opaque counterparts due to the lack of reflection from the rear metallic electrode, resulting in their net absorption being limited to single path absorption. This is responsible for the decreased near bandgap EQE signal of simulated and experimental devices, shown in **Figure 4-12**, when compared to optimal simulated devices. Increasing the absorber thickness ensures that low energy photons can be absorbed and extracted even without a rear metallic electrode. These results are corroborated in literature, which have demonstrated the feasibility of similarly high thicknesses in perovskite absorbers without a significant drop in charge carrier mobility.[190,321,325,326]

The final notable enhancement is achieved by replacing the front MgF_2 ARC with micro-textures to further enhance light incoupling, which will lead to a PCE improvement of 0.73%$_{abs}$. Micro-textures allow multiple reflections at the texture surface, which can increase optical path length through the absorber by inducing reflections with substantial angles, and reduce light outcoupling.[29,291,327–336] Furthermore, textures minimize the angular reflectance spectra for light incident between -60° and 60°, reducing the angular dependency in a tandem device compared to devices without a texture, and increasing light incoupling to a greater extent than an ARC.[329,337]

4.5.3 Simulated bandgap optimization

In theory, the perovskites utilized in this work in not optimum for use in 4T perovskite/CIGS tandems, due to a relatively low bandgap. Previous literature has stated that an optimal bandgap for this architecture would be 1.73 eV. Therefore, Fabrizio Gota performed additional simulations to determine if shifting the perovskite bandgap to the expected optimum will grant a notable boost in performance. These results show that an optimal bandgap with no change in electrical properties would lead to a 0.3%$_{abs}$ increase in maximum achievable PCE for a fully optimized device using of a 1.73 eV bandgap, as shown in **Figure 4-16**. However, increasing perovskite bandgap is unlikely to be as simple as his simulations assume. V_{OC} deficit increases with respect to bandgap, and secondary concerns such as halide migration arise when increasing the bandgap above certain thresholds.[124,318–320,338] For that reason, these supplemental simulations were not considered for our broader optimization series.

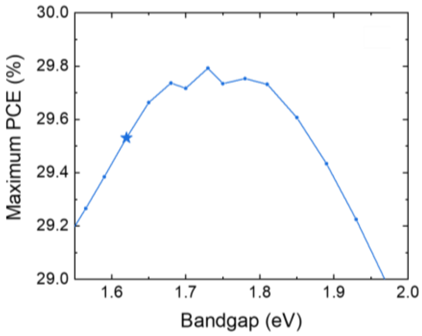

Figure 4-16. Simulation results indicating the maximum achievable PCE of a perovskite/CIGS 4T tandem with respect to variation in perovskite bandgap. At an optimal bandgap of 1.73 eV, the maximum achievable PCE is 29.8%, compared to 29.5% for the 1.62 eV bandgap perovskite utilized in this paper, which is marked with a star. Reproduced from Wiley-VCH GmbH ©2022 with permission.[35]

4.6 Summary

In this chapter, we evaluated the impact of optical optimization focussed on improving the NIR transmission of the ST-PSC top subcell on overall device performance of 4T perovskite/CIGS tandems. We revealed that how crucial maximizing weighted NIR transmission is for obtaining high performance 4T tandem devices, achieving 28.3% PCE perovskite/CIGS tandems, a world record at time of initial publication, and outlined the method to achieve and surpass these values. This has been in response to **Challenge 1**, identifying how systematic optimization of optical properties can improve bottom subcell current and performance for a set perovskite absorber.

In **Section 4.2**, we first developed a new ALD-SnO_x recipe to protect co-evaporated or solution-processed absorber layers during TCO sputtering with an exceptionally low extinction coefficient. The optimized buffer layer facilitated a systematic optical optimization in **Section 4.3**. Layer performance was evaluated and quantified using a combination of layer electrical properties (characterized via shunt resistance of TCOs) and optical properties determined *via* UV-vis spectroscopy and ellipsometry results. IO:H as a front TCO better matches the ideal broad spectrum n values for the perovskite/glass optical interface compared to the typical commercial ITO, while IZO exhibits drastically reduced parasitic absorption compared to our in-house ITO. TCO thickness was optimized to maximize optical transmittance without a drop in sheet resistance. Independent optimization of ARCs on both sides of these devices further improved these optical interfaces. Overall, when incorporated into solution-processed perovskite top subcells, we increased weighted NIR transmission of our top subcell from 62.0% to 88.8%. To the best of our knowledge, this was the first work to perform such a systematic optimization, or achieve this level of weighted NIR transmission.

Applying our optimized top subcells to solution-processed ST-PSCs, then further application to 4T perovskite/CIGS tandem solar cells *via* an equivalent optical filter in **Section 4.4** achieved a maximum PCE of 27.3% for IO:H as a front TCO and 25.2% for ITO as a front TCO to reinforce the potential of optical optimization. Similar optimizations of co-evaporated perovskites achieve 23.8%, with the lower co-evaporated device performance determined as due to the continued use of ITO as a front TCO, with a 1.2%$_{abs}$ drop in the CIGS subcell PCE due to inferior NIR-transmission. Co-evaporated devices were kept as entirely vapour-based, meaning Spiro-TTB was utilized as a HTL instead of the typical 2PACz, and lacked passivation, exhibiting in a 0.9%$_{abs}$ drop in ST-PSC PCE. Hence we also responded to **Challenge 2**, meaningfully comparing between vapour-based and solution-based perovskites based perovskites. Development of evaporated nPACz SAM-HTLs will be covered in **Chapter 5** and the complexity of interactions between nPACz SAM-HTLs and co-evaporated perovskites, preventing their easy combination, will be covered in **Chapter 6**.

To expand upon our results, and determine what PCE is possible exclusively via optical optimizations, in **Section 4.5** we simulated further optical enhancements with our ideal solution-processed devices. The most substantial improvements result from an index matching liquid between the perovskite and CIGS subcells, a thicker perovskite absorber to minimize near bandgap transmission, and microtextures on the glass substrate to further reduce light incoupling. Together with either minor thickness variations, these optimizations, result in a theoretical achievable 4T perovskite/CIGS tandem efficiency of 29.5%. A final set of simulations modifying the bandgap of the top PSC, indicate that, for a completely optically optimized stack, the difference in maximum achievable PCE between our 1.62 eV perovskite and a theoretically optimal 1.73 eV perovskite is only 0.3%$_{abs}$ PCE. These results highlight that optical improvements are a more important optimization than bandgap in perovskite/CIGS 4T tandem devices.

While not much research into 4T perovskite/CIGS tandems has occurred since this study, the approach of using optical optimization and modelling to maximise 4T tandem performance as provided in this chapter has become increasingly popular,[280,339,340] including the use of alternative materials such as organic top-subcells.[341] Coupling such optimizations with an improved top subcell has allowed the current champion perovskite/CIGS 4T tandem efficiency of 28.4%.[280]

5 Vapour-phase thermal evaporation of self-assembled monolayer hole transport layers

Abstract

In this chapter, we report on a vapour-phase deposition method for common carbazole-based self assembled monolayer-based hole transport layers (SAM-HTLs). We observe no chemical differences in evaporated SAMs compared to their solution-processed counterparts. Perovskite half-stacks and PSCs using evaporated SAM-HTLs demonstrate the expected near lossless interfacial properties are preserved or slightly improved. This is determined via photoluminescence measurements, an enhancement in open-circuit voltage and comparable performance of PSCs utilising evaporated nPACz compared to their solution-processed counterparts. Finally we demonstrate that vacuum deposition improves solution-processed perovskite wetting and fabrication yield on previously non-ideal materials, improving the versatility of these materials without sacrificing their beneficial properties.

The work in this chapter resulted in the publications: **'Evaporated Self-Assembled Monolayer Hole Transport Layers: Lossless Interfaces in Perovskite Solar Cells'**, published in **Advanced Energy Materials** by Dr. Ahmed Farag and Thomas Feeney as shared first authors[261] and '**Understanding and exploiting interfacial interactions between phosphonic acid functional groups and co-evaporated perovskites**,' published in **Matter** by Thomas Feeney and Julian Petry as shared first authors.[221]

This work is the result of collaborative research between Karlsruhe Institute of Technology, Max Planck Institute for Solid State Research (MPI-FKF), InnovationLab GmBH and 4th Physics Institute and Research Center (SCoPE).

Thomas Feeney as a first author of this study developed the original concept with Dr. Ahmed Farag and designed all experiments for the initial optimization of the nPACz layer. Dr. Ihteaz M. Hossain performed the first evaporation of 2PACz with assistance from Thomas Feeney. Thomas Feeney developed the deposition process of the evaporated SAMs used in this work, fabricated all co-evaporated perovskites, performed and analysed co-evaporated XRD and PLQY measurements. He also fabricated almost all evaporated nPACz layers presented in this work. Dr. Ahmed Farag fabricated the spin-coated PSCs with assistance from Thomas Feeney, and deposited the relevant spin-coated nPACz layers. Alexander Diercks performed SEM measurements. Dr. Fabian Schackmar performed contact angle measurements. Roja Singh performed the EIS measurements. Dr. Rainer Bäuerle and Dr. Mario Hentschel performed and analysed the RAIRS measurements. Kathrin Küster and Prof. Dr. Ulrich Starke performed and *analysed the XPS measurements. Dr. Yang Li and Benjamin Hacene performed the TrPL measurements. Dr. Paul Fassl performed and analysed the PLQY measurements for solution-process perovskites. The project was under the supervision of Prof. Dr. Ulrich Wilhem Paetzold. Dr. Paul Fassl helped supervise the co-evaporated perovskite section.*

5.1 Motivation

Enhancing the power conversion efficiencies (PCEs) of planar *p-i-n* perovskite solar cells (PSCs) is crucial due to several inherent advantages of the architecture. Specifically, these entail low current-voltage hysteresis, an inherently high operational stability, and ready incorporate into tandem devices. [45,342–346] They are compatible with established thin film technologies to form 2T tandem photovoltaic (PV) devices,[70,284,338,347,348] and have access to higher quality buffer layers, allowing easy incorporation into 4T tandem photovoltaic devices such as in **Chapter 4**. These characteristics make planar *p-i-n* PSCs a promising candidate for eventual commercialization.[45,194,349,350] The most relevant issue for *p-i-n* PSCs is the high potential for surface recombination at the HTL/perovskite interface, which is highly detrimental in terms V_{OC} losses for the completed PSC, making choice of a proper HTL essential. Various HTLs have been employed in the past for the *p-i-n* architecture. However, common options require post-deposition treatment or doping to improve their poor interfacial properties,[123,167,342,351,351–361] exhibit interfacial degradation,[351,362–365] have inferior wettability for common solution-processed perovskite coatings,[366] and utilise polar solvents that are less suitable for tandem devices, especially those with multiple perovskite layers.[37,367]

A promising alternative was investigated early in PSC history, self-assembled monolayer based hole transport layers (SAM-HTLs).[368–372] SAMs are materials that autonomously form a self-limiting functional layer by developing covalent bonds to the substrate whose component parts can be readily tailored to increase application flexibility.[373,374] These components include a binding group which interacts with the substrate, a functional group which can be modified to control interfacial properties, and a connection linking or chain group. The latest major breakthrough in the HTL interface occurred when Albrecht *et al.* developed a series of SAM-HTLs that form an essentially lossless HTL/perovskite interface.[70] They developed three promising SAMs, termed nPAC SAM-HTLs, derived from carbazole bodies with phosphonic acid binding groups.[375,376] They comprise: [2-(9H-Carbazol-9-yl)ethyl]phosphonic acid (2PACz), [2-(3,6-Dimethoxy-9H-carbazol-9-yl)ethyl]phosphonic acid (MeO-2PACz) and [4-(3,6-Dimethyl-9*H*-carbazol-9-yl)butyl]phosphonic acid (Me-4PACz). These materials achieved the highest perovskite/Si tandem PCE of 29.2% at the time.[293,377] A schematic demonstration of each molecule is shown in **Figure 5-1**.

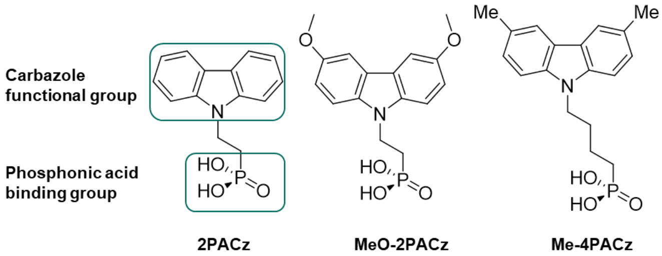

Figure 5-1 Chemical models of the nPACz materials investigated in this chapter with the indicators of the primary functional group and phosphonic acid binding group.

Due to a careful selection of functional groups, nPACz SAM-HTLs exhibit exceptionally high hole selectivity, fast charge carrier extraction, and very low non-radiative recombination at the HTL/perovskite interface.[70] Carbazole bodies form strong hole selective materials,[378] while the phosphonic acid functional group exhibits self-limiting and self-assembling growth to form very thin stable layers on transparent conductive oxides (TCOs), which are ubiquitous to PSCs.[377,379] MeO-2PACz SAM-HTLs have achieved special interest in the field of co-evaporated perovskites, where they stabilize the photoactive black α-phase in $FAPbI_3$ based perovskites absorber materials.[54] A further investigation into the mechanism of this interaction, which also applies to other nPACz materials, along with ancillary effects of this interaction, is provided in **Chapter 6**.

nPACz SAM-HTLs have dominated recent record PCEs for single-junction and monolithic tandem devices,[43,293,338,347,380,381] while more novel high performance HTLs are commonly based on modification of the nPACz base molecule or other phosphonic acid functional groups.[382–384] Commercialisation of perovskites requires upscalable deposition methods for all layers. Upscalable deposition methods SAM-HTLs have included ultrasonic spray pyrolysis, blade coating and dip coating.[54,185,381,382,385] However, commercial PV production lines predominantly utilize vacuum-based deposition methods, and industry research favours vapour-phase deposition techniques.[51] Hence, development of a vapour-phase scalable deposition method, such as vacuum-based thermal evaporation, is crucial to improve process flexibility, and enable ready incorporation into commercial production lines for large-scale perovskite production. Finally, evaporation grants a unique benefit in that it facilitates conformal and uniform coatings, even over textured surfaces, and evaporated organic HTLs consistently demonstrate conformal coating of large textures.[31,261,386] This is important for monolithic Si/perovskite tandem production, where monetary constraints ensure textured Si substrates are highly preferred and thus uniform coating is expected to boost flexibility and reproducibility.

In response to **Challenge 3**, this chapter reports on the development of a method to deposit widely known nPACz SAM-HTLs (2PACz, MeO-2PACz, and Me-4PACz) *via* thermal evaporation based physical vapour deposition (hereafter referred to as evaporation), and demonstrate they can readily be incorporated into highly-efficient planar *p-i-n* PSCs.

In **Section 5.2**, we consider that evaporation requires high temperatures with the potential to degrade or decompose the organic molecules. Hence, we perform an analysis into the chemical changes of the molecules upon evaporation. This analysis also includes investigating the binding mode and approximations of surface coverage.

We continue in **Section 5.3** by determining ideal processing parameters for this vapour-based deposition method. This begins with considering the effect of deposition speed, material re-use and delay times pre and post SAM deposition. With these basic considerations confirmed, we identify ideal film thickness and evaluate the nescessity for post-deposition washing to remove unbound molecules.

In **Section 5.4** we compare and contrast the interfacial properties of each evaporated nPACz SAM-HTL with the solution processed counterpart for both evaporated and solution processed perovskites, which reveals an overall trend of an improved HTL/perovskite interface for evaporated nPACz SAM-HTLs for spin-coated perovskites, and a comparable HTL/perovskite interface for co-evaporated perovskites. Our interfacial analysis is expanded to include how surface free energy is impacted by evaporation in **Section 5.5**.

Finally, **Section 5.6** considers the impact of deposition method on perovskite crystal structure for evaporated and spin-coated nPACz SAM-HTLs for both spin coated and co-evaporated perovskites, which will partially address **Challenge 5**.

5.2 Chemical environment and surface chemistry of evaporated nPACz SAM-HTLs

In this section, we consider the chemical environment and surface chemistry of evaporated nPACz SAM-HTLs as compared to their spin-coated counterparts. As thermal evaporation exposes the material to relatively high temperatures, the potential exists for a change in chemical properties (i.e through material degradation), or a lack of binding to the substrate. XPS and RAIRS were utilised to analyse these possibilities.

5.2.1 X-ray photoelectron spectroscopy analysis of nPACz layers

In order to determine if the chemical environment and surface chemistry was changed by our deposition method, Kathrin Küster and Ulrich Starke from MPI-FKF performed and analysed x-ray photoelectron spectra (XPS) of nPACz SAM-HTLs deposited onto glass/ITO substrates *via* evaporation. These measurements were compared with similar measurements of raw powder XPS, spin-coated nPACz layers, and the original reported data of spin-coated 2PACz layers from their introductory paper.[70,387] The comparison to the introductory paper is important for 2PACz because of the unexpected signal shape shown in the spin-coated 2PACz layer, shown in **Figure 5-2**, which exhibited relative intensities that deviate from both the powder and literature references.

5.2.1.1 XPS analysis of nPACz molecules

Focussing on this literature reference, there exists no significant differences in characteristic XPS peak positions and relative areas for the evaporated 2PACz film compared to the solution–processed layer, though both exhibit a slight shift to lower binding energies compared to the powder form. The surface sensitive XPS spectrum of the evaporated 2PACz film exhibits the expected prominent peak relating to C 1s, P 2p and N 1s (shown in the Appendix **Figure S5-1**) core levels in the corresponding binding energy regions. No evidence of unexpected contributions to the signal are observed, which would indicate degradation induced chemical changes in the 2PACz molecule upon evaporation compared to previously reported spin-coated samples.[70]

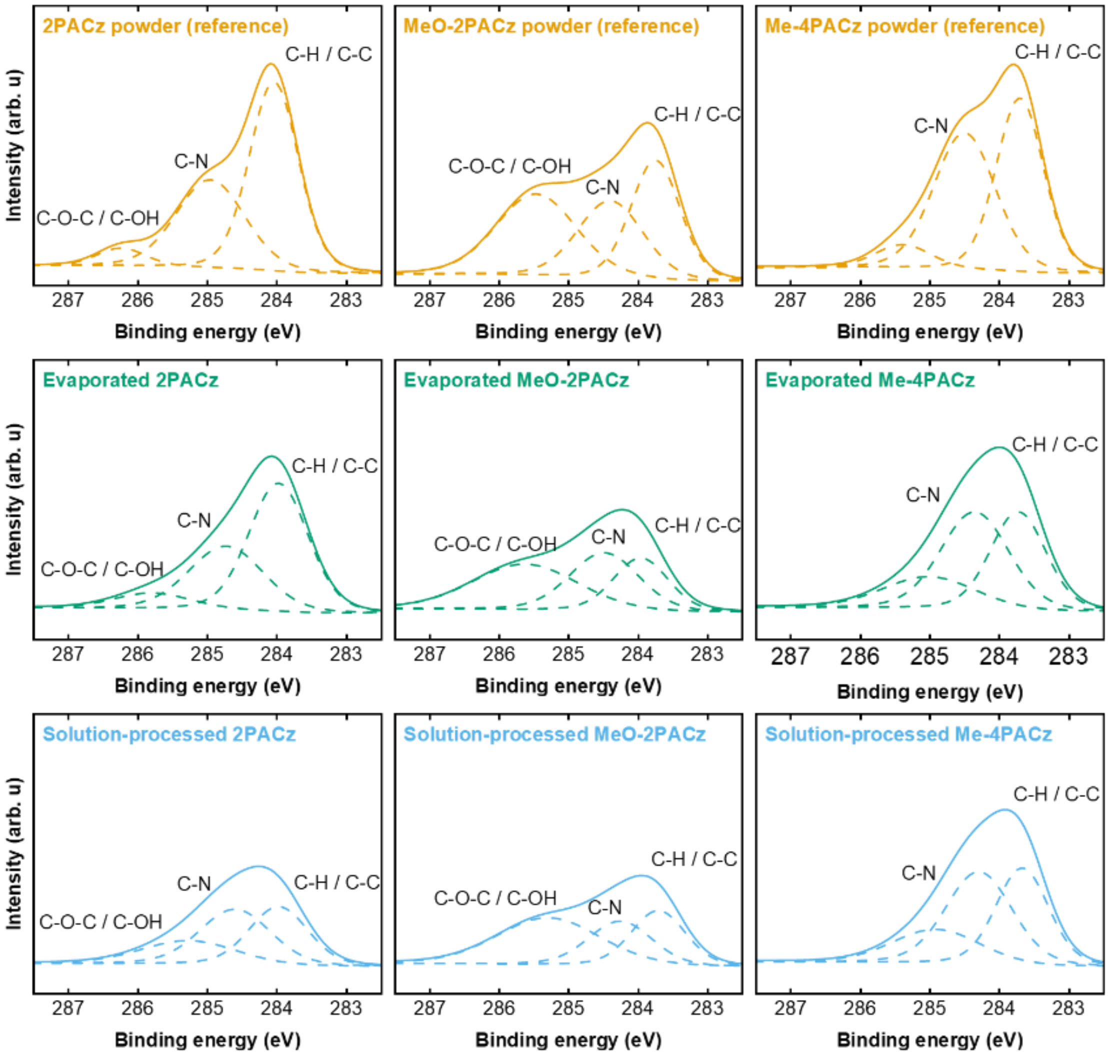

Figure 5-2 XPS fits for the C1s region of each nPACz material. Shown is a powder reference (orange), a ~6 nm evaporated nPAC thin film deposited onto glass/ITO substrate (dark green) and a nPACz thin film deposited onto a glass/ITO substrate via spin-coating (blue). The solid line represents a fit to the real data points and the dashed lines show the components. Measurements were performed by our collaborators (MPI-FKF). Part of figure adapted from Wiley-VCH GmbH ©2023 with permission.[261]

The C 1s spectra is the most relevant for comparison of chemical environment, which we associate with 3 characteristic components. These can be attributed to C-C and C-H bonds with a binding energy of ~284.0 eV and a relative weight/area of 56.4%, a C-N bond with binding energy ~284.7 eV and a relative weight/area of 35.0%, and a third peak at ~285.8 eV with a relative weight/area of 8.6%. This peak was originally attributed to carbazole C atoms bonded to three other atoms by Al-Ashouri *et al*.[70] A second explanation was later posited by Levine *et al*., who attributed this peak to C-P bonds.[387] Our collaborators postulate a third possibility. The binding energy separation between this third peak and the main C-C/C-H peak is similar to the energy separation between the C-C/C-H peak and the C-O-C peak for MeO-2PACz.[70] Therefore, it can theoretically be attributed to a C-atom binding to an electronegative element in the form of C-O-C or C-OH.[388] Direct comparisons to literature are difficult, because relative area /weights are not given for all peaks, and the presence of additional peaks in the ~286.9 eV for 2PACz and ~286.5 eV and 287.3 eV for MeO-2PACz, the high energy peaks of which they attribute to C-P. These additional peaks are not evident in powder references for 2PACz and MeO-2PACz and hence are assumed to be leftovers from the synthesis technique. Nonetheless, these results indicate similar relative intensities of peaks between evaporated 2PACz, the literature 2PACz reference and the powder reference. The primary difference between films and the powder reference is the FWHM of the XPS peaks, shown in **Table S5-2**.

MeO-2PACz and Me-4PACz exhibit similar classes of XPS peaks, referring to similar approximate chemical environments, as expected for nPACz materials. An exception occurs for the C-O-C /C-OH peak for MeO-2PACz, which was expected due to the presence of methoxy-functional-groups. These materials also exhibit similar peak locations and relative areas for solution processed compared to evaporated nPACz layers, further reinforcing the concept that thermal evaporation does not result in material degradation. A full table of peak areas, weights and full width half maximum for measured and literature referenced C 1s spectra are present in **Tables 5-1, S5-1 and S5-2**. Similar tables are present in the SI for the O 1s, N 1s, and P 2p regions, along with the the N 1s and O 1s spectra.

Table 5-1 Relative peak area/weights of X-ray photoelectron spectra fits for the C 1s region of each nPACz material. Shown is the powder reference (Pow.), evaporated vapour-phase thin film (Evap.), spin-coated solution-processed layer (Sol.) and estimates determined from a literature reference (Lit.).

	2PACz				MeO-2PACz				Me-4PACz		
	Pow.	Evap.	Sol.	Lit.	Pow.	Evap.	Sol.	Lit.	Pow.	Evap.	Sol.
C-H / C-C	57.4%	56.4%	36.2%	57.0%	33.8%	25.1%	28.2%	~38%	46.0%	36.6%	36.3%
C-N	37.3%	35.0%	41.0%	30.0%	28.8%	34.3%	26.5%	~27%	46.9%	44.2%	43.3%
C-O-C / C-OH	5.3%	8.6%	22.9%	13.0%	37.3%	40.7%	45.3%	~21%	7.0%	19.2%	20.4%

The absence of apparent degradation peaks in the C 1s binding energy region is promising, however it also remains necessary to ensure the presence of the functional phosphonic anchoring functional group component in the evaporated thin film. Our collaborators achieve this by investigating the P 2p binding energy region, shown in **Figure 5-3**. The evaporated 2PACz thin film signal can be extracted into two peaks representing P $2p_{3/2}$ at ~133 eV with a relative area/weight of 66.7% and P $2p_{1/2}$ at ~134 eV with a relative area/weight of 33.3%, which literature correlates to P-O species.[389–392] Similar peaks with identical relative intensities are observed for all spin-coated and evaporated nPACz layers. Interesting is the comparison of the powder P 2p regions for each nPACz material with their thin film counterparts. Each powder spectrum displays an identical weighting, but shift in each peak location to higher binding energies. Such shifts are indicative of changing chemical environments,[393] providing potential evidence of the formation of a monolayer at the ITO interface. A minor shift in N 1s, O 1s and P 2p peak positions for MeO-2PACz (**Figure 5-3 and S5-1**) is indicative of either mild charging, or different coverage density.[393,394] Full data is available in the Appendix, **Table S5-3** to **Table S5-8.**

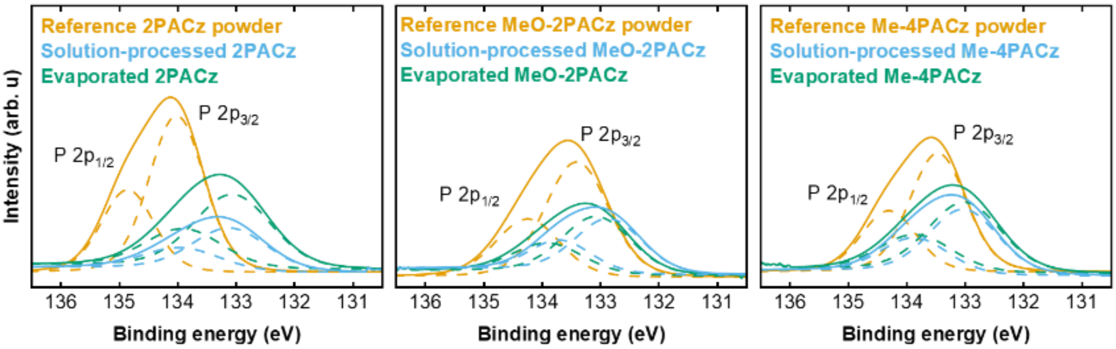

Figure 5-3 XPS fits for the P 2p region of each nPACz material. Shown is a powder reference (orange), a ~6 nm evaporated nPACz thin film deposited onto glass/ITO substrate (dark green) and an nPACz thin film deposited onto a glass/ITO substrate via spin-coating (blue). The solid lines represents fits to the real data points and dashed black lines show the requisite components. Measurements were performed by our collaborators (MPI-FKF). Part of figure adapted from Wiley-VCH GmbH ©2023 with permission.[261]

5.2.1.2 XPS analysis of underlying substrate

XPS of the Sn 3d and In 3d regions of the XPS spectra for evaporated and spin-coated nPACz layers provides some additional information, but the thin nature of these films makes precise information impossible to determine. The substantial difference in In and Sn signal intensity for 2PACz and MeO-2PACz may indicate a difference in surface coverage, as film thickness is expected to be comparable, which would also potentially contribute to why the spin-coated 2PACz results were different than expected. However, such theories are by nature speculative, definitive statements are not possible for the obtained results. The mean free path of ~400 eV electrons for organic compounds is in the ~2 nm range,[395,396] meaning that it is not expected to detect the Sn and In signal for films thinner than ~6 nm. Therefore these signals are expected for both evaporated nPACz samples (~6 nm thickness), and spin-coated layers (~3 nm thickness).[397] However, nPACz is not guaranteed to form a uniform monolayer.[398–400] Hence, it is not possible to determine if the drop in signal intensity is exclusively related to film thickness, or if it is related to surface coverage. The strong agreement in peak positions outlines in Appendix **Table S5-9**, indicates that no notable charging of the ITO surface is occurring.

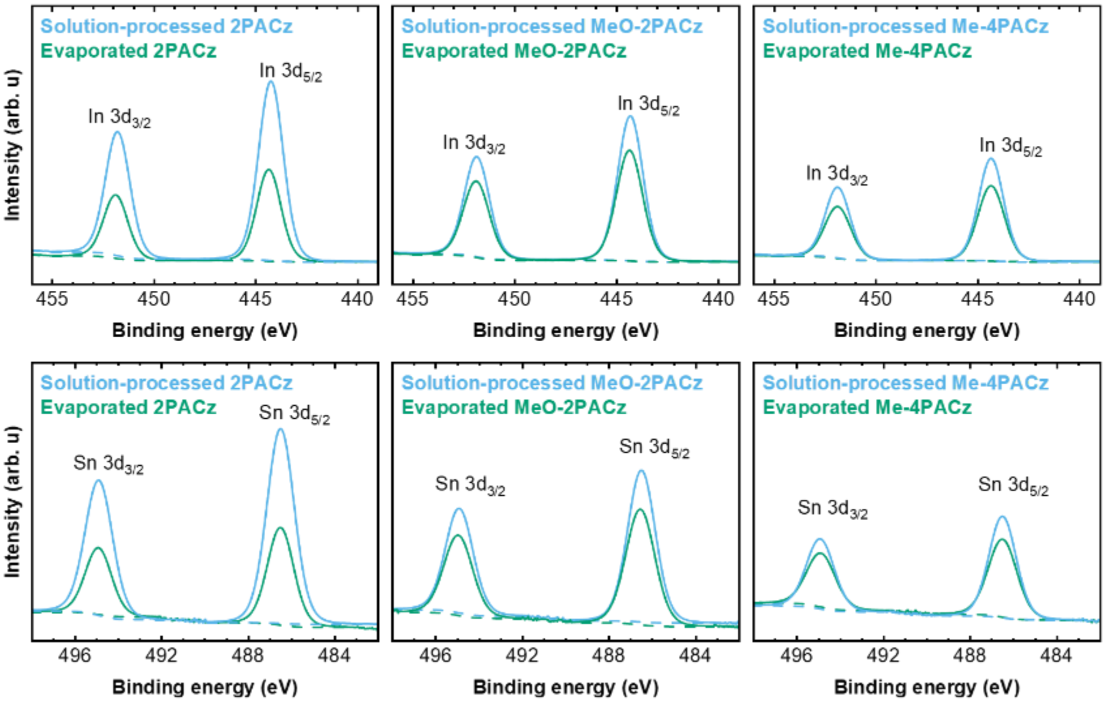

Figure 5-4 XPS fits for the In 3d (*top*) and Sn 3d (*bottom*) regions of each nPACz material. Shown is a ~6 nm evaporated nPACz thin film deposited onto glass/ITO substrate (dark green) and an nPACz thin film deposited onto a glass/ITO substrate via spin-coating (blue). The solid lines represents fits to the real data points and dashed black lines show the requisite components. Due to the simple nature of the spectra, each peak can be attributed to a single signal. Measurements were performed by our collaborators (MPI-FKF). Part of figure adapted from Wiley-VCH GmbH ©2023 with permission.[261]

5.2.2 Reflection-absorption infrared spectroscopy analysis

To confirm the presence of phosphonic acid binding overserved in **Section 5.2.1**, and further evaluate surface chemistry and chemical environment, Rainer Bäurle from InnovationLab GmbH and Mario Hentschel from SCoPE employed reflection-absorption infrared spectroscopy (RAIRS) on evaporated 2PACz thin films. They studied three films, a 6 nm film with a dominant monolayer response, then a 100 nm and a 200 nm film to show the evolution of bulk properties. All characteristic absorption bands of the evaporated 2PACz thin film molecular vibrational modes are shown in **Figure 5-5**. Each thin film exhibits comparable molecular vibrational bands comparable to previously reported spin-coated 2PACz monolayers.[70] The presence of carbazole ring stretching vibration bands in the 1454 – 1486 cm^{-1} region, and the two characteristic carbazole ring stretching at 1239 and 1346 cm^{-1} provide further evidence that the carbazole ring is intact and degradation does not occur.[70]

More importantly for demonstrating the practical applications of our evaporated nPACz thin films, they observe additional evidence of covalent bonding between the phosphonic acid functional group and the underlying ITO. This is indicated by the black peak at ~101 cm^{-1}, which has been previously assigned to the P-O species bound to the ITO, and is a strong indication that comparable bonding occurs as for spin-coated 2PACz.[70] The fingerprint of the P-O bond remains evident in thicker films, where not all the phosphonic acid anchoring groups are deprotonated, demonstrating bonding is similar independent of thickness. Bulk 2PACz films display an addition green peak at ~951 cm^{-1} representing bulk P-OH, which increases with thickness and is not present in the 6 nm film. Previously reported Fourier-transform infrared (FTIR) spectrum obtained from 2PACz powder pressed into a KBr tablet is in agreement with this observed peak position, as designated by the green dashed reference line.[70] The presence of this peak indicates that thick 2PACz films possess bulk material chemical properties.

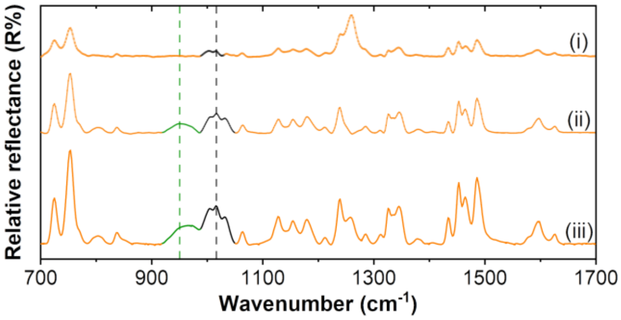

Figure 5-5 RAIRS of evaporated 2PACz thin films with different thickness onto glass/ITO substrates. The green dashed line represent the peak position of P-OH vibration band of the bulk 2PACz reported in ref. while the black dashed line represent the P-O monolayer signature in a spin-coated 2PACz layer. Measurements were performed by our collaborators (InnovationLab GmbH and SCoPE). Reproduced from Wiley-VCH GmbH ©2023 with permission.[261]

This RAIRS spectral analysis (**Figure 5-5**), coupled with previous XPS data (**Figure 5-2 to 5-4** and **Figure S5-1**), indicates that evaporated 2PACz thin films exhibit similar chemical environments and for equivalent interfacial bonds with ITO compared to spin-coated SAMs.

5.3 Determination of ideal processing parameters

In this section, we perform a systematic determination of ideal processing parameters, which is vital to determine before accurate comparisons to established (solution-based) techniques can be made. For all optimizations covered in this section, we employ the inverted *p-i-n* architecture: glass/indium tin oxide ITO/SAM HTL/perovskite/LiF/C_{60}/BCP/Ag or a half stack of ITO/SAM-HTL/perovskite to preclude prominent non-radiative recombination losses at the perovskite/C_{60} interface.[124,401] A spin-coated ~1.68 eV triple-cation perovskite absorber layer with a composition of $Cs_{0.05}MA_{0.22}FA_{0.73}Pb(I_{0.77}Br_{0.23})_3$, as outlined in **Chapter 3**, is widely used, including extensive use in monolithic perovskite/Si tandem solar cells.[293,380] Dr. Ahmed Farag fabricated all spin-coated perovskites and Thomas Feeney deposited all nPACz layers. Where possible, optimizations and comparisons are considered primarily for interfacial properties, as the photovoltaic properties are less important for the overarching focus of this chapter.

5.3.1 Determining ideal material deposition conditions

We consider a number of parameters as important for material deposition, namely: deposition speed, material reuse, processing time between spin-coating perovskite and 2PACz evaporation and time between ozone preconditioning and 2PACz evaporation.

5.3.1.1 Material re-use and deposition speed

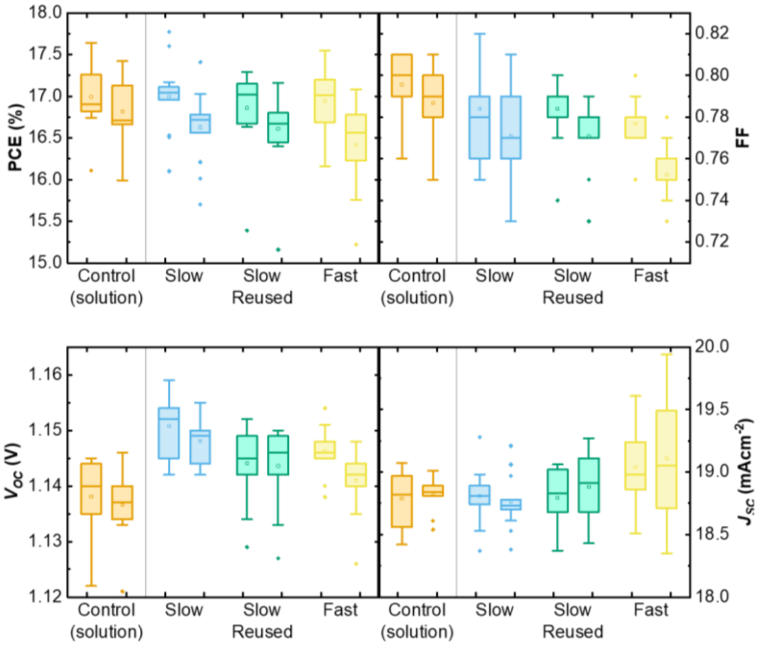

Figure 5-6 Photovoltaic parameter statistics derived from forward and reverse *J-V* scans for spin-coated PSCs with a 2PACz substrate with varying deposition rate. Shown are 2PACz films deposited via various deposition regimes for a 6 nm evaporated 2PACz layer compared to a spin-coated control. Slow refers to deposition rates of 0.1 – 0.3 Å.s^{-1}. Fast refers to deposition rates of 0.3 – 0.5 Å.s^{-1}. Reused indicates the crucible was not cleaned between depositions.

Deposition speed and material reuse were analysed by comparing 2PACz in a crucible with all residual material was removed before leading fresh material, with a layer where the residual material remained in the crucible. Some organic materials, such as C_{60}, can perform drastically differently on subsequent evaporations. Others, such as BCP, remains essentially unchanged given sufficient material remains in the crucible. Our second comparison was deposition speed. In theory, a faster deposition speed may lead to non-uniform coverage and increased result spread. However, fast deposition speeds are more preferable for industrial processes. For that reason, 2PACz deposited in the 0.1 – 0.3 Å.s^{-1} region (slow) was compared with 2PACz deposited in the 0.3 – 0.5 Å.s^{-1} region (fast). Three conditions: slow (new), slow (reused) and fast (new) were compared with a standard spin-coated 2PACz layer in **Figure 5-6**. While there exists some variation in photovoltaic parameters, potentially indicating a difference in surface coverage,[402] the process is overall reasonably resilient to deposition speed in the tested region. This is especially promising, as wide process windows are beneficial for scalable and reproducible production. Similarly, the material appears capable of reuse if required. However, to maximise consistency, all future depositions remain in the slow deposition region with crucibles cleaned before each deposition. This ensures any changes in PSC PCE can be attributed to changes in deposition parameters.

5.3.1.2 Pre- and post- deposition delay times

Our processing experience for optimal spin-coated 2PACz reveals two times that are important to minimize: (i) t_1, the time between UV-ozone preconditioning and 2PACz deposition should be minimized and (ii) t_2, the time between 2PACz deposition and perovskite spin-coating should be minimized. *Kim et al.* revealed two oxygen states for ITO thin films: either bound to the In and Sn or free O^{2-} ions with increased electron density at tetrahedral indices of the In^{3+} ion array.[403,404] This ratio is shifted to favour more In and Sn bound oxygen by UV-ozone treatment, coupled with a shift in O 1s and Sn $3d_{5/2}$ peaks to lower binding energy. Overall this treatment corresponds to an increase of the work function by ~0.2 eV, a decrease in organic contaminants (and hence an increase in interfacial –OH density),[404] and reduced surface carrier density.[404] This change in chemical properties is beneficial for the HTL/ITO interface.[313,405] However, airborne organic contaminants will passively remerge on the ITO surface,[406] decreasing -OH density. As SAMs preferentially bind to –OH,[407–410] and are highly dependent on surface chemical composition,[411,412] minimizing t_1 is crucial. The reasons for exploring t_2 is not explained by literature. However, over the course of this thesis, for solution-based 2PACz, a high t_2 is correlated to reduced device PCE.

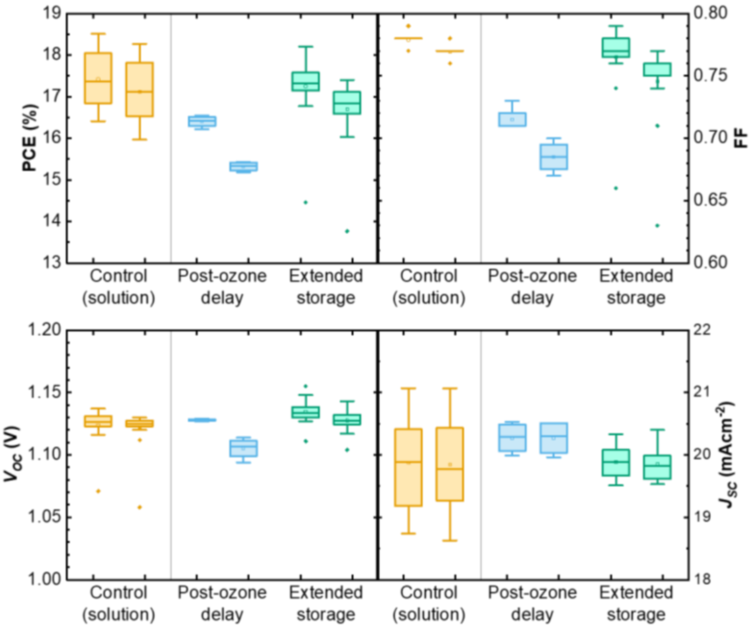

Figure 5-7 Photovoltaic parameter statistics derived from forward and reverse J-V scans for spin-coated PSCs with a 2PACz substrate with various delay times, deposited at various deposition regimes for a 6 nm evaporated 2PACz layer compared to a spin-coated control. Post-ozone delay samples had a t_1 of approximately 1 hour delayed between ozone pre-treatment and loading substrates. Extended storage samples were stored in a N_2 glovebox for 10 days (t_2) prior to perovskite deposition.

We therefore compare, in **Figure 5-7**, a control solution processed perovskite deposited on a solution processed 2PACz layer with two evaporated 2PACz layers: one with a t_2 of 10 day (stored in an N_2-glovebox) and a fresh 2PACz where t_1 was delayed by approximately 1 hour relative to normal 2PACz. Normal 2PACz evaporation, as shown in **Figure 5-5**, involves immediate sample loading (minimizing t_2), as our evaporation process inherently experiences an extended delay to account for system evacuation and source heating. Hence, a control evaporated 2PACz was not considered critical for this comparison.

As expected, samples with an extended delay between UV-ozone pre-treatment and evaporated 2PACz deposition display a substantial drop in resultant PCE. A small drop in V_{OC} and a sharp decrease in FF is indicative of decreased SAM-HTL coverage[413] or an inferior interface between the ITO and evaporated 2PACz due to a change in energetic alignment from ITO surface chemical composition.[414] As a positive aspect, evaporated 2PACz layers appear stable for a period of at least 10 days without a drop in PCE, continuing to achieve comparable PCEs to solution processed references, with a slightly lower average FF and slightly higher average V_{OC}. This is highly promising, especially as it reveals enhanced shelf-life of evaporated SAM-HTL substrates compared to observations of their solution processed counterparts. Therefore, all future optimizations ensured sample loading occurred immediately following UV-ozone surface pre-treatment, and did not consider substrate age to be important up to a period of 10 days.

5.3.2 Optimal nPACz layer thickness

With an established set of deposition parameters, a systematic study of thickness dependent interfacial properties is undertaken for each material. A comparison of the optimised evaporated layers with spin-coated nPACz SAM-HTLs will be covered in **Section 5.3.4**. 2PACz based molecules have an unbound length of approximately 1 - 1.3 nm,[414] hence 2 nm is chosen as a minimum thickness as complete coverage is expected beyond this point. Optimized, spin-coated MeO-2PACz layers have a measured thickness of 3.5 nm,[176,382,414] so the optimal evaporated SAM-HTL thickness was tested from a range of 2 nm to 8 nm. A 20 nm 2PACz layer was included as an intentional outlier for PLQY measurements to exacerbate thickness dependent trends. **Figure 5-8** outlines the results of these studies.

PLQY was measured of the aforementioned half-stacks at 1 sun illumination. To obtain the internal ideality factor (n_{id}), an intensity-dependent PLQY series was undertaken for the relevant half-stacks and a fit to the calculated implied V_{OC} (iV_{OC}) was performed, as has been extensively reported in literature.[124,131] The evaporated 2PACz/perovskite interface is of high quality, with non-radiative recombination effectively suppressed independent of the evaporated 2PACz film thickness as indicated by the PLQY, iV_{OC}, n_{id}, and TrPL data.

While the interface appears high quality for all thicknesses, there does exist a minor thickness dependence. Every nPACz material displays similar apparent thickness dependence in the following ways: increasing the thickness of the layer increases PLQY / iV_{OC}, PL signal, minor increases in charge carrier lifetime (from TrPL) and decreases n_{id}. Notably, the optimum in terms of TrPL and PL intensity is not necessarily the same thickness as the optimum in terms of

PLQY, iV_{OC} and n_{id}. This is generally unexpected, as higher thicknesses are expected to lead to reduced interfacial properties from an increased resistance of the HTL. Employing evaporated MeO-2PACz exhibits comparable results to its spin-coated counterpart, with minor improvements in PLQY, iV_{OC}, n_{id} and decay lifetime for evaporated MeO-2PACz compared to the solution processed counterparts. In a similar manner, evaporated Me-4PACz layers with an optimized thickness of ~6 nm slightly outperform their spin-coated counterparts.

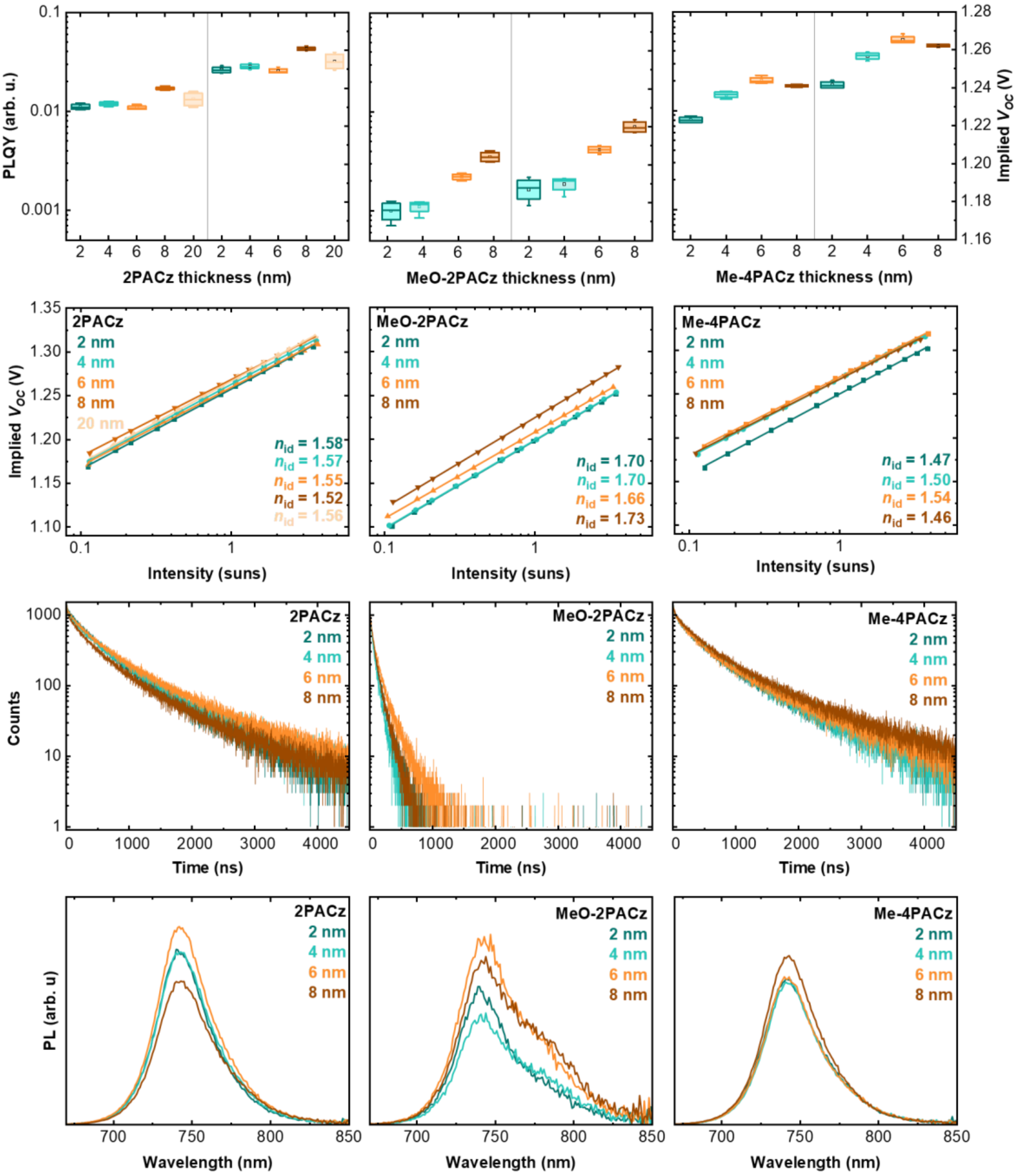

Figure 5-8 Thickness dependent interfacial properties of each evaporated nPACz layer. (*Top*) PLQY for the half-stack shown on left of each graph with the corresponding iV_{OC} shown on the right for various thickness samples. (*Top-middle*) n_{id} extracted from a fit to the intensity-dependent iV_{OC}. (*Bottom-middle*) TrPL for the corresponding half-stack. (*Bottom*) PL spectrum for the corresponding half-stack. All y-axis scales are consistent within each row. Reproduced from Wiley-VCH GmbH ©2023 with permission.[261]

5.3.2.1 Impact of post-deposition washing

The impact of a washing step was investigated to further analyse the effect of thickness and uniformity. Unbound molecules in SAM-HTLs are bound to the SAM portion by Van der Waals forces. Hence, they can be removed by washing the layer with anhydrous ethanol, ensuring a pure monolayer remains. This principle holds independent of deposition method. When the above characterisations are repeated with a 6 nm evaporated 2PACz layer, with half the samples washed once, they resulted in essentially unchanged interfacial properties, as shown in **Figure 5-9**.

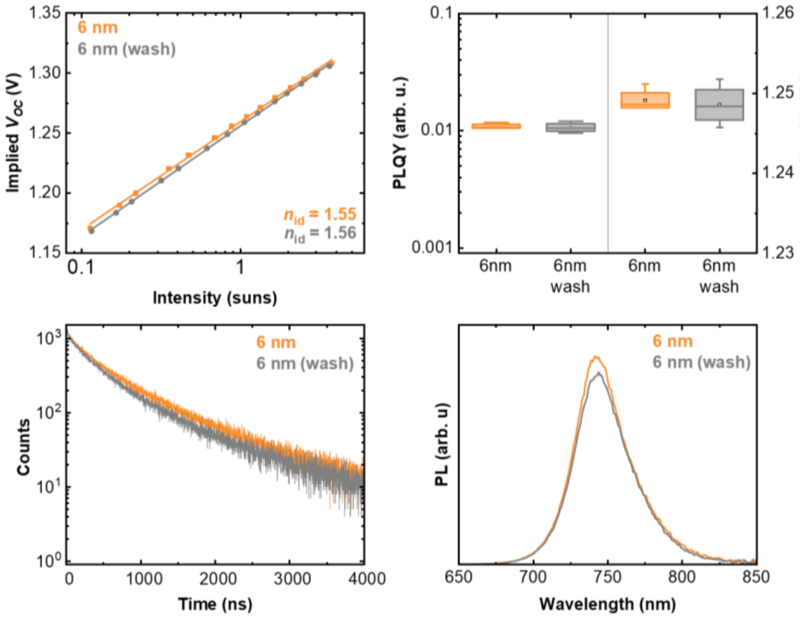

Figure 5-9 Interfacial properties of evaporated 2PACz layer with and without a washing step. (*Top-right*) Comparison of the PLQY for the half-stack ITO/evaporated 2PACz/(spin-coated perovskite) with the corresponding iV_{OC} for 6 nm samples with and without a washing step. (*Top-left*) nid extracted from a fit to the intensity-dependent iV_{OC}. (*Bottom-left*) TrPL for the corresponding half-stack. (*Bottom-right*) PL spectrum for the corresponding half-stack. Reproduced from Wiley-VCH GmbH ©2023 with permission.[261]

These results are crucial to understanding the broad optimum observed for each layer. We postulate that, for spin-coated perovskites, the perovskite deposition will remove the majority of unbound molecules, essentially acting as a *de facto* washing step. The vastly different interfacial properties for 2PACz layers with co-evaporated perovskites, which will be covered in **Chapter 6**, collaborate this theory. Evaporated perovskites do not disturb the unbound nPACz molecules, and hence layer thickness or washing steps become much more important for layer optimization. Sufficiently thick layers may not be completely washed by the perovskite deposition step, as seen by the photovoltaic comparisons in **Figure S5-2**, which exhibit a slight drop in FF for spin-coated perovskites deposited on 20 nm evaporated 2PACz compared to 6 nm evaporated 2PACz. For this reason an optimum thickness is considered to be from 4 nm to 8 nm. Films below this thickness may exhibit non-complete coverage, explaining some of the thickness dependence. All future films utilised a thicknesses of 6 nm for evaporated 2PACz, 6 nm for evaporated MeO-2PACz and 8 nm for evaporated Me-4PACz. 6 nm was chosen instead of 8 nm for 2PACz due to the drop in charge carrier lifetime and PL intensity.

5.4 Interfacial properties of evaporated and spin-coated nPACz

In this section, we consider the interfaces between the perovskite absorber and evaporated or spin-coated nPACz SAM-HTLs to assess their suitability for PSCs. We consider half stacks (ITO/SAM-HTL/perovskite) of two perovskites: a spin-coated triple-cation perovskite absorber layer with a composition of $Cs_{0.05}MA_{0.22}FA_{0.73}Pb(I_{0.77}Br_{0.23})_3$, as studied in **Section 5.3**, and a co-evaporated double-cation perovskite absorber layer with a composition of $Cs_{0.13}FA_{0.87}Pb(I_{0.95}Cl_{0.05})_3$. A comparable triple-cation perovskite absorber was not utilised due to the added complexity of FAMA-based perovskite evaporation,[54] instead this composition is based on perovskite of Lohmann *et al.*, who performed bulk passivation of co-evaporated perovskites *via* $PbCl_2$.[415]

5.4.1 nPACz comparison using spin-coated perovskites

With optimal deposition conditions determined, and comparable crystal structure established, **Figure 5-10** provides a detailed direct comparison of non-radiative recombination at the HTL/perovskite interface between evaporated nPACz materials with their equivalent spin-coated counterparts. For the spin-coated 2PACz reference, we measure an average PLQY of ~1.26% corresponding to an implied V_{OC} of 1.253 V, which is comparable to previously reported values for this perovskite composition.[293,416] PLQY and iV_{OC} values for evaporated 2PACz are slightly enhanced to average values of ~1.7% and 1.261 V, respectively. The n_{id} for evaporated and spin-coated 2PACz is 1.48 and 1.50 respectively, a comparable value which emphasizes that the recombination mechanism at the HTL/perovskite interface is similar in both cases. These similarities are corroborated by TRPL measurements, which exhibit similar decay dynamics, with an average lifetime of 435 ns and 474 ns for spin-coated and evaporated 2PACz, respectively.

Further investigations of charge-carrier dynamics, presented in **Figure 5-11**, are conducted for comparing evaporated 2PACz with the solution processed counterpart. Due to the complex electrical properties of perovskites, direct considerations of trap recombination and electrical conductivity of the 2PACz layer is impossible.[417,418] However, impedance spectroscopy, and the resultant Nyquist plot of the high frequency spectrum, can indicate similar recombination resistance at the interface.[419,420] In a similar manner, transient photocurrent decay curves indicate relatively similar decay lifetimes of 2.01 ± 0.33 µs and 1.84 ± 0.40 µs for evaporated and spin-coated 2PACz respectively. Overall, this data suggests that the quality of the perovskite/nPACz interface is maintained when transitioning deposition method and that non-radiative recombination is effectively suppressed.

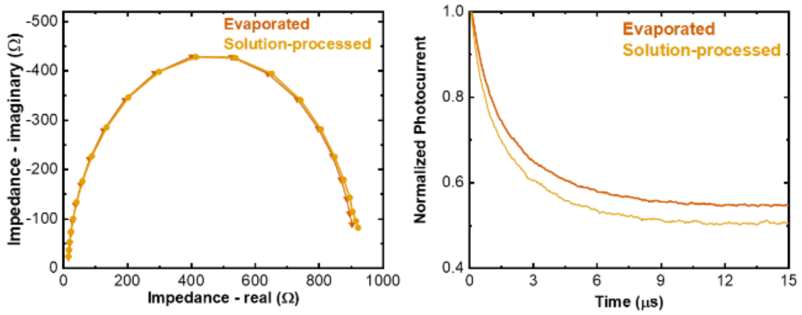

Figure 5-10 Additional interface characterisations. (*Left*) Nyquist plot of spin-coated PSCs employing spin-coated and evaporated (~6 nm) 2PACz SAM-HTLs under bias equivalent to device V_{OC} and light exposure. (*Right*) A comparison of the transient photocurrent decay between corresponding PSCs. Reproduced from Wiley-VCH GmbH ©2023 with permission.[261]

5.4.2 nPACz comparison using co-evaporated perovskites

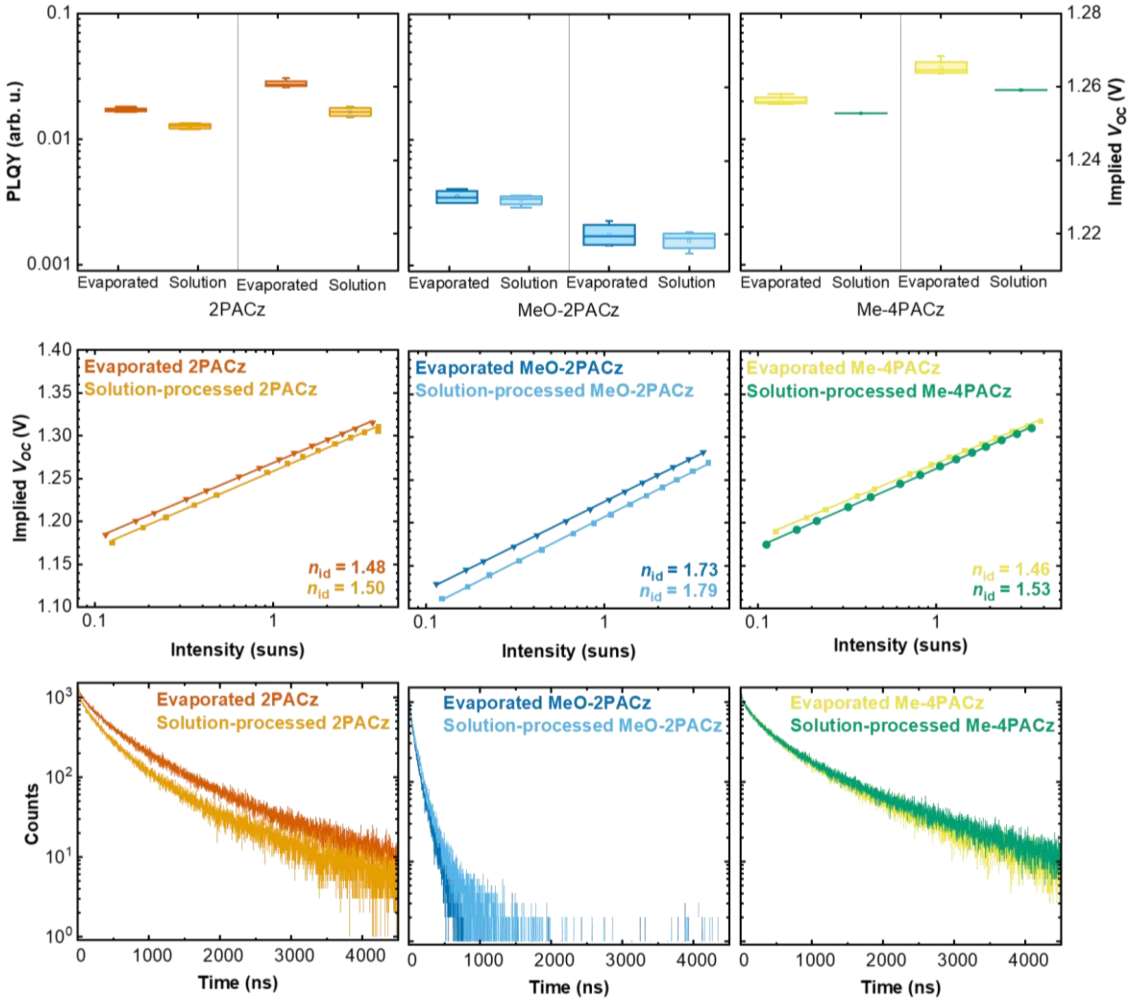

Figure 5-11 Comparison of interfacial properties for spin-coated perovskites with evaporated or spin-coated nPACz. (*Top*) Comparison of the PLQY for the half-stack ITO/SAM-HTL/(spin-coated perovskite) with the corresponding iV_{OC}. (*Middle*) n_{id} extracted from a fit to the intensity-dependent iV_{OC}. (*Bottom*) TrPL for the corresponding half-stack

employing these SAM-HTLs. All y-axis scales are consistent within each row. Reproduced from Wiley-VCH GmbH ©2023 with permission.[261]

We next consider interfacial comparisons for co-evaporated perovskites. **Figure 5-12** illustrates how changes between evaporated and solution processed nPACz layers are both more substantial and less distinct. Time-correlated single photon counting is used to calculate decay lifetimes, and some of the drop can be attributed to perovskite age, as the time between sample fabrication and TrPL measurement varied between samples. Co-evaporated perovskites on evaporated nPACz substrates were fabricated approximately 14 days earlier than their spin-coated counterparts, but measurements occurred at the same time, explaining the potential drop in charge carrier lifetimes as sample degradation. PLQY and correlated results are less clear. These measurements were taken from perovskites of similar age and observe shifts when comparing PLQY and iV_{OC}.

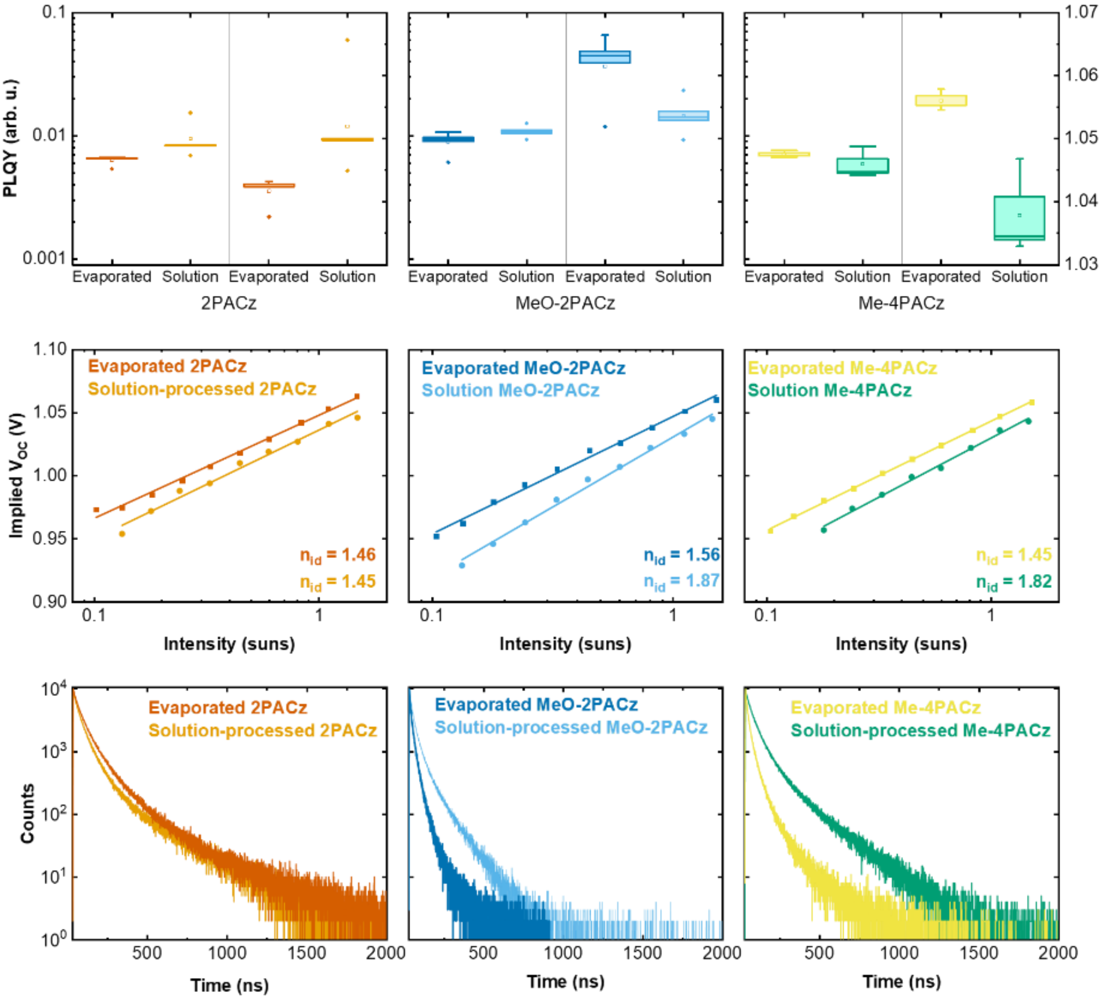

Figure 5-12 Comparison of interfacial properties for co-evaporated perovskites with evaporated or spin-coated nPACz. (*Top*) Comparison of the PLQY for the half-stack ITO/SAM-HTL/(co-evaporated perovskite) with the corresponding iV_{OC}. (*Middle*) n_{id} extracted from a fit to the intensity-dependent iVOC. (*Bottom*) TrPL spectra for the corresponding half-stack employing these SAM-HTLs. All y-axis scales are consistent within each row. Reproduced from Elsevier Inc ©2024 with permission.[221]

One potential explanation for the difference in iV_{OC} and PLQY trends is a difference in Urbach energy between samples (shown in Appendix **Figure S5-3**), which can impact iV_{OC} values which do not fit the expected trend.[102,103] Overall, these results indicate that co-evaporated perovskites are far more vulnerable to the substrate than spin-coated perovskites, an effect generally already known in literature,[104] and hence comparisons between evaporated and spin-coated nPACz SAM-HTLs are non-trivial. Further investigations into the interaction between nPACz and the perovskite are the focus of **Chapter 6**.

5.5 Perovskite wettability on evaporated nPACz HTLs

Substrate wettability is crucial to solution-based perovskites, especially when upscaling device areas, as poorly wetting substrates will lead to uncoated regions.[208,256,361,366,421,422] Me-4PACz was first developed in 2020, demonstrating increased stability, reduced interfacial non-radiative recombination and more efficient charge carrier extraction as compared to the previously reported carbazole-based SAM-HTLs of 2PACz and MeO-2PACz.[293,387] Despite this, it remains underutilised, the primary reason being poor spin-coated perovskite coverage (as shown in **Figure 5-13**, illustrating poor growth limited exclusively to ITO coated areas) and hence very low fabrication yield. Literature utilising Me-4PACz typically includes additional additives or textured surfaces to overcome this problem.[347,380,423]

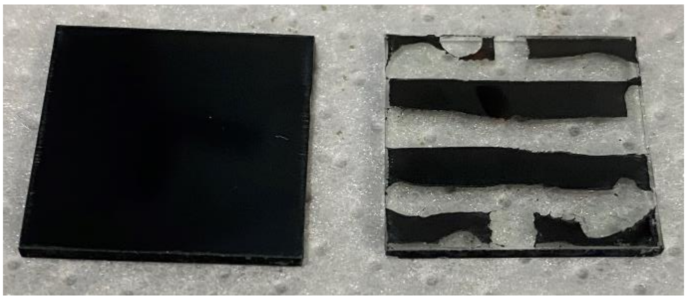

Figure 5-13 Surface coverage of perovskite on Me-4PACz. (*Right*) Poor surface coverage of the perovskite film when deposited over spin-coated Me-4PACz on patterned ITO. (*Left*) Uniform coverage when evaporated Me-4PACz is used on similar patterned ITO. Reproduced from Wiley-VCH GmbH ©2023 with permission.[261]

Tockhorn *et al*. reported a world record (at the time) 29.80% PCE for a monolithic perovskite/Si tandem solar cell employing Me-4PACz as HTL.[380] Their study emphasised by poor surface coverage of spin-coated perovskites on Me-4PACz coated planar Si bottom cells, causing a low fabrication yield (~50%), which improved dramatically (up to ~95% yield) utilising a nano-textured Si bottom cell to improve precursor solution droplet retention. In the similar manner, Jošt *et al*. reported the current world record monolithic perovskite/CIGS tandem solar cells with a PCE of 24.2% employing Me-4PACz as HTL, also experiencing low fabrication yield due to poor wetting.[347] Other attempts to improve wetting have included Taddei *et al*. employing a layer of Al_2O_3 nanoparticles on top of Me-4PACz,[423] and Al-Ahouri et al. adding a diphosphonic acid material into their Me-4PACz.

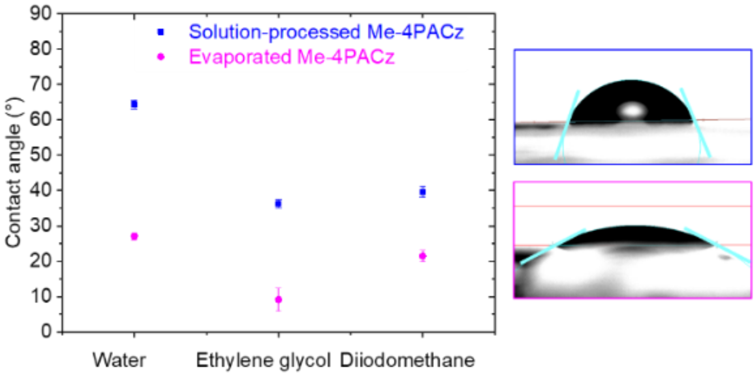

Figure 5-14 Comparison of the contact angle of water, ethylene glycol, and diiodomethane droplets deposited on evaporated and spin-coated Me-4PACz. Right are images of the water droplet in the two cases. The light blue line, indicating the tangent of the solvent at the surface is used to calculate contact angle. Reproduced from Wiley-VCH GmbH ©2023 with permission.[261]

The spin-coated Me-4PACz surface exhibits exceptionally poor surface wettability, even if washed, indicated by high contact angles as summarized in **Table 5-2**.[366,424,425] This results in poor perovskite thin film surface coverage (shown in **Figure 5-13**). Strikingly, evaporated Me-4PACz exhibits significantly lower contact angles for H_2O, $C_2H_6O_2$, and CH_2I_2, (27.1°, 9.2°, and 21.5° respectively), in stark contrast to the spin-coated counterpart (64.4°, 36.2°, and 39.6° respectively), as evident in **Figure 5-14**. This results in the perfect coverage shown in **Figure 5-13**, and represents a method to solve the Me-4PACz wettability issue without additives, surface modification or substrate tailoring, enhancing the utility of this material as a SAM-HTL.

MeO-2PACz and 2PACz do not typically suffer the same wettability issues exhibited by Me-4PACz, yet it is still potentially interesting to consider their contact angles. This can be due to other potential interactions, such as shifts in co-evaporated perovskite growth and considerations for wettability of alternative solvents for spin-coated perovskites, such as green solvents.[206,426]

Evaporated MeO-2PACz exhibits no statistically significant change in contact angle compared to spin-coated MeO-2PACz for H_2O, and $C_2H_6O_2$ (62.5° / 63.6° and 39.1° / 39.7° respectively), while CH_2I_2 decreases slightly (29.6° / 22.9°). The low CH_2I_2 contact angle are indicative of a higher dispersive free energy at the sample surface (estimated in **Table 5-2** using the Owens, Wendt, Rabel and Kaelble method (OWRK)),[267] which can explain the lack of reported wetting problems when utilizing MeO-2PACz. Even if the H_2O contact angle is similar to that of spin-coated Me-4PACz, dispersive free energy is more relevant for low polarity solvents, such as DMF. Evaporated 2PACz films exhibit significantly reduced contact angles for polar solvents compared to their spin-coated counterparts (52° / 17.7° for H_2O and from 31.7° / complete wetting for $C_2H_6O_2$), with a minor decrease in the non-polar CH_2I_2 (29.7° / 25.7°). There exists a clear overall trend of lower contact angles for evaporated nPACz SAM-HTLs. This is indicates improved wettability and surface coverage, consequently a higher fabrication yield of spin-coated PSCs. The impact of a washing step on contact angles of evaporated and spin-coated nPACz layers is of most interest to co-evaporated perovskites, and will be discussed in **Chapter 6**.

Table 5-2 Contact angle measurements for the spin-coated and evaporated SAMs along with the calculated dispersive, polar, and total free energies, using the OWRK method. Reproduced from Wiley-VCH GmbH ©2023 with permission.[261]

Film on glass/ITO	Contact angle (°)			Free energy (eV)		
	H_2O	$C_2H_6O_2$	CH_2I_2	Dispersive	Polar	Total
Solution-processed Me-4PACz	64.4	36.2	39.6	39.81	10.08	49.89
Solution-processed Me-4PACz (washed)	64.1	36.8	38.9	39.9	10	50.1
Evaporated Me-4PACz	27.1	9.2	21.5	47.32	26.39	73.71
Solution-processed 2PACz	52	31.7	29.7	44.35	15.06	59.41
Evaporated 2PACz	17.7	*Complete wetting*	25.7	45.90	30.51	76.41
Solution-processed MeO-2PACz	62.5	39.1	29.6	44.38	9.58	53.96
Evaporated MeO-2PACz	63.6	39.7	22.9	46.88	8.34	55.21

5.6 Perovskite crystal structure on evaporated nPACz

Considering the similarities between evaporated and spin-coated SAM-HTLs, it is important to consider if the crystal structure of the resultant perovskite is impacted. In this section we will analyse SEM and XRD data of the spin-coated and co-evaporated perovskites from **Section 5.2.3**. to obtain additional understanding of how evaporated SAM-HTLs impact growth.

5.6.1 Crystal growth of spin-coated perovskites

Top view SEM images, displayed in **Figure 5-15**, do not show significant changes in perovskite crystal structure when grown on evaporated or spin-coated 2PACz layers. Crystallite size distribution (crystallite definitions shown in **Figure S5-4**) indicates a roughly comparable distribution between evaporated and equivalent spin-coated nPACz substrates. The only notable observation is an increased density of small bright crystallites for spin-coated 2PACz, which have been previously associated with Pb-rich regions.[124] Washed 2PACz layers display a larger density of small grains, but an otherwise comparable distribution to its unwashed counterpart. Other nPACz SAM-HTLs, present in the Appendix **Figure S5-5**, also show a high degree of similarity in top-view SEM appearance and grain size.

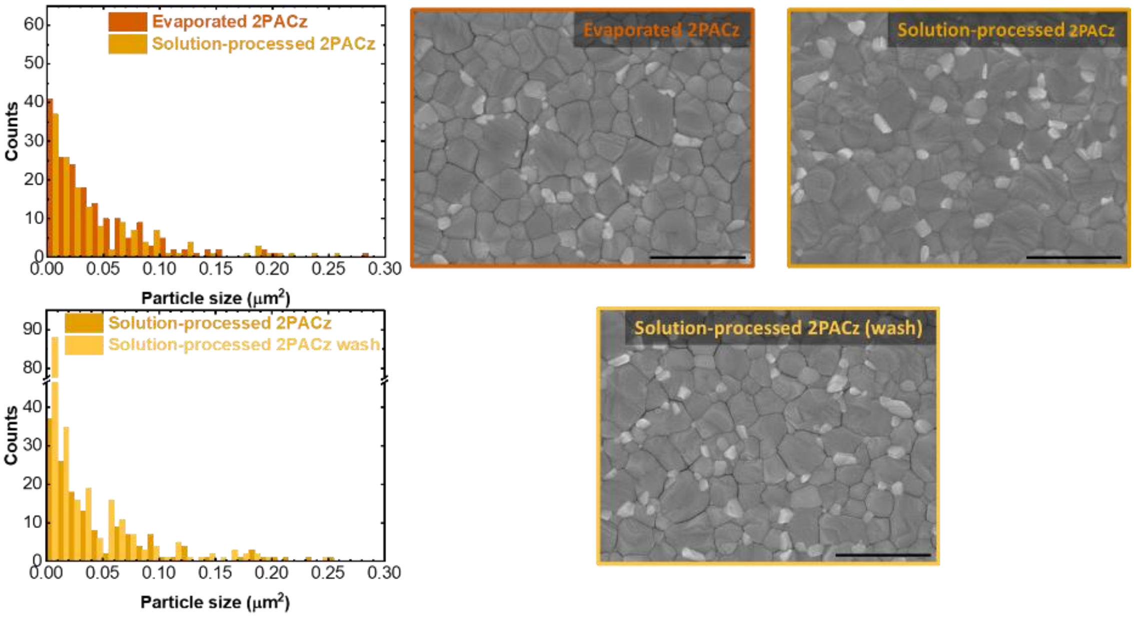

Figure 5-15 Grain size analysis for spin-coated perovskites on 2PACz. Distribution of grain size (*left*) for top view scanning electron microscope images of perovskite thin films deposited over evaporated 2PACz layer (*top-middle*), spin-coated 2PACz layer (*top-right*) and a washed spin-coated 2PACz substrate (*bottom-middle*). The scale bar represents 1 μm. Part of figure adapted from Wiley-VCH GmbH ©2023 with permission.[261]

XRD, spectra shown in **Figure 5-16**, was performed to investigate if these surface similarities also extends to bulk properties. These results find an exceptional level of similarity between spin-coated perovskites in terms of peak positions and areas, indicating no substantial change in crystal growth. The sole exception is the relative areas of the crystalline PbI_2 peak at 12.6° and the first perovskite peak at ~14.1°. Evaporated SAM-HTL samples unilaterally show a reduced crystalline PbI_2 peak area compared to spin-coated counterparts. For MeO-2PACz and Me-4PACz this is not associated with a decrease in the perovskite peak intensity, leading to a shift in the PbI_2 / perovskite ratio.

We postulate three explanations for this difference

The first potential explanation, which the author considers most likely, is that the change in growth is indicative of a difference in surface coverage. This was one potential explanation of the changing In and Sn peak intensities observed in **Figure 5-4**. The impact of surface coverage on XRD spectra can be potentially attributed to the stabilization of the perovskite/SAM-HTL interface via chelation of Pb^{2+} with carbazole functional groups,[427] or any heterocyclic amine.[428] Carbazole related compounds act as Lewis bases due to their electron-rich pi systems[429,430] (which also enhances their hole-selective nature)[429] and have been shown a strong tendency to coordinate with Pb^{2+}.[427] Chelation of Pb^{2+} by heterocyclic amines has been found to improve perovskite stability, preventing PbI_2 formation due to decomposition of the perovskite.[427] Furthermore, surface modification of oxides with MeO-2PACz has been previously shown to decrease PbI_2 peak intensity[397,431,432] due to interfacial degradation of perovskite/metal oxide interfaces.[362,377] As coverage is associated with PbI_2 suppression, reduced coverage can be correlated to increased PbI_2 intensity.

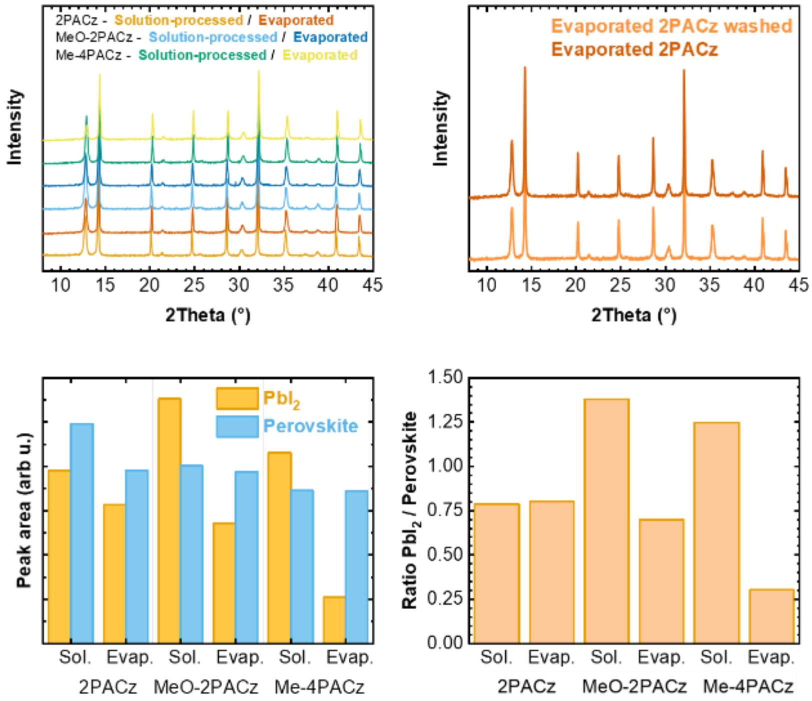

Figure 5-16 XRD analysis of spin-coated perovskites on various nPACz layers. (*Top-right*) XRD spectra of spin-coated perovskites deposited onto every possible combination of nPACz SAM-HTL. (*Top-left*) Comparison between spin-coated perovskites deposited onto washed and unwashed evaporated 2PACz. (*Bottom*) Relative peak areas between first perovskite and PbI_2 peaks, along with the resulting ratio. Part of figure adapted from Wiley-VCH GmbH ©2023 with permission.[261]

The next potential explanation assumes interactions between residual bulk nPACz molecules and the perovskite solution. The suppression of crystalline PbI_2 has previously been associated with the presence of phosphonic acid containing additives in the organic cation solution of hybrid perovskites.[433] Furthermore, top surface passivation with pentafluorobenzyl phosphonic acid resulted in a slight decrease of the PbI_2 peak.[352] Phosphonic acid functional groups are capable of passivating defects by forming coordination bonds with Pb^{2+}.[434–438] This is because the phosphonic acid functional group can behave as both electron donating and proton accepting group, and hence can act as a Lewis base under Bronsted-Lowry acid-base theory. *Lin et al*. demonstrated that materials possessing multiple functional groups able to act as Lewis bases improves their overall passivation ability,[439] meaning both phosphonic acid functional groups and carbazole functional groups will exhibit improved passivation properties. However, it is not likely that unbound molecules, and hence exposed phosphonic acid functional groups, are the cause of the lower PbI_2 signal for spin-coated perovskites. Spin-coated perovskites deposited on washed evaporated or spin-coated 2PACz (shown in **Figure 5-16**) display no identifiable differences in peak areas compared to their unwashed counterparts, which would not be expected if residual nPACz was incorporating into the perovskite solution and impacting organic cation incorporation. The similarity of these signals provides further evidence to the theory that solution-processing of perovskites causes a mild washing effect on SAM-HTLs, removing some unbound bulk molecules.

The final explanation primarily considers the change in perovskite peak intensity. While spin-coated perovskites exhibit less substrate dependent growth than co-evaporated perovskites, there are some reported trends between substrate characteristics and spin-coated perovskite growth based on heterogeneous nucleation theory. H_2O contact angle has been extensively correlated to perovskite crystallisation due to its impact on solvent-surface interactions.[366,440–442] Beneficial modification of the surface can reduce the density of nucleation sites and allow further Oswald ripening, resulting in enhanced grain sizes.[366,443,444] This theory is considered less likely due to the similar surface grain sizes displayed in **Figure 5-15** and **Figure S5-5** and, with the exception of the (0 0 1) peak for 2PACz, the near identical sizes of all perovskite XRD peaks in **Figure 5-16** for Me-4PACz substrates. If H_2O contact angle was responsible for the shift in (001) peak intensity for 2PACz, it would be expected for a similar shift to be observed for Me-4PACz, as evaporated Me-4PACz displays a comparable drop in H_2O contact angle (as discussed in **Figure 6-7**).

For these reasons the first postulated explanation, of slight changes in XRD spectrum relating to surface coverage is the most likely explanation. However, the proposed subsidiary theories cannot be fully discounted. A full understanding of the exact mechanism was outside the scope of this work.

5.6.2 Crystal growth of co-evaporated perovskites

Comparing spin-coated perovskites with their co-evaporated counterparts reveals a striking number of both similarities and differences in the XRD spectra shown in **Figure 5-17**. Overall spectral shape between nPACz SAM-HTLs remains similar, but peak area trends are very disparate. MeO-2PACz and Me-4PACz continue to show reduced PbI_2 intensity for evaporated samples. However, evaporated nPACz displays significant increase in peak area (approximately doubled) for both peaks. Ratios are also much less consistent, all indicating a far greater substrate dependence compared to spin-coated perovskites, as known in literature.

What is most striking is the difference between washed and unwashed evaporated 2PACz. While spin-coated perovskites are essentially unchanged, co-evaporated perovskites display a significant increase in perovskite peak intensity and a near complete disappearance of the PbI_2 peak. This is indicative of increased organic cation incorporation, as has been potentially observed in literature, and are investigated further in **Chapter 6**. The results of this section, and those of **Section 5.3** show clearly and repeatedly that utilising nPACz SAM-HTLs is a complicated process for co-evaporated perovskites independent of the SAM deposition method.

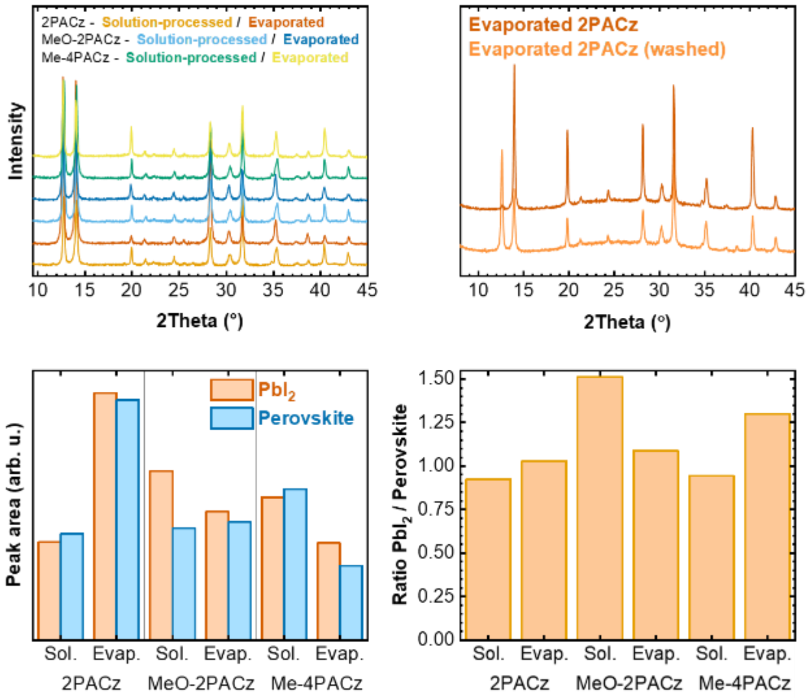

Figure 5-17 XRD analysis of co-evaporated perovskites on various nPACz layers. (*Top right*) XRD spectra of co-evaporated perovskites deposited onto every possible combination of nPACz SAM-HTL. (Top left) Comparison between co-evaporated perovskites deposited onto washed and unwashed evaporated 2PACz. (*Bottom*) Relative peak areas between (0 0 1) perovskite and PbI_2 peaks, along with the resulting ratio. Part of figure adapted from Elsevier Inc ©2024 with permission.[221]

5.7 Summary

In this chapter, we present the development of the vacuum-based thermal evaporation of common nPACz SAM-HTLs (2PACz, MeO-2PACz and Me-4PACz), which maintain the high-quality HTL/perovskite interface. The evaporation deposition technique enhances process flexibility, continue our theme of establishing industrially compatible deposition techniques that are upscalable and exhibit conformal coatings of textured surfaces, crucial for coating textured monolithic tandems.[31,445] Hence, we have addressed **Challenge 3**, producing vapour-processed HTLs that exhibit low interfacial losses.

Material analysis in **Section 5.2** indicates no significant change in chemical properties when comparing evaporated nPACz SAM-HTLs with powder references and spin-coated counterparts. Specifically, no evidence of chemical degradation is observed in XPS or FTIR spectra. Analysis of secondary XPS peaks, combined with FTIR spectral analysis indicates comparable binding occurs at the substrate. **Section 5.3** entailed extensive process optimization, which found that the evaporation deposition technique is resilient to deposition speeds of up to 0.5 Å.s^{-1}, material reuse and substrate storage of up to 10 days. The increased storage stability is promising for process flexibility and ease of future optimization. Full thickness optimization of half stacks with a spin-coated perovskite defined optimum thicknesses to be from 6 – 8 nm for each substrate, but overall shifts were relatively minor, indicating the high quality of the interface independent of thickness.

Interfacial property analysis in **Section 5.4** found that the established high quality of the perovskite/SAM-HTL interface is preserved or even slightly improved for spin-coated perovskites on every evaporated SAM-HTL with an optimized thickness, with effective suppression of non-radiative recombination. As part of investigating evaporated nPACz properties, we characterised the surface energies of ITO/nPACz substrates in **Section 5.5**, revealing clear trends of improved wettability for every solvent, which correlated to enhanced surface coverage of spin-coated perovskite thin films.

Surface morphology and crystal structure is similar for spin-coated and co-evaporated perovskites over our developed SAM-HTLs, as outlined in **Section 5.6**. XRD spectra of spin-coated perovskites reveals a suppression of the crystalline PbI_2 signal for each evaporated SAM-HTL compared to its spin-coated perovskites. This is typically not accompanied by meaningful change in the perovskite XRD spectra. Washing evaporated or solution processed 2PACz did not shift their spectra in any noticeable manner, demonstrating that unbound nPACz is most likely not preserved for spin-coated perovskites, providing an explanation for their thickness independence. Meanwhile, co-evaporated perovskites exhibit a more complex behaviour.

This work represents a new vapour-based method of upscaling for nPACz materials, joining existing solution-based methods. [185,381,382,385,446] The evaporation of SAM-HTLs pioneered in this chapter has now been shown as comparable to spray-coated SAM-HTL layers,[446] and has been incorporated into an efficient 128 cm^2 module with a slot-die coated perovskite layer.[447] The method is not without limitations, with additional experimentation on evaporated SAM-HTLs revealing that thermal decomposition is possible at significantly increased temepratures.[446] Furthermore, evaporation has shown itself as a powerful research tool, enabling investigations of surface coverage properties without solvent-surface interactions.[448] Moreover, uniform coverage of textured silicon has proven to be difficult for spin-coated SAM-HTLs, with variation in thickness and coverage between the peaks and valley of the textures.[449,450] Evaporation is an effective method to solve this problem, achieving conformal coatings on textured glass and textured silicon without sacrificing the SAM interfacial properties.[261,386]

6 Interfacial interactions between phosphonic acid functional groups and co-evaporated perovskites

Abstract

In this chapter, we explore how exposed phosphonic acid functional groups impact the initial phase and final bulk crystal structure of co-evaporated perovskites and their resultant PCE. Specifically, by coupling maximum device performance with material analysis using x-ray diffraction and decay lifetimes of the final perovskite films, we observe shifts in bulk perovskite phase and formamidinium iodide (FAI) incorporation rate where the SAM-HTL exhibits exposed phosphonic acid functional groups. We compare interfacial properties *via* photoluminescence measurements, performance of PSCs and impedance spectroscopy. Density functional theory computations reveal that the explored surface interaction is mediated by hydrogen bonding with interfacial iodine, and we hypothesize that the observed stabilization of bulk α-$FAPbI_3$, is due to a kinetic trapping effect. Finally, we demonstrate that such results are preserved for monolayer films with exposed phosphonic acids, highlighting the potential such interactions represent for future substrate development.

The work in this chapter resulted in the publication: '**Understanding and exploiting interfacial interactions between phosphonic acid functional groups and co-evaporated perovskites**,' published in **Matter** by Thomas Feeney and Julian Petry as shared first authors.[221]

This work is the result of collaborative research between Karlsruhe Institute of Technology, Heidelberg University and University of Nevada, Las Vegas (UNLV).

Thomas Feeney conceived the initial idea of this study and designed all experiments with support from Julian Petry and Dr. Abderrezak Torche for relevant sections. He fabricated all presented devices and samples, performed and analysed JV, EQE, MPP, XRD, PLQY measurements, and analysed TrPL measurements. Julian Petry performed and analysed all NMR measurements. Dr. Abderrezak Torche, Dr. Michelle Ernst and Assoc. Prof. Dr. Ganna Gryn'ova performed and analysed all DFT calculations. Dr. Dirk Hauschild, Dr. Constantin Wansorra, Dr. Lothar Weinhardt and Prof. Dr. Clemens Heske performed and analysed all XES measurements. Benjamin Hacene performed all TrPL measurements and provided the fitting routine. Alexander Diercks performed all SEM measurements. The project was undertaken with the supervision of Prof. Dr. Ulrich W. Paetzold and Dr. Paul Fassl.

6.1 Motivation

Part of the extensive utility of perovskites comes from the wealth of available fabrication methods, each with a suite of challenges and opportunities. Vapour-phase vacuum-based thermally evaporated or sublimated (hereafter referred to as vapour-phase) perovskites require no solvents, are highly suited to deposit on textured surfaces and readily maintain homogeneity over larger areas – leading to reduced upscaling losses for industrially relevant active areas.[47,49,212] Vapour-phase perovskites have recently expanded into a wide range of potential compositions and bandgaps.[68,172,451-453] Among these options, perovskites utilizing formamidinium (FA) halides as organic cations are particularly promising due to the expected improved performance and stability.[68]

Co-evaporated perovskites, more than any other fabrication method, rely on a suitable substrate for optimum absorber growth and subsequent perovskite solar cell (PSC) performance, with substrate variations necessitating optimized deposition parameters for high quality crystal formation.[54,71,72,73,222,454–456] Abzieher *et al.* were the first to attempt a universal explanation on this phenomena, reporting on changes in initial perovskite growth for $MAPbI_3$ or $Cs_xMA_{1-x}Pb(I_yBr_{1-y})_3$ perovskites through suppression or incitement of Oswald ripening caused by substrate properties,[72,277] which persist for more complex perovskites. Initial film quality was correlated to substrate surface polarity, with Abzieher *et al.* theorizing that polar interactions between the substrate and MA^+ vapor governs the initial organic incorporation. The strong influence of initial crystal growth conditions on bulk material properties were corroborated by Yan *et al.*, who showed that high quality co-evaporated perovskite films can be formed on a variety of substrates by incorporating an initial ultrathin high-quality perovskite template layer.[222]

6.1.1 State of the art

Substrate functional group interactions have recently added further complexity for surface-dependent growth, with the clearest reported example being the influence of MeO-2PACz on co-evaporated $FAPbI_3$-based absorbers.[54] MeO-2PACz is a member of the nPACz family – a group of self-assembled monolayer based hole-transporting layers (SAM-HTLs), with a carbazole functional body and a phosphonic acid anchoring group, that are lauded for their near-lossless contact properties.[70,373] Ross *et al.* observed substantial differences in co-evaporated perovskite crystal growth, dependent on whether residual bulk SAM was removed from the MeO-2PACz *via* an ethanol wash. They postulated that the differences can be attributed to the formation of hydrogen bonds between exposed phosphonic acid functional groups and FAI.[54]

Hydrogen bonding is an established interaction mechanism within perovskites, with extensive reporting of interfacial interactions between FA^+ cations and substrate materials. [54,377,457] Such bonding has been attributed to a reduced formation energy for alpha (α)-phase $FAPbI_3$,[354,377,457] as well as an increased defect formation energy and enhanced thermal stability for solution-processed perovskites.[457,458] Recent work has evaluated the impact of bulk phosphonic acids on interfacial and bulk properties of phosphonic acids.[459] However, there remains no understanding on the role of interfacial hydrogen bonding on mediating crystal growth.

6.1.2 Outline

In **Chapter 5** we introduced deposition of nPACz SAM-HTLs of controlled thickness *via* thermal evaporation from a crucible in vacuum, restricting our analysis of co-evaporated perovskites to washed samples to limit potential bulk impacts.[261] Our analysis in **Chapter 6** will employ a combination of evaporated and solution-processed deposition of SAM-HTLs in order to perform an in-depth analysis of the role of exposed phosphonic acid functional groups on co-evaporated perovskite film formation in response to **Challenge 4 and 5**. The presence of exposed phosphonic acid functional groups is controlled by washing the SAM layers with ethanol to remove unbound molecules, as shown in **Figure 6-1**.

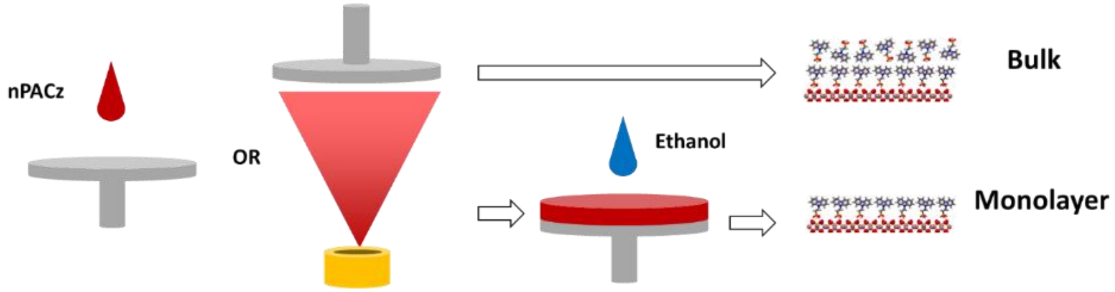

Figure 6-1 Schematic of deposition processes to produce bulk and monolayer nPACz films with solution-processed or evaporated SAM-HTLs. Monolayer films were prepared by dynamically washing the SAMs with ethanol. Reproduced from Elsevier Inc ©2024 with permission.[221]

In **Section 6.3**, we examine the material impact of the presence of interfacial hydrogen bonding groups on co-evaporated perovskite formation by analysing the relative incorporation rate of FAI, measured by the rate required for maximum PCE. X-ray emission spectroscopy (XES) analysis of thin co-evaporated perovskite and FAI films grown on bulk and monolayer 2PACz SAM-HTLs corroborates the observed additional FAI-surface interaction, and the resultant perovskite growth changes. We consider the differences in material properties *via* XRD and SEM, which reveals a strong change in growth and initial perovskite phase. Bulk layers suppress the formation of the photo-inactive δ-$FAPbI_3$ phase, enabling reproducible room temperature deposition of α-$FAPbI_3$ without annealing.

Section 6.4 entails ^{1}H-NMR and DFT analysis of our studied interactions in solution and at the interface to allow identification of the chemical and physical causes for these observations. ^{1}H-NMR shows that interactions occur *via* the halide, rather than the previously assumed organic, component of FAI. DFT calculations in **Section 6.5** demonstrate that α-$FAPbI_3$ naturally forms during initial perovskite growth even in the absence of interfacial effects, with XRD providing corroborating evidence. We find hydrogen bonding between surface iodine of the perovskite and nPACz phosphonic acid functional groups are of equal strength for α-$FAPbI_3$ and δ-$FAPbI_3$, indicating that while such bonds can be responsible for increased FAI incorporation, they are not directly responsible for the observed change in perovskite phase. We postulate instead a kinetic trapping mechanism, where hydrogen bonding provides an energetic barrier for the conversion of α-$FAPbI_3$ to δ-$FAPbI_3$.

We next compare, in **Section 6.6**, perovskite devices using bulk and monolayer SAM-HTLs. This entails interfacial comparison via PLQY and TrPL, and PSC comparisons via photovoltaic properties. These results demonstrate that the presence of bulk materials is beneficial for interface properties but that this does not necessarily correlate to superior device power conversion efficiency (PCE). Our analysis includes the evolution of EQE and XRD with respect to FAI rate, which reveals potential general rules for optimal stoichiometry.

Finally, as an outlook, **Section 6.7** addresses the potential for rational design of SAM-HTLs that benefit from this interfacial interaction while remaining a monolayer. We demonstrate this through XRD and photovoltaic parameter analysis of a series of PSCs utilizing 2PACz with molar fractions of 4dPA, a monolayer material with duel phosphonic acid functional groups, allowing controllable tuning of surface phosphonic acid functional groups.

6.2 Preface

To account for the differences in co-evaporated perovskites on evaporated or solution-processed SAM-HTLs observed in **Chapter 5**,[261] we will compare at times both evaporated and solution-processed washed and unwashed samples. Due to the 1.3 nm length of unbound 2PACz, all evaporated nPACz thin films mentioned in this work have a QCM measured thickness of 4 nm to guarantee a bulk component. Solution processed nPACz films use a 4 mM concentration of nPACz, similar to the previous work of Ross *et al*.[54]

Bulk nPACz molecules are form a bilayer on the monolayer with exposed phosphonic acid functional groups due to π- π interactions between carbazole functional groups, which are a particularly strong form of non-covalent bonds.[460] However, the substituent dependence of the interaction strength means the expected density of exposed phosphonic functional groups may differ between various nPACz molecules.[461,462] This disordered bulk SAM layer is removed during standard solution-processed perovskite deposition, but vapour-phase perovskites do not disturb this bulk SAM layer. Hereafter, unwashed SAM layers with the presence of exposed phosphonic acids as are referred to as bulk films, and to washed SAM layers without exposed phosphonic acids as monolayer films.

When discussing optimum FAI rates in this chapter, it is important to define optimal stoichiometry. In this workt, optimal stoichiometry does not inherently correspond to an equimolar perovskite, as often a slight PbI_2 excess is beneficial for PSC PCE.[463] Precise determination of perovskite composition is complex due to varying precursor solubility for solution-processed perovskites,[173] and variations in sticking coefficients coupled with evaporation dynamics (such as precursor mean free path) in vapour-phase perovskites.[72,464,465] Optimum stoichiometry in this chapter refers to the highest reported PCE, and does not guarantee equivalent stoichiometry. This is relevant because, for co-evaporated perovskites, initial growth conditions have a substantial impact on the bulk material and required organic rates to form an optimum stoichiometry.[72,455] As shifts in initial organic incorporation rates are preserved throughout the deposition, the surface interactions discussed in this chapter are expected to influence bulk properties. We employ a double-cation perovskite absorber with the composition $Cs_{0.13}FA_{0.87}Pb(I_{0.95}Cl_{0.05})_3$ as outlined in **Chapter 3**, in the architecture: glass/indium tin oxide (ITO)/SAM-HTL/perovskite/C_{60}/SnO_x/Au.[415] Inorganic sources (PbI_2, $PbCl_2$ and CsI) were kept at constant deposition rates (0.23 $Å.s^{-1}$, 0.01 $Å.s^{-1}$ and 0.025 $Å.s^{-1}$ respectively) to preclude deposition speed related effects,[74,455] which will be investigated in **Chapter 7**.

6.3 Substrate dependent FAI incorporation rate

In this section we will outline how the substrate impacts the crystal growth and the level of FAI incorporation in the perovskite, including direct evidence for substrate-dependent FAI adsorption.

6.3.1 Required FAI rate for formation of optimum perovskite

We performed a FAI stoichiometry series to analyse the substrate dependent optimal FAI rate. For this, inorganic rates were kept constant and FAI rate was varied from 0.6 $Å.s^{-1}$ to 1.1 $Å.s^{-1}$. As shown in **Figure 6-2**, bulk SAM-HTL layers require substantially lower FAI sublimation rates to obtain maximum PCE. with approximately 25% higher rates required for washed solution-processed layers and +75% to +100% higher rates required for washed evaporated layers compared to each bulk counterpart. As the optimum for evaporated MeO-2PACz and Me-4PACz was not obtained in this series, 0.55 $Å.s^{-1}$ was assumed as an approximate optimum. Previous studies on substrate-dependent growth have not observed substantial shifts in the process window,[54,72] while our findings require large changes in rate even for chemically similar substrate materials.

PCE decline is primarily induced by a substantive drop in J_{SC} for most SAM-HTLs (see also **Figure S6-2 and S6-2**). This is associated with excess organic cations in the perovskite film,[54,466–468] and is therefore attributed to a change in the required FAI rate for ideal stoichiometry. Below the optimum PCE remains relatively stable, with drops in J_{sc} typically compensated for an increase in V_{OC} due to the beneficial impact of PbI_2. A similar trend, shown in **Figure S6-3**, was observed for 2 nm evaporated nPACz SAM-HTLs. However, due to the lower maximum PCE of 2 nm evaporated nPACz, it appears that a partial bulk film is not suitable for high efficiency co-evaporated perovskites.

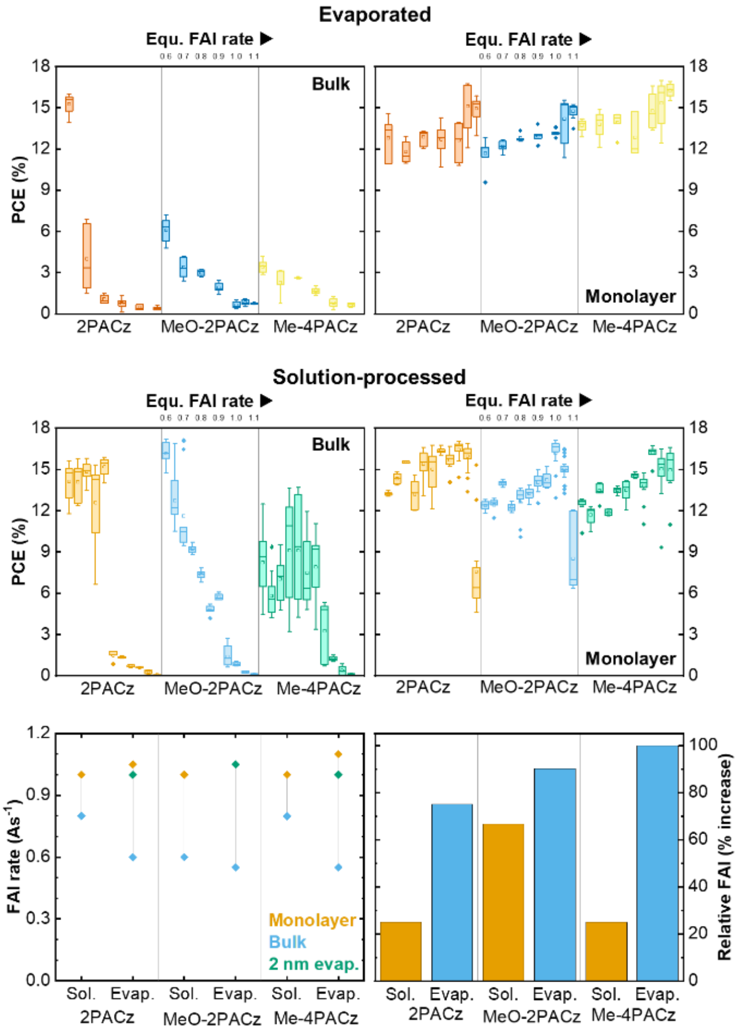

Figure 6-2 Photovoltaic parameter statistics derived from forward and reverse J-V scans of PSCs with varying rates of FAI for evaporated (*top*) and solution-processed (*middle*) nPACz as SAM-HTLs. nPACz layers were left as deposited to leave residual bulk material (left) or with a washing step to ensure the presence of a monolayer (*right*). (*Bottom*) FAI rate required for optimal PSCs, in addition to the required FAI rate for an alternative 2 nm evaporated bulk film (full statistics shown in **Figure S6-3**) and % increase in FAI rate required for monolayer films compared to bulk counterparts. For evaporated MeO-2PACz and Me-4PACz it is assumed that 0.55 Å.s^{-1} would have been optimum following trends in evaporated 2PACz. Part of figure reproduced from Elsevier Inc ©2024 with permission.[221]

6.3.2 XES analysis of FAI deposition and perovskite thin films

To obtain a better experimental understanding of the observed increased FAI adsorption, and to obtain a precursory understanding of the impact of interfacial interactions between the SAM-HTL and the perovskite film, Dr. Dirk Hauschild, Dr. Lothar Weinhardt and Prof. Dr. Clemens Heske from Institute for Photon Science and Synchrotron Radiation (IPS) and Institute for Chemical Technology and Polymer Chemistry (ITCP) in Karlsruhe Institute of Technology and UNLV along with Dr. Constantin Wansorra (IPS, KIT) employed synchrotron-based soft x-ray emission spectroscopy (XES) to determine the element-specific electronic structure at the nitrogen atoms. XES measurements involve exposing the sample to a high intensity x-ray beam, which has the potential to cause degradation. An initial scan of a 2PACz sample shown in **Figure 6-3** revealed degradation below a scanning speed of 600 µm.s^{-1}, which corresponds to a 50 ms dwell time, due to the change in shape of the spectral feature at ~397.5 nm. Hence, our collaborators utilized a scan speed of 600 µm.s^{-1}. They restrict the XES measurements to films deposited on evaporated nPACz due to the expected higher substrate uniformity. We expect substrate uniformity to lead to a uniform perovskite sample and hence enhance XES accuracy.

Our collaborators considered non-resonant N K XES spectra ($hv = 420$ eV) of two different sample sets: bulk evaporated 2PACz and monolayer evaporated 2PACz. The sample sets consisted of a ~25 nm FAI and a ~25 nm perovskite film (with the relevant optimum FAI rate), similar to previous XES work performed on FA-based perovskites.[469] For the bulk 2PACz substrate, they also measured the interface formation with ~25 nm PbI_2 or ~25 nm CsI to determine if such sample interactions are also impacted. Finally, a bare ITO substrate, a bulk 2PACz powder reference, and a bulk $FAPbI_3$ were measured to act as reference spectra, while the reference FAI spectrum was taken from previous work.[470]

The reference N K XES spectrum for ITO, shown at the bottom of **Figure 6-3**, exhibits a broad and relatively weak spectral structure with a primary peak at ~394 eV. ITO is not expected to exhibit any signal in the N K XES spectrum due to the complete absence of nitrogen. Therefore, this signal is likely due to contamination such as residual nitrogen incorporated into the bulk of the ITO film during preparation. In contrast, the reference spectrum for the bulk 2PACz powder displays a clear characteristic multi-peak structure, with the most prominent peak at ~398 eV. Our collaborators attribute this particular peak to the transition of an electron from the highest occupied molecular orbital, located at the nitrogen atom within the carbazole ring, into the N 1s core hole. Other peaks in the 385 eV to 397 eV region are associated with transitions from lower energy molecular orbitals into the N 1s core hole. High signal intensity for the 2PACz reference spectrum necessitated multiplication by a factor of 0.15 to enable comparison with other spectral series.

While the bulk 2PACz substrate sample (labelled 2PACz/ITO in **Figure 6-3**) consists of a superposition of the ITO N K signal and the reference 2PACz spectrum, the monolayer 2PACz/ITO substrate did not require a 2PACz contribution to reproduce the signal. These results suggest that the chemical structure of the evaporated 2PACz on ITO is equivalent to the powder reference, which provides further evidence to the results presented in **Chapter 5**, which stated that 2PACz is not chemically changed during evaporation. Meanwhile, the monolayer substrate result indicates that the 2PACz the monolayer film is very thin, as expected for a monolayer, with a signal intensity sufficiently below that of the ITO substrate to be unmeasurable.

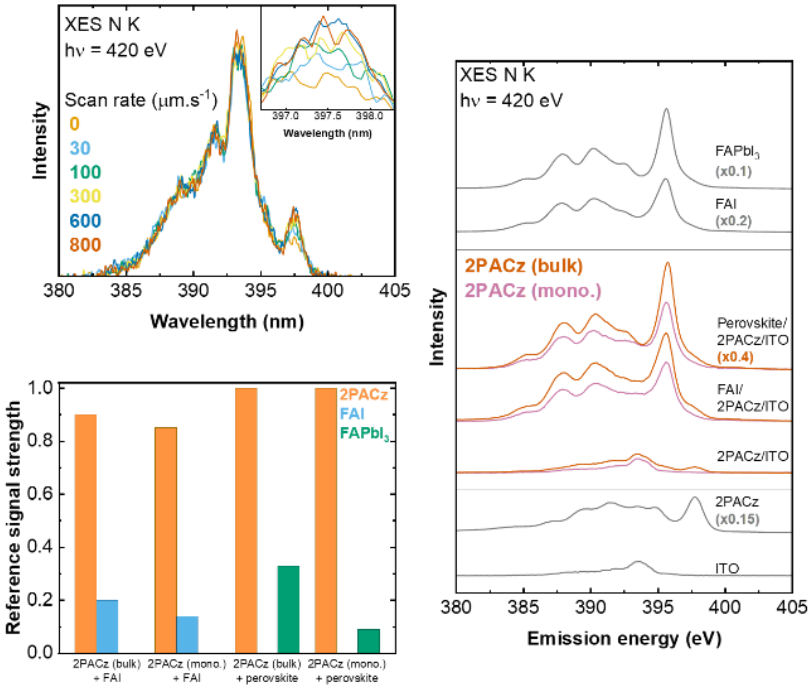

Figure 6-3 XES results indicating changes in perovskite and FAI deposition in thin films. (*Top-left*) XES spectra of 2PACz thin films deposited on ITO, with a variation in scan speed. Inset shows evidence of beam induced degradation. (*Right*) XES spectra of ~25 nm FAI and ~25 nm $FAPbI_3$ perovskites deposited onto bulk or monolayer 2PACz films. Reference 2PACz (pressed powder pellet), ITO, FAI, and $FAPbI_3$ spectra are provided for comparison. Some spectra were multiplied by the given truncation factor for easier viewing. (*Bottom-left*) Overview of the signal contributions of respective reference fit components to the description of the spectra in right with relevant reference spectra. Measurements taken by collaborators (IPS and ITCP, KIT plus UNLV). Part of figure reproduced from Elsevier Inc ©2024 with permission.[221]

Both substrates with 25 nm FAI/2PACz/ITO (labelled thus in **Figure 6-3**) strongly resemble the characteristic N K FAI spectral fingerprint of the FAI reference spectra.[470] Similarly, both samples with a 25 nm $FAPbI_3$ perovskite deposition (perovskite/2PACz/ITO in **Figure 6-3**) resemble the $FAPbI_3$ spectral fingerprint, which differs slightly from bulk FAI due to the combination of FA^+-ion and halide-derived hybrid orbitals. For spectral pair, the bulk substrate exhibits a significantly higher intensity, especially for the $FAPbI_3$/2PACz/ITO samples, as evidenced by the x0.4 truncation factor.

To quantify these differences and determine the relative spectral contribution of the reference spectra, Dr. Dirk Hauschild performed a fit analysis of the spectra using the respective 2PACz substrate signal and the relevant FAI or $FAPbI_3$ reference spectrum as fitting components. These contributions are not precisely proportional to the nitrogen concentration due to possible differences in the photoionization cross sections of the different compounds. The monolayer FAI spectrum can be reproduced using a combination of the substrate and FAI reference spectra: [0.85x 2PACz + 0.14x FAI] while the bulk spectrum required a larger FAI component [0.90x 2PACz + 0.20x FAI]. Due to the low thickness of the substrate spectra, variation in substrate reference is expected. Perovskite growth rates follow a similar trend of [1.0 x 2PACz + 0.09x perovskite] and [1.0x 2PACz + 0.35x perovskite] for monolayer and bulk

2PACz, respectively. In regards to the additional experiments regarding the bulk 2PACz, shown in **Figure S6-4**, no significant spectral changes are observed for the 2PACz SAMs after deposition of 25 nm CsI or PbI_2. While some spectral features at the lower end of the valence region appear sharper after deposition of these layers, the overall spectral shape is retained, indicating only weak (if any) interactions between these materials and the underlying 2PACz substrates. These XES results indicate that an increased affinity of FAI to adhere to bulk 2PACz mediates a clear increase in crystalline perovskite growth rate.

6.3.3 Substrate dependence of perovskite crystal structure

The previous XES analysis revealed a significant shift in crystal growth parameters between bulk and monolayer 2PACz samples. Hence, we utilized XRD to gain further understanding into the differences. Although our perovskite film is more complex than a simple $FAPbI_3$, our discussion of observed crystal phases will refer to α-$FAPbI_3$ and δ-$FAPbI_3$ for simplicity. The inclusion of sufficiently low Cs and Cl content may lead to a shift in peak position[471] but will not cause peak splitting[174,472] or prevent the formation of phases analogous to $FAPbI_3$. Comparing the positions of the (0 0 1) peak for α-$FAPbI_3$ and δ-$FAPbI_3$ in the XRD spectra discussed in **Figure 6-4,** we observe shifts from the ISCD average locations of α-phase and δ-phase $FAPbI_3$. Compared to the fabricated perovskites, these shifts are from 13.9° to 14.16° and from 13.78° to 13.98° respectively, with full results presented in **Table 6-1**. As peak positions are normalised to ITO peaks to minimise differences in measurement setup, we assume such differences are can be attributed to the Cs and Cl induced peak shift.[174,471]

The change in required FAI rate could potentially lead to a change in material stoichiometry, as a higher required FAI rate will lead to a higher concentration of formamidinium and iodine within the reactor and the interplay of unincorporated FAI with the substrate is currently unknown in literature. There are two potential indicators of a change in stoichiometry: (i) a shift in the perovskite wavelength and (ii) a shift in XRD peak position. However, as seen in **Table S6-1**, comparing bulk and monolayer samples does not result in consistent correlations between peak position and perovskite bandgap. Hence, it can be assumed that perovskite composition is not is not meaningfully changing and will not impact on our XRD results.

There exist three distinct trends between XRD patterns of glass/ITO/SAM-HTL/perovskite half-stacks grown on monolayer and bulk nPACz, shown in **Figure 6-4**. First, the presence of bulk nPACz molecules suppresses the formation of δ-$FAPbI_3$ peaks (at 2Theta = 11.79°) for unannealed samples. While all monolayer samples display this initial peak, it is absent for bulk 2PACz and MeO-2PACz, indicating room temperature formation of α-$FAPbI_3$. The one deviation to this rule, bulk Me-4PACz, can be attributed to uneven growth. It is well established that solution-processed Me-4PACz exhibits non-optimal coverage,[208,347,380,473,474] and our solution-processed Me-4PACz films exhibit clear inhomogeneities. As discussed in **Chapter 5**, evaporated Me-4PACz does not exhibit such poor growth and the unannealed XRD spectrum for evaporated Me-4PACz, present in **Figure S6-6**, does not exhibit a δ-$FAPbI_3$ peak. Perovskites grown on washed monolayer solution-processed Me-4PACz films display a slight inhomogeneity to a far lower extent compared to bulk solution-processed Me-4PACz.

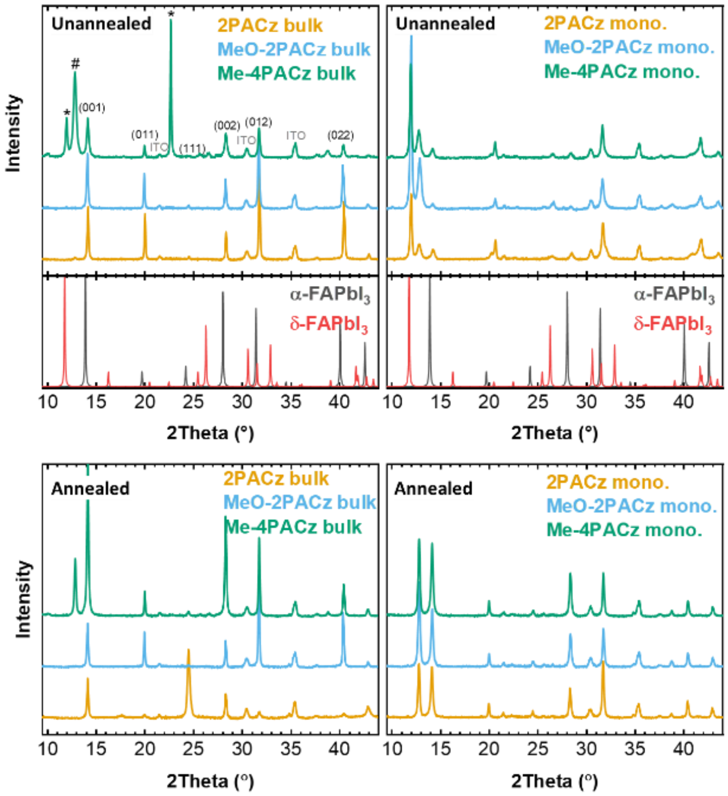

Figure 6-4 Crystal structure changes between materials and deposition methods. XRD of unannealed (*top*) and annealed (*bottom*) films, deposited at the same stoichiometry as the best-performing PSCs with bulk (*left*) and monolayer (*right*) solution-processed nPACz. In A, δ-$FAPbI_3$ peak locations are labeled with *, PbI_2 peak locations with #, ITO peaks, and important perovskite orientations are also given. We assign the Me-4PACz peak at 22.6° to δ-$FAPbI_3$, the over pronounced height of the peak is assumed due to the highly irregular surface coverage (see **Figure S6-5**). Annealed and washed data has been previously shown in **Figure 5-17** when comparing different nPACz deposition methods. Reproduced from Elsevier Inc ©2024 with permission.[221]

The next notable XRD change is a significant reduction in the relative presence of crystalline PbI_2 for both annealed and unannealed perovskites grown on bulk SAM-HTLs compared to their monolayer counterparts. The exception for Me-4PACz persists, with the previously discussed uneven coverage as a likely explanation. Abzieher et al previously attributed the presence of significant PbI_2 peaks as an indication that perovskite film growth is non-ideal in terms of organic cation adsorption.[72]

Finally, we observe significant changes in relative XRD peak intensity between monolayer and bulk nPACz materials that can be attributed to changes in preferential growth.[72] Notably, when considering monolayer samples, relative peak areas of studied peaks remain roughly equivalent, indicating comparable growth (see **Figure 6-5**). This also indicates that additional functional groups, such as methoxy- and methyl-, present on exposed carbazole for some monolayers, do not significantly impact FAI optimal rate or perovskite growth.

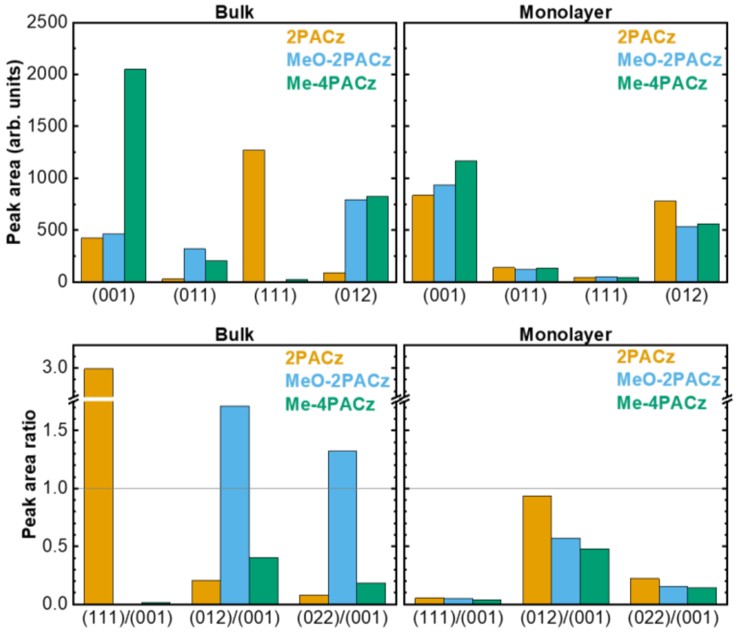

Figure 6-5 XRD analysis of perovskites on various nPACz layers. Peak area (*top*) of annealed XRD spectra shown in **Figure 6-4**, calculated using a Gaussian fit. Relative area (*bottom*) of each peak as a ratio with the (0 0 1) peak from the relevant spectra. Figure reproduced from Elsevier Inc ©2024 with permission.[221]

Conversely, bulk nPACz materials exhibit decreased (0 0 1) crystal plane intensity relative to secondary planes. The two most noteworthy peak area ratios, compared to the (0 0 1) plane are 2.99, for the (1 1 1) peak on bulk 2PACz and 1.71 for the (0 1 2) peak on bulk MeO-2PACz. Perovskite samples with a bulk Me-4PACz substrate exhibited the highest (0 0 1) peak of all samples, more than 50% larger than the next highest (0 0 1) peak, which has a significant impact on relative peak area comparisons. In general, bulk nPACz displays significant variation in peak intensity and distribution between materials, while monolayer nPCz samples remain remarkably consistent. As all materials were deposited using equimolar solutions, this inconsistency is considered to be an indicator that the density and arrangement of exposed phosphonic acid functional groups can differ between bulk materials. We propose two mechanisms, one unique to bulk Me-4PACz and the other more general, as an explanation for the differences in observed growth.

The change in expected density of bulk nPACz materials with exposed phosphonic functional groups can be explained by considering that π-π interactions between carbazole functional groups are substituent dependent.[461,462] Differences in π-π interaction strength are a potential explanation for variations in exposed phosphonic acid density, which thus explains the differences in relative FAI rate required for PSCs with bulk SAM-HTLs. The next explanation applies exclusively to Me-4PACz, which exhibits uneven coverage. Such uneven growth, caused by a non-uniform substrate, would lead to unexpected perovskite crystal phases. Substrate non-uniformity is exacerbated by the expectation that phosphonic acid functional group orientation will vary for low coverages due to the potential for titled SAM configurations, which are more likely for SAMs with increased alkyl chain length.[373] Conversely, the similar XRD spectra for monolayers indicates that additional functional groups present on exposed carbazole do not significantly impact FAI optimal rate or perovskite growth. Furthermore, the similarity also indicates comparable coverage of the ITO, as perovskite growth on ITO is expected to differ significantly from 2PACz.[72]

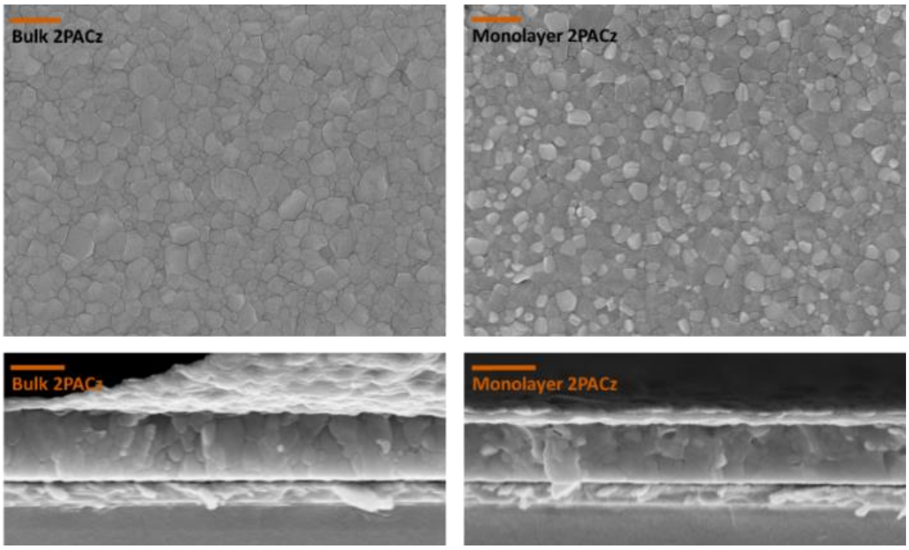

Figure 6-6 SEM of perovskites grown on bulk and monolayer 2PACz. (*Top*) Surface and (*bottom*) cross-sectional SEM of perovskites grown on bulk and monolayer 2PACz with approximate magnification of 100,000x. In each image, the scale bar corresponds to 400 nm. Figure reproduced from Elsevier Inc ©2024 with permission.[221]

Previous studies have attributed several observed changes in the XRD spectrum as indicative of a more suitable substrate for growth of co-evaporated perovskites. Specifically, they posit minimization of a residual crystalline PbI_2 signal and increases in the peak intensities of (0 1 1), (1 1 1) and (0 1 2) relative to the (0 0 1) peak.[54,72] These changes have also been previously been seen as indicative of columnar growth. Cross sectional SEM images of complete PSCs with bulk and monolayer 2PACz as the HTL, shown in **Figure 6-6**, do not indicate clear columnar growth for perovskite thin films. Accompanying surface SEM measurements allow for crystal grain size analysis similar to the work presented in **Chapter 5**. We do not observe statistically significant differences for the studied substrates, with 113.7 ± 4.3 nm for bulk and 100.0 ± 3.2 nm for monolayer 2PACz. Some grains within the monolayer substrate exhibit significantly higher SEM response, leading to brighter coloration. This phenomena has previously been associated with Pb-rich perovskite grains,[124] supporting the increased crystalline PbI_2 signal observed **Figure 6-4**.

6.3.4 Expanding on surface polarity to explain substrate dependence

Established literature provides a potential explanation for our observed change in required organic rate and crystal growth, which must be excluded in establishing our hypothesis. Abzieher *et al*. correlated surface polarity, estimated *via* H_2O droplet contact angle measurements, with preferential crystal growth during co-evaporation.[72] Lower water contact angle was associated with inferior co-evaporated perovskite growth. As a corollary, they found that substantial changes in surface polarity lead to minor changes in organic rate required for maximum PCE.

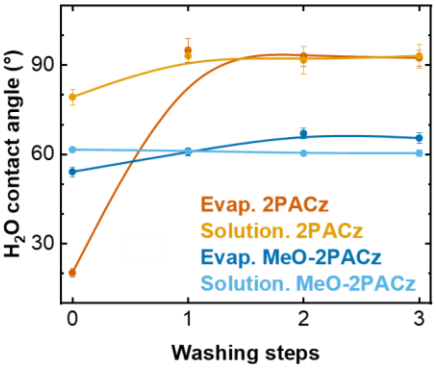

Figure 6-7 Shift in H_2O contact angle of various nPACz substrates with respect to a number of washing steps. Figure reproduced from Elsevier Inc ©2024 with permission.[221]

To further analyse washed nPACz films, **Figure 6-7** shows the water contact angle for evaporated 2PACz and MeO-2PACz with respect to a number of washing steps with ethanol. While evaporated 2PACz experiences a highly non-ideal surface initially, a single washing step brings it into the optimal regime (above 80°). Changes in solution-processed 2PACz and all MeO-2PACz are less significant. Furthermore, water contact angles are essentially unchanged between equivalent nPACz HTLs with a single washing step, and hence cannot explain the changes in interfacial properties. Notably, although MeO-2PACz exhibits a greater difference than 2PACz when comparing washed and unwashed required FAI rates in **Figure 6-2**, it observes a lower shift in contact angle when washing. This indicates that H_2O contact angle is not correlated with required FAI rate and hence excludes H_2O contact angle as a sole explanation for the observed differences in required relative organic cation rate or crystal structure.

Based on this analysis, we conclude that interfacial interactions due to exposed phosphonic acid functional groups are more significant in determining perovskite growth than surface polarity.[72] There is a strong interaction between exposed phosphonic acid functional groups, which are expected for bulk materials,[460] and the initial perovskite films. Initial growth conditions are well established to inform bulk crystal properties for co-evaporated perovskites.[72,222] Hence, this can explain the observed difference between unwashed evaporated and solution-processed films, previously attributed to hydrogen bonding to FA^+ cations.[54]

6.4 Liquid-phase ^{1}H-NMR investigation into phosphonic acid interactions

This section entails a series of ^{1}H-NMR investigations to demonstrate the interactions between phosphonic acids present in various SAM materials, and perovskite precursors. Julian Petry performed the NMR measurements.

6.4.1 Interactions between 2PACz and FAI

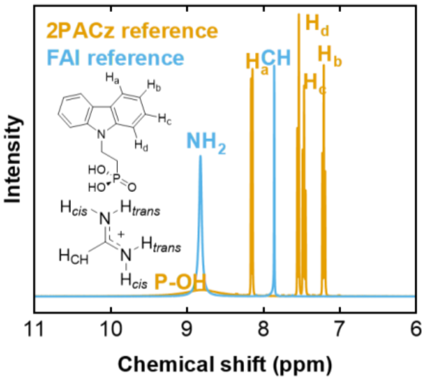

Figure 6-8 ^{1}H-NMR spectra of reference 2PACz and FAI solutions, with inset displaying each molecule and labelling relevant hydrogen. In the absence of any interaction, NH_{cis} and NH_{trans} are equivalent. Figure reproduced from Elsevier Inc ©2024 with permission.[221]

Two dominant forms of hydrogen bonding have been established between phosphonic acid functional groups and FAI.[54,458,475] (i) H···O hydrogen bonding between the phosphono oxygen of the phosphonic acid and the amidine moiety from FA^+, and (ii) OH···I hydrogen bonding between the acidic group from phosphonic acid and iodine. Liquid-state ^{1}H-NMR measurements in a deuterated dimethylsulphoxide (DMSO) solvent were conducted by Julian Petry to potentially isolate the form of this interaction for nPACz materials. Initial studies focussed on 2PACz. Reference raw spectra, along with a visualisation of each molecule of 2PACz and FAI are shown in **Figure 6-8**. In the absence of any interaction NH_{cis} and NH_{trans} from the FAI molecule are equivalent, leading to the single ^{1}H-NMR peak. Each spectrum represents 0.013 M solutions of each material. Peak positions were determined relative to the signal of residual solvent at 2.50 ppm. When molar ratio is mentioned in **Section 6.4**, it will refer to the ratio of the nPACz material to the other studied material.

Introducing equimolar 2PACz to a FAI solution induces a number of changes in both spectra, as shown in **Figure 6-9**. Among the FAI peaks, labelled in blue, protons attributed to the amidine moiety split into two doublets. Julian Petry attributes this splitting to the formation of a delocalized double bond. This will planarize the molecule, inhibiting rotation of FA^+ amidine groups. Interactions with the CH proton occur through vicinal ^{3}J cis and trans coupling (coupling constant J_{trans} = 15.2 Hz) will disrupt the previously equivalent chemical environment for amidine protons.[476] The converse interaction with the now inequivalent amide protons (coupling constants J_{cis} = 6.4 Hz and J_{trans} = 15.1 Hz) splits the CH proton signal into a triplet of a triplet (tt). Such splitting has been previously described in literature, with some publications attributing it to the introduction of a Lewis acid.[475,477]

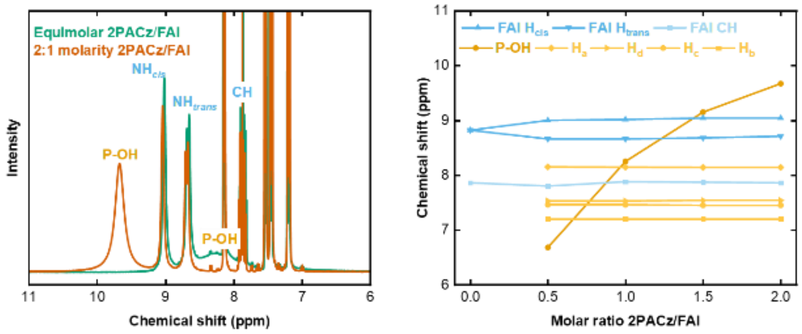

Figure 6-9 ^{1}H-NMR spectra of 2PACz and FAI solutions with increasing 2PACz molarity. (*Left*) Equimolar and 2:1 molar ratio solutions of 2PACz and FAI with labelling of relevant hydrogen. (*Right*) Chemical shift of each identified peak with respect to concentration for a varied 2PACz / FAI molar ratio. Figure reproduced from Elsevier Inc ©2024 with permission.[221]

Concurrent changes occur in the 2PACz spectra, upon the introduction of FAI the peak decreases from its reference position of 8.80 ppm in Figure 6-8. Performing a concentration series, shown in **Figure 6-9**, by varying 2PACz molar concentration from 0 M to 0.026 M (in 0.0065 M or 0.5 molar ratio steps) reveals a consistent increase with increasing 2PACz concentration from 6.68 ppm for a molar ratio of 0.5 to 9.67 with a molar ratio of 2.0. Despite this clear shift in the phosphonic acid peak position with respect to concentration, there is no complementary shift in the FAI cation peak positions beyond the initial splitting. This indicates that hydrogen bonding between FA^+ and the phosphonic acid functional group of 2PACz is not observed in solution, and that OH···I bonding is occurring.[478] Were this the case, the formation of an equivalent hydrogen bond with the halide portion of other organic cations, such as MAI and GAI, would be possible.

6.4.2 Concentration series to determine bonding mode

To derive a material-dependent trend for bonding strength, and to evaluate the hypothesis at the end of **Section 6.4.1**, several liquid phase series were conducted, presented in **Figure 6-10**. The first series investigated interactions between common organic perovskite cations (MAI, FAI, and GAI), with 2PACz as a constant SAM-HTL. A second series compared interactions between FAI with three phosphonic acid containing SAM-HTLs (2PACz, MeO-2PACz and Me-4PACz). Due to peak broadening, overlap and a relatively low peak intensity for Me-4PACz, the potential error in determining the peak position for low concentrations is too substantial for meaningful analysis. Even if the precise peak location is not provided for low concentrations, a concentration dependent chemical shift remains apparent for Me-4PACz. To demonstrate that such effects are not unique to organic cations, a final series using the inorganic cation PbI_2 was produced. For all series, cation concentrations were maintained at 0.13 M, while nPACz concentrations were varied from 0 M to 0.26 M. ^{1}H-NMR spectra associated with each series are presented in the Appendix, **Figure S6-7**.

In each spectral variation there is no complementary shift in the organic cation peak positions. Furthermore, when varying organic cations, peak shift magnitudes are roughly equivalent between studied cations, reinforcing the observation made in **Section 6.4.1** that observed hydrogen bonding in solution is between the halide portion of these materials and the phosphonic acid.[478] This result also indicates that the observed interactions, and changes in optimal organic cation rate or crystallization, are potentially not exclusive to FAI.

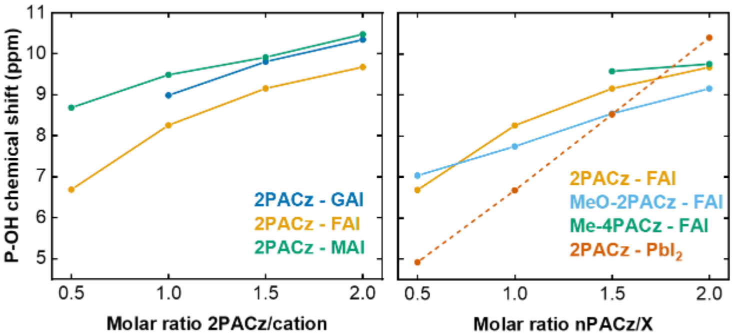

Figure 6-10 ^{1}H-NMR chemical shifts for P-OH group in various nPACz solutions combined with various halide contributors. (*Left*) Chemical shift of POH group peak with respect to concentration for a varied 2PACz / XAI molar ratio for MAI, GAI and FAI. (*Right*) Chemical shift of P-OH group peak with respect to concentration for a varied nPACz / FAI molar ratio for 2PACz, MeO-2PACz and Me-4PACz plus varied 2PACz / PbI_2 molar ratio. Figure reproduced from Elsevier Inc ©2024 with permission.[221]

This study using the alternative nPACz materials of MeO-2PACz and Me-4PACz (see **Figure 6-10**) supports this hypothesis and indicates that the hydrogen-bonding strength is approximately equivalent between nPACz materials. Further interactions of MeO-2PACz through the methoxy groups can be excluded, as no significant shifts of the corresponding signal were observed. These results support the observed similarity in crystal growth between monolayers reported in **Section 6.3.3**.

The final presented analysis is of varying 2PACz / PbI_2 molar ratios, which result in comparable peak shifts, indicating that such interactions are not exclusive to organic precursors. Due to the dual halide nature of PbI_2, the required concentrations of PbI_2 were calculated for the whole molecule and not in respect for the iodide fraction. The observed shift extent differs slightly in intensity from the baseline 2PACz / FAI system, which is also shown. This effect can be attributed to additional interactions of the solvent d^6-DMSO with lead ions which might perturbate the system. As signal shifts are within the expected range we assume that the interaction strength is independent from the iodide source.

Despite these results, nPACz / PbI_2 interactions are not expected to change perovskite formation. The influence of substrate on organic sources is attributed to their partial of full dissociation when sublimating and eventual recombining on the substrate, making their deposition rate highly substrate dependent.[72,75,465,479] Inorganic precursors sublimate in a directional manner and their sticking coefficients are less susceptible to substrate variations.[72,480,481] Relevant XES experimental results, presented in **Section 6.3.2**, did not present evidence of significant PbI_2-2PACz interactions. If PbI_2 interactions were significant, the similarity in interaction mechanism means their impact would merely be to reduce the substrate impact on effective FAI rate.

The strong evidence of OH···I hydrogen bonding between the acidic group from phosphonic acid and iodine, independent of the studied SAM or cation, is sufficient to provide precursory evidence that such interactions occur. However, the limitations of liquid-phase ^{1}H-NMR, means additional studies are required to definitively preclude other potential causes for such shifts, as will be briefly discussed in **Section 6.4.3**.

6.4.3 Limitations of liquid-phase ^{1}H-NMR results

While liquid-phase ^{1}H-NMR results indicate an interaction between 2PACz and the halide component of the studied cations is present, there exists several limitations to these results, which will be discussed in the following.

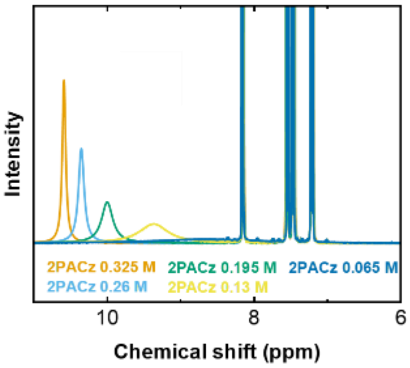

Figure 6-11 ^{1}H-NMR spectra of 2PACz solutions with varying 2PACz concentrations. Figure reproduced from Elsevier Inc ©2024 with permission.[221]

First, the liquid-phase ^{1}H-NMR results can only consider each precursor independently, instead of full perovskite interactions. NMR investigations of a combined FAI/PbI_2 system is inherently challenging due to many overlaying interaction pathways. FAI and DMSO are both able to bond to PbI_2 through hydrogen bonding and electrostatic interactions respectively.[482] Next, the quantitative assessment of bonding strength is not possible. In the absence of a halide source, concentration variation of 2PACz will lead to a shift in the phosphonic acid peak, as shown in **Figure 6-11**. Julian Petry attributes this shift to interactions of phosphonic acids in non-polar and aprotic solvents such as d^6-DMSO, which were employed for this study.[483]

Furthermore, the reference 2PACz peak position of 8.80 ppm was inconsistent with the 2PACz/FAI trend shown in **Figure 6-9**. Julian Petry concludes that 2PACz alone is not a suitable reference to be compared to the more complex 2PACz/FAI system as different interaction pathways and strengths are relevant in each case. Hence, the strength of hydrogen bonding between phosphonic acid functional groups and halides of organic cation precursors cannot be precisely quantified by liquid-phase ^{1}H-NMR. While these liquid-phase results are thus qualitative rather than quantitative, this does not invalidate the observation that hydrogen bonding is not observed between phosphonic acid and the organic portion of the cation precursors. Intermolecular interactions stem primarily from hydrogen bonding of free phosphonic acid functional groups with halide ions, which will be confirmed in **Section 6.5**.

6.5 Atomistic-level insights from DFT calculations

6.5.1 Recreation of α-$FAPbI_3$ and δ-$FAPbI_3$ unit cells

The presence of an interaction between interfacial phosphonic acid functional groups and co-evaporated perovskites can be considered established. However, additional knowledge of the precise form necessitates alternative techniques. To gain atomistic-level insights into this interaction and establish a viable hypothesis for whether such interactions can form the basis for the experimental differences observed between substrate, Dr. Abderrezak Torche, Dr. Michelle Ernst and Dr. Ganna Gryn'ova from Heidelberg University utilized density functional theory to model these systems.

This modelling utilized the PBE-D3 method of dispersion-corrected density functional theory, which is among the most commonly used approaches for the modelling of materials properties. PBE-D3 affords accuracy comparable to that of density functionals from higher rungs of the Jacob's ladder, a common term to describe the general performance of DFT methods.[484] It accurately reproduces qualitative trends from high-level coupled cluster computations, and can qualitatively describe the phase transitions in halide perovskites.[485,486] This method is typically used as a reference for benchmarking the performance of lower-level theories.[487] Hence, it can be considered a suitable method for analyzing the observed interaction.

Due to the high computational load of performing calculations on complex perovskites, our collaborators chose $FAPbI_3$ for a simplified perovskite model (as FA^+ is the dominant cation in the investigated perovskite). For similar reasons, they constrained his investigation into SAM-HTLs to 2PACz. Based on the similarity between XRD spectra for studied monolayer substrates shown in **Figure 6-4 and 6-5**, they assume that additional functional groups on the carbazole, or variations in alkyl chain length, will not significantly impact the studied interactions and were thus not required for *in silico* models. They consider two potential $FAPbI_3$ unit cells, the photo-inactive hexagonal P6mmc phase (δ-$FAPbI_3$), and the photoactive cubic Pm3m phase (α-$FAPbI_3$). While $FAPbI_3$ possesses potential additional photoactive phases, the orthorhombic β-$FAPbI_3$ and tetragonal γ-$FAPbI_3$ to be precise, their formation requires temperatures below 153 K and 93 K, respectively, which are incompatible with standard perovskite fabrication or operation.[478]

Literature has extensively established the role of FA$^+$ cation orientation on the stability of α-FAPbI$_3$ and δ-FAPbI$_3$ perovskite phases.[478,488,489] The large unit cell of δ-FAPbI$_3$, with a lower energetic cost of encapsulating the organic FA$^+$ cation, is more stable at room temperature. C···I and NH$_2$···I interactions fix the FA$^+$ cation position within the δ-FAPbI$_3$ unit cell, and hence the associated entropic gain is insignificant.[490] While less stable at room temperature, free rotation of the FA$^+$ cation within α-FAPbI$_3$ causes a positive correlation between the entropy of this phase and temperature, resulting in this phase becoming more stable than δ-FAPbI$_3$ at temperatures above ~430 K.[489]

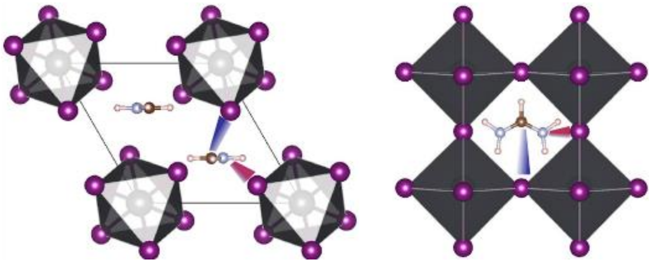

Figure 6-12 Visualization of studied FAPbI$_3$ perovskite phases under relaxed conditions. (*Left*) δ-FAPbI$_3$ and (*right*) α-FAPbI$_3$ visual representations with magenta and blue lines indicating of C···I and NH$_2$···I interactions respectively. Simulations performed by collaborators from Heidelberg University. Figure reproduced from Elsevier Inc ©2024 with permission.[221]

Similar to the findings of Zheng *et al.*,[489] when the positions of FA$^+$ cations within the cubic and hexagonal phases were optimized, free FA$^+$ ions position themselves in the midplane of the α-FAPbI$_3$ unit cell, oriented along the plane to minimize C···I and NH$_2$···I contacts. A more complex arrangement forms for δ-FAPbI$_3$, featuring ribbons of coordinated PbI$_3$ with fixed orientation interstitial FA$^+$ between parallel ribbons to minimize C···I and NH$_2$···I contacts. The encapsulation of FA$^+$ cations reduces unit cell strain, resulting in a free energy difference of 279 meV under bulk conditions and room temperature. A visualization of these geometries and the associated interaction modes is present in **Figure 6-12**.

6.5.2 Thin slab conditions

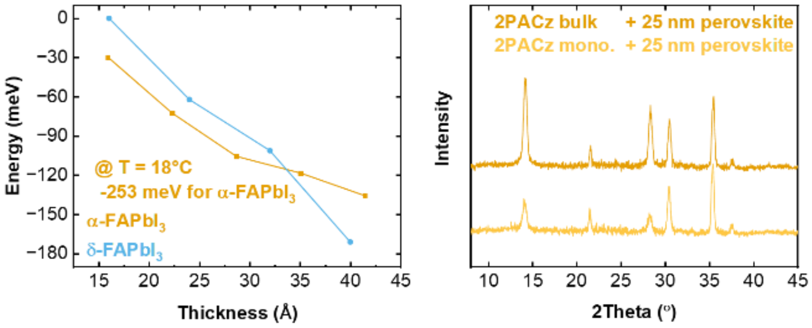

Figure 6-13 Stabilization of thin perovskite slabs deposited on 2PACz. (*Left*) Interaction energies of α-FAPbI$_3$ and δ-FAPbI$_3$ slabs, determined by energy per unit cell as a function of slab thickness. These values do not include entropic contribution or surface functionalization. (*Right*) Unannealed perovskite thin films grown on bulk or monolayer 2PACz exhibiting exclusively the α-FAPbI$_3$ phase at room temperature. Simulations performed by collaborators from Heidelberg University. Figure Reproduced from Elsevier Inc ©2024 with permission.[221]

With a recreation of unit cells established, and conforming to expected results, our collaborators from Heidelberg University next considered thin slab conditions. They simulated a series of perovskite slabs up to thicknesses of 50 Å, with all surface interactions absent to allow the structures to fully relax. It is possible to consider perovskite growth as a function of unit cell layers, or as a function of overall thickness. They considered comparing equivalent thickness as a better method to evaluate phase stability during the initial perovskite growth. The choice of focusing on thickness and variation in unit cell size between α-$FAPbI_3$ and δ-$FAPbI_3$ necessitates interpolation for intermediary thicknesses for **Figure 6-13**.

For equivalent slab thicknesses below 35 Å, in the absence of entropic contributions, α-$FAPbI_3$ is more stable than δ-$FAPbI_3$, with an energy difference of 30 meV at the lowest simulated thickness of ~16 Å. This difference between bulk and thin slab stability can be attributed to the fact that the α-$FAPbI_3$ surface energy is lowered than δ-$FAPbI_3$ in the thin slab limit. Furthermore, when considering entropic contributions, they will favour α-$FAPbI_3$ due to the free movement of interstitial FA^+, which is restricted in δ-$FAPbI_3$. At 18°C these effects will contribute ~-253 meV at 18 °C. The resulting enhanced stability are expected to increase the maximum thickness at which α-$FAPbI_3$ is the more stable phase. XRD spectra of ~25 nm thick perovskite films support these findings. For monolayer 2PACz, which is not expected to experience meaningful surface contributions, films exhibit pure α-$FAPbI_3$ growth in the thin film region even without an annealing step. As a corollary, co-evaporated thin films grown on bulk 2PACz exhibit higher XRD peak intensity than their monolayer counterparts, providing further evidence for the enhanced crystalline perovskite signal in the presence of exposed phosphonic acid functional groups, which will support the results presented in the following section.

6.5.3 Interfacial interactions between phosphonic acids and perovskites

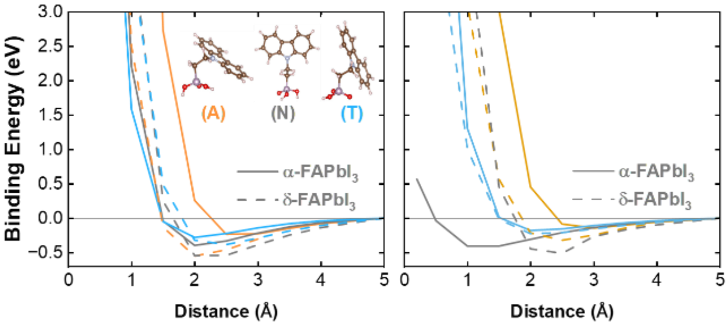

Figure 6-14 Binding energy of various 2PACz conformations as a function of the distance between substrate and material for both potential phases of (*left*) FA^+-terminated and (*right*) Pb -terminated $FAPbI_3$ perovskites. Inset (*left*) are possible 2PACz conformations. In these simulations, phosphonic acid is assumed to be directly exposed to the perovskite surface, corresponding to a bulk film. Simulations performed by collaborators from Heidelberg University. Figure reproduced from Elsevier Inc ©2024 with permission.[221]

The theoretical results presented in **Section 6.5.2** suggest that, while α-phase is more stable during early crystal growth, δ-$FAPbI_3$ is thermodynamically preferred in the bulk limit. However, α-$FAPbI_3$ is the only experimentally observed crystalline phase in unannealed perovskite films deposited on bulk nPACz, as outlined in **Figure 6-6**. To explain this observation, our collaborators from Heidelberg University tested if the presence of phosphonic acid promotes α-$FAPbI_3$ growth over δ-$FAPbI_3$.

DFT computations revealed three potential configurations of the 2PACz molecule, termed: A – anionic, N – neutral, and T – trans-conformation, and shown as an inset in FIGURE 6-14A. For all conformations, computed binding energies with FA^+- and Pb-terminated perovskites were found to be relatively similar for α-$FAPbI_3$ and δ-$FAPbI_3$. The strongest interactions occur at distances of ~2 Å, which is commensurate with non-covalent interactions, such as hydrogen bonding, rather than covalent bonds. Computed maximum non-covalent interaction (NCI) energies, presented in **Table 6-1**, did not differ significantly between each perovskite phase, indicating comparable interaction strength between the 2PACz and the perovskite surface for both FA^+- and Pb-terminated slabs. Remaining associated data points for these plots are present in the appendix, **Table S6-2 and S6-3**.

Table 6-1 Maximum NCI interaction energy for z-direction variation of 2PACz interacting with each studied perovskite phase (α-$FAPbI_3$ and δ-$FAPbI_3$), surface (FA-terminated and Pb-terminated) and all calculated 2PACz conformations (A, N and T). Simulations performed by collaborators from Heidelberg University. Table reproduced from Elsevier Inc ©2024 with permission.[221]

	A (α-FAPI)	N (α-FAPI)	T (α-FAPI)	A (δ-FAPI)	N (δ-FAPI)	T (δ-FAPI)
FA^+-term.	-0.23343	-0.3949	-0.27978	-0.55062	-0.54375	-0.38349
Pb-term.	-0.14252	-0.40603	-0.17905	-0.32018	-0.51087	-0.22453

To more precisely define the diverse potential interaction modes between 2PACz and perovskite surfaces, our collaborators scanned interaction energy profiles by laterally shifting the 2PACz molecule at a fixed 2 Å distance above the 3×3 (0 0 1) perovskite surface, as shown in **Figure 6-15**.

These results computed maximum energies of 470 meV for α-$FAPbI_3$ and 720 meV for δ-$FAPbI_3$, indicating that phosphonic acid interactions are an insufficient explanation for the change in bulk perovskite phase. While α-$FAPbI_3$ is thermodynamically preferred during initial film formation, δ-$FAPbI_3$ is both the dominant phase in the bulk limit and more strongly stabilized by interactions with the phosphonic acid moieties of 2PACz. When visualizing the geometries corresponding to minima for scanned interaction energies, the geometry minimizes the distance between the OH group of the phosphonic acid in 2PACz and surface iodine anions of the perovskite. This supports our findings in **Section 6.4**, indicating that bonding primarily occurs between phosphonic acid functional groups and the halide component of organic cations and provides additional evidence that halide interactions are more relevant than cation interactions such as FA^+ or Pb^{2+}.

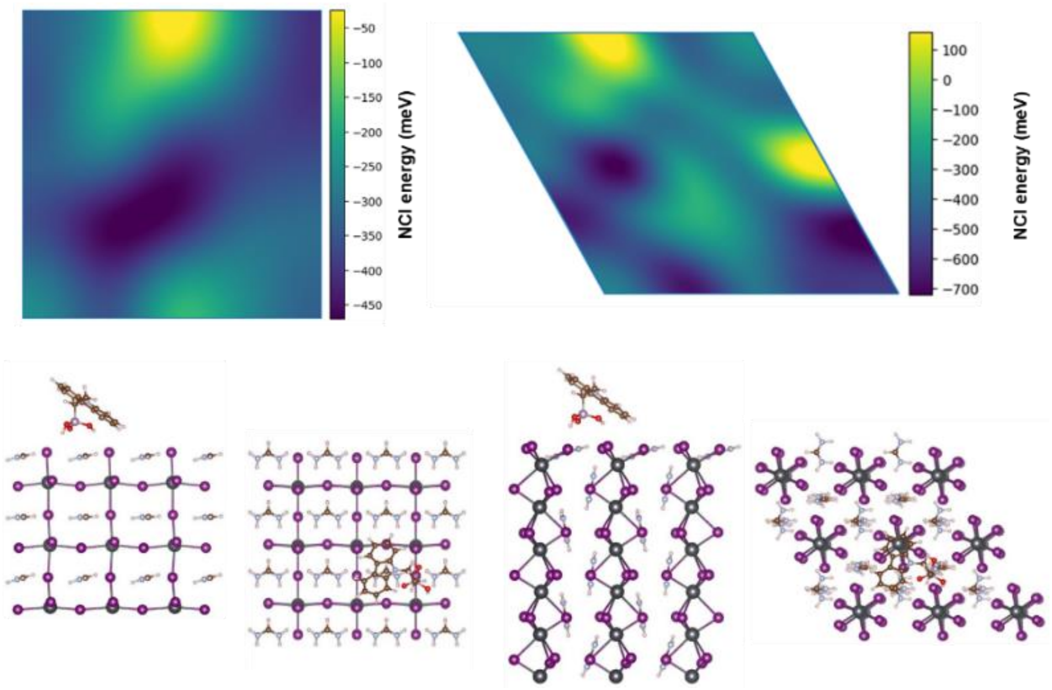

Figure 6-15 DFT visualizations of interactions between nPACz and perovskites. (*Top*) Computed non-covalent interaction (NCI) energies for laterally shifted 2PACz, fixed at a 2 Å distance from the surface of α-FAPbI$_3$ (*left*) and δ-FAPbI$_3$ (*right*). Geometries corresponding to the NCI energy minima of 2PACz on α-FAPbI3 (*bottom-left*) and δ-FAPbI3 (*bottom-right*) surfaces (side and top views). Simulations performed by collaborators from Heidelberg University. Figure reproduced from Elsevier Inc ©2024 with permission.[221]

6.5.4 Phase stabilisation *via* kinetic trapping

Our collaborators from Heidelberg University propose that the concepts of kinetic and chemical trapping, visualized in **Figure 6-16**, comprise explain the experimentally observed preference for the α-FAPbI$_3$. Specifically, the entropic contributions discussed in **Section 6.5.2**, combined with the lowered surface energy outlined in **Section 6.5.3**, mean that α-FAPbI$_3$ is formed initially and preferentially to δ-FAPbI$_3$.[488,491] According to Chen *et al.*,[488,491] cubic and hexagonal space groups lack a simple group/subgroup connection, and transitions between each phase necessitates complex movements and Pb–I bond breaking and forming. Therefore, such a phase transition first requires dissociation of the perovskite film from the 2PACz molecules. Interaction with free phosphonic acid moieties introduces a passivation barrier for the conversion of α-FAPbI$_3$ into δ-FAPbI$_3$ when transitioning from thin film to bulk limit as a form of chemical trapping.

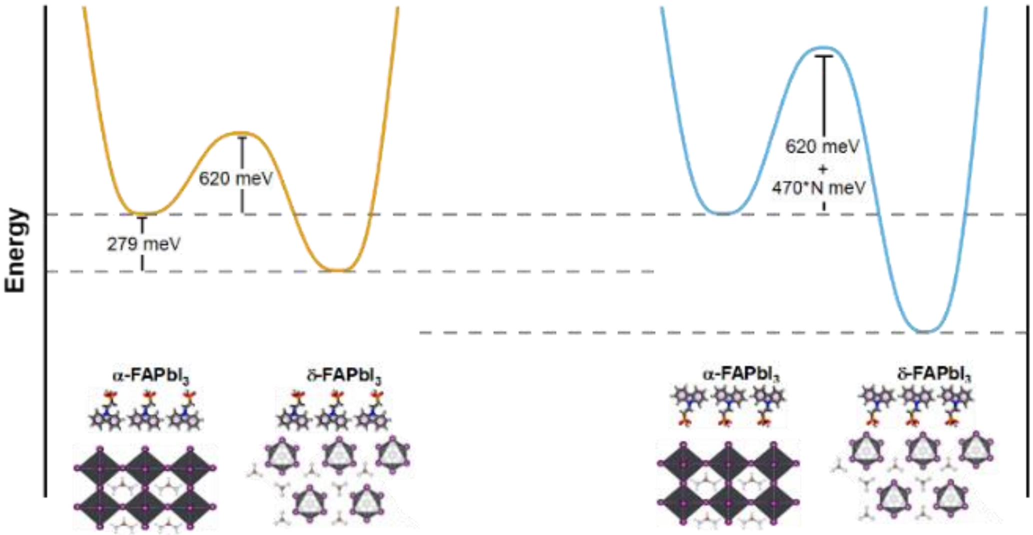

Figure 6-16 Energy diagram representation of kinetic trapping for α-FAPbI$_3$ stabilization. Activation energy of phase transitions in the absence of phosphonic acid functional groups were taken from Chen et al.[488,491] Figure reproduced from Elsevier Inc ©2024 with permission.[221]

The height of the corresponding passivation barrier can be approximated as N*470 meV, where N is the maximum number of phosphonic acid functional groups per 3×3 (0 0 1) surface. Interfacial passivation strategies have been previously shown to enhance the stability of α-FAPbI$_3$ and reduce the formation of δ-FAPbI$_3$ through similar surface functionalization and entropic stabilization methods.[490] Furthermore, the relatively low growth rate of co-evaporated perovskites compared to solution-processed or sequentially evaporated films make them more vulnerable to this trapping effect.

The combined results from **Sections 6.3 - 6.5** can lead to an explanation for the lower FAI rates required for optimal co-evaporated perovskites on SAM-HTLs with exposed phosphonic acid functional groups. The investigated interactions covered in these sections, between FAI and phosphonic acid functional groups enhances FAI sticking. This results in less FAI required to form the initial perovskite layer, as mentioned in **Section 6.3**, while perovskite formation under exposure to excess cations has been correlated to increased formation of α-FAPbI$_3$ in literature.[492] This initial perovskite layer is more stable and crystalline, mediated by NCIs between the perovskite and exposed phosphonic acid functional groups as discussed in **Sections 6.5.2 and 6.5.3**. Abzieher *et al.* and Yan *et al.* have demonstrated that initial perovskite growth conditions propagate during film deposition to control bulk properties.[72,222] In the similar manner, combined with kinetic trapping, our initial α-FAPbI$_3$ will persist into the bulk, continuing to exhibit increased FAI uptake. The presented results reveals how functional groups can be a driver for initial growth conditions that radically change film formation.

6.6 Interfacial interactions and resultant device properties

To determine the tangible impact these interactions will have on PSCs, we compare the maximum achievable PCEs employing various nPACz SAM-HTLs. Some results in this section are repeated from **Chapter 5** where relevant, but expanded on in the context of comparing bulk and monolayer nPACz SAM-HTLs rather than merely evaporated and solution-processed.

6.6.1 Substrate dependent photovoltaic properties

We start by comparing maximum achievable PSC PCEs employing various 2PACz layers. *J-V* curves and associated MPP-tracking of champion PSCs for bulk and monolayer, evaporated and solution-processed 2PACz are presented in **Figure 6-16**, with monolayer results a repeat of those already shown in **Chapter 5**. Statistics for each shown configuration are presented in **Table 6-2,** with equivalent tables for MeO-2PACz and Me-4PACz in the appendix (**Table S6-4 and S6-5**).

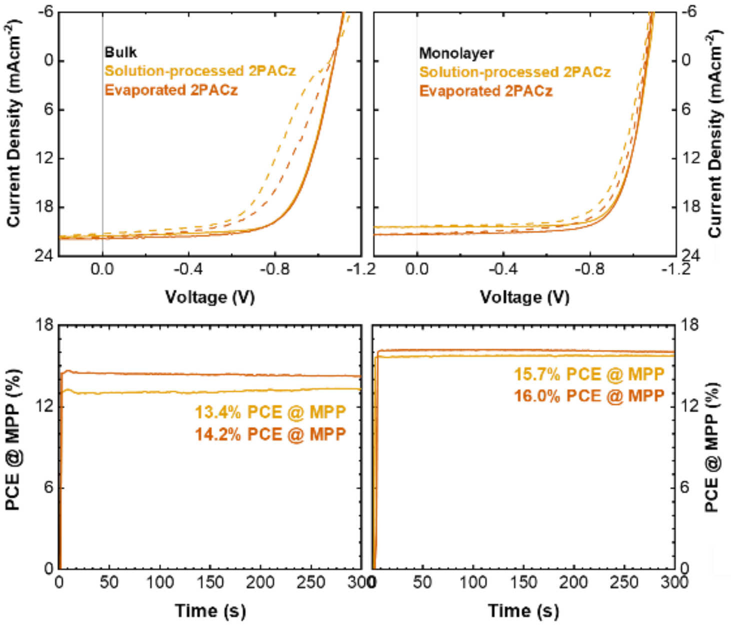

Figure 6-17 Champion PSCs for all studied variation of 2PACz SAM-HTLs. *J-V* curves of PSCs utilizing bulk (*top-right*) and monolayer (*top-left*) 2PACz, with corresponding MPP measurements (*bottom-right*) and (*bottom-left*) respectively. Figure reproduced from Elsevier Inc ©2024 with permission.[221]

Integrated J_{SC} derived from EQE show higher currents for monolayer and lower currents bulk 2PACz from both evaporated and solution processed sources. However, these values are within 10% of the *J-V* values, which is considered reasonably accurate due to differences in measuring conditions.[268] Notably, PCE at MPP of the best PSCs with bulk films is ~1.5 - 2% absolute lower as compared to monolayer films, as shown in **Figure 6-17**. This could be attributed to a higher series resistance and possibly enhanced magnitude of ion migration, in line with the significantly larger hysteresis for bulk 2PACz samples.[493,494]

Table 6-2 *J-V* and EQE statistics for the optimum perovskite of each configuration with 2PACz SAM-HTLs. The average value is shown in brackets and the integrated J_{SC} derived from EQE of the champion PSC provided in bold.

	PCE (%)	FF	V_{OC} (V)	J_{SC} (mA cm^{-2})	
				Solar simulator	EQE
Evaporated monolayer	16.7 (16.7) 15.7 (15.6)	0.74 (0.74) 0.71 (0.70)	1.08 (1.07) 1.07 (1.07)	21.4 (21.1) 21.3 (21.0)	21.6
Solution monolayer	17.0 (16.4) 15.7 (14.9)	0.78 (0.76) 0.73 (0.71)	1.07 (1.0) 1.06 (1.05)	20.6 (20.1) 20.4 (20.0)	22.1
Evaporated bulk	16.0 (15.3) 13.6 (13.3)	0.69 (0.67) 0.6 (0.59)	1.07 (1.06) 1.05 (1.04)	21.9 (21.8) 21.8 (21.6)	20.2
Solution bulk	16.2 (15.2) 12.5 (11.8)	0.70 (0.68) 0.56 (0.54)	1.07 (1.04) 1.06 (1.03)	21.6 (21.4) 21.5 (21.3)	20.7

Expanding upon our results from **Chapter 5**, we find that, when the FAI rate is suitably tuned, both monolayer and bulk evaporated 2PACz yield comparable maximum PCE in the reverse scan direction as compared to their solution-processed counterparts. While PSCs with bulk 2PACz substrates exhibit greater overall differences in PV parameters between evaporated and solution-processed nPACz, these differences can be attributed as being due to either: i) variations in the bulk SAM-HTL thickness considering the lack of accurate measurement methods for the thickness of ultra-thin solution-processed layers, differences in the coverage and/or ii) changes in orientation of the bulk component. The difference in required FAI rate to achieve an optimum perovskite between evaporated and solution-processed nPACz layers provides additional evidence for a difference in some combination of bulk properties. We assume comparable ITO surface coverage between deposition methods due to the similar PSC performance and interfacial properties presented in **Chapter 5**.[261] However, we have no method of determining if the bulk component coverage is also as comparable between evaporated and solution-processed layers. EQE measurements are provided in the Appendix, in **Figure S6-8**, along with *J-V* for optimized PSCs using MeO-2PACz and Me-4PACz as a SAM-HTL, in **Figure S6-9**. Notably, bulk MeO-2PACz samples do not exhibit the same high hysteresis displayed in bulk 2PACz samples. As the evaporated layer thickness and solution concentration was equivalent between nPACz materials, this indicates that the high hysteresis is, in some way, material dependent.

6.6.2 Substrate dependent interfacial properties

To obtain a deeper understanding of the interfacial properties for co-evaporated perovskites grown on SAM-HTLs with and without exposed phosphonic acids, we next performed extensive analysis on a series of half-stacks ITO/nPACz/perovskite. Our half-stacks refrain from introducing an electron transport layer (ETL) to exclude the known substantial non-radiative recombination losses that occur at the perovskite/ETL interface when employing C_{60}.[495] All analysis in this section was performed on optimal substrates, those corresponding to the highest PCE devices. A short analysis of some properties in non-optimal substrates is presented in **Section 6.6.3**.

Bulk evaporated and solution-processed 2PACz obtains implied V_{OC} values of 1.06 V and 1.07 V, compared to 1.03 V and 1.04 V for the respective monolayer counterparts, as shown in **Figure 6-18**, with PLQY data and plots used to calculate ideality factors shown in **Figure S6-10**. These implied V_{OC} values are indicative of a slight change in surface recombination properties that persists independent of the deposition method. Expanding the comparison of bulk and monolayer implied V_{OC} to include MeO-2PACz and Me-4PACz show a persistent trend of increased implied V_{OC} for bulk SAM-HTLs. Ideality factors for optimized monolayer evaporated and solution-processed 2PACz are 1.46 and 1.45, respectively, while the bulk ideality factors are both 1.47, providing no evidence of a significant change in the recombination mechanism at the HTL/perovskite interface between bulk and monolayer SAM-HTLs.

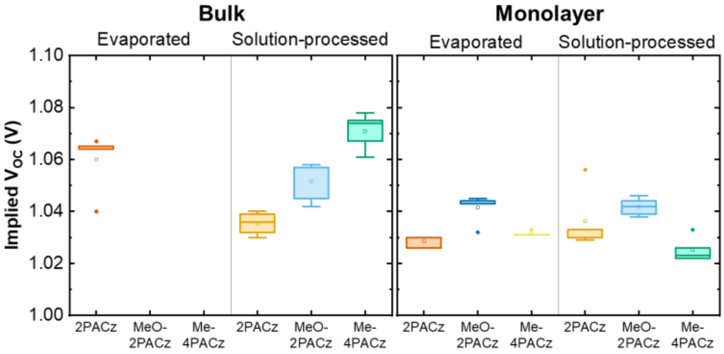

Figure 6-18 Implied V_{OC} for optimized perovskite layers deposited on all studied nPACz coated substrates. Implied V_{OC} for bulk (left) and monolayer (right) nPACz deposited via solution processing or evaporation. Co-evaporated bulk samples only display results from 2PACz, as optimal MeO-2PACz and Me-4PACz stoichiometries were not achieved over the course of the series. Figure reproduced from Elsevier Inc ©2024 with permission.[221]

TrPL spectra, used in this work to determine charge carrier lifetimes, are biphasic with a relatively high weighting of Shockley-Read-Hall lifetimes,[496] making binomial fits to accurately determine both phases exceptionally difficult. This initial decay phase, with an associated lifetime τ_1, is associated with the monomolecular non-radiative filling of surface trap states.[164,497] Hence, a large τ_1 is commonly associated with a high trap state density.[497,498] Typical perovskite analysis using TrPL will exclude charge transport layers to minimise the influence of τ_1.[497] However, our desire to specifically analyse substrate dependent growth precludes such solutions. To obtain information on the lifetime of the bimolecular direct recombination term (τ_2), attributed to the second phase of the TrPL spectrum,[164,497,498] we perform a monoexponential fit of a truncated region of decay data at later times. A biexponential fit is also attempter. However, for the overwhelming majority of samples this fit does not accurately describe the decay curve in the region where τ_2 is dominant. Hence, all quoted lifetimes refer to the results obtained from the monoexponential fit.

Bulk solution-processed SAM-HTLs, shown in **Figure 6-19**, exhibit high τ_2 lifetimes, ranging from 604.3 ± 1.6 ns for Me-4PACz to 1585.8 ± 12.9 ns for MeO-2PACz. Respective monolayer SAM-HTLs, shown in **Figure 6-19**, exhibit lower lifetimes from 121.6 ± 0.5 ns for MeO-2PACz to 227.7 ± 1.4 ns for 2PACz. Monolayer samples show lower variation between SAM-HTLs, with a coefficient of variation of 0.255 for monolayer samples and 0.368 for bulk samples. Including evaporated monolayers into the calculation, presented in **Figure S6-11**, increases the monolayer coefficient slightly to 0.322, still well below the evaporated coefficient. These results are in line with two previously observed results. The comparison between bulk and monolayer samples is in agreement with the previously mentioned higher implied V_{OC} values for bulk SAMs, indicating that a thicker SAM layer more efficiently suppresses non-radiative recombination at the HTL/perovskite interface. Meanwhile, the reduced variability of monolayer samples is in agreement with our observed similar monolayer behaviour, first discussed in **Section 6.3.3**.

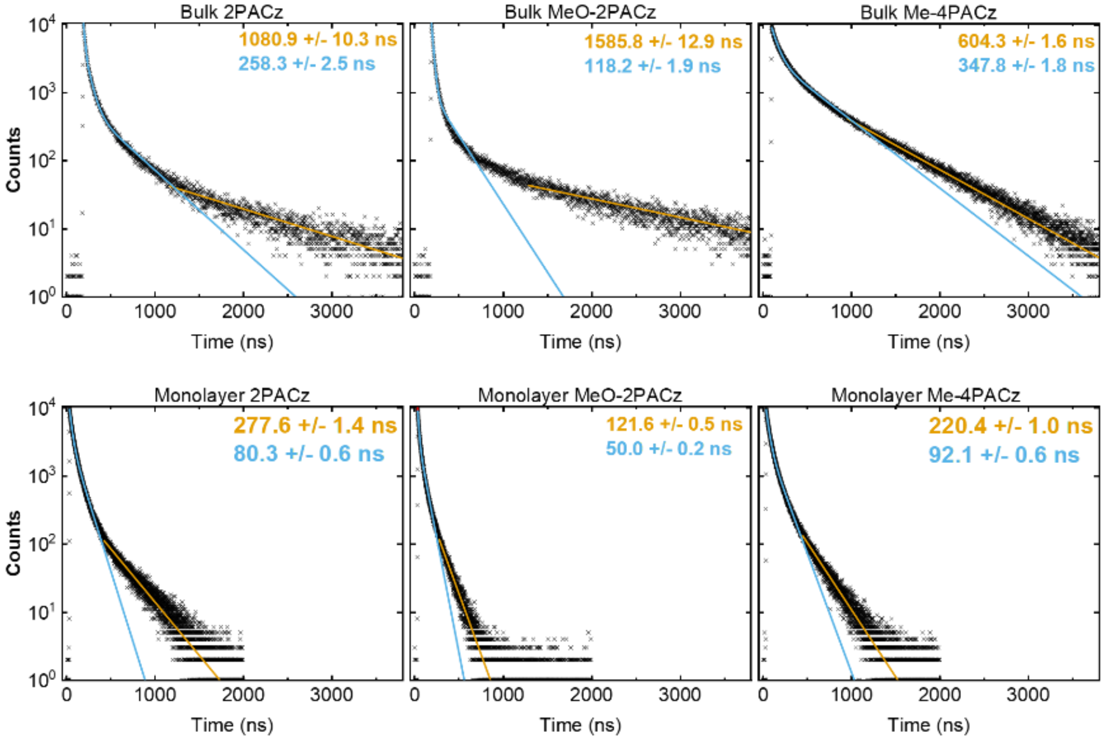

Figure 6-19 TrPL curves for optimized perovskite layers deposited on studied solution-processed nPACz coated substrates. TrPL of best-performing ITO/SAM-HTL/perovskite half-stacks for both bulk (*top*) and monolayer (*bottom*) nPACz to determine charge carrier lifetimes. Data is plotted with biexponential (blue) and truncated monoexponential (orange) fits. The inset shows the resultant monoexponential (orange) and biexponential (orange, weighted average) lifetimes (see **Table S6-2**). Errors represent one standard deviation of the lifetime. Figure reproduced from Elsevier Inc ©2024 with permission.[221]

6.6.3 Impact of stoichiometry on material and device properties

As our analysis included a variation in stoichiometry through FAI rate variation, we have the opportunity to observe how structural properties evolve with respect to stoichiometry, both under-stoichiometric (with relative excess PbI_2) and over-stoichiometric (with a relative excess of FAI). Such analysis has been reported for solution-processed perovskites, which provides a useful reference.[499] However, potential differences with our results must be considered due to the different methods of perovskite formation.

The analysis considered in this section will not address the performance variation covered in **Section 6.3.1**, except when designating the 'optimum' perovskite. Within this section a specific colour code will be utilized. Measurements of samples corresponding to maximum PCE will be black coloured. Increased PbI_2 compared to the optimum is denoted by a red colour and increased FAI by a blue, with intensity corresponding to distance from optimum. Hence, a dark red sample is in slight PbI_2 excess compared to the optimum.

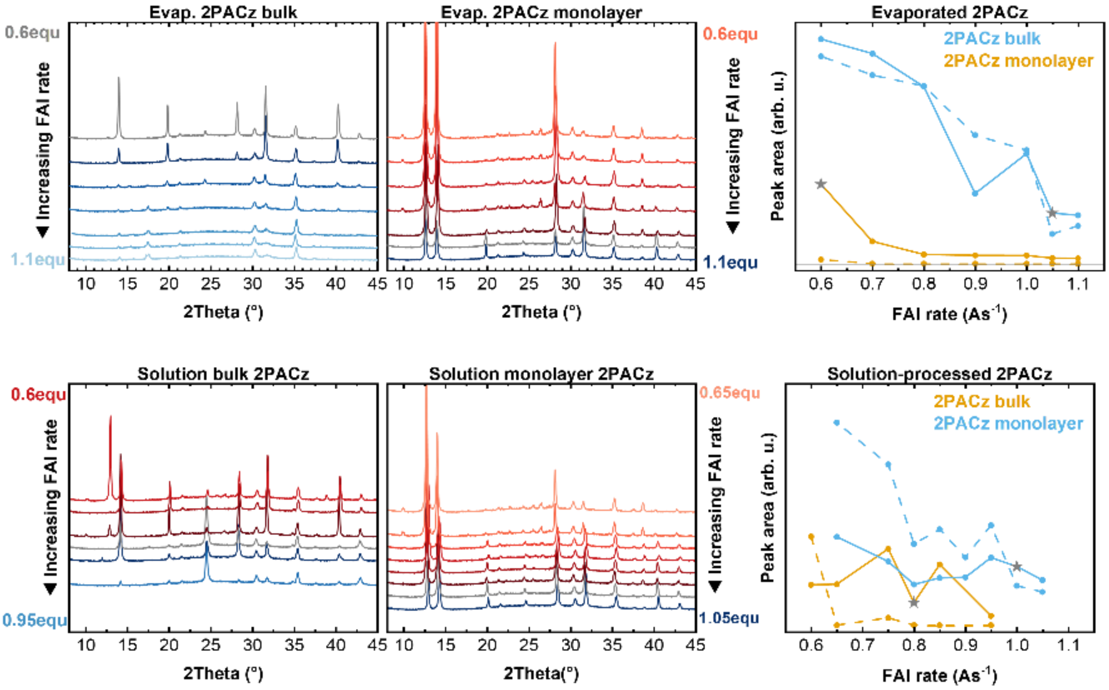

Figure 6-20 Sets of XRD spectra for co-evaporated perovskites deposited onto evaporated (*top*) and solution-processed (*bottom*) 2PACz. (*Right*) peak areas for (0 0 1) perovskite (solid) and PbI_2 (dashed) from these graphs. The FAI rate corresponding to the perovskite with the highest performance is marked with a star.

XRD series of half stacks, shown in **Figure 6-20**, results in variation between evaporated bulk and monolayer samples. 2 nm evaporated 2PACz, which display an intermediary effect but the same overall trends, are present in **Figure S6-12**. While device performance for 2 nm samples was lower, their FAI variation incorporates significant over- and under-stoichiometric regions. Furthermore, there is a consistent rate-dependent trend in peak area for PbI_2 and (0 0 1) peaks between samples. Both perovskite and PbI_2 peak areas are negatively correlated to increasing

FAI rate for all samples, clearly different from similar studies on solution-processed perovskites.[500] This indicates that sublimated FAI, either in the reactor or incorporated in the film, can a negative impact on perovskite crystallisation. A second, smaller, observation is the presence of a small peak at ~10 ° in the XRD spectrum. Such peaks have previously been observed in all-inorganic $CsPbI_3$ films.[501] As these films are FAI-deficient, the formation of a secondary perovskite phase without FAI is thus a potential explanation. This peak is this a potential indicator of FAI deficit in our studied perovskites.

Continuing this analysis, we consider the EQE shapes of samples deposited on evaporated nPACz SAM-HTLs discussed in **Section 6.3.1**, with a similar trend shown as the previous XRD comparison. The results are presented in **Figure 6-21**. EQEs of co-evaporated samples are found to be highly dependent on relative FAI content, apparently to a greater extent that solution-processed perovskites.[125,499,500] This is due to the methodology of this study. By varying FAI rate in discrete steps, a 0.1 equ rate change for evaporated bulk and monolayer 2PACz represents a 16.7% and 9.5% change in FAI content respectively (relative to the performance optimum). This explains the relatively broader process window for monolayer perovskites. With a higher optimum FAI rate, deviations around that optimum result in smaller changes in relative FAI content. Solution processed perovskites can assume their nominal perovskite concentrations are equivalent to the dissolved precursor materials in solution, making changes more consistent.

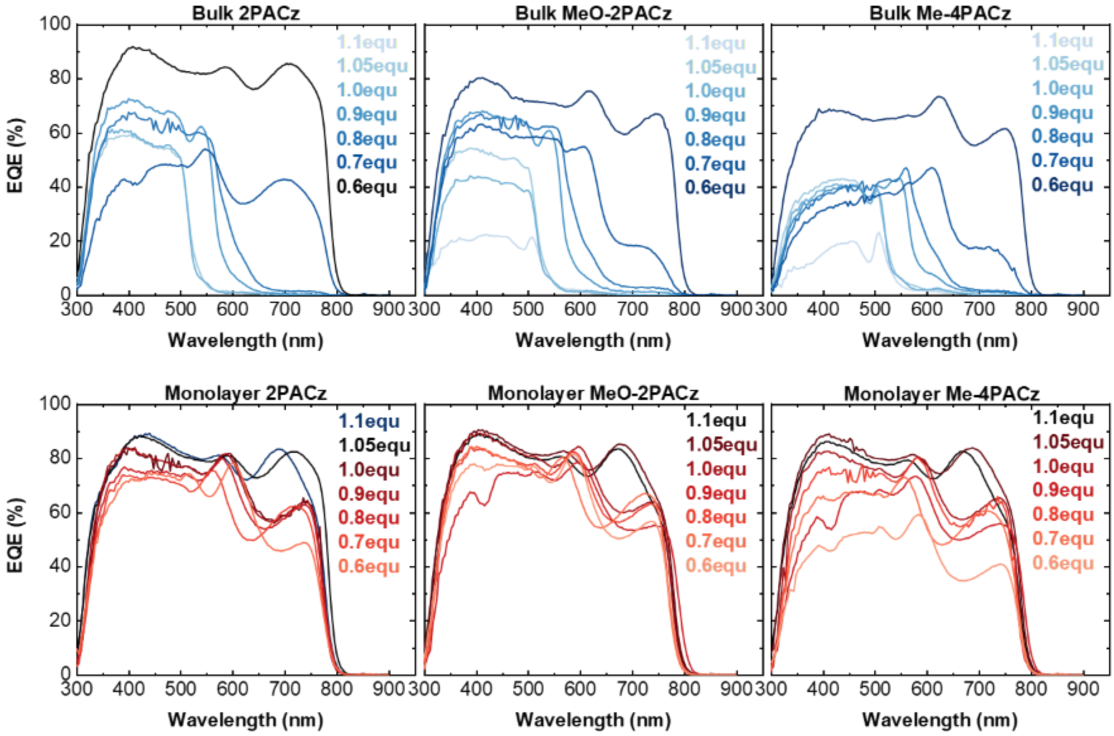

Figure 6-21 Sets of EQE spectra for co-evaporated perovskites deposited onto bulk (*top*) and monolayer (*bottom*) evaporated nPACz showing how spectral shape changes with respect to relative FAI content.

However, there are consistent changes in relative EQE shape that may be useful for approximately identifying the relative stoichiometry of unknown samples. Like solution-processed perovskites, an increase in relative FAI concentration results first in a unilateral decrease of the EQE spectrum.[499] With even a small further increase in relative FAI content, the EQE spectrum completely collapses with an apparent change in bandgap, which is not supported by PL spectra, with a representative set shown in **Figure S6-13** In contrast, excess PbI_2 first displays a drop in near bandgap absorption, which is theorized as due to the presence of the alternate perovskite phase mentioned in our analysis of **Figure 6-20**, and may explain the difference with solution-processed perovskites who do not see the emergence of this peak.[125,499,500,502] Increasing deviation from optimum results in the expected unilateral decline.[125,499] This is followed by a disproportionate drop in EQE below ~450 nm, coupled with the emergence of a specific trough at ~420 nm, which is attributed to typical PbI_2 absorption.[125,499,502]

While EQE is potentially a powerful tool for analysing relative stoichiometry, it is not fool-proof. The near bandgap drop is not a universal phenomena, and cannot be relied upon. Furthermore, it was found that for selected samples, a decline in PSC performance was not always mirrored in a drop of EQE, see **Figure 6-22**. Here, the shunted sample on the right (blue) gave a superior EQE by 0.6 mA.cm^{-2} compared to the champion device (grey). This representative result was seen multiple times. We assume it to be due to the lower incident light intensity, and hence absolute measured current, used for EQE measurements.[268]

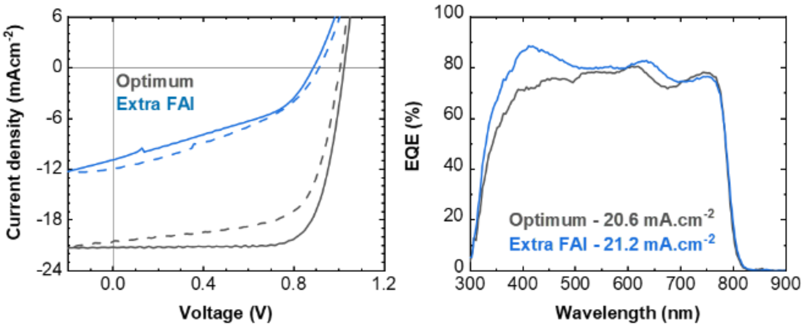

Figure 6-22 Representative EQE spectrum comparison of a PSC with poor *J-V* characteristics due to excess FAI, but superior EQE characteristics.

6.7 Rational design of monolayer SAM-HTLs with exposed phosphonic acids

The results presented thus far in this chapter provide a clear guide on how interfacial phosphonic acids can impact device properties. However, there remain two questions that must be answered before this study can be considered concluded. First, whether these interactions are definitively due exclusively to surface properties, or whether they result in nPACz migrating into bulk material to act as a bulk passivant, as has recently been demonstrated for co-evaporated perovskites with phosphonic acid containing additives.[459] Next is whether the observed changes in crystal structure can be replicated with a purely monolayer material. Both questions can be answered by depositing co-evaporated perovskites on a monolayer material with exposed phosphonic acid functional groups.

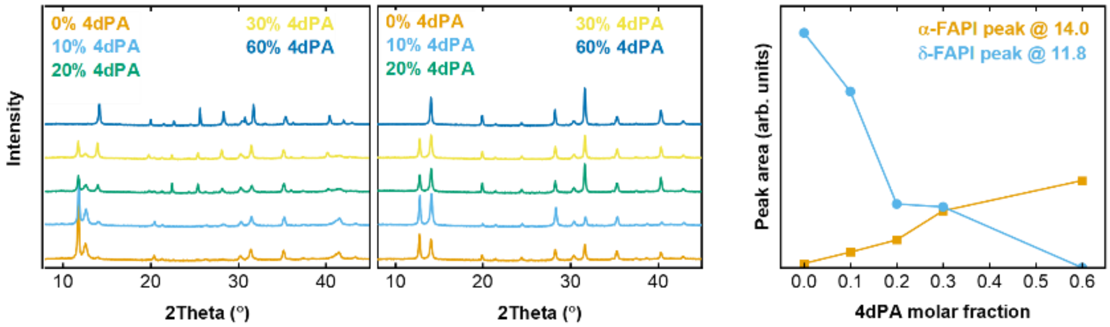

Figure 6-23 XRD spectra of perovskites on 4dPA monolayers. Trends of XRD patterns for (*left*) unannealed and (*middle*) annealed peroskites deposited on monolayers with varied molar fractions of 4dPA. (*Right*) trends in peak area for perovskite peaks at 11.8° and 14.0°. Figure reproduced from Elsevier Inc ©2024 with permission.[221]

A suitable class of materials can be found in recent literature. Al-Ashouri *et al*. incorporated 1,6-hexylenediphosphonic acid (6dPA) into Me-4PACz, and washed the subsequent film to form a SAM with exposed phosphonic acid functional groups.[208] As this present work has its primary focuss on 2PACz, this effect was replicated using the shorter chain 1,4-butylenediphosphonic acid (4dPA). To form monolayers layers with varying levels of exposed phosphonic acids, washed 2PACz/4dPA films with varying molar fractions (0%, 10%, 20%, 30%, 60%) of 4dPA were prepared. Equivalent FAI rate was kept constant at 0.75 Å s^{-1}, which is expected, to form exclusively α-$FAPbI_3$ during co-evaporation in the presence of exposed phosphonic acids. As shown in **Figure 6-23**, increasing the molar fraction of 4dPA is correlated with a trend of decreasing intensity in the (0 0 1) δ-$FAPbI_3$ XRD peak and increasing intensity of the (0 0 1) α-$FAPbI_3$ XRD peak. 60% 4dPA displays complete conversion to α-$FAPbI_3$, confirming our expectations that a monolayer with exposed interfacial phosphonic acids will also display the observed changed in bulk perovskite phase, demonstrating that the observed effects can be exclusively surface-based.

All tested molar fractions resulted in reduced PCE compared to bulk or monolayer SAMs with equivalent FAI rates, as shown in **Figure 6-24**. Due to the impact of excess PbI_2 on photovoltaic parameters,[125,499] comparisons are inherently non-ideal, as increasing 4dPA will decrease excess PbI_2 by increasing organic cation incorporation. Maximum V_{OC} remains steady up to 20% 4dPA, while average decreases slightly, before a sharp decline at 30% and above. A potential explanation is that 60% devices are experiencing an excess FAI condition due to the high density of exposed phosphonic acids. However, this is not a sufficient explanation for the entire overall performance trend as excess FAI was found in **Section 6.3** to cause a non-linear drop in V_{OC}, as opposed to the linear decrease observed with respect to 4dPA concentration. This observed drop in V_{OC} and associated decrease in PCE is attributed to the insulating behaviour of alkyl linkers, with any inclusion of 4dPA reducing the conductivity and hole extraction capabilities of 2PACz.

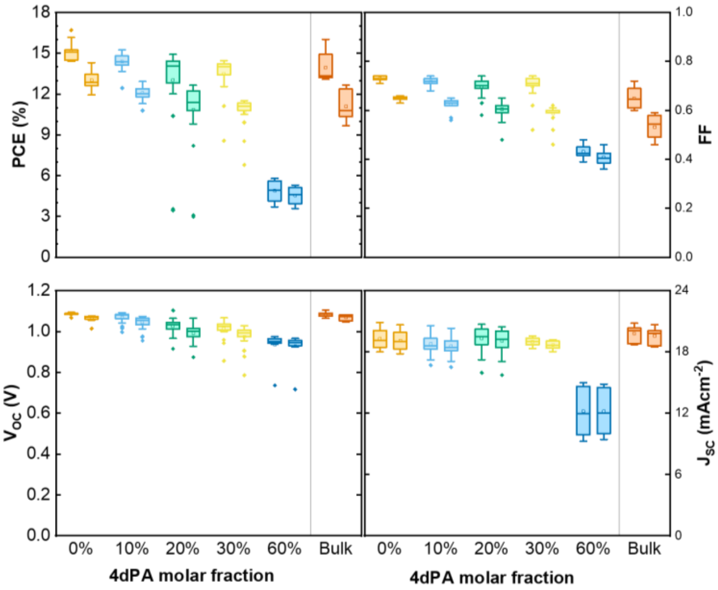

Figure 6-24 Photovoltaic parameter statistics derived from forward and reverse *J-V* scans of PSCs utilising hybrid 4dPA/2PACz monolayer HTLs with varying molar fractions of 4dPA and a comparison to a bulk 2PACz layer. All layers were deposited with a 0.75 Å.s^{-1} equivalent FAI rate. Figure reproduced from Elsevier Inc ©2024 with permission.[221]

6.8 Summary

In this chapter, we present an in-depth analysis of the interfacial interactions between phosphonic acid containing molecules (2PACz, MeO-2PACz, Me-4PACz and 4dPA) and co-evaporated perovskite films. This provides important additional understanding to existing literature on substrate dependent growth of co-evaporated perovskites, addressing **Challenge 4,** revealing alternate interaction mechanisms that also must be considered in development and application of new transport materials.

Interfacial phosphonic acids are found by a combination of XES and photovoltaic parameter analysis *via* a stoichiometric series to increase organic cation incorporation by an estimated maximum of 100% for evaporated SAM-HTLs and 65% for solution-processed SAM-HTLs, with specific values heavily dependent on the type of material. Material analysis of resultant perovskite films with XRD and SEM indicates that phosphonic acids suppress δ-$FAPbI_3$ and crystalline PbI_2 formation while shifting perovskite growth, as evidenced by the change in XRD peak areas. These results, coupled with analysis from **Chapter 5**, allow us to address **Challenge 5**. Contact angle measurements confirm that the reported shifts in perovskite growth are not attributed to the change in surface polar free energy.

Liquid phase ^{1}H-NMR of interactions between nPACz and the common organic cations of MAI, FAI, and GAI demonstrates the presence of an interaction between the halide component of the precursor and phosphonic acids from the nPACz. DFT computations confirm this observation and reveal a potential cause for the observed preference for α-$FAPbI_3$ growth. Although phosphonic acid binding interacts more strongly with δ-$FAPbI_3$ than with α-$FAPbI_3$, initial growth prefers formation of a thin α-$FAPbI_3$ film. The phosphonic acid bonding serves as a trap for the α-phase, creating a passivation barrier which inhibits conversion into δ-$FAPbI_3$.

Our studies result in photovoltaic performances of 16.2% for unwashed and 17.0% for washed solution-processed 2PACz as HTL. We observe improvements in interfacial properties for substrates with exposed phosphonic acids through an improvement in PLQY and TrPL lifetimes. Comparing EQE and XRD results for our stoichiometric series shows how co-evaporated perovskites differ to established solution-processed studies with respect to perovskite stoichiometry. To confirm the results of this chapter are due to a surface interaction rather than the recently reported bulk migration of PA-containing molecules, we replicated our XRD trends using 4dPA as a source of exposed phosphonic acid functional groups that remains a bound monolayer.

This chapter’s findings provide an explanation for the shift in required FAI rates based on surface functionalization, broadening established literature on the substrate dependent growth of co-evaporated perovskites.[72] We showcase the unique capacity of co-evaporated perovskites in exploiting surface functionalization to control growth characteristics, optimal FAI rate, and PSC PCE. Furthermore, the reported interactions between phosphonic acids and perovskites have been expanded in subsequent literature, and has been found to be beneficial for perovskite performance and stability in solution-process and co-evaporated perovskites.[446,449,503]

7 Practical concerns for increasing deposition rate of wide bandgap FA-based co-evaporated perovskites

Abstract

In this chapter, we investigate the impact of deposition rate on FA-based perovskite formation and resultant device efficiency, with a relatively large 23%$_{\mathrm{rel}}$ drop in PCE when increasing deposition rate from 5 nm.min^{-1} to 18 nm.min^{-1}. By investigating bulk perovskite and residual crucible material properties, we show that the degradation behaviour of formamidinium iodide (FAI) is crucible shape dependent. High deposition rates result in the formation of coke in the residual crucible material, which is deposited onto the substrate as a spit defect. When utilizing an addition FAI source, our relative PCE loss at 18 nm.min^{-1} decreases to only ~9%$_{\mathrm{rel}}$. Monolithic tandems reveal that this decrease is also dependent on substrate texturing. Comparing dual source 18 nm.min^{-1} with 5 nm.min^{-1} devices results in a ~18%$_{\mathrm{rel}}$ drop in PCE for textured silicon bottom cells.

The work in this chapter resulted in the submitted publication: **'High rate FA-based co-evaporated perovskites: Understanding rate limitations and practical considerations to overcome their impact,'** with Thomas Feeney and Aleksandra Miaskiewicz as shared first authors.[504]

This work is the result of collaborative research between Karlsruhe Institute of Technology and Helmholtz Zentrum Berlin (HZB).

Thomas Feeney as a first author of this study designed the experiments and developed the original concept.

As a first author of this study, Thomas Feeney conceived the initial idea, developed research plans and experimental design with collaboration from Aleksandra Miaskiewicz. Thomas Feeney fabricated Process A thin-film samples, performed and analysed relevant JV, EQE, MPP and XRD measurements and analysed PL mapping measurements. He also performed some PL mapping measurements and assisted in all others. Aleksandra Miaskiewicz fabricated Process B thin-film samples with assistance from Viktor Škorjanc, Stefanie Severin and Dr. Marcel Roß. Aleksandra Miaskiewicz also measured SEM for Process B and EDX for Process A. Together, Thomas Feeney and Felix Laufer performed and analysed all PL mapping measurements. Julian Petry performed and analysed all NMR measurements. Alexander Diercks measured SEM data for Process A. Dr. Suresh Maniyarasu performed all XPS measurements. Roja Singh measured extended MPP tracking. Prof. Dr. Ulrich Wilhelm Paetzold, Dr. Paul Fassl, Dr. Marcel Roß, Dr. Lars Korte and Prof. Dr. Steve Albrecht supervised the study.

7.1 Motivation

Wide-bandgap (here defined as $E_g > 1.65$ eV) perovskites utilizing formamidinium (FA) halides as organic precursor are a promising material to be used in conjunction with common low bandgap subcells (Si, CIGS, ect) to form 2T tandem devices that surpass the Shockley-Queisser limit for single-junction solar cells.[17,31,505–507] FA-based perovskites are particularly interesting for industrial applications due to their typically reported enhanced stability under simultaneous light and thermal exposure compared to methylammonium (MA)-based perovskites.[68,508–510]

Vacuum-based vapour phase deposition methods (hereafter termed vapour-phase) are particularly interesting for industrial tandem manufacturing due to their conformal coating properties and precise thickness control, with reduced upscaling losses for industrially relevant active areas.[47,49,212] A recent study by Abzieher *et al*. reported that even though ~95% of publications use solution-based deposition methods, 40% of companies are investigating vapour-phase methods.[51] It is therefore worthwhile to explore their capacity to incease deposition rate to accelerate perovskite commercialisation.

The industrial relevance of vapour phase methods remains uncertain for two key reasons.[51] The first is that reported device performance of *p-i-n* architectures is lower than solution-based processes. This is usually attributed to the limited options for bulk and surface passivation. While this field that has received significant recent attention,[214–216,511] the low publication numbers for vapour phase methods means progress will always be slow compared to solution-based methods. The other problem is that vapour phase processes demonstrate deposition rates well below industrially relevance.[51] Flash sublimation is promising, albeit exotic, deposition method, and has demonstrated deposition rates above 1000 nm.min^{-1} for MA-based perovskites.[217–219] However, the focus of this thesis, co-evaporation, remains a comparatively slow process. **Figure 7-1** outlines the relation between deposition rate and device performance for co-evaporated perovskites with MA, FA or a MAFA combination. Typical deposition rates are below 8 nm.min^{-1}.[51] Recently there has been some research focus on increasing deposition rate, studies on $MAPbI_3$ achieved maximum deposition rates of ~26 nm.min^{-1}.[74,512] However, no such study exists for FA-based perovskites, or perovskites with bandgaps suitable for incorporation into tandem devices.

Our analysis in **Chapter 7** will explore why deposition rates for FA-based perovskite remains comparatively low even compared to co-evaporated MA-based perovskites, and will explore methods to negate these problems in response to **Challenge 6**.

In **Section 7.2**, we discuss the impact of effective deposition rate on reactor pressure. Pressure is found to enforce a minor limit on deposition rate, with excessively high reactor pressure impacting overall perovskite absorber formation. Through the use of mass spectrometry measurements, we explore the relative proportions of FAI decomposition products to determine if an increase in such products is expected to be deleterious to device performance.

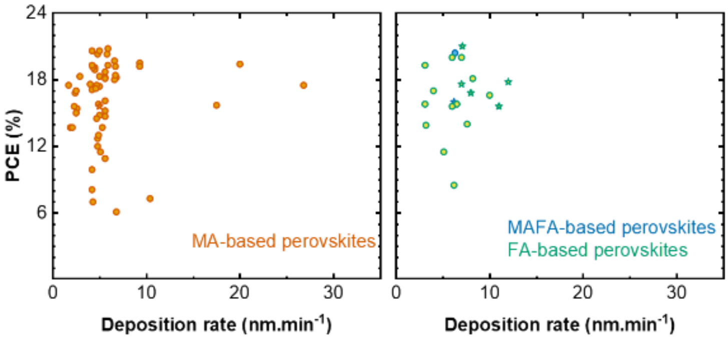

Figure 7-1 Device PCE plotted against deposition rates of organic-inorganic co-evaporated perovskite absorbers with MA as the only cation (*left*), and including FA (*right*). Circle points represent $E_g < 1.65$ eV, star points represent $E_g > 1.65$ eV. A tabulated set of all values is presented in the Appendix, **Table S7-1**.

Section 7.3 will evaluate the impact of deposition rate on device performance for a standard perovskite deposition. We note a substantial decrease in device performance and process repeatability at increased perovskite deposition rates. We first seek to determine if compositional changes are the driving force for performance losses. Bandgaps derived from EQE measurements confirm that samples do not undergo a noticeable change in bandgap at increased rates, and performance remains stable even under extended MPP tracking. We consider this evidence that our perovskite composition remains consistently stable independent of rate. XRD spectral analysis confirms this, with no significant shift in peak positions, although a minor shift in relative peak intensity is observed. Finally, EDX spectra remain relatively consistent between deposition rates.

Next, in **Section 7.4** we investigate spatial film homogeniety *via* photoluminescence (PL) mapping as a potential explanation of the decreased PCE at high deposition rates. High rate samples exhibit a substantial decrease in sample uniformity for samples with deposition rates at or above 13 nm.min^{-1} with the emergence of µm-scale inhomogeneities. Analysis of these inhomogeneities using EDX spectrometry reveals their chemical makeup cannot be attributed to any known decomposition product of FAI. We further analyse the residual crucible material using a combination of ^{1}H-NMR and XPS, finding that the residual material forms a large amount of coke, which is likely deposited on the sample as spit defects. Coke formation is dependent on both deposition rate and thermal homogeneity, both of which are impacted by crucible shape.

Section 7.5 explores utilising a second FAI source to enable high deposition rates. Two FAI sources allows a lower rate for each individual source while maintaining the same effective deposition rate. Device performance and repeatability are both significantly improved compared to equivalent rate single source depositions. An alternative method, pre-treating the FAI source to improve temperature homogeneity, also improves PL map homogeneity but was not explored as a method to improve device performance. This work thus provides a framework for enhancing co-evaporation deposition rates.

As an outlook, and to respond to **Challenge 7**, we demonstrate the potential of our methods to improve tandem device performance by comparing 2T tandem PCE on various Si substrates for low and high perovskite deposition rates in **Section 7.5**. Even with the improved performance for single-junction devices, high rate (~18 nm.min^{-1}) monolithic tandems on textured Si are significantly lower than baseline deposition rates.

7.2 Improving measurement fidelity at high rates

Effective comparisons of co-evaporation deposition rates requires a standardised labelling system and an understanding of the conditions within our reactor. Hence, this section will detail some potential causes of variations, and a method to establish a consistent labelling method. Unless otherwise specified, this chapter discusses Process A, which was undertaken at our laboratory (KIT, Karlsruhe). At times during this chapter we will refer to Process B. Process B is undertaken at another laboratory (HZB, Berlin) but with an equivalent method to calculate deposition rates, as outlined in the next section.

7.2.1 Considerations of deposition rate

This section will outline and explain a labelling method for enhanced rates that is independent of reactor conditions. The simplest issue is tooling factor, which can vary depending on the reactor layout and tooling method. Deposition rates measured on quartz crystal microbalances (QCM) are susceptible to systematic differences in measurement routine.[72,75,466] Furthermore, the method for heating sources and measuring their temperature can also lead to changes in measured source temperature. Furthermore, there is the potential for tooling factor to shift depending on deposition rate. Inorganic deposition rates are expected to maintain a relatively consistent tooling factor within the studied range, based on previous high rate perovskite depositions.[74] However, organic cation deposition rates are more likely to experience variations due to their highly substrate dependent sticking coefficients.[72,221]

To minimize the potential for tooling factor to impact the results in this chapter, perovskite deposition rate was increased by simultaneously and linearly increasing every source deposition rate. To avoid the potential of non-linear FAI scaling from occurring, where the optimum FAI rate may change depending on the overall deposition rate, a truncated FAI optimization series was performed for each set of constant inorganic deposition rates, similar to the optimizations in **Chapter 6**. For each deposition rate the best devices are then selected *via* champion PCE at MPP, which is used to calculate deposition rate. Effective deposition rate is obtained by dividing the final perovskite thickness by the deposition time to give an nm.min^{-1} rate, rounded to the nearest integer. In this work non-optimal devices exhibited thickness variations from the expected 560 nm due to the continued incorporation of FAI into the lattice. This further highlights the need to only compare the champion devices, where the thickness variations were substantially lower. Furthermore, recent literature regarding increasing $MAPbI_3$ deposition rates illustrates why having a process independent method to detail deposition rate is important. Comparing two recent publications, stated deposition time decreased from ~50 min to 25 min.[74,512] However, when considering the different perovskite thicknesses, this resulted in a deposition rate increase from ~20 nm.min^{-1} to ~28 nm.min^{-1}.

Utilising this methodology, this work will present a range of deposition rates from a baseline 5 nm.min^{-1} to a maximum ~19 nm.min^{-1}. Perovskite thicknesses for champion perovskite devices were typically around 560 ± 20 nm for single FAI source perovskite films. Measured dual FAI source perovskite films exhibited a slight reduction in final film thickness to an average of 500 – 520 nm, leading to a slightly lower stated deposition rate for equivalent inorganic deposition rates. In the studied perovskite thickness range, such variations do not have a meaningful impact on device PCE.[515] Hence, it is not expected that observed variations in perovskite thickness will result in variations of device performance.

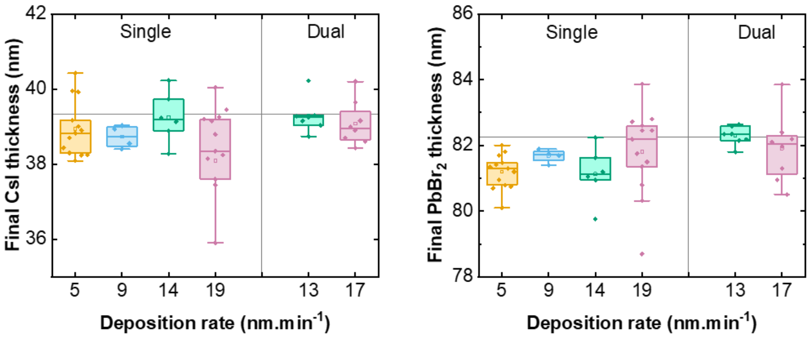

Figure 7-2 (*left*) Final CsI and (*right*) PbBr$_2$ thickness measured on the QCM for every perovskite deposition at each of the studied deposition rates. Reproduced from Wiley-VCH GmbH ©2025 with permission.[504]

There is also the possibility that observed deposition rates for inorganic materials may result in natural variations in overall perovskite composition due to systematic machine errors. For sublimation rates of 0.1 Å.s^{-1} the machine has a systematic error of 5%$_{rel}$, which is reduced 1.25%$_{rel}$ deviation for 0.4 Å.s^{-1} deposition rates. Hence the final thickness of CsI and PbBr$_2$ for a set final PbI$_2$ thickness are compared, as presented in **Figure 7-2**. FAI needs to be tuned for each deposition rate and is difficult to compare, and PbI$_2$ is selected as the control deposition rate. Minor variations of ~1.8%$_{rel}$ in final thickness are observed at deposition rates of 5 nm.min^{-1} compared to 19 nm.min^{-1}, however the 19 nm.min^{-1} shows large variation. At high rates control of the source becomes non-trivial, and the deviations may be due to occasional rate fluctuations. Low rate deviations from the expected final thickness are attributed to systematic machine error.

7.2.2 Impact of pressure on measured deposition rate

One important consideration when discussing reactor conditions is the impact of reactor pressure on perovskite deposition. Reduced mean free path at high pressures has been reported as a limitation for early deposition of MA-based perovskites.[72,516,517] While the pressures reported in this work are typically lower, at high rates mean free path may become important. **Figure 7-3** outlines the various starting and finishing pressures observed for each deposition rate studied in this chapter. When comparing the relation between starting pressure and final FAI thickness on the right side of **Figure 7-3**, each variation follows a linear relation. Moreover, with the exception of the 5 nm.min^{-1} and 19 nm.min^{-1} single source values, the relationship between processes is also linear.

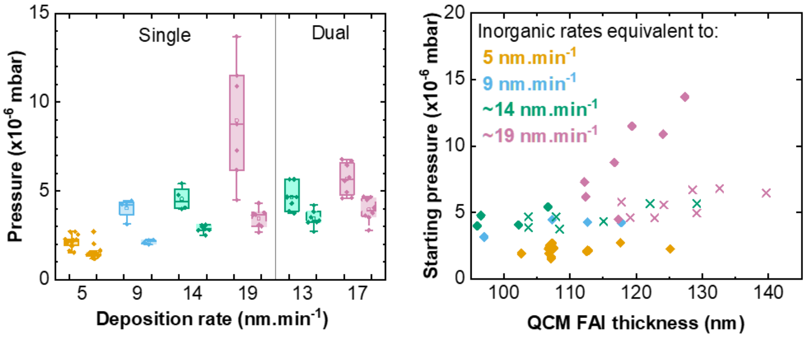

Figure 7-3 Pressure changes in the reactor for each process. (*Left*) Starting and finishing pressures for all processes explored in this chapter, using single and dual FAI sources. Starting pressure is on the left. (*Right*) Correlations between final FAI thickness (which correlates to relative FAI rate) and starting process pressure. Circles represent single source while crosses represent dual source. Reproduced from Wiley-VCH GmbH ©2025 with permission.[504]

Utilizing a similar methodology and set of assumptions as in previous calculations of mean free path for co-evaporated perovskites,[72,246] and calculated effective radii for formamidinium,[177,249] we can estimate the impact of chamber pressure on mean free path for other precursor materials. However, calculating the impact of pressure in a FA-based deposition is more complex than MA-based due to the increased range of decomposition products available.[75] Hence, all calculations must make numerous assumptions. The first assumption is that measured pressure is approximately the same as the effective pressure within the reactor. Kroll *et al*. postulated that they experience higher pressures near the FAI crucible,[75] indicating that this concern is not unique to this work. However, as our reactor does not possess a pressure gauge within the deposition chamber, this assumption is unavoidable. To explain the next assumption, we refer to two key figures of merit from **Chapter 2**, mean free path and the associated molar flux ratio. These figures of merit are dependent on which gas is the majority contributor to background pressure.

Figure 7-4 outlines the effect of the chosen carrier gas. While FA^+ and NH_3^+ are other alternative gases based on the decomposition and dissociation behaviour of FAI,[75] their resultant mean free paths are incredibly similar to HI. Instead of plotting molar flux ratio for the substrate, or the mean free path, we consider the difference in molar flux ratio for the QCM and the substrate, which is here termed Γ_{eff}. Crucially, while tooling factor inherently considers this value, it assumes the value remains constant between and within depositions. As shown in **Figure 7-4**, at high pressures (such as those observed for 19 nm.min^{-1} depositions), the process pressure enters a region where the Γ_{eff} can differ substantially between the start of the process (dark grey region) and the end of the process (light grey region). Even discounting the effect of scattering on vapour phase perovskite formation (which is as yet unexplored), the tooling factor is expected to change over the course of the deposition.

Furthermore Γ_{eff} changes differently for each precursor material, meaning the composition for the deposited film potentially changes over the course of the deposition. A final concern for this finding is that the distance to substrate is variable, as the substrate is relatively large. Γ_{eff} was calculated assuming the centre of the substrate, hence variation in Γ_{eff} over the substrate is expected. At high pressures this variation can cause substantial changes in composition over the substrate. The expected magnitude of variation is dependent on which gas comprises the majority of background pressure.

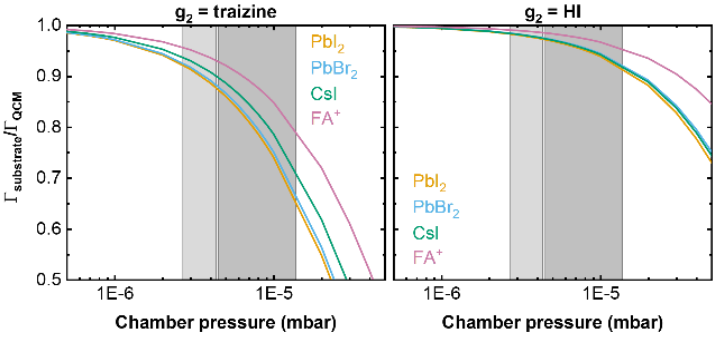

Figure 7-4 Molar flux ratio between the substrate and the QCM for the two extremes of carrier gases, assuming no coloumbic interactions. The dark grey region corresponds to the range of pressures observed at the start of 19 nm.min^{-1} depositions, while the light grey represents the end pressures. Reproduced from Wiley-VCH GmbH ©2025 with permission.[504]

Unfortunately, this effect may impact the attempts to control device stoichiometry outlined in the previous section. Hence, supplemental measurements must be taken for high rate samples, which will be discussed in the coming chapter, a level of material uncertainty must be considered as implicit for sufficiently high deposition rates.

7.3 Rate dependent prevalence of FAI decomposition products

Decomposition of FAI is a potential problem for high rate samples, which we will discuss in this section through the use of mass spectrometry (MS). Under vacuum conditions and relatively high temperatures, such as those associated with high deposition rates, FAI experiences both dissociation and decomposition. FAI is commonly assumed to dissociate in three distinct pathways, as outlined in **Figure 7-5**. The formation of $C_3H_3N_3$ (1,3,5-triazine or sym-triazine) is typically associated with material decomposition.[75,518–520] Some works also attribute the formation of HCN from formamidine as an irreversible pathways, which would render it an alternative decomposition product, but consensus is lacking. [75,475,518–520]

MS data of FAI and associated by-products for baseline (6 nm.min^{-1}) and elevated (12 nm.min^{-1} and 21 nm.min^{-1}) rates during Process B perovskite deposition was obtained and analysed by Aleksandra Miaskiewicz, Stefanie Severin, Dr. Viktor Škorjanc and Dr. Marcel Roß from HZB, and is shown in **Figure 3**. Measurements were taken during the heating and deposition phases, with the reference line indicating when perovskite deposition begins. The FA^+ signal ($m/z = 45$) disappears during the first minutes of the process, is suspected to be due to FA^+ reacting with inorganic materials within the reactor space, as has been previously theorised for co-evaporated MA-based perovskites.[72,75,456] The remaining MS signals represent the potential dissociation and decomposition products outlined in **Figure 7-5**, comprising HCN^+, CNH_2^+, sym-triazine and HI. As CO, N_2 and CNH_2^+ have the same signal in MS, it is difficult to distinguish between them. Hence the CNH_2^+ signal could potentially be caused by such gases outgassing from the FAI material.

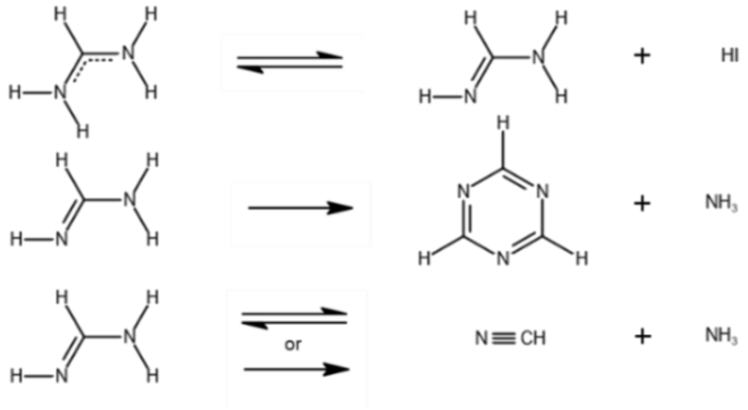

Figure 7-5 Dissociation and decomposition pathways of FAI. First is the dissociation of FAI into FA^+ and HI. Next is the irreversible decomposition of FA^+ into sym-triazine and NH_3. Finally is the debated conversion of FA^+ into HCN and NH_3.

There are four key observations from the MS data. As expected, reactor pressure is strongly correlated to the detector counts of each product, which is as expected. HI and CNH_2^+ (or the alternatives previous mentioned) are found to be the primary process gases, meaning the actual behaviour of $\Gamma_{eff.}$ outlined in **Figure 7-4** will more closely represent the right graph than the left, indicating a relatively small change in $\Gamma_{eff.}$ during the process. Consensus on whether decomposition products incorporate into the bulk perovskite material has not been reached,[75,522] yet low mean free paths have been associated with poor perovskite crystal growth.[72,75] The pressures observed for high rate Process B are even higher than presented in **Figure 7-3**, indicating further problems for perovskite formation and a worse $\Gamma_{eff.}$ are expected.

Second, there is a significant increase in the intensity of the HI-signal ($m/z = 128$) when the substrate shutter opens and deposition begins. Process B uses a similar cooled enclosure to our reactor, outlined in **Figure 3-1**. This enclosure can potentially cause a build-up of a higher partial pressure for some materials, which escape when the substrate shutter opens. This observation reinforces the concern about the difference in measure pressure and effective pressure within the reactor.

Next, note that the $m/z = 28$ signal, which belongs to either CO, N_2 or CNH_2^+, starts relatively high when the sources first become heated, before quickly decreasing, and is correlated to a high initial pressure. This could either indicate early outgassing of decomposition products, or the presence of trapped gases in the FAI powder.

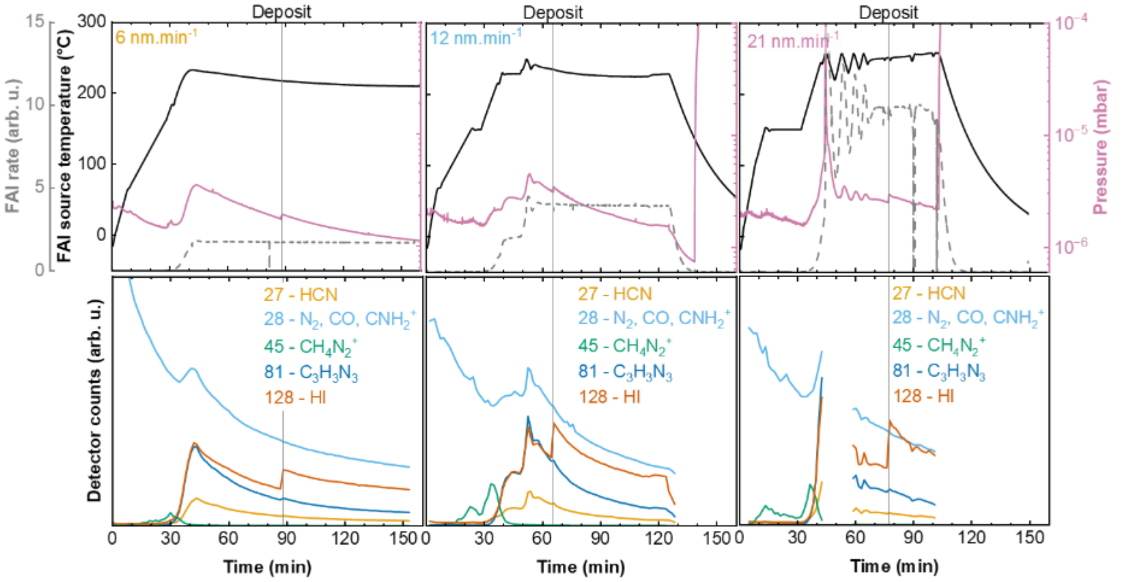

Figure 7-6 Mass spectrometry data of ionic FAI byproducts during Process B deposition rates equivalent to 6, 12 and 21 nm.min^{-1}. Source temperature, reactor pressure and deposition rate are shown above while corresponding detector counts for decomposition and dissociation products are shown below. Measurements performed by our collaborators (HZB). Reproduced from Wiley-VCH GmbH ©2025 with permission.[504]

Finally, there is not an observed correlation between sublimation rates and an increase in the relative presence of decomposition products such as sym-triazine. While detection of sym-trazine and HCN/CNH_2^+ increases with increasing perovskite deposition rate, their detection is not linearly correlated to deposition rate. The similar relative presence of these products for 12 nm.min^{-1} and 21 nm.min^{-1} rates means it is valid to assume that the any change in device performance and uniformity at high deposition rates is not due to an increased relative concentration of these decomposition products.

This discussion must also consider a difference with established literature. As mentioned in **Section 7.2.1**, measured source temperatures can vary between setups. Our collaborators data is at a significantly higher temperature (217 °C - 234 °C) than previous MS literature,[75] which corresponds to temperatures above where Kroll *et al.* observed a complete breakdown of the sublimation process. This shows that they cannot assume that the previously reported decomposition temperatures for FAI perfectly correlate to the observed decomposition temperatures in our systems, especially as temperature measurements under high vacuum can be unreliable.

7.4 Impact of vertical rate scaling on devices

With a unified framework for determining perovskite deposition rate, and with potential issues explored and evaluated where possible, this next section will evaluate the tangible impact increasing of deposition rate on device performance and bulk properties. We first consider a vertical scaling technique, where we increase the deposition rate of our baseline without changes to the overall system. As discussed in **Chapter 3**, we employ a double cation 1.68 eV bandgap perovskite absorber with the nominal compositions of $Cs_{0.17}FA_{0.83}Pb(I_{0.75}Br_{0.25})_3$ with the inverted *p-i-n* architecture of: glass/indium tin oxide (ITO)/MeO-2PACz/perovskite/C_{60}/BCP/Au unless otherwise stated.

7.4.1 Performance and stoichiometry with respect to deposition rate

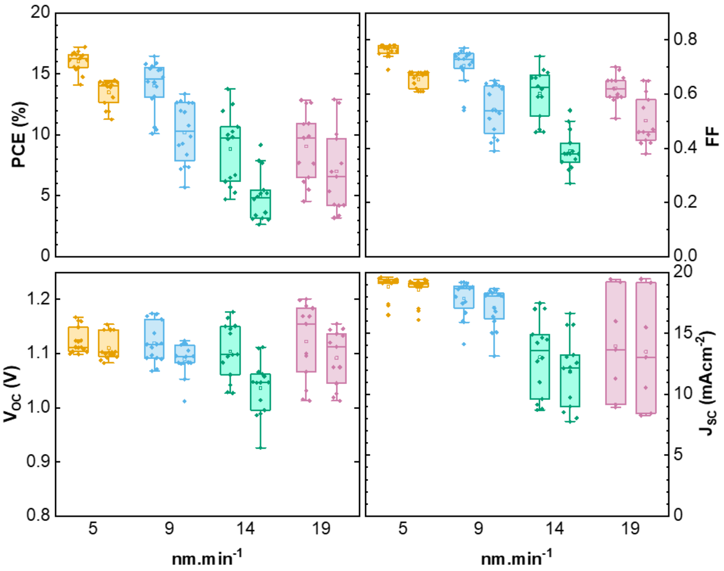

Figure 7-7 Photovoltaic parameter statistics derived from forward and reverse *J-V* scans for champion batches with perovskite deposition rates ranging from 5 nm.min^{-1} to 19 nm.min^{-1}. Reproduced from Wiley-VCH GmbH ©2025 with permission.[504]

We first consider the maximum achievable device performances for perovskites with deposition rates varying from ~5 nm.min^{-1} to ~19 nm.min^{-1} with a single FAI source. Due to high hysteresis for high deposition rates MPP values are used to determine the champion device in each FAI optimization series. Statistics are provided in **Figure 7-7**, with current density-voltage (*J-V)* curves, external quantum efficiency (EQE) measurements and maximum power point (MPP) tracking of the best-performing devices in **Figure 7-8**. At elevated deposition rates a clear decrease in device performance and increase in overall hysteresis is observed. Comparing reverse scans reveals a decrease in champion PCE from 17.2% to 12.7% when increasing deposition rate from 5 nm.min^{-1} to 19 nm.min^{-1}.

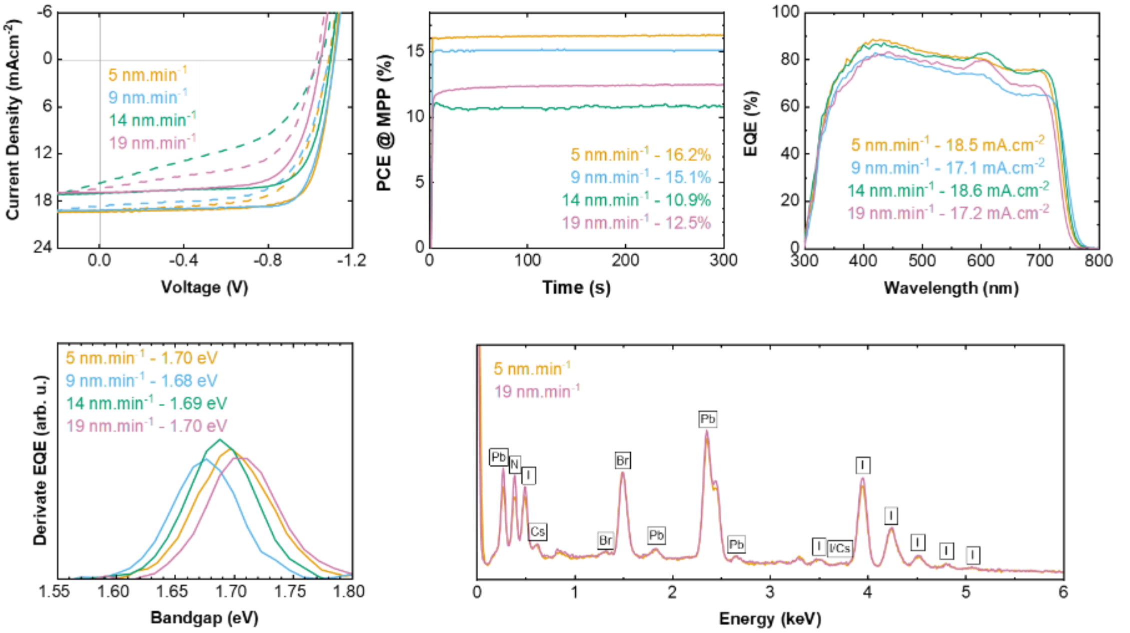

Figure 7-8 Additional photovoltaic parameter and material analysis based on deposition rate. (*Top-left*) *J-V* curve, (*top-middle*) 300 seconds of MPP tracking, (*top-right*) relevant EQE curve and (*bottom-left*) corresponding EQE-derived bandgap for the champion device of each batch. (*Bottom-right*) Comparison of EDX spectra for representative samples deposited at perovskite deposition rates of 5 nm.min^{-1} and 19 nm.min^{-1}. The stability of MPP tracking, coupled with consistent bandgap and relative EDX response indicate composition and stoichiometry are relatively consistent. EDX measured by Aleksandra Miaskiewicz (HZB). Reproduced from Wiley-VCH GmbH ©2025 with permission.[504]

Despite this substantial drop in PCE, all champion devices exhibited stable PCE at MPP tracking for a minimum of 300 seconds. This indicates there is not a substantial increase in halide or cation migration at high rates.[317] If using PCE at MPP values to evaluate the decline of PCE, preventing hysteresis impacting the stated values, there is a clear decrease in PCE at MPP from 16.2% to 12.5% when increasing deposition rate from 5 nm.min^{-1} to 19 nm.min^{-1}, corresponding to a 23%$_{rel}$ drop in PCE. When we performed extended MPP tracking at 25 °C, performance remains stable for every rate up to ~250 hours, along with N_2 storage stability of over 100 days and a T_{80} of ~250 hours for a 9 nm.min^{-1} at 85 °C (see **Figure S7-1**). Deriving integrated J_{SC} from each EQE spectrum reveals J_{SC} values within 10% of those obtained from *J-V* scans, which is within the expected deviation range.[268,523]

Furthermore, there is not a significant bandgap shift when deriving bandgap from the EQE spectrum. Importantly, the minor fluctuations that are observed are random, indicating that they are not caused by rate based effects. The stable MPP tracking, lack of bandgap shift and relatively small EQE discrepancies all provide circumstantial evidence that presented devices are near optimum stoichiometry.[467,499,500,524] EDX spectra of 5 nm.min^{-1} and 19 nm.min^{-1} samples show no significant change in overall spectral shape or relative intensity between these two deposition rates. This provides further evidence that a change in material stoichiometry is not responsible for the observed changes in device performance. Together, these results indicate that the observed changes in device performance are primarily due to the change in bulk properties rather than a shift in stoichiometry.

Table 4-1 Photovoltaic parameters of champion single-junction PSCs with a single FAI source at various deposition rates. . Average values for *J-V* parameters are presented in brackets.

Solar cell	PCE [%]	FF [%]	V_{OC} [V]	J_{SC} [mA.cm^{-2}]	
				Solar simulator	EQE
5 nm.min^{-1}	17.2 (16.0) 14.5 (13.5)	78 (76) 68 (66)	1.17 (1.12) 1.15 (1.11)	19.6 (18.8) 19.4 (18.6)	18.5
9 nm.min^{-1}	16.5 (14.0) 13.4 (10.2)	77 (71 65 (54)	1.17 (1.12) 1.12 (1.09)	19.2 (17.9) 18.7 (17.1)	17.1
14 nm.min^{-1}	13.8 (8.8) 9.2 (4.9)	74 (60) 54 (39)	1.18 (1.10) 1.11 (1.04)	17.5 (13.1) 16.6 (11.9)	17.1
19 nm.min^{-1}	12.8 (9.0) 12.9 (7.0)	70 (62) 65 (50)	1.20 (1.12) 1.16 (1.09)	19.4 (14.0) 19.5 (13.5)	17.1

Another important metric that has only recently been considered is repeatability, the change in process between batches with equivalent fabrication conditions.[525,526] We consider two metrics: performance repeatability being the amount the champion device performance varies between batches and process repeatability being the amount the optimum FAI rate varies to achieve those champion batches. The results of both analysis are shown in **Figure 7-9**. Here, μ denotes mean batch PCE, σ denotes the standard deviation of PCE and CV refers to the coefficient of variation, which is the ratio of σ to μ, and is used to denote variation about the mean.

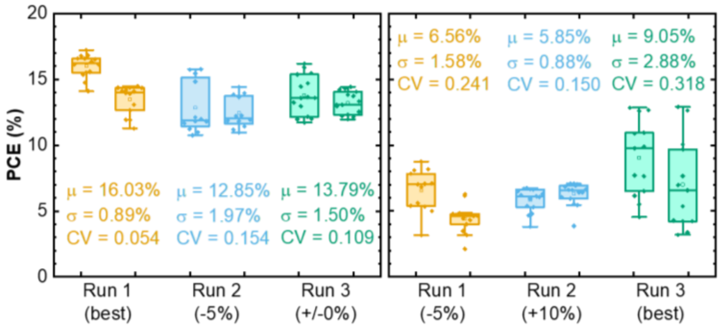

Figure 7-9 Demonstration of the change in repeatability of 5 nm.min^{-1} (left) and 19 nm.min^{-1} (right) perovskite deposition rates by comparing the champion set from several batches. Provided in the graphs are the relevant values of the mean (μ), standard deviation (σ) and coefficient of variability (CV) for each batch. Reproduced from Wiley-VCH GmbH ©2025 with permission.[504]

We also consider the CV between batches, which can give us a numerical approximation of the repeatability. Performance repeatability is significantly reduced from $CV_{mean} = 0.094$ for 5 nm.min^{-1} and $CV_{mean} = 0.195$ for 19 nm.min^{-1}. This indicating a significant increase in cross batch variation for higher rate devices. Without a large dataset, process repeatability is more difficult to analyse. However, comparing the FAI rate of each champion batch will still show how much optimum FAI rate is changing. The change in optimal FAI rate is given by a % under each heading in **Figure 7-9**. There is a maximum variation of ~5% in relative FAI rate for 5 nm.min^{-1} and ~10% for 19 nm.min^{-1}, indicating high rates also see an increase in process variability. This reinforces our theory on behaviours of $\Gamma_{eff.}$ at higher pressures outlined in **Section 7.2**.

7.4.2 Perovskite crystal properties with respect to deposition rate

This section will address an evaluation of device bulk properties in order to determine a cause for the observed rate-dependent changes in device performance. XRD spectral analysis, as shown in **Figure 7-10**, indicates only minor changes in crystal orientation and structure. Relative peak areas, calculated using Gaussian fits, for peaks corresponding to the (0 0 1), (1 1 1) and (1 1 2) Miller indices shift slightly with respect to deposition rate. It is worth considering that shifts to a lower relative proportion of the (0 1 1) and (0 1 2) have been previously assumed to be beneficial for the perovskite in the case of $MAPbI_3$, and thus cannot be cited as a definitive indicator for inferior growth.[72,221] Crucially, there is not a clear trend in these changes in relative intensity, hence it is not definite that rate has a consistent impact on crystal growth. The decline in (0 0 1) XRD signal intensity is potentially indicative of a decrease in crystal quality,[527,528] but should not be sufficient to explain the observed changes in device performance.

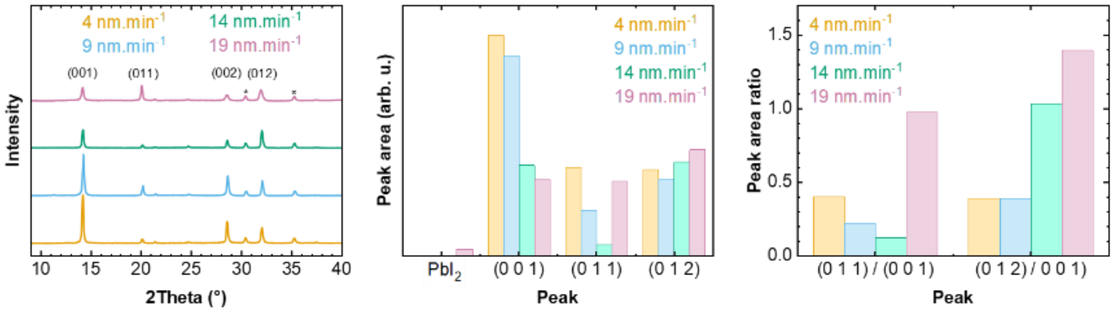

Figure 7-10 XRD analysis of perovskites at various deposition rates. (*Left*) XRD spectra of films grown at each studied perovskite deposition rate with relevant Miller Indices labelled, and ITO denoted using *. Peak area (*middle*) and peak area ratio (*right*) for the shown XRD spectra. Reproduced from Wiley-VCH GmbH ©2025 with permission.[504]

7.4.3 Bulk analysis from PL and EDX mapping

Due to the inconsistent changes in bulk properties, lateral homogeneity of the samples were measured to determine other potential causes for the decline in device performance. Photoluminescence mapping, provided in **Figure 7-11**, allows us to probe sample homogeneity for each of the stated rates.

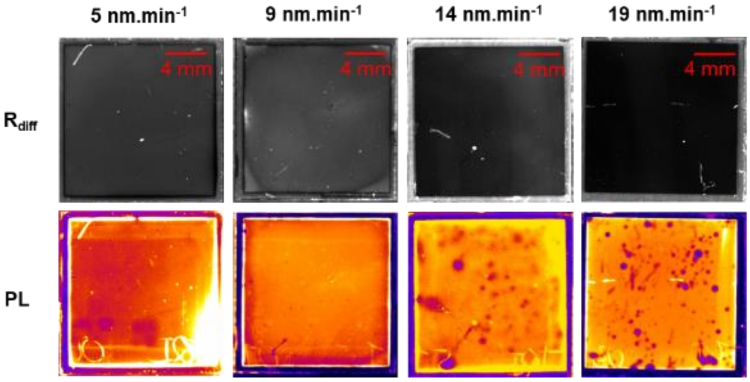

Figure 7-11 PL maps of perovskites at various deposition rates. Shown is R_{diff} (*top*), which uses a neutral density filter to represents visual data, and filtered under a longpass 775 nm filter (*bottom*), revealing inhomogeneities at high perovskite deposition rates. Reproduced from Wiley-VCH GmbH ©2025 with permission.[504]

Visually the samples appear to be uniform, which can be represented by taking a measurement using a neutral density filter termed R_{diff}. There are minor scratches, particulates and spin coating artefacts from the SAM-HTL deposition (such as the dust particle near the centre of the 9 nm.min^{-1} sample). However, PL maps using a 725 nm long pass filter reveals a large number of µm-scale inhomogeneities, which are mostly comprised of dark spots. The shown PL maps are qualitative rather than quantitative as absolute PL intensity is not provided. This is because it is more important to highlight inhomogeneities on individual samples rather than inter-sample changes in PL intensity. Multiple PL maps were measured for each deposition rate to preclude sample dependent variations, the PL maps shown here are indicative of the general trends.

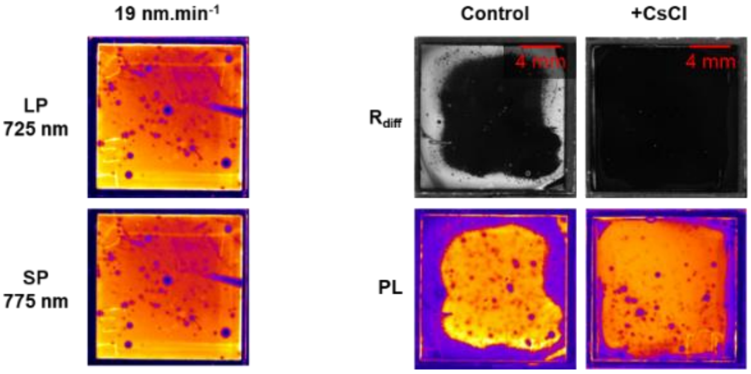

Figure 7-12 PL maps exploring alternative explanations of µm-scale inhomogeneities. (*Left*) PL maps of a 19 nm.min^{-1} sample under shortpass and longpass filters to show the equivalent PL behavior. (*Right*) PL maps of 14 nm.min^{-1} samples with and without a CsCl underlayer. Reproduced from Wiley-VCH GmbH ©2025 with permission.[504]

We consider and attempt to disprove two alternative explanations for the µm-scale dots. First is whether the µm-scale dots are the result of localised bandgap shifts, rather than a flat decrease in PL intensity. To disprove this, **Figure 7-12** shows both the 775 nm short pass and 725 nm long pass PL maps of a high rate sample, revealing that inhomogeneities are unlikely to be the result of a bandgap shift. Next, it is possible that substrate inhomogeneities may be a factor for the reduced homogeneity, due to the substrate dependent growth of co-evaporated perovskites.[72,221] To ensure this was not the case, a CsCl seed layer was deposited on selected samples prior to perovskite deposition. Seed layers, including CsCl specifically, have been reported as a potential method to reduce the substrate impact on co-evaporated perovskites growth. [214,222] It is clearly evident in **Figure 7-13** that even when the substrate has an impact on sample homogeneity, the central core of the sample continues to present µm-scale dots. Furthermore, the CsCl does prevent substrate dependent inhomogeneity, but does not prevent the formation of these µm-scale dots. It is therefore valid to assume that the observed µm-scale dots arise during perovskite deposition.

EDX spectrometry was utilised by Aleksandra Miaskiewicz from HZB in order to further investigate the observed µm-scale dots. A representative set of EDX spectra for a 19 nm.min^{-1} sample, along with the corresponding SEM image, is shown in **Figure 7-13**. Several additional sets of EDX spectra from the same and another sample, illustrating the myriad of forms these µm-scale dots take, are presented in the Appendix **Figure S7-2**. As shown in **Figure 7-10**, the bulk spectra of the 19 nm.min^{-1} deposition rate perovskites is relatively similar to that of 5 nm.min^{-1} perovskites, meaning these inhomogeneities are point-defects. EDX spectra for iodine and bromine are overlayed, revealing how some distorted perovskite formation still occurs near the point defect.

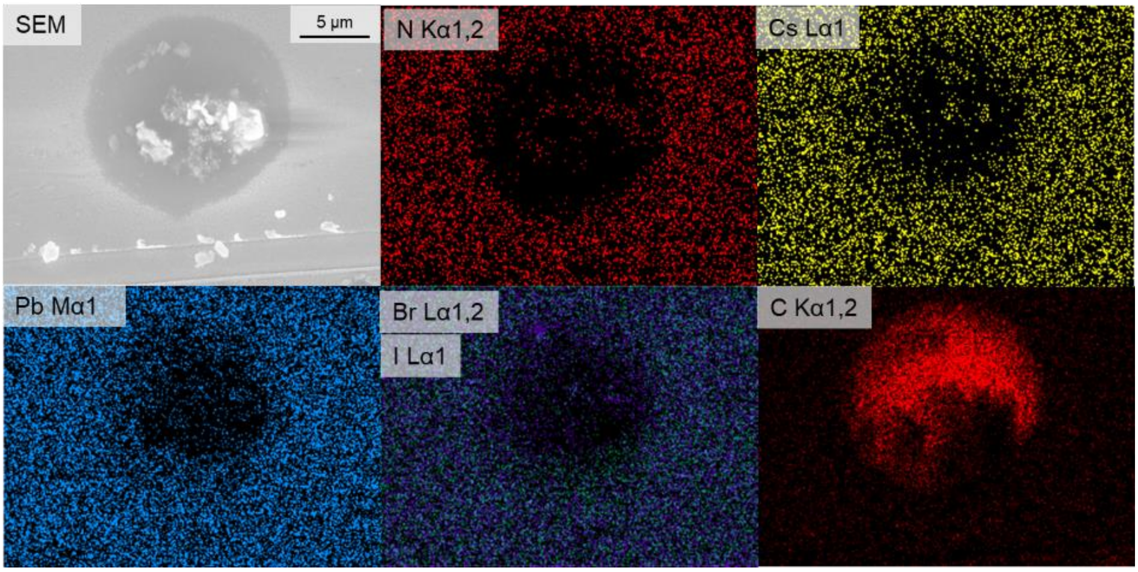

Figure 7-13 SEM image and relevant EDX data of a representative dark spot, measured on the 19 nm.min^{-1} sample from **Figure 7-11**. Iodine and bromine components are overlaid. Carbon is detected outside the carbon-rich region of the EDX spectra, but is not readily apparent due to the high concentration of carbon at the defect. Measurement performed by Aleksandra Miaskiewicz (HZB).

The primary 'dark' region, which we attribute to be a µm-scale dot, displays a significant reduction in the expected perovskite element signals compared to the surrounding region, indicating a significant reduction in perovskite film thickness and / or a highly localised disruption of the perovskite formation process. As FAI consists of a combination of carbon and nitrogen (with EDX unable to directly detect hydrogen), the relative absence of nitrogen in this region precludes this dark spot as being a spit defect of pure FAI. Spit defects occur when localised vapour bubbles, from rapid or uneven heating, lead to the ejection of particulates from a crucible. Instead, a strong relative carbon signal of sufficient relative intensity as to distort the carbon signal elsewhere is observed. If the emergence of the µm-scale dots are the origin of the performance drop at high deposition rates, which is a valid assumption, then these carbon-rich inhomogeneities are a primary cause of the reduced device PCE at high deposition rates. Hence, it is necessary to obtain an explanation for the origin of these carbon-rich inhomogeneities.

7.5 Changes in residual crucible material

In this section we will evaluate, using a combination of visual analysis, liquid phase NMR and XPS, how the residual FAI from each deposition changes as a potential explanation for the emergence of carbon-rich inhomogeneities.

7.5.1 Visual changes in crucible material

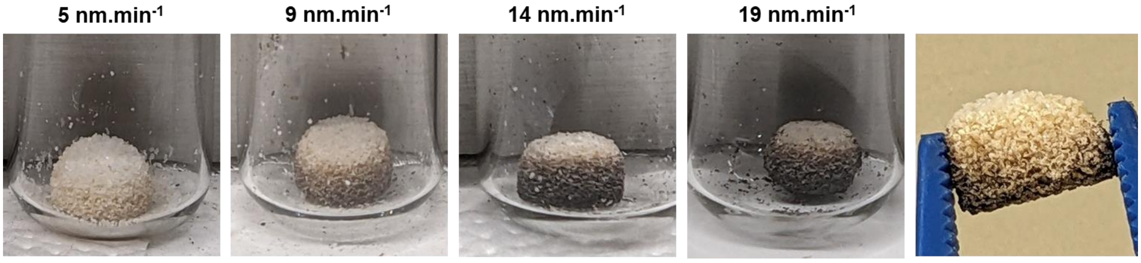

Figure 7-14 Residual crucible material at each studied sublimation rate. Original (raw) source material was taken from the same batch of FAI. Also shown is a cross section of residual crucible material at 14 nm.min^{-1} sublimation rate. Reproduced from Wiley-VCH GmbH ©2025 with permission.[504]

Shown in **Figure 7-14** is a representative series of images taken of residual crucible material from each deposition rate. Even at the lowest deposition rate of 5 nm.min^{-1} residual FAI material exhibits a slight yellowing. This yellowing can potentially be attributed to the powder being infused by residual hydrogen iodine produced during FAI dissociation,[522] indicating that not all hydrogen iodide is volatised. Furthermore, a black carbon coke forms at elevated rates, becoming significant at 14 nm.min^{-1}, the same rate where µm-scale dots are first observed in the PL maps of **Figure 7-11**. If the carbon rich regions observed in **Section 7.3.3** are this coke, it is likely that high rates lead to spit defects of this material. Recent work on FAI decomposition *via* quartz tube sublimation have observed the formation of coke from FAI at temperatures above 240 °C. This is in excess of the observed deposition temperatures for Process A and Process B. The most likely cause of this discrepancy is that the crucibles used in this study experience uneven temperatures. FAI is known to have poor thermal conductivity, and the FAI powder utilised in this work is comprised of relatively large particulates (200 - 500 µm), which would further decrease effective conductivity.

As seen in the cross section of a puck of residual material from **Figure 7-14**, FAI material in the crucible experiences uneven decomposition. Coke formation is primarily restricted to the bottom and edges of the puck, where it is in contact with the crucible walls. This is also potentially why µm-scale inhomogeneities are not present for 9 nm.min^{-1} samples, despite coke formation. Coke forms originally on the bottom of the puck, and only on the edges at sufficiently high temperatures. Further study into the precise dynamics of thermal degradation is potentially interesting to further development of high-rate processes, but beyond the scope of the chapter.

7.5.2 Chemical analysis of residual crucible material

In this section we further analyse the residual crucible material after a range of deposition conditions to obtain further information about FAI decomposition in our process. This is performed using ^{1}H-NMR on various FAI powders, a brief XPS analysis of FAI and inorganic precursors and finally a discussion about the role of crucible shape on FAI decomposition.

7.5.2.1 ^{1}H-NMR analysis of residual FAI powder

To determine if consider if it is possible to observe other evidence of material degradation for residual crucible material, Julian Petry performed a series of ^{1}H-NMR measurements on residual material. Unless otherwise stated, each spectra was made by dissolving 30 mg of material in 0.6 mL d_6-DMSO to form a solution of ~0.29 M.

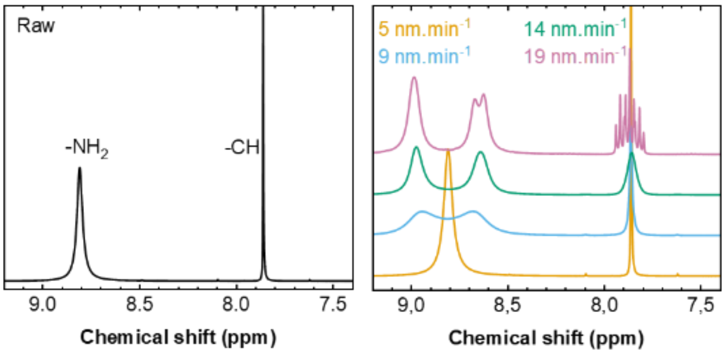

Figure 7-15 ^{1}H-NMR spectra of raw FAI (*left*) and FAI harvested from residual crucible material after various perovskite depositions (*right*). Reproduced from Wiley-VCH GmbH ©2025 with permission.[504]

Residual crucible material for each puck shown in **Figure 7-14** was measured and compared to a raw sample of FAI powder, with the resultant spectra shown in **Figure 7-15.** Note that neither the presented, nor previous, ^{1}H-NMR or ^{13}C-NMR (see **Figure S7-3**) spectra have observed additional peaks that can be assigned to this coke,[522] due to its insolubility in d_6-DMSO and lack of defined chemical structure. Undissolved coke will slightly change the concentration of the FAI in the residual material, as they will result in slightly less than 30 mg of material being present. However, the change in concentration is expected to be extremely minor.

^{1}H-NMR peak at 8.80 ppm corresponds to the amide moiety, which undergoes peak splitting for deposition rates above 9 nm.min^{-1}, with the level of splitting increasing with respect to rate. ^{1}H-NMR splitting of amide moiety in FAI has been associated with the presence of acidic compounds.[221,477,529] This phenomena was observed in **Chapter 6** , along with a split of the CH peak at 7.80 ppm into a triplet of a triplet,[221] however such splits are not detected until 19 nm.min^{-1} spectra. The lack of coupling for other deposition rates can be attributed to the high exchange rate for spin-spin coupling (J-coupling) preventing it from being detected at lower HI concentrations. Hydrogen bonding can significantly shift J-coupling constants, including depressing them for certain molecules.[530–532] Potentially, at 19 nm.min^{-1} this depression is sufficient for J-coupling to be resolved, splitting the NH_2 peak at ~8.6 ppm into a doublet and splitting the CH peak at 7.80 ppm.

Yellowing of the residual crucible material has already been assumed to be due to the presence of HI, which is an acidic compound that can cause the observed splitting. There exists some literature supporting this, with a similar peak split to the 19 nm.min^{-1} residual material occurring by exposing an FA-based perovskite to HI.[529] HI exposure was experimentally replicated by exposing a ~0.29 M FAI solution to an aqueous HI solution. As HI is an aqueous solution, a pure water solution was included in the series as a second control. As evident in **Figure 7-16**, pure water was sufficient to cause splitting comparable with the 9 nm.min^{-1} spectra of **Figure 7-15**, with the addition of merely 1 mM causing splitting equivalent to the 19 nm.min^{-1} spectra.

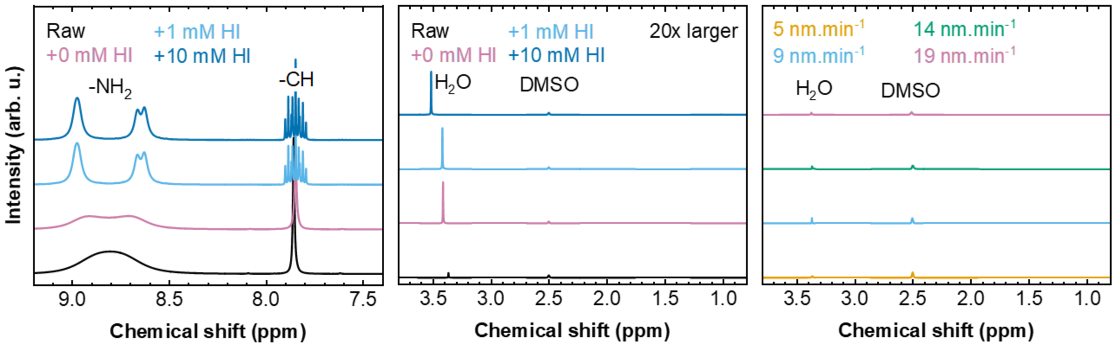

Figure 7-16 ^{1}H-NMR spectra of FAI exposed to varying concentrations of aqueous HI, with the FAI relevant region (*left*) and the water relevant region (*middle*) of the spectra. Also shown is the water spectra of Figure 7-15 (*right*), showing the minimal water contamination. Reproduced from Wiley-VCH GmbH ©2025 with permission.[504]

This study has produced two key findings. The first is that water exposure is sufficient to cause some level of peak splitting, although the amount of added water was relatively high, as shown in the water peak, which varies from 3.36 ppm to 3.51 ppm, of **Figure 7-16**, which is ~10x the height of the control. As the intensity of the water peak remains relatively consistent between spectra, and is substantially lower for samples from **Figure 7-15** to **Figure 7-16**, water-based splitting is unlikely to be the cause of the reported rate-dependent splitting. The second learned piece of information is that HI can indeed cause the peak splitting observed in the high-rate spectra. However, due to the aforementioned water-based peak splitting, the relative content of HI could not be calculated.

No additional carbon-containing compounds are observed in the ^{1}H-NMR spectra, indicating that other degradation products such as sym-triazine and hydrogen cyanide are volatised during FAI sublimation.[522] To guarantee trace degradation products or impurities are not present, Julian Petry also performed analysis of solutions formed from 300 mg in 0.6 mL d_6-DMSO (referred to as ~2.9 M) for raw, vacuum-exposed, 5 nm.min^{-1} and 14 nm.min^{-1} residual crucible material. **Figure 7-17** outlines the plethora of new peaks detected in both the FAI and H_2O regions.

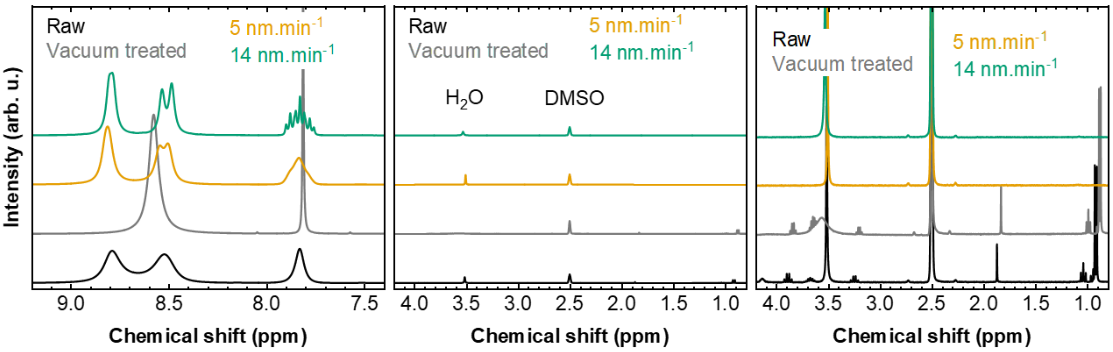

Figure 7-17 ^{1}H-NMR spectra of high concentration FAI from residual crucible material and raw powder with and without exposure to high vacuum for 12 hours. The water section of the ^{1}H-NMR spectrum is shown twice, indicating the change in the water peak intensity between samples which explains the differences in splitting behavior (*middle*). Also shown in a magnified view of this section to shown the plethora of new peaks (*right*). Reproduced from Wiley-VCH GmbH ©2025 with permission.[504]

First, the inconsistent peak splitting must be addressed. Some high concentration samples exhibited peak splitting, while others did not. This is attributed to water-induced peak splitting arising from a change in measurement routine. Some samples were not measured for some time after dissolving, allowing excess water to contaminate the sample, as shown in the higher water peak. While this has an impact on peak splitting and peak shift, the primary information remains unchanged. To confirm changes in relative concentration are not the cause for peak splitting, ^{1}H-NMR measurements of 600 mg raw FAI in 0.6 mL d_6-DMSO, plus a 30 mg in 0.6 mL d_6-DMSO dilution of this solution are present in **Figure S7-3**, which do not observe peak splitting, only an expected shift in peak position, as seen in **Chapter 6**.[221]

The key information from these high concentration spectra is the plethora of new peaks detected in the H_2O region. Due to sample acidity and water content, which also shifts peaks between the raw and vacuum-treated powders, precise identification of these impurities is non-trivial, they are assumed to be residual material from the fabrication of the FAI powder.[170,533] Two peaks can be assigned to acetic acid (1.87 pm singlet) and diethyl ether (1.04 ppm triplet), which are used in FAI production, giving credence to this assumption.[533] Impurity peaks remain in samples exposed to high vacuum (10^{-6} mbar) for 12 hours, indicating that they are not volatile under vacuum exposure, and may still be present during the initial heating of material. They are absent in spectra for residual crucible material. This indicates that they are removed during sample heating and are unlikely to be due to sample contamination before or during the ^{1}H-NMR measurement.

7.5.2.2 XPS measurements of residual crucible material

Peak positions of the FAI material for the C 1s and N 1s regions of the XPS spectra, shown in **Figure 7-18**, were obtained by Dr. Suresh Maniyarasu (HZB), and are mostly consistent with previous literature.[534–536] Inconsistent with this literature are the small additional peaks, at ~287.5, 284.0 and 282.0 eV in the C 1s region, and at 398.0 eV in the N 1s region. These peaks can potentially be assigned to impurities, either those observed in **Figure 7-16**, or residual decomposition products. The absence of new peaks in the 19 nm.min^{-1} carbon spectrum means no additional information about the properties of the observed coke substance is obtained. If it is amorphous carbon, all primary peaks will overlap with existing FAI peaks, with the primary peak at ~287 eV, which could potentially account for the local levelling of the signal.[537]

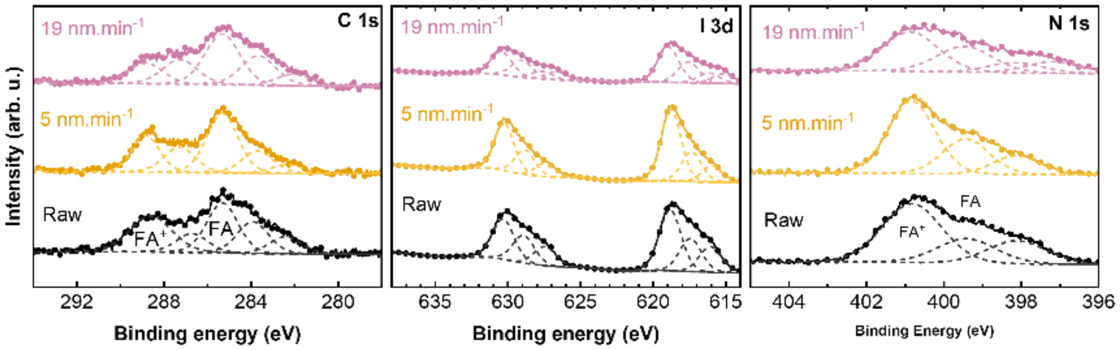

Figure 7-18 XPS spectra of raw FAI powder compared to residual material at baseline (5 nm.min^{-1}) and elevated (19 nm.min^{-1}) deposition rates. Shown are the C 1s (*left*), I 3d (middle) and N 1s (*right*) regions of the XPS spectra. Measurement performed by Dr. Suresh Maniyarasu (HZB). Reproduced from Wiley-VCH GmbH ©2025 with permission.[504]

Dr. Suresh Maniyarasu (HZB) also obtained XPS spectra of residual inorganic materials PbI_2, $PbBr_2$ and CsI from Process B with and without a 21 nm.min^{-1} perovskite deposition, which are shown in **Figure 7-19**. Inorganic materials are assumed to behave in a similar manner to Process A. The metallic and halide components of these spectra do not display new peaks or noticeable changes in peak intensity when comparing crucible material pre- and post-deposition, indicating no substantial change in material for high-rate samples. Increased carbon signals post-deposition are assumed to be cross contamination from FAI products during deposition. Cross-contamination has been visually observed in inorganic materials for Process A, with an extreme example shown in **Figure S7-4**.

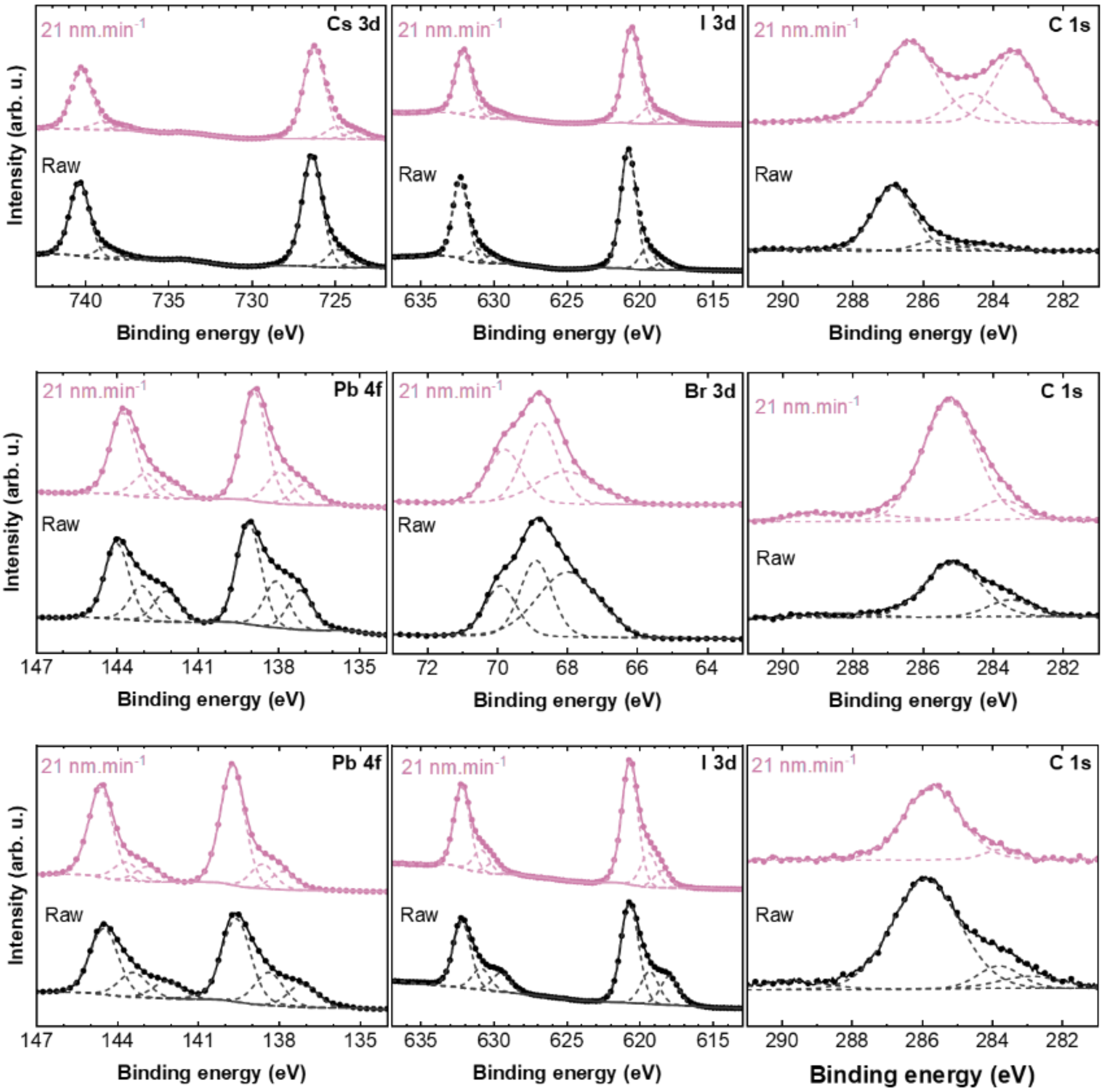

Figure 7-19 XPS spectra of raw inorganic materials compared to residual material at elevated (21 nm.min^{-1}) perovskite deposition rates. Shown is CsI (*top*), $PbBr_2$ (*middle*) and PbI_2 (*bottom*). Each set shows the metallic region (*left*), halide region (*middle*) and carbon region (*right*), which reveals the potential presence of cross-contamination. Measurement performed by Dr. Suresh Maniyarasu (HZB). Reproduced from Wiley-VCH GmbH ©2025 with permission.[504]

7.5.2.3 Impact of crucible shape on material decomposition

Recent literature has highlighted the strong impact of crucible shape on sublimation behaviour. Furthermore, Process A and Process B use different types of crucible. Process A uses an 8 ccm conical crucible, while Process B uses a 1 ccm cylindrical crucible. It was considered prudent to perform similar analysis as outlined above on Process B 1 ccm crucible.

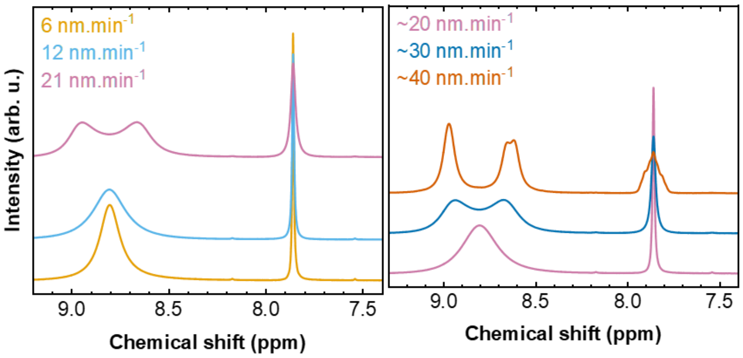

Figure 7-20 ^{1}H-NMR spectra of FAI harvested from residual crucible material after various perovskite depositions using cylindrical crucibles from Process B (*left*) and Process A (*right*). Reproduced from Wiley-VCH GmbH ©2025 with permission.[504]

^{1}H-NMR spectra, shown in **Figure 7-20**, already reveals a significant change. The rate-dependent ^{1}H-NMR trend of Process B is similar to **Figure 7-14**, but is offset. Despite the comparable perovskite deposition rates, the 21 nm.min^{-1} Process B spectra is more similar in characteristic signal shape to the 9 nm.min^{-1} deposition rate of Process A than the 19 nm.min^{-1}. The most likely cause for this is an increase in the effective thermal conductivity of the material. While the actual thermal conductivity of FAI is the same, in a cylindrical crucible the surface area exposed to the crucible is higher for an equivalent mass of FAI.[521] To confirm this theory, Julian Petry recreated the high rate spectra of Process A using 10 ccm cylindrical crucibles. As perovskite was not formed, these rates are given as approximate values, corresponding to the expected perovskite thickness. They reveal an even greater offset behaviour, with lower peak slitting for ~40 nm.min^{-1} equivalent sublimation rates than the 19 nm.min^{-1} spectra.

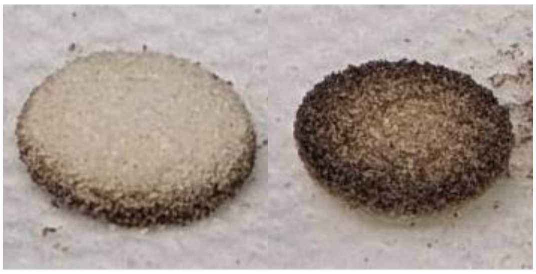

Figure 7-21 Residual crucible material at the ~40 nm.min^{-1} equivalent sublimation rate. Original (raw) source material was taken from the same batch of FAI as **Figure 7-14**. Reproduced from Wiley-VCH GmbH ©2025 with permission.[504]

When we observe residual crucible material from the ~40 nm.min^{-1} rate, as in **Figure 7-21**, this difference becomes even more apparent. Despite the doubling in effective sublimation rate, coke formation is roughly comparable to the 19 nm.min^{-1} residual crucible material in **Figure 7-14**.

XPS measurements of Process B residual material by Dr. Suresh Maniyarasu (HZB) from cylindrical crucibles, equivalent to the NMR measurements of **Figure 7-20**, are provided in

Figure 7-22, and reveals a slightly different trend to the conical crucibles of Process A. The residual material peaks from the raw powder decrease in intensity with increasing deposition rates. If the initial impurities are synthesis impurities, this would indicate a reduction in synthesis impurities with the exception of the observed coke. Overall, the XPS measurements of Process B powders reinforce the observed differences in ^{1}H-NMR spectrometry between Process A and B.

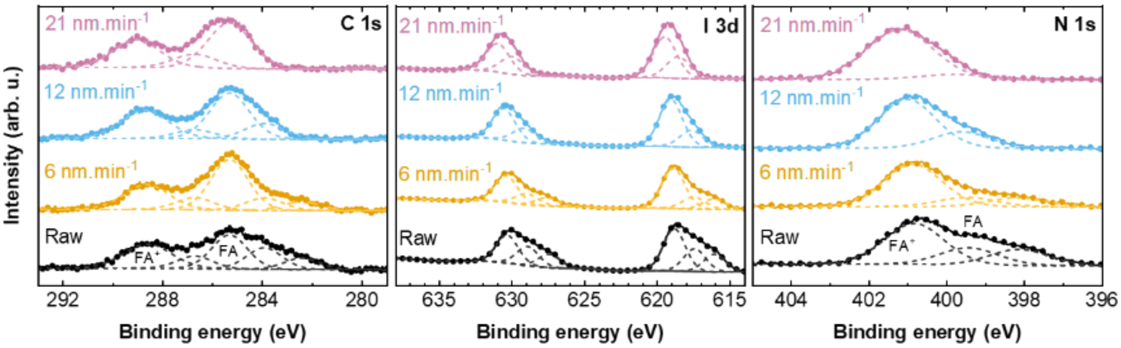

Figure 7-22 XPS spectra of raw FAI powder compared to residual material various deposition rates from Process B. Measurement performed by Dr. Suresh Maniyarasu (HZB). Reproduced from Wiley-VCH GmbH ©2025 with permission.[504]

The results of this section reveals that decomposition, characterized by peak splitting and coke formation, follows an expected rate dependency. However, crucible shape also strongly impacts this behaviour, reinforcing the need to consider proper crucible design to achieve high-rate processes that are replicable across reactors and processes.

7.6 Strategies to realise elevated deposition rates without performance losses

In this section we will discuss two methods to achieve higher deposition rates. First is a horizontal scaling method, using an additional organic source to reduce effective FAI sublimation rates. Next, we will investigate the potential of preconditioning the FAI material, as used by our collaborators at HZB, and using cylindrical crucibles to reduce the PL inhomogeneities. This study was the focus of Process B and a more in-depth discussion is present in the associated publication.

7.6.1 High-rate perovskite deposition with dual organic sources

With the cause of the reduction in device performance at elevated rates identified as FAI decomposition during high-rate sublimation, we consider if high deposition rates can achieve more comparable device performance in the absence of such deposition. By utilising two organic cation sources FAI rate can be horizontally scaled, allowing an investigation into if alternative issues will limit perovskite device performance at high deposition rates. As the aim is directly compare with single source results, conical crucibles are utilised despite the potential for reduced decomposition demonstrated in **Section 7.4.3**. Dual source depositions at inorganic sublimation rates equivalent to the 14 nm.min^{-1} and 19 nm.min^{-1} deposition single source depositions were considered to allow direct comparisons. As discussed, a slight reduction in final film thickness (560 nm to 520 nm) results in the stated deposition rates being slightly lower comparable single source depositions.

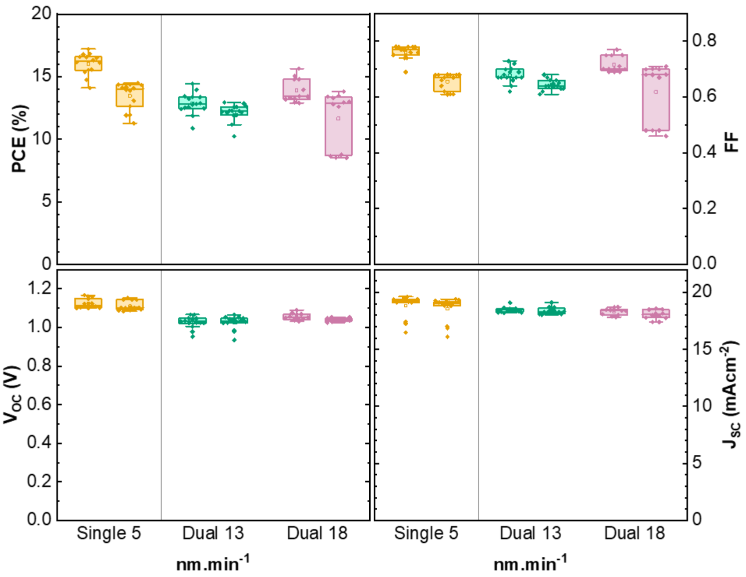

Figure 7-23 Photovoltaic parameter statistics derived from forward and reverse *J-V* scans for champion batches using two FAI sources to achieve elevated deposition rates compared to the baseline 5 nm.min^{-1} single FAI source shown in **Figure 7-7**. Reproduced from Wiley-VCH GmbH ©2025 with permission.[504]

Dual FAI source 18 nm.min^{-1} samples manage to achieve a much higher PCE than the single source 19 nm.min^{-1} samples, as shown in **Figure 7-23**. Some 18 nm.min^{-1} samples demonstrated increased hysteresis, yet the champion device under MPP tracking did not, with MPP and J-V scans shown in **Figure 7-24**. The champion dual FAI source 18 nm.min^{-1} device achieved a PCE of 14.0%, FF of 0.71, V_{OC} of 1.057 V and J_{SC} of 18.5 mA.cm^{-2}. EQE derived bandgap is also unchanged between deposition rates and source setups.

Table 7-2 Photovoltaic parameters of champion single-junction PSCs with a dual FAI source at various deposition rates. Average values for *J-V* parameters are presented in brackets.

Solar cell	PCE [%]	FF [%]	V_{OC} [V]	J_{SC} [mA.cm^{-2}]	
				Solar simulator	EQE
13 nm.min^{-1}	14.4 (12.9)	73 (68)	1.07 (1.03)	19.5 (18.5)	17.1
	13.0 (12.1)	68 (64)	1.07 (1.03)	19.1 (18.4)	
18 nm.min^{-1}	15.7 (13.8)	77 (72)	1.09 (1.05)	18.7 (18.3)	17.9
	13.8 (11.7)	71 (62)	1.05 (1.04)	18.6 (18.1)	

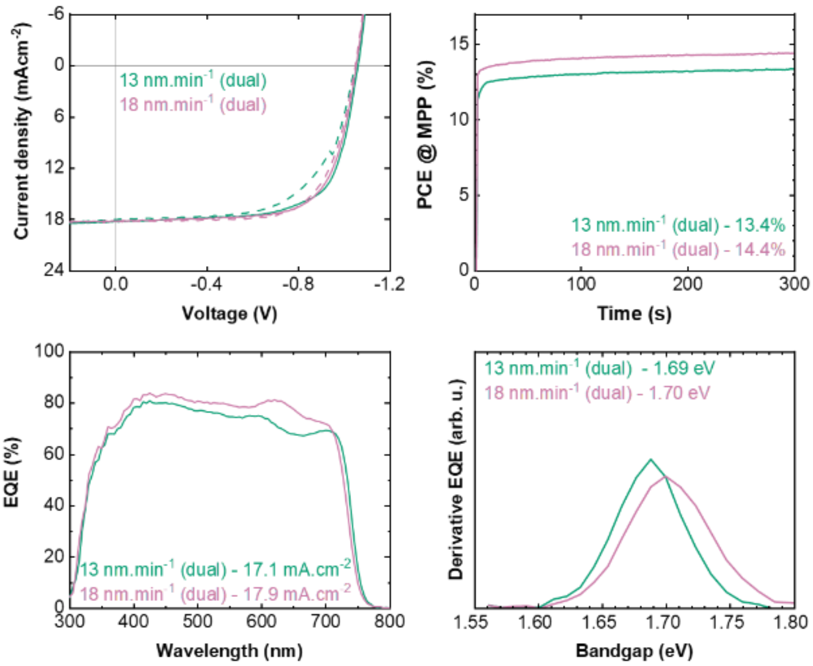

Figure 7-24 Additional photovoltaic parameter analysis for dual FAI source perovskites. (*Top-left*) J-V scans, (*top-right*) MPP, (*bottom-left*) EQE and (*bottom-right*) EQE derived bandgap corresponding to the champion devices of **Figure 7-23**. Reproduced from Wiley-VCH GmbH ©2025 with permission.[504]

Process and performance repeatability both improve when utilising a dual FAI source setup, as shown in **Figure 7-25**. This comparisons is not perfect, as Run 2 and Run 3 were single-junction devices with ALD-SnOx instead of BCP as an ETL, fabricated during tandem optimization, as will be addressed in **Section 7.6**. Hence the CV_{mean} of 0.048 cannot be considered entirely correct as the data sets are not entirely comparable. However, the increased repeatability remains evident, especially in optimal FAI rate. This is potentially attributed to the reduced process pressure first outlined in **Section 7.2**. The reduced chamber pressure for high-rate dual FAI source depositions means Γ_{eff} does not vary substantially between or within depositions.

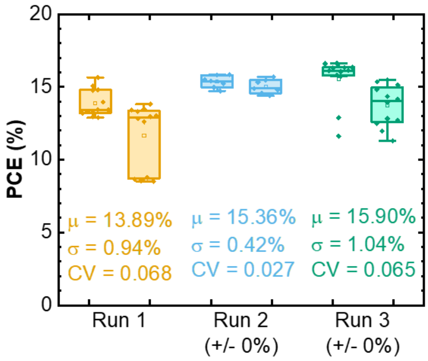

Figure 7-25 Repeatability of dual FAI source 18 nm.min^{-1} perovskite deposition rates by comparing the champion set from several batches. Provided in the graph is the relevant values of the mean (μ), standard deviation (σ) and coefficient of variability (CV) for each batch. Reproduced from Wiley-VCH GmbH ©2025 with permission.[504]

Investigations of bulk properties using PL imaging in **Figure 7-26** reveal a significant improvement in sample uniformity, indicating this process is sufficient to avoid spit-defects. XRD patterns continue to deviate between deposition rates, also relative to equivalent rates shown in **Figure 7-9**. Specifically, the (0 0 1) peak area is consistently smaller for dual source sample. This means that, while the (0 1 2)/(0 0 1) ratio is broadly comparable between single and dual source, the (0 1 1)/(0 0 1) ratio is vastly different, and the trend between ~13 nm.min^{-1} and 18 nm.min^{-1} is reversed. These results indicate crystal growth is impacted both by perovskite deposition rate and either FAI sublimation rate or reactor pressure, as these effects can not be disentangled in the current work. SEM images of 18 nm.min^{-1} dual FAI source compared to 5 nm.min^{-1} single FAI source perovskites is provided in **Figure S7-5**, and does not appear to show meaningful differences.

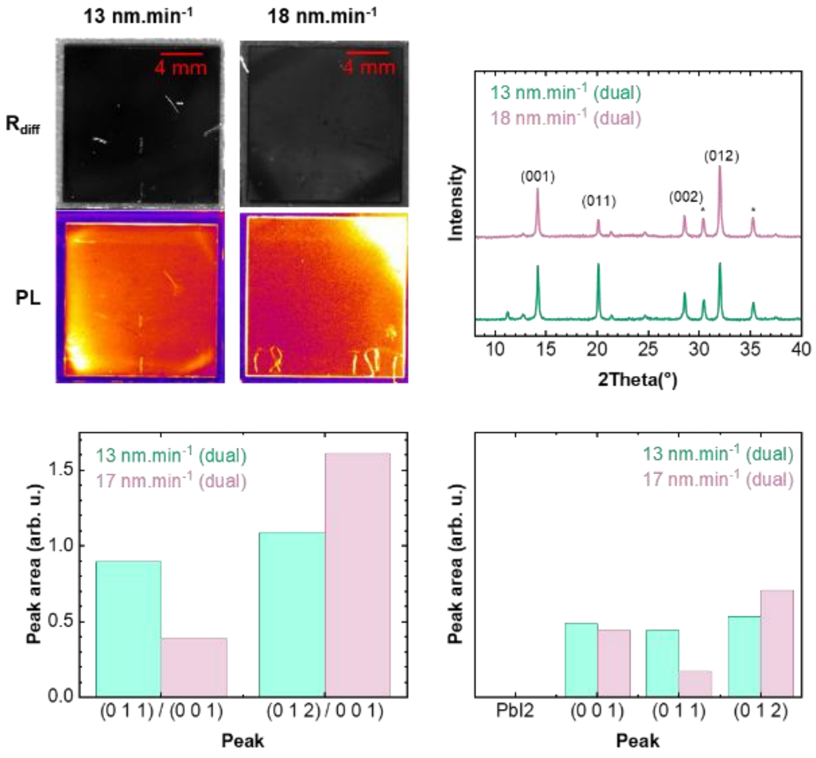

Figure 7-26 Bulk material analysis of dual FAI source perovskites. (*Top-left*) PL maps of each dual FAI source deposition rate. Shown is R_{diff} (*top*), which uses a neutral density filter to represents visual data, and filtered under a longpass 775 nm filter (*bottom*), revealing no inhomogeneities at high perovskite deposition rates. (*Top-right*) XRD spectra of films grown at each studied perovskite deposition rate with relevant Miller Indices labelled, and ITO denoted using *. Peak area (*bottom-left*) and peak area ratio (*bottom-right*) for the shown XRD spectra. Reproduced from Wiley-VCH GmbH ©2025 with permission.[504]

7.6.2 Alternative methods to avoid spit-defects

As FAI decomposition during sublimation is tied to the formation of spit defects, there exist two potential methods to decrease the formation of spit-defects. The first is to utilise cylindrical crucibles, as was shown in **Section 7.3.3** to reduce coke formation and presence of HI. The next is to precondition the FAI by keeping it at a baseline deposition rate for a set period prior to deposition. Preconditioning would remove the contaminants observed in **Section 7.3.2**, facilitate thermalisation to reduce temperature inhomogeneities and will decrease process pressure and outlined in **Section 7.3.1**.

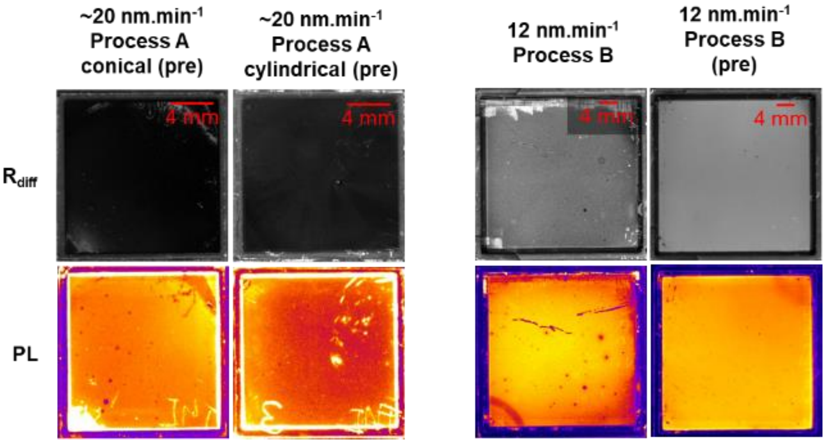

Figure 7-27 PL maps of samples prepared using pre-conditioning and different crucibles to demonstrate a reduction in the µm-scale dots. Also shown are 12 nm.min^{-1} samples prepared Process B with and without the pre-conditioning. Approximate (~) values are used when the perovskite thickness is not known. Process B samples prepared by our collaborators (HZB). Reproduced from Wiley-VCH GmbH ©2025 with permission.[504]

PL maps, as shown in **Figure 7-27**, reveal that both methods are able to reduce the density of µm-scale dots. Preconditioning a conical FAI crucible caused a significant in this density compared to the 19 nm.min^{-1} sample of **Figure 7-10**, and µm-scale dots are completely absent when coupling preconditioning with a cylindrical crucible. Process B demonstrated a similar reduction in µm-scale dots when preconditioning during their perovskite deposition process.

7.7 Monolithic tandems at elevated perovskite deposition rates

As an outlook, this section will consider the impact of deposition rate on the performance of various perovskite/silicon monolithic tandem solar cells. Only two deposition rates are considered, the baseline 5 nm.min^{-1} single FAI source deposition and the elevated 18 nm.min^{-1} dual FAI source deposition. We utilize a nanotextured (texture size <1 µm) silicon subcell provided within the NEXUS project by CEA INES.

The perovskite composition is unchanged and subcells take the form: substrate/MeO-2PACz/perovskite/C_{60}/ALD-SnOx/electrode. Tandems used IZO/Ag-fingers as the electrode with an MgF_2 antireflective coating, as optimized in **Chapter 4**, while single-junction devices continued to use Au. Single-junction devices were manufactured simultaneously to tandems to provide a comparison. Due to persistent discrepancies between EQE derived J_{SC} and J-V derived J_{SC}, tandem performances and J_{SC} values were shifted based on the EQE. **Figure 7-28** outlines the device performances of champion batches. Tandems achieve a champion PCE of

23.9% (FF = 0.76, V_{OC} = 1.73 V, J_{SC} = 18.2 mA.cm^{-2}) for 5 nm.min^{-1} and 19.0% (FF = 0.70, V_{OC} = 1.74 V, J_{SC} = 15.6 mA.cm^{-2}) for 18 nm.min^{-1} devices.

Table 4-4 Photovoltaic parameters of champion single-junction PSCs at baseline and elevated deposition rates, along with two-terminal tandem PCE on nanotextured silicon. Due to the often strong disagreement between EQE and J_{SC} for tandem devices, EQE values were used to calculate the performance of tandem devices.

	PCE [%]	FF [%]	V_{OC} [V]	J_{SC} [mA.cm^{-2}]	
				Solar simulator	EQE
Single-junction 5 nm.min^{-1}	14.5 (13.6) 9.9 (9.3)	69 (67) 50 (48)	1.14 (1.12) 1.12 (1.10)	18.5 (18.2) 17.7 (17.4)	16.5
Single-junction 18 nm.min^{-1}	17.4 (15.2) 16.2 (12.6)	77 (72) 74 (62)	1.17 (1.11) 1.14 (1.09)	20.2 (19.0) 20.0 (18.4)	17.6
Tandem (nano.) 5 nm.min^{-1}	23.9 (23.1) 23.9 (21.8)	76 (73) 76 (70)	1.75 (1.73) 1.72 (1.70)		18.2
Tandem (nano.) 18 nm.min^{-1}	19.2 (15.4) 15.4 (14.1)	70 (68) 56 (54)	1.78 (1.75) 1.72 (1.64)		15.6

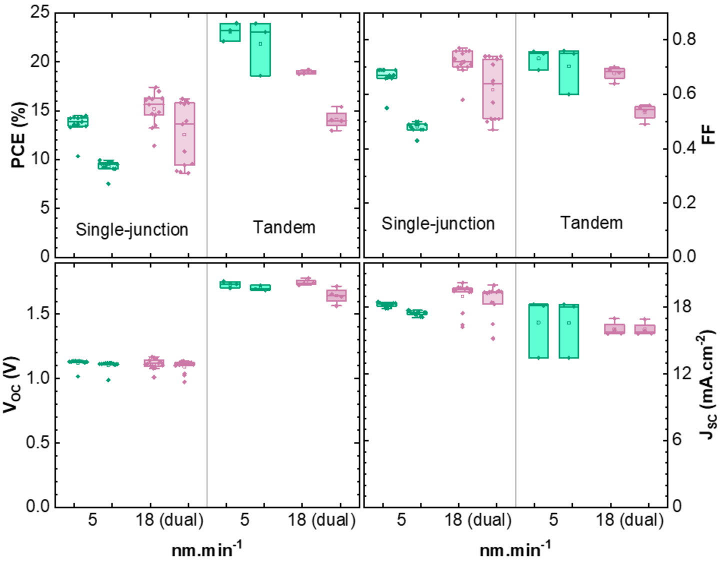

Figure 7-28 Photovoltaic parameter statistics derived from forward and reverse *J-V* scans for tandem devices on nanotextured silicon, along with corresponding single-junction devices fabricated in the same batch.

What is noteworthy is that single-junction 18 nm.min^{-1} represents the highest reported value for this rate observed. Despite this, the tandem devices barely outperform the single-junction, and show substantial hysteresis. EQE measurements, outlined in **Figure 7-29**, reveal that the difference arises from 5 nm.min^{-1} tandem perovskites outperforming the comparable single-junction in EQE, while 18 nm.min^{-1} tandem perovskites are significantly lower. It is expected that the textured surface will enhance light incoupling, as briefly mention in **Chapter 4**. It is possible that textures lead to different incorporation rates for organic cations, however samples with higher or lower FAI rate than the optimum showed similar trends between single-junction and tandem PCE, as shown in **Figure S7-6**. These results highlight that more research is required into how perovskite formation on textured surfaces changes with respect to deposition rate.

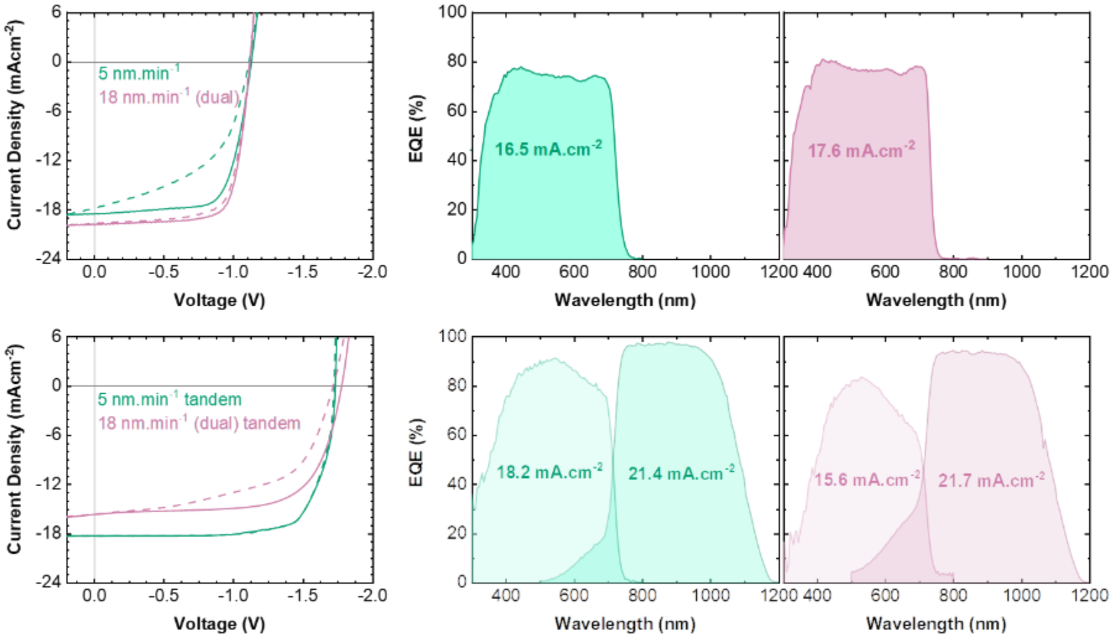

Figure 7-29 (*Left*) *J-V* scans of single-junction (*top*) and tandem (*bottom*) perovskite solar cells on nanotextured silicon, along with EQE spectra for 5 nm.min^{-1} devices (*middle*) and for 18 nm.min^{-1} devices (*right*).

7.8 Summary

In this chapter, we explored the impact of deposition rate on the performance of wide-bandgap FA-based co-evaporated PSCs. We reveal that the decline in deposition rate is due to FAI decomposition and, by preventing degradation, achieved the highest recorded deposition rate for FA-based co-evaporated perovskites at the time, with only a 9%$_{rel}$ drop in PCE compared to the baseline values.

We first outlined a labelling method that is resilient to potential variations in reactor conditions that would occur between different research laboratories or at different deposition rates. We also briefly explored how reactor conditions may vary based on deposition rate and methods to compensate for those variations. Our analysis reveals that the high pressures observed at high deposition rates can lead to material tooling factors shifting between and within processes, increasing variability.

Varying deposition rate from 5 nm.min^{-1} to 19 nm.min^{-1} resulted in a 23%$_{rel}$ drop in PCE when increasing deposition rate, along with a significant increase in cross batch variability. Using EQE, XRD and EDX spectra, we reveal that the bulk perovskite remains similar based on deposition rate, with no change in bandgap or composition and slight but random changes in crystal orientation. However, PL mapping indicates that high rates correspond to the emergence of µm-scale inhomogeneities, which explains the decline in device performance. EDX measurements of these dots reveal them to be carbon-rich and buried within the perovskite layer.

To investigate these inhomogeneities we analysed the residual crucible material with a combination of ^{1}H-NMR and XPS measurements. Coke formation is observed on the edges of the residual crucible material, which also have trace HI present. The presence of these products is found to be dependent on both crucible shape and sublimation rate. By utilising a second FAI cation source, we manage to achieve a deposition rate of 18 nm.min^{-1} without the deposition of coke on our substrates, reducing the loss in PCE to 9%$_{rel}$ and increasing repeatability. We also briefly explore the potential for preconditioning of the FAI material and utilising cylindrical crucible in order to minimise coke formation.

Applying our baseline and elevated deposition rates to monolithic perovskite/silicon tandem devices, and considering applicable optical enhancements addressed in **Chapter 4** results in champion tandem device performances of 23.9% for nanotexture silicon bottom cells. When comparing this to the enhanced rate devices we observe a drop of PCE of 18%$_{rel}$ when using textured silicon bottom cells. These results highlight the varied possible impacts of deposition rate on perovskite solar cells, and provides strategies to minimize the most egregious negatives associated with increasing deposition rate.

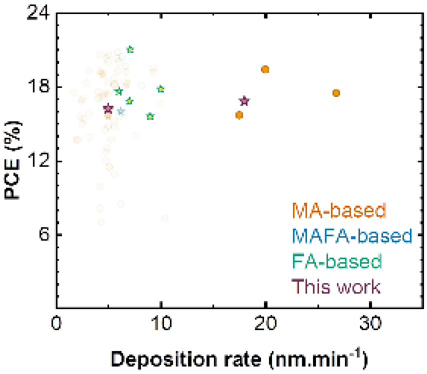

Figure 7-30 Device PCE plotted against deposition rates of organic-inorganic vacuum-processed perovskite absorbers. Circle points represent $E_g < 1.65$ eV, star points represent $E_g > 1.65$ eV. A tabulated set of all values is presented in the Appendix, **Table S7-1**.

When the results presented in this chapter are framed in the broader co-evaporated literature base, as outlined in **Figure 7-30** and **Table S7-1**, we can confirm our 18 nm.min^{-1} represents the highest reported deposition rate for FA-based perovskites. Furthermore, our deposition rate is nearly comparable rate the highest MA-based perovskites. This is a notable achievement, as literature has not indicated concerns for MAI degradation in the studied sublimation rate region.[74,75,220,456] Hence the high deposition rates reported for MA-based perovskites do not have to contend with the similar organic cation decomposition mechanisms.

8 Conclusion and outlook

8.1 Conclusion

Perovskite solar cells (PSCs) are an incredibly promising technology for high performance multi-junction photovoltaics. However, widespread commercialisation requires several key challenges to be solved, which can be roughly divided into developing stable and scalable deposition methods that are compatible with industrial manufacturing without sacrificing their promising achieved power conversion efficiencies (PCEs). This thesis evaluates co-evaporated perovskites as a fabrication method that can potentially overcome these challenges. In brief, the contributions of this thesis are: creation of high-efficiency 4T tandem photovoltaics through optical optimizations of the semitransparent (ST) PSC, development of a vapour-phase deposition method for self-assembled monolayer based hole transport layers (SAM-HTLs), analysis of the interface between SAM-HTLs and co-evaporated perovskites and a substantial increase in the deposition rate of FA-based co-evaporated perovskites.

Chapter 4 provides a guide for formation of high performance 4T tandem photovoltaics, addressing **Challenge 1** and **Challenge 2**. We explore the role of transparent conductive oxides (TCOs) and antireflection coatings on the near infrared (NIR) transmission of solution-processed ST-PSCs. Optically optimized devices achieved a weighted NIR transmission of 88.8%. By applying these optimizations to a 4T perovskite/CIGS tandem solar cell via an equivalent optical filter we reported on a maximum PCE of 27.3%, a champion at time of publication. All vapour-phase, 4T perovskite/CIGS tandem solar cells with a co-evaporated absorber achieved only 23.8% due to absorber incompatibility with IO:H leading to reduced NIR transmission and the use of Spiro-TTB instead of 2PACz. Finally, a series of optical optimizations unveiled the method to achieve a theoretical 4T perovskite/CIGS tandem efficiency of 29.5%, and revealed that bandgap matching is relatively unimportant for high performance 4T perovskite/CIGS tandem solar cells. This work provides an important guide for the capacity of optical optimization in achieving high-performance 4T tandem solar cells.

Chapter 5 develops and optimizes vapour-phase self-assembled monolayer based hole-transport layers (SAM-HTLs) that preserve their high quality interfacial properties, addressing **Challenge 3** and **Challenge 5**. We confirm using XPS and FTIR that there are no significant changes in material degradation or substrate binding by comparing evaporated and solution-processed nPACz layers. The process parameters were optimized, revealing an optimum thickness of 6 – 8 nm. When combined with solution processed and co-evaporated perovskites, equivalent or slightly improved interfacial properties are observed. As part of our interfacial investigation, we uncover clear trends of improved wettability for solution-based perovskite solvents. Furthermore, for monolayer SAM-HTLs, surface morphology and crystal characteristics of subsequently deposited absorbers are found to be similar for solution-processed and co-evaporated perovskites. Non-monolayer SAM-HTLs were also similar for solution-processed perovskites, with the differences for co-evaporated perovskites being discussed in **Chapter 6**.

Chapter 6 analysed interfacial interactions between phosphonic acid containing SAM-HTLs and co-evaporated perovskite films in order to address **Challenge 4** and **Challenge 5**. We find that the presence of interfacial phosphonic acids lead to an increase in organic cation absorption by 65 – 100% depending on the material and deposition method, which is independent of changes in surface polar free energy and was replicated using a monolayer 4dPA. Furthermore, their presence suppresses formation of δ-$FAPbI_3$ and crystalline PbI_2. We determine, using a combination of liquid phase ^{1}H-NMR and density functional theory computations, that the interaction takes the form of hydrogen bonding between phosphonic acids and the halide component of the organic cation, resulting in kinetic trapping of α-$FAPbI_3$. This interaction improves interfacial properties, but do not necessarily result in improved device performance, with PCEs of 16.2% for unwashed and 17.0% for washed solution-processed 2PACz.

Chapter 7 explores and explains the impact of deposition rate on the performance of wide-bandgap FA-based co-evaporated PSCs in order to respond to **Challenge 6**. We observe a $23\%_{rel}$ drop in PCE when increasing the deposition rate from 5 nm.min^{-1} to 19 nm.min^{-1}, despite a lack of consistent change in bandgap or substantial change in x-ray diffraction patterns. Further investigation into perovskite bulk properties reveals high rates lead to unexpectedly severe FAI decomposition on the edges of the material, forming a coke substance that is deposited onto the sample as a spit defect. Coke formation and presence is dependent on crucible shape, sublimation rate and if the material was preconditioned by maintaining the source at an elevated temperature for an extended time before deposition. Utilising a second FAI source inhibits coke deposition at high deposition rates and reduces PCE loss to $9\%_{rel}$. Fabricating monolithic tandem solar cells with baseline and elevated deposition rates reveals a decrease in performance for high deposition rates on nanotextured perovskite/silicon tandem solar cells which are not mirrored by low deposition rates. We achieve PCEs of up to 23.9% for nanotextured silicon bottom cells.

8.2 Outlook

While **Chapter 4** has provided a theoretical guide for further improving NIR transmission of ST-PSCs, these strategies need to be systematically applied to demonstrate the validity of our simulated results. Furthermore, the performance of co-evaporated perovskite 4T tandem solar cells lags significantly behind the solution processed equivalent. The reduction in NIR transmission directly results in a $1.2\%_{abs}$ drop in the CIGS subcell due to a 2.6 mA.cm^{-2} drop in J_{SC}. While the solution-processed perovskite gains $1\%_{abs}$ PCE under maximum power point tracking when using an IO:H substrate, due to a substantial increase in J_{SC}, the co-evaporated absorber appears incompatible with this substrate. Hence, further study is required to either develop or modify TCOs that exhibit low parasitic absorption and high NIR transmission while remaining compatible with co-evaporated absorber materials. Furthermore, recent literature on seed layers has provided potential methods to overcome substrate limitations of co-evaporated perovskites.[214,222] Seed or template layers on overcoming substrate limitations may enable perovskite deposition on IO:H without modification. Finally, even on ITO, solution-processed perovskites outperformed co-evaporated perovskites by 0.9%$_{abs}$. This can be attributed to the use of 2PACz as a HTL, and the lack of effective vapour-phase bulk passivants resulting in a 60 mV$_{abs}$ drop in V_{OC}. While **Chapter 5** and **Chapter 6** addresses this first point, poor bulk properties and a lack of vapour-phase passivation strategies continue to limit achievable PCEs.[161,537–539] Some research into vapour-phase passivation has already occurred,[213,508,540] and needs be applied to high-performance co-evaporated ST- PSCs to evaluate the new comparative baseline.

The vapour-phase self-assembled monolayers developed in **Chapter 5** have enhanced flexibility, their performance comparative to other upscaling deposition methods remains to be proven. In some aspects, subsequent literature has already demonstrated use cases, such as for deposition over textured surfaces and large areas, as well as their impact on co-evaporated perovskite growth.[261,386,447] However, a comparison of large-area suitability between different SAM-HTL deposition techniques has not currently been reported, and is important to evaluate if this deposition technique is suitable for commercial-scale manufacturing. Furthermore, while we did not observe material degradation from the evaporation process, subsequent literature has reported it possible for sufficiently high deposition rates,[402] indicating a greater understanding of optimal process parameters is required for widespread adoption of this technique. Next, there does not yet exist an understanding on how SAM-HTL deposition method will impact long-term device stability under operational conditions. As this is a critical part of the perovskite research field, it is important to explore if this technique will impact it. Finally, as new SAM-HTLs for PSCs continue to be developed, any new material would also need to be independently investigated to ensure evaporation does not change material properties.

Chapter 6 found that the investigated interfacial effect is replicable for monolayer materials, but the low conductivity of 4dPA inhibits the effective device efficiency. As 4dPA utilises an alkyl linker chain, conductivity can easily be improved *via* alternate linker chains with improved conductivity, such as phenyl groups, or using naturally di-phosphonic acid SAMs.[373,541] Furthermore, while the impact on perovskite phase formation has so far only been reported for vapour-phase perovskites,[221,459] overall interfacial effects may not be limited to benefiting co-evaporated perovskites. Hydrogen bonding is a common effect in perovskites, is important for Dion-Jacobson and alternating-cation-interlayer 2D-perovskite structures,[146,542–544] and can potentially impact 2D perovskite formation.[545,546] Furthermore, hydrogen bonding substrates, including those using SAM bilayers,[547] have been shown to passivate the rear contact of solution-processed perovskites.[544] Hence, developing hydrogen bonding substrates for co-evaporated perovskites are potential pathways to modify the buried interface and improve overall device performance independent of fabrication method. Furthermore, performing the reverse action and applying substrates and buried interface passivation strategies that were developed for solution-processed perovskites to co-evaporated perovskites can be expected to positively impact perovskite formation and merits further study.

The results presented in **Chapter 7** remain well below the deposition rates required for commercial fabrication (~1000 nm.min^{-1}).[51] Combining preconditioning with multiple cylindrical sources are expected to lead to incremental increases in achievable deposition rate, but it is obvious that any substantial increase will inevitably reach sufficiently high pressures to disrupt perovskite growth. This higher pressure can be controlled in two ways within the studied vapour-phase deposition system. FAI grain size has been found to be substantially impact background pressure,[522] with smaller grains generating higher pressures. A homogenization of source material, such as a pre-processing step to form a uniform pellet similar to those used in close space sublimation, is therefore expected to further decrease pressure at high deposition rates.[211] Reactor design is the next potential method to increase deposition rate. As seen in our mass spectroscopy data, we observe a spike after opening the substrate shutter, indicating some level of precursor build-up within the reactor space, increasing local pressure.[75] Furthermore, changing the relative positions of the crucibles could lead to a higher deposition rate on the substrate for a given crucible deposition rate.[522] Additional process control could be achieved by emulating high-rate MA-based perovskite literature, which included a second quartz crystal monitor directly adjacent to the substrate.[74] Any further reactor optimization for high rates would ideally utilise commercially relevant evaporation chambers using linear sources, which have substantially different evaporation profiles that are expected to exhibit different sublimation behaviour compared to our current point sources.[522]

9 Appendix

9.1 Appendix for Chapter 4

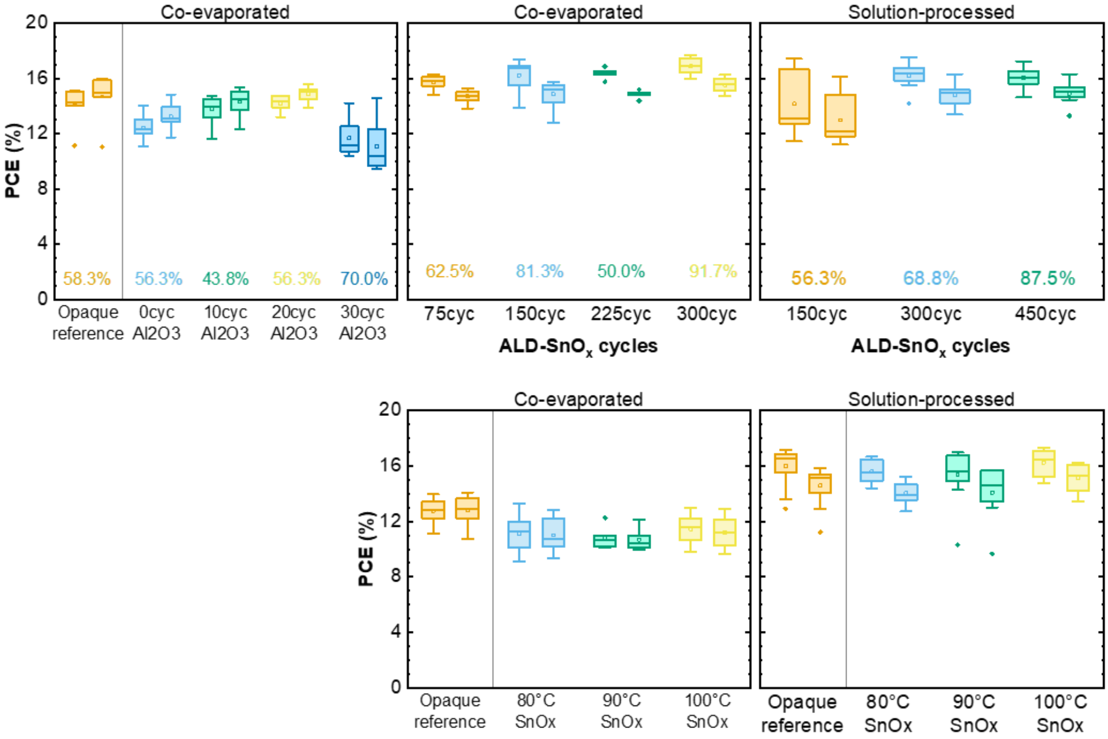

Figure S4-1 Photovoltaic parameter statistics derived from forward and reverse *J-V* scans for various additional SnO_x optimizations series. When an opaque reference is specified, that device utilizes C_{60}/BCP as an electron selective layer, while semitransparent devices utilized C_{60}/SnO_x or $C_{60}/Al_2O_3/SnO_x$. Co-evaporated devices utilized 20 cycles Al_2O_3 between the C_{60} and SnO_x layers unless otherwise specified. (top) Impact of Al_2O_3 or SnO_x thickness, defined by number of cycles, on performance of ST-PSCs and their yield given in (Bottom) Impact of SnO_x deposition temperature on performance of ST-PSCs.

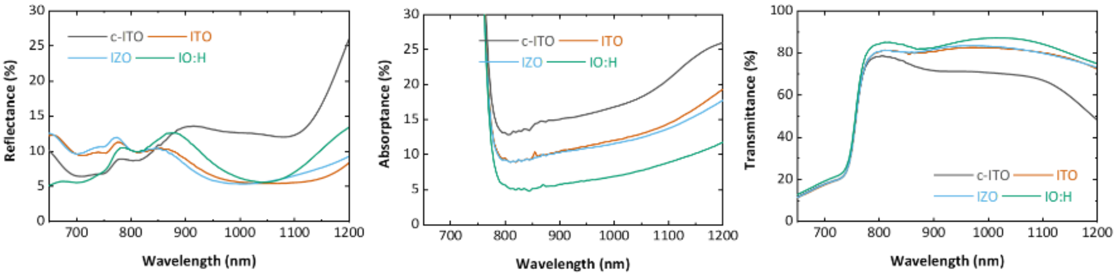

Figure S4-2 TRA measurements of the various TCOs studied in **Section 4.3.1**. Reproduced from Wiley-VCH GmbH ©2022 with permission.[35]

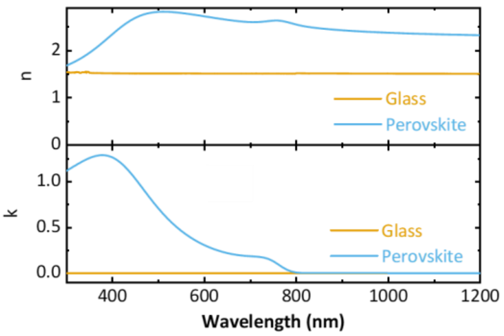

Figure S4-3 Ellipsometry data for glass and perovskite, used in calculations of optimum *n* values for TCO in **Section 4.3.1**.

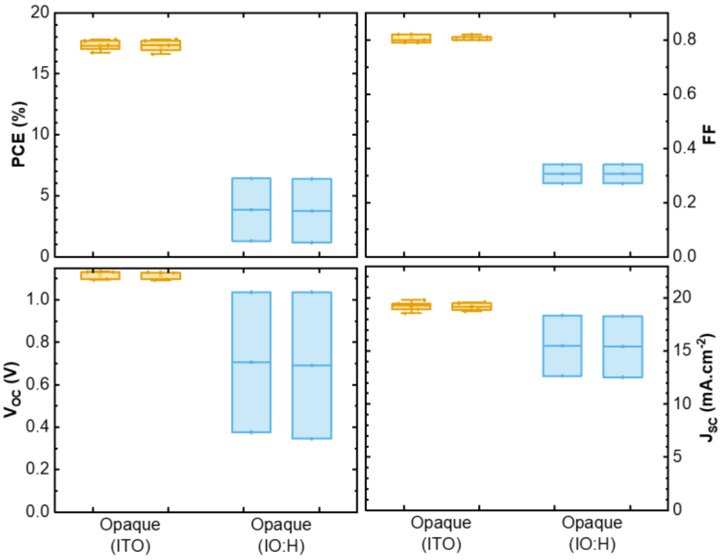

Figure S4-4 Photovoltaic parameter statistics derived from forward and reverse *J-V* scans of opaque co-evaporated devices on IO:H and ITO. IO:H only had two pixels which PCEs above 0.5%.

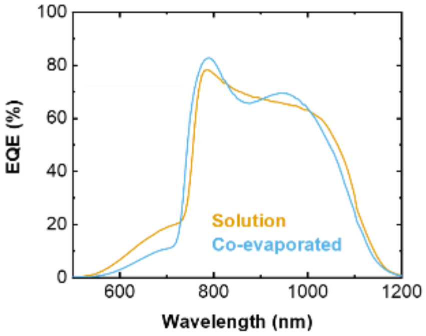

Figure S4-5 Comparison of EQE for CIGS filtered by o-evaporated and solution-processed ST-PSCs with ITO substrates. Adapted from Wiley-VCH GmbH ©2022 with permission.[35]

9.2 Appendix for Chapter 5

Table S5-1 Peak locations of X-ray photoelectron spectra fits for the C 1s region of each nPACz material. Shown is the powder reference (Pow.), evaporated thin film (Evap.), spin-coated layer (Sol.) and estimates determined from a literature reference (Lit.).

	2PACz				MeO-2PACz				Me-4PACz		
	Pow.	Evap.	Sol.	Lit.	Pow.	Evap.	Sol.	Lit.	Pow.	Evap.	Sol.
C-H / C-C	283.7	283.7	283.7	283.9	283.8	284.0	283.7	284.0	284.0	284.0	284.0
C-N	284.5	284.4	284.3	284.8	284.4	284.5	284.3	284.9	285.0	284.7	284.6
C-O-C / C-OH	285.4	285.0	284.9	285.7	285.5	285.6	285.3	285.8	286.2	285.8	285.3

Table S5-2 Full width half maxima of X-ray photoelectron spectra fits for the C 1s region of each nPACz material. Shown is the powder reference (Pow.), evaporated thin film (Evap.) and spin-coated layer (Sol.).

	2PACz			MeO-2PACz			Me-4PACz		
	Pow.	Evap.	Sol.	Pow.	Evap.	Sol.	Pow.	Evap.	Sol.
C-H / C-C	0.83	1.00	1.00	0.84	0.93	0.92	0.80	0.94	0.89
C-N	1.16	1.26	1.20	1.11	1.17	1.08	1.04	1.15	1.12
C-O-C / C-OH	0.82	1.29	1.61	1.36	1.79	1.75	0.94	1.57	1.47

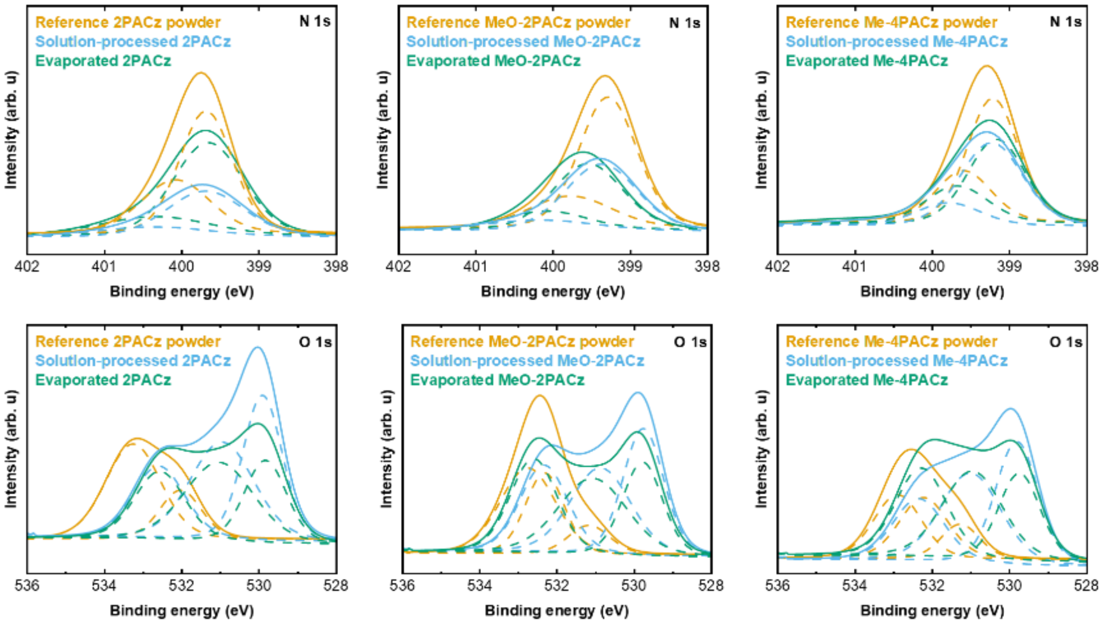

Figure S5-1 X-ray photoelectron spectra fits for the N 1s and O 1s regions of each nPACz material. Shown is a powder reference (orange), a ~6 nm evaporated nPACz thin film deposited onto glass/ITO substrate (dark green) and a nPACz thin film deposited onto a glass/ITO substrate via spin-coating (blue). The solid lines represents fits to the real data points and dashed black lines show the requisite components. Part of figure adapted from Wiley-VCH GmbH ©2022 with permission.[35]

Table S5-3 Peak locatons of X-ray photoelectron spectra fits for the O 1s and N 1s regions of each nPACz material. Shown is the powder reference (Pow.), evaporated thin film (Evap.) and spin-coated layer (Sol.).

	2PACz			MeO-2PACz			Me-4PACz		
	Pow.	Evap.	Sol.	Pow.	Evap.	Sol.	Pow.	Evap.	Sol.
O 1s		529.8	529.9		529.8	529.8		529.7	529.8
O 1s	532.0			531.2			531.3		
O 1s	533.3			532.3			532.2		
O 1s				532.8			532.9		
ITO		531.0	531.0		531.1	530.9		531.0	531.0
ITO		532.6	532.6		532.6	532.3		532.3	532.4
N 1s	399.7	399.7	399.7	399.3	399.6	399.4	399.2	399.2	399.2
N 1s	400.1	400.3	400.4	399.8	400.1	400.2	399.6	399.7	399.8
N 1s							400.6	401	400.7

Table S5-4 Full width half maxima of X-ray photoelectron spectra fits for the O 1s and N 1s regions of each nPACz material. Shown is the powder reference (Pow.), evaporated thin film (Evap.) and spin-coated layer (Sol.).

	2PACz			MeO-2PACz			Me-4PACz		
	Pow.	Evap.	Sol.	Pow.	Evap.	Sol.	Pow.	Evap.	Sol.
O 1s		1.28	1.2		1.22	1.24		1.26	1.3
O 1s	1.27			1.27			1.17		
O 1s	1.68			1.18			1.48		
O 1s				1.7			1.46		
ITO		2.1	1.95		2.1	1.84		1.83	1.84
ITO		1.53	1.56		1.43	1.45		1.57	1.56
N 1s	0.81	1.07	1.17	0.88	1.06	1.09	0.78	0.87	0.95
N 1s	1.05	1.67	1.71	1.26	1.25	1.68	0.85	0.95	0.97
N 1s							0.84	1.59	1.86

Table S5-5 Relative peak area/weights of X-ray photoelectron spectra fits for the O 1s and N 1s regions of each nPACz material. Shown is the powder reference (Pow.), evaporated thin film (Evap.) and spin-coated layer (Sol.).

	2PACz			MeO-2PACz			Me-4PACz		
	Pow.	Evap.	Sol.	Pow.	Evap.	Sol.	Pow.	Evap.	Sol.
O 1s		28.2%	36.7%		28.0%	35.7%		26.9%	38.0%
O 1s	27.9%			13.2%			18.1%		
O 1s	72.1%			34.4%			40.4%		
O 1s				52.3%			41.5%		
ITO		44.2%	39.7%		39.0%	35.8%		39.2%	39.1%
ITO		27.6%	23.5%		33.0%	28.6%		33.9%	22.9%
N 1s	63.8%	75.7%	76.1%	74.4%	75.2%	80.7%	68.1%	63.2%	72.5%
N 1s	36.2%	24.3%	23.9%	25.6%	24.8%	19.3%	30.8%	30.7%	20.2%
N 1s							1.1%	6.1%	7.3%

Table S5-6 Peak locations of X-ray photoelectron spectra fits for the P 2p regions of each nPACz material. Shown is the powder reference (Pow.), evaporated thin film (Evap.) and spin-coated layer (Sol.).

	2PACz			MeO-2PACz			Me-4PACz		
	Pow.	Evap.	Sol.	Pow.	Evap.	Sol.	Pow.	Evap.	Sol.
P 2p3/2	134.0	133.1	133.1	133.4	133.1	132.9	133.5	133.0	133.0
P 2p1/2	134.9	133.9	133.9	134.3	133.9	133.7	134.3	133.8	133.9

Table S5-7 Full width half maxima of X-ray photoelectron spectra fits for P 2p regions of each nPACz material. Shown is the powder reference (Pow.), evaporated thin film (Evap.) and spin-coated layer (Sol.).

	2PACz			MeO-2PACz			Me-4PACz		
	Pow.	Evap.	Sol.	Pow.	Evap.	Sol.	Pow.	Evap.	Sol.
P 2p3/2	1.11	1.55	1.51	1.28	1.39	1.35	1.14	1.47	1.39
P 2p1/2	1.06	1.54	1.54	1.29	1.4	1.23	1.11	1.46	1.33

Table S5-8 Relative peak area/weights locations of X-ray photoelectron spectra fits for the P 2p regions of each nPACz material. Shown is the powder reference (Pow.), evaporated thin film (Evap.) and spin-coated layer (Sol.).

	2PACz			MeO-2PACz			Me-4PACz		
	Pow.	Evap.	Sol.	Pow.	Evap.	Sol.	Pow.	Evap.	Sol.
P 2p3/2	66.7%	66.7%	66.7%	66.7%	66.7%	66.7%	66.7%	66.7%	66.7%
P 2p1/2	33.3%	33.3%	33.3%	33.3%	33.3%	33.3%	33.3%	33.3%	33.3%

Table S5-9 Peak locations of X-ray photoelectron spectra fits for the In 3d and Sn 3d regions of each nPACz material. Shown is the evaporated thin film and spin-coated layer.

	2PACz		MeO-2PACz		Me-4PACz	
	Evaporated	Solution	Evaporated	Solution	Evaporated	Solution
Sn 3$d_{5/2}$	486.5	486.5	486.6	486.5	486.5	486.5
Sn 3$d_{3/2}$	494.9	494.9	495.0	494.9	494.9	494.9
In 3$d_{5/2}$	444.4	444.3	444.4	444.3	444.4	444.3
In 3$d_{3/2}$	451.9	451.8	451.9	451.9	451.9	451.9

Table S5-10 Full width half maxima of X-ray photoelectron spectra fits for the In 3d and Sn 3d regions of each nPACz material. Shown is the evaporated thin film and spin-coated layer.

	2PACz		MeO-2PACz		Me-4PACz	
	Evaporated	Solution	Evaporated	Solution	Evaporated	Solution
Sn 3$d_{5/2}$	1.44	1.49	1.58	1.51	1.57	1.49
Sn 3$d_{3/2}$	1.43	1.5	1.57	1.51	1.57	1.52
In 3$d_{5/2}$	1.4	1.43	1.52	1.46	1.53	1.44
In 3$d_{3/2}$	1.4	1.42	1.51	1.45	1.52	1.43

Table S5-11 Relative peak area/weightss of X-ray photoelectron spectra fits for the In 3d and Sn 3d regions of each nPACz material. Shown is the evaporated thin film and spin-coated layer.

	2PACz		MeO-2PACz		Me-4PACz	
	Evaporated	Solution	Evaporated	Solution	Evaporated	Solution
Sn $3d_{5/2}$	59.4%	59.0%	59.3%	59.3%	59.2%	58.7%
Sn $3d_{3/2}$	40.6%	41.1%	40.7%	40.7%	40.8%	41.3%
In $3d_{5/2}$	59.1%	59.3%	59.3%	59.3%	59.4%	59.4%
In $3d_{3/2}$	40.9%	40.7%	40.7%	40.7%	40.6%	40.6%

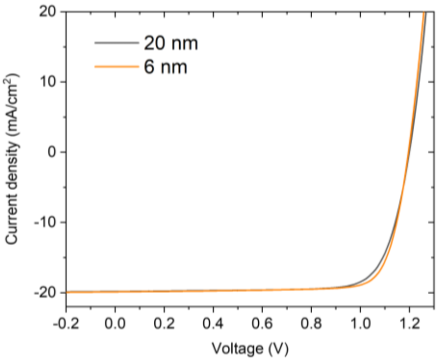

Figure S5-2 Comparison of the *J-V* scans of two PSCs employing different layer thickness of evaporated 2PACz. It indicates a slight drop in FF in the thicker HTL case. Reproduced from Wiley-VCH GmbH ©2023 with permission.[261]

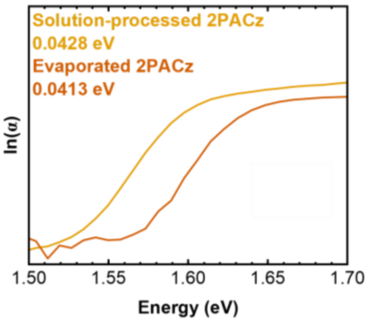

Figure S5-3 Natural logarithm of absorbance plotted against bandgap. Quoted Urbach energy is derived from the gradient of the slope at the point of inflection.

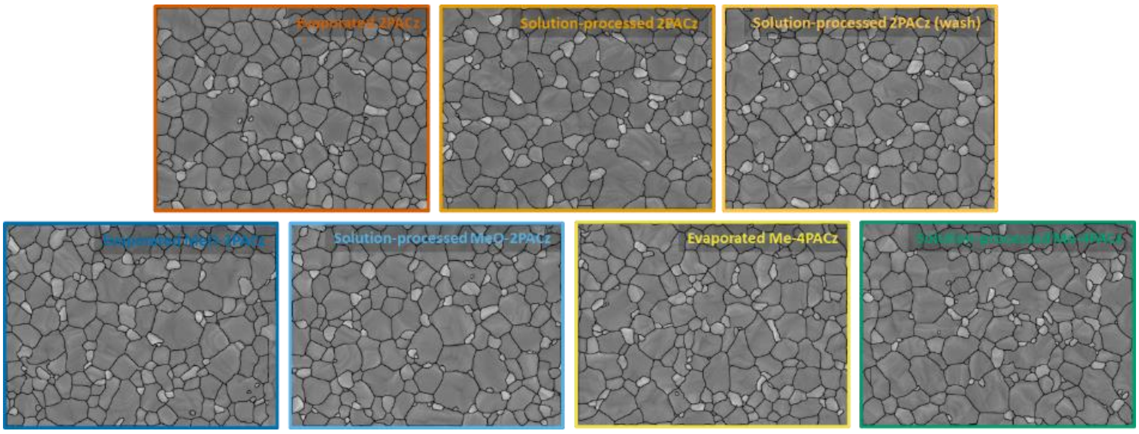

Figure S5-4 Defined crystallites for grain size analysis of each substrate presented in **Figure 5-15** and **Figure S5-5.** Part of figure adapted from Wiley-VCH GmbH ©2023 with permission.[261]

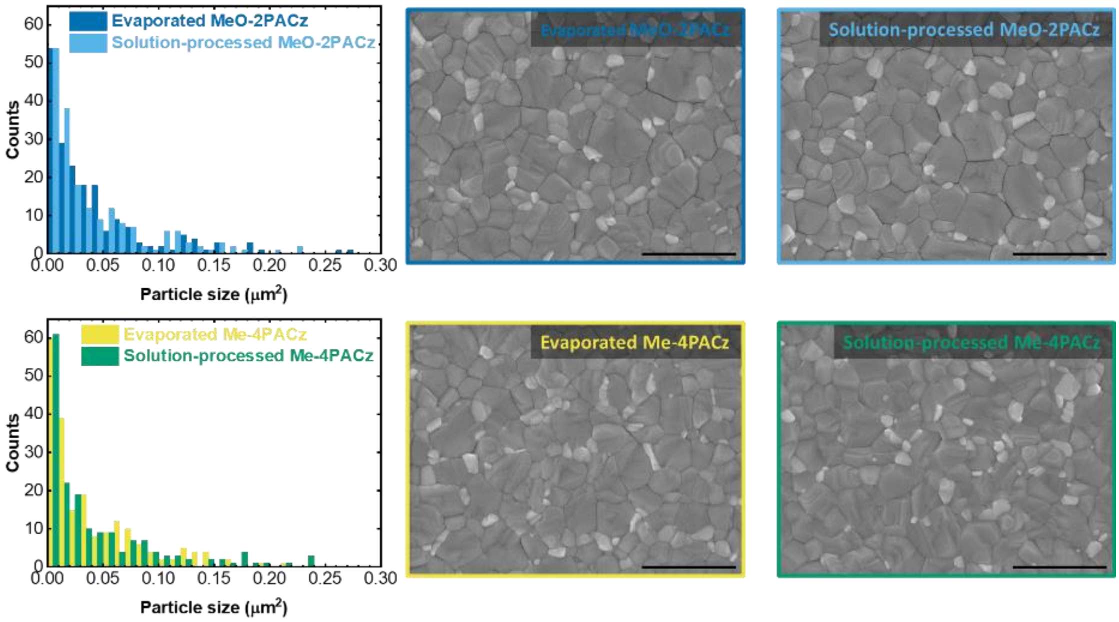

Figure S5-5 Distribution of crystallite sizes (*left*) for top view scanning electron microscope images of perovskite thin films deposited over evaporated (*middle*) and spin-coated 2PACz layer (*right*) MeO-2PACz and Me-4PACZ substrates. The scale bar is 1 μm. Part of figure adapted from Elsevier Inc ©2024 with permission.[221]

9.3 Appendix for Chapter 6

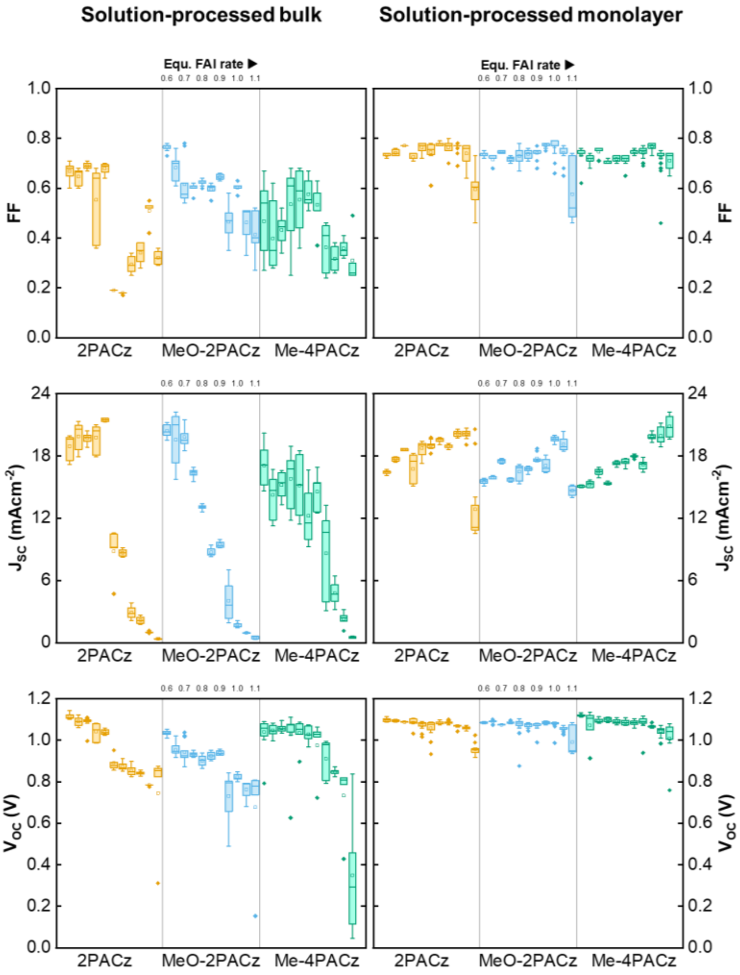

Figure S6-1 Photovoltaic parameter statistics derived from forward and reverse scans of PSCs with with varying rates of FAI for solution-processed nPACz SAM-HTLs. nPACz layers were kept as deposited to ensure that residual bulk SAM remained in the film (*left*) or washed to ensure a monolayer (*right*). Figure reproduced from Elsevier Inc ©2024 with permission.[221]

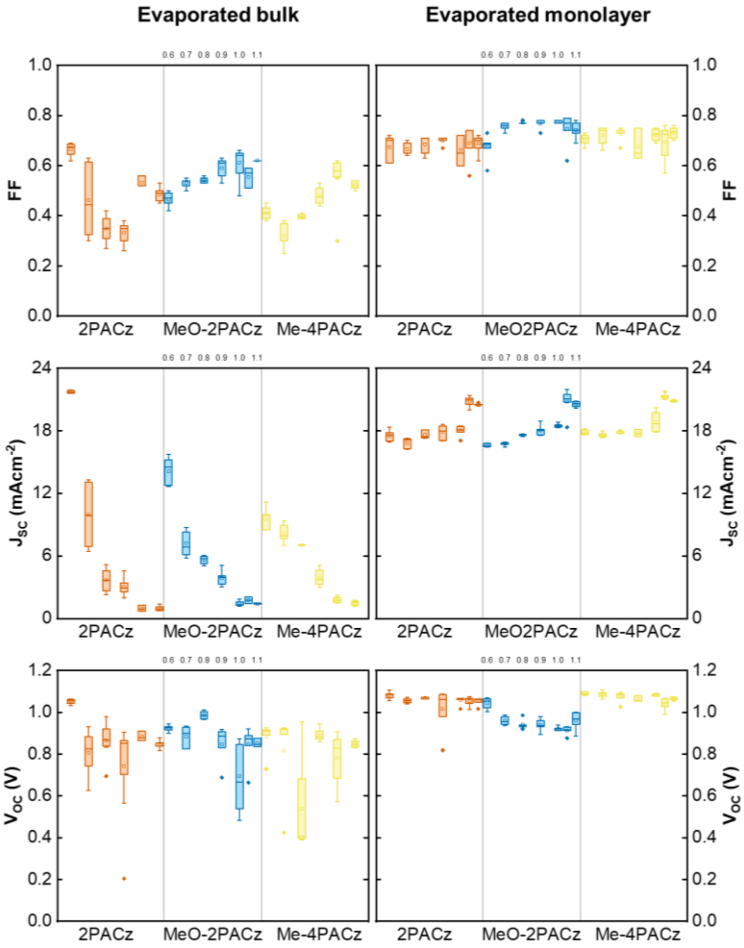

Figure S6-2 Photovoltaic parameter statistics derived from forward and reverse scans of PSCs with with varying rates of FAI for 4 nm evaporated nPACz SAM-HTLs. nPACz films were left as deposited to ensure that residual bulk SAM remained in the film (*left*) and washed to ensure a monolayer (*right*). Figure reproduced from Elsevier Inc ©2024 with permission.[221]

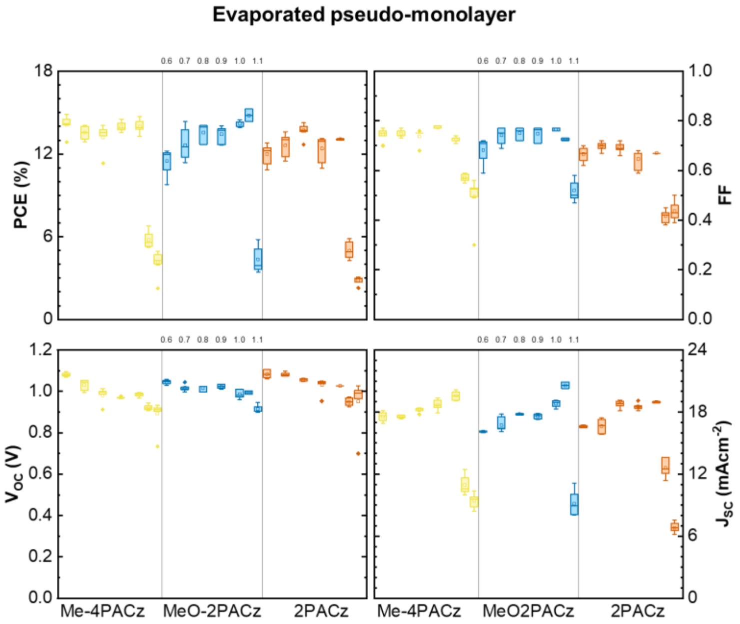

Figure S6-3 Photovoltaic parameter statistics derived from forward and reverse scans of PSCs with with varying rates of FAI for 2 nm evaporated nPACz SAM-HTLs. nPACz films were left as deposited to ensure that residual bulk SAM remained in the film.

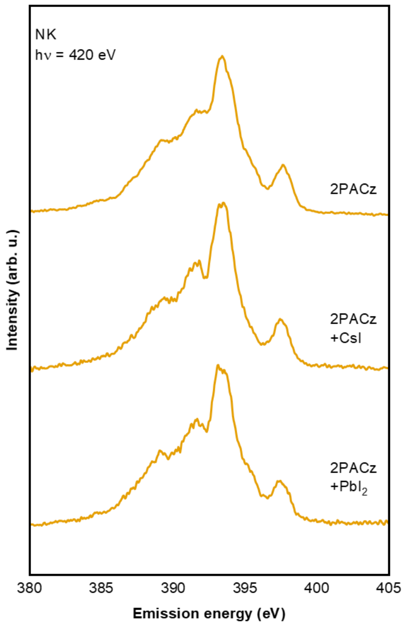

Figure S6-4 Normalized XES spectra of ~25 nm CsI and ~25 nm PbI_2 films deposited onto bulk 2PACz substrates. A reference spectrum of the bulk 2PACz/ITO substrate is also shown. Figure reproduced from Elsevier Inc ©2024 with permission.[221]

Table S6-1 (0 0 1) peak positions for XRD and PLQY measurements of best performing devices for every utilized SAM-HTL underlayer before and after the films were annealed.

Sample		XRD peak position			PLQY wavelength	
		δ-FAPbI$_3$	α-FAPbI$_3$	PbI$_2$	nm	eV
2PACz	Bulk unannealed		14.18	12.82		
	Bulk annealed		14.16		793	1.56
	Monolayer unannealed	11.99	14.25	12.81		
	Monolayer annealed		14.12	12.79	788	1.57
MeO-2PACz	Bulk unannealed		14.12			
	Bulk annealed		14.14		789	1.57
	Monolayer unannealed	11.99	14.2	12.87		
	Monolayer annealed		14.1	12.82	788	1.57
Me-4PACz	Bulk unannealed	11.98	14.16	12.84		
	Bulk annealed		14.16	12.87	788	1.57
	Monolayer unannealed	11.95	14.18	12.78		
	Monolayer annealed		14.15	12.82	787	1.58

Figure S6-5 Camera image of perovskite film grown on solution-processed bulk Me-4PACz. This filter corresponds to the highest performance stoichiometry. The two distinct colors indicates two different perovskites form on the same sample, highlighting surface inhomogeneity. Figure reproduced from Elsevier Inc ©2024 with permission.[221]

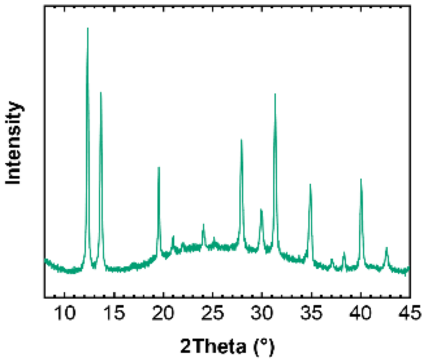

Figure S6-6 XRD spectrum of an unannealed perovskite deposited on evaporated bulk Me-4PACz showing no evidence of a δ-FAPbI$_3$ peak.

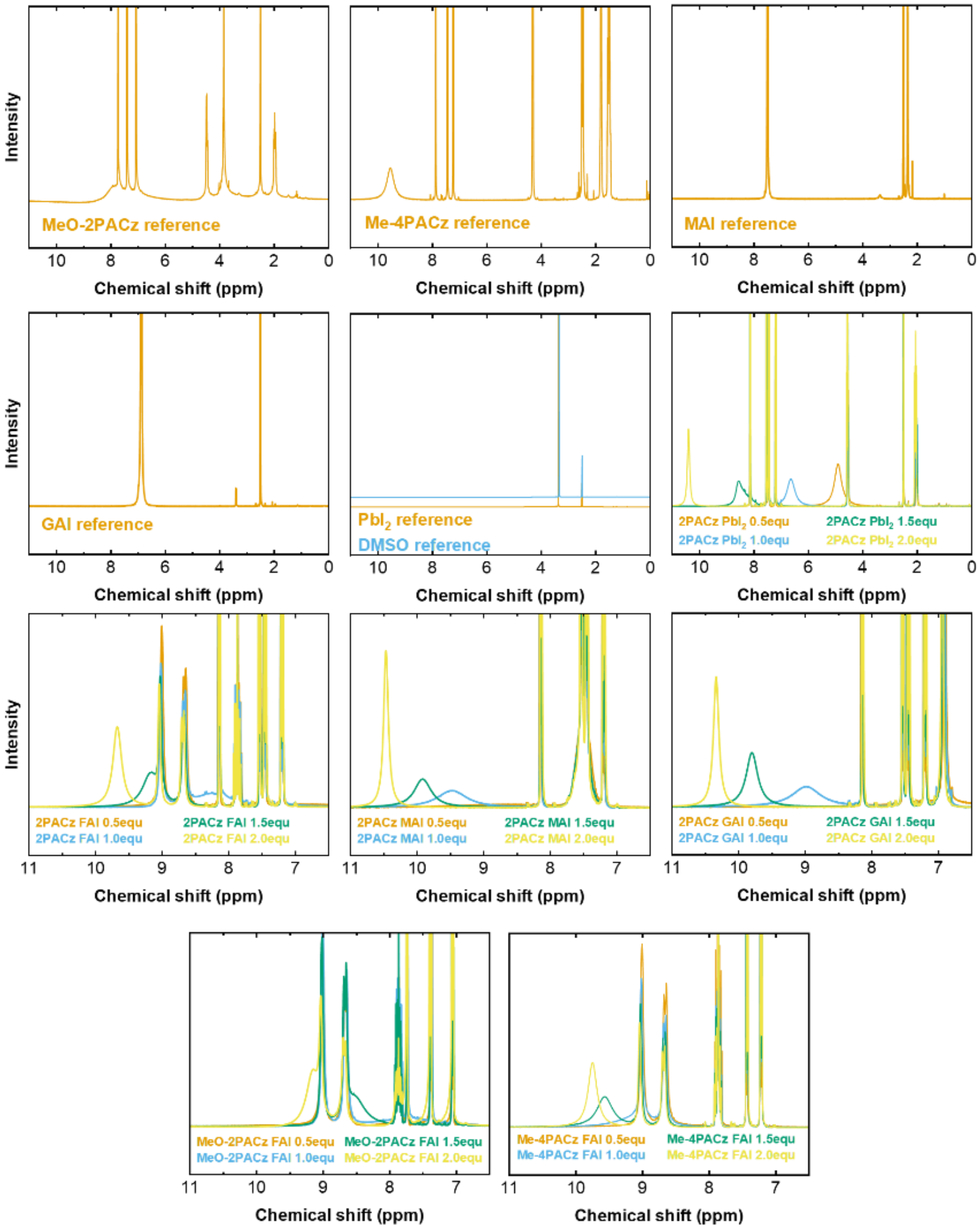

Figure S6-7 Supporting NMR spectra for **Section 6.4**. Reference spectra for MeO-2PACz, Me-4PACz, MAI, GAI, PbI$_2$ and DMSO. ^{1}H-NMR series relating to data from **Section 6.3**. Measurement performed by Julian Petry. Figure reproduced from Elsevier Inc ©2024 with permission.[221]

Table S6-2 Raw values for binding energies of various 2PACz conformations as a function of the distance between substrate and material for both phases of Pb-terminated FAPbI$_3$ (FAPI) perovskite. Values are given in eV. Simulations performed by collaborators from Heidelberg University. Table reproduced from Elsevier Inc ©2024 with permission.[221]

Distance (Å)	*A (α-FAPbI$_3$) (eV)*	*N (α-FAPbI$_3$) (eV)*	*T (α-FAPbI$_3$) (eV)*	*A (δ-FAPbI$_3$) (eV)*	*N (δ-FAPbI$_3$) (eV)*	*T (δ-FAPbI$_3$) (eV)*
5	0	0	0	0	0	0
4	-0.0547	-0.04701	-0.0366	-0.05997	-0.09784	-0.06066
3.5	-0.09975	-0.08428	-0.06622	-0.14446	-0.16886	-0.10289
3	-0.14252	-0.13822	-0.10767	-0.24608	-0.26673	-0.15435
2.5	-0.08505	-0.21036	-0.15516	-0.32018	-0.51087	-0.20996
2	0.45323	-0.30719	-0.17905	-0.21482	-0.44586	-0.22453
1.5	3.01881	-0.40603	0.01117	0.56629	0.45196	-0.01703
1	15.37158	-0.40566	1.30351	3.1124	4.01203	1.00473
0.5	58.10208	-0.03544	7.57486	6.62931	9.30671	4.44633
0.2	85.21186	0.56551	19.08457	27.55357	43.31166	9.08604

Table S6-3 Raw values for binding energies of various 2PACz conformations as a function of the distance between substrate and material for both phases of FA-terminated FAPbI$_3$ perovskite. Values are given in eV. Simulations performed by collaborators from Heidelberg University. Table reproduced from Elsevier Inc ©2024 with permission.[221]

Distance (Å)	*A (α-FAPbI$_3$) (eV)*	*N (α-FAPbI$_3$) (eV)*	*T (α-FAPbI$_3$) (eV)*	*A (δ-FAPbI$_3$) (eV)*	*N (δ-FAPbI$_3$) (eV)*	*T (δ-FAPbI$_3$) (eV)*
5	0	0	0	0	0	0
4	-0.08052	-0.06509	-0.0392		-0.13741	-0.10498
3.5	-0.14874	-0.12662	-0.07969		-0.24599	-0.18448
3	-0.22723	-0.21682	-0.14096	-0.30296	-0.38726	-0.2891
2.5	-0.23343	-0.33184	-0.2228	-0.45935	-0.53944	-0.38349
2	0.25716	-0.3949	-0.27978	-0.55062	-0.54375	-0.31987
1.5	2.72323	-0.04145	-0.04957	-0.13079	0.24952	0.48334
1	15.51543	2.20361	1.58058	2.49745	4.02091	3.78278
0.5	85.40069	11.49011	8.58544	12.36805	17.85572	15.25542
0.2	193.01395	26.50992	20.41288	27.55357	43.31166	34.77314

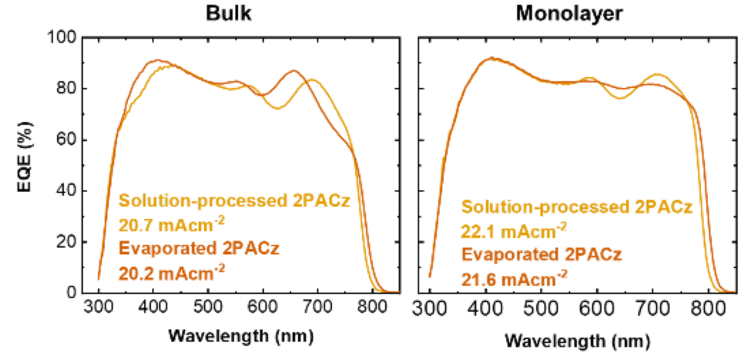

Figure S6-8 EQE of best-performing samples with bulk (*left*) and monolayer (*right*) 2PACz deposited via both evaporation and solution-processed methods. Figure reproduced from Elsevier Inc ©2024 with permission.[221]

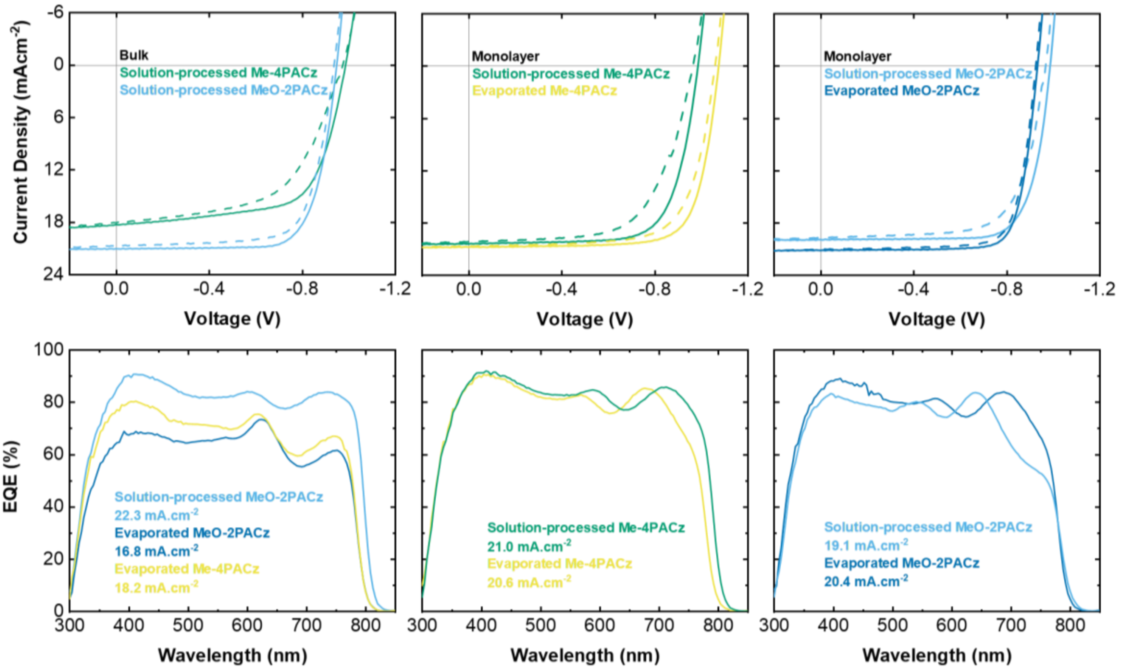

Figure S6-9 EQE and J-V scans of best-performing samples with bulk (*left*) and monolayer (*middle/right*) MeO-2PACz and Me-4PACz deposited via either evaporation or solution-processed methods. Figure reproduced from Elsevier Inc ©2024 with permission.[221]

Table S6-4 *J-V* and EQE statistics for the optimum perovskite of each configuration with MeO-2PACz SAM-HTLs. The average value is shown in brackets and the integrated J_{SC} derived from EQE of the champion device provided in bold.

	PCE (%)	FF	V_{OC} (V)	J_{SC} ($mA.cm^{-2}$)	
				Solar Simulator	EQE
Evaporated monolayer	15.5 (14.2)	0.79 (0.77)	0.93 (0.92)	22.0 (20.8)	20.4
	15.0 (14.7)	0.77 (0.76)	0.92 (0.91)	21.8 (21.2)	
Solution monolayer	17.1 (16.2)	0.79 (0.77)	1.09 (1.07)	20.0 (19.6)	19.1
	15.3 (14.7)	0.73 (0.72)	1.07 (1.06)	19.6 (19.4)	
Evaporated bulk	7.2 (6.1)	0.50 (0.46)	0.94 (0.92)	15.7 (14.1)	16.8
Solution bulk	17.2 (16.2)	0.78 (0.77)	1.05 (1.03)	21.2 (20.4)	22.3
	16.3 (14.8)	0.76 (0.72)	1.04 (1.02)	21.0 (20.0)	

Table S6-5 *J-V* and EQE statistics for the optimum perovskite of each configuration with Me-4PACz SAM-HTLs. The average value is shown in brackets and the integrated J_{SC} derived from EQE of the champion device provided in bold.

	PCE (%)	FF	V_{OC} (V)	J_{SC} ($mA.cm^{-2}$)	
				Solar Simulator	EQE
Evaporated monolayer	16.9 (16.3)	0.76 (0.73)	1.07 (1.06)	21.0 (20.8)	20.6
	15.6 (14.9)	0.71 (0.69)	1.06 (1.05)	20.9 (20.7)	
Solution monolayer	16.7 (16.2)	0.78 (0.77)	1.07 (1.04)	20.4 (19.8)	
	14.9 (14.5)	0.72 (0.70)	1.06 (1.05)	20.2 (19.7)	
Evaporated bulk	4.2 (3.4)	0.45 (0.41)	0.93 (0.88)	11.2 (9.5)	18.2
Solution bulk	13.7 (11.8)	0.68 (0.55)	1.09 (1.07)	18.5 (17.1)	
	11.7 (10.4)	0.60 (0.58)	1.07 (1.06)	18.3 (16.8)	

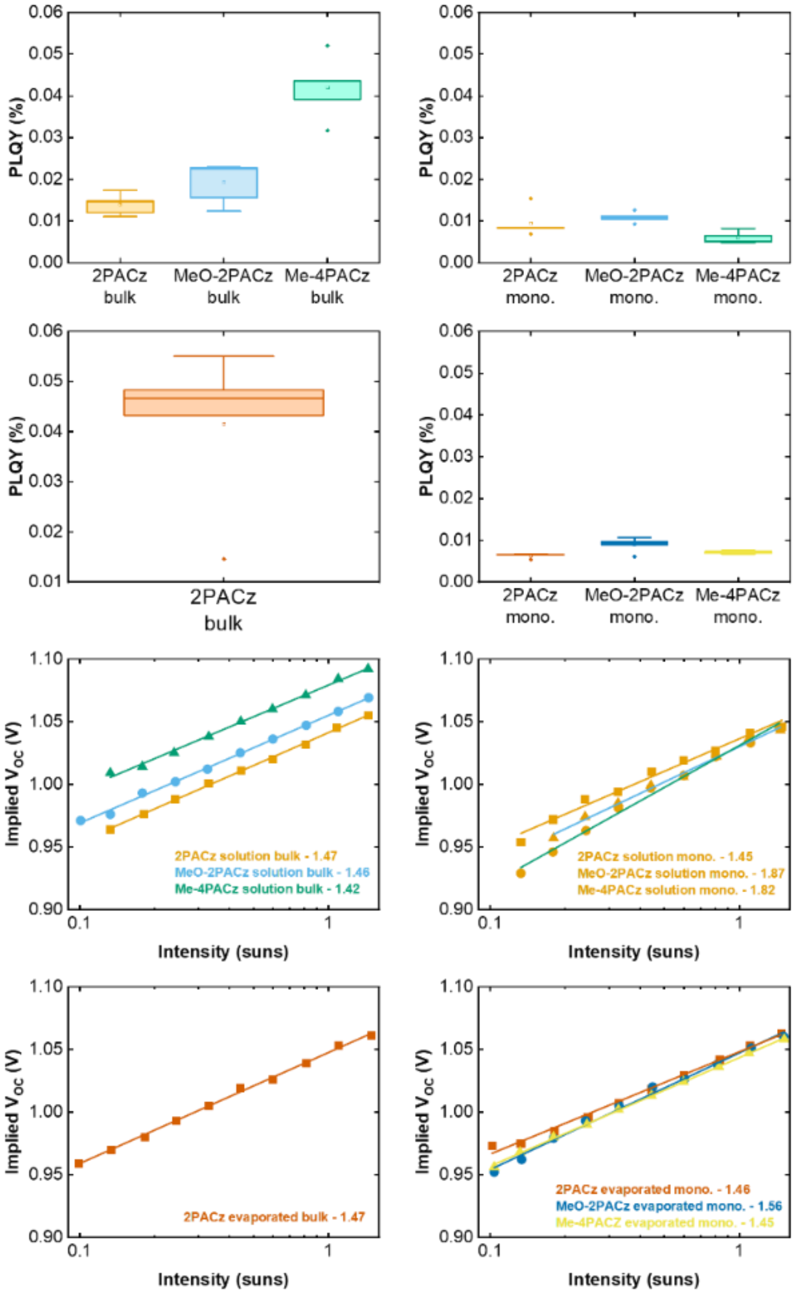

Figure S6-10 PLQY results and ideality factor calculations for optimized perovskite layers deposited on all studied nPACz coated substrates. Bulk (*left*) and monolayer (*right*) nPACz were deposited via solution processing or evaporation. Evaporated bulk samples only tested 2PACz, as optimal MeO-2PACZ and Me-4PACz stoichiometries were not achieved over the course of the series. Figure reproduced from Elsevier Inc ©2024 with permission.[221]

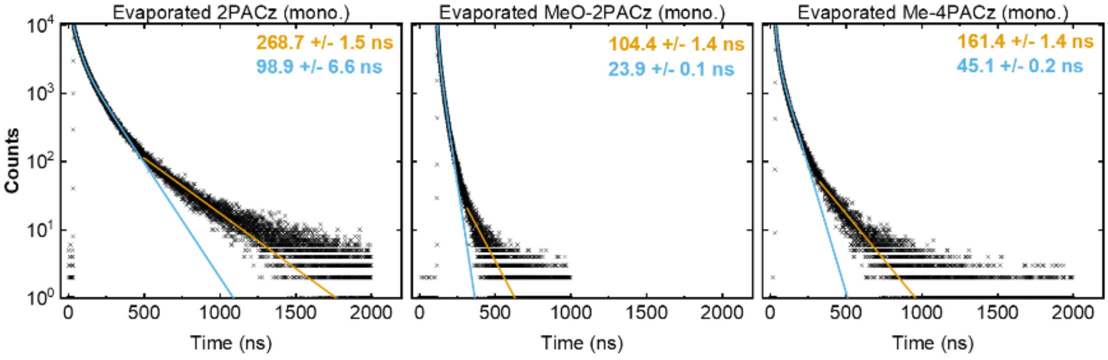

Figure S6-11 TrPL curves for optimized perovskite layers deposited on studied evaporated nPACz coated substrates. TrPL of best-performing ITO/SAM-HTL/perovskite half-stacks for monolayer nPACz to determine charge carrier lifetimes. Data is plotted with biexponential (blue) and truncated monoexponential (orange) fits. The inset shows the resultant monoexponential (orange) and biexponential (orange, weighted average) lifetimes (see **Table S6-2**). Errors represent one standard deviation of the lifetime. Figure reproduced from Elsevier Inc ©2024 with permission.[221]

Table S6-6 Truncated monomial (SRH) and binomial decay lifetimes and errors of best performing ITO/HTL-SAM/perovskite half-stacks for both bulk and monolayer nPACz. Errors represent one standard deviation of each parameter. Table reproduced from Elsevier Inc ©2024 with permission.[221]

Material	Deposition	Exponential	A_1	τ_1 (ns)	A_2	τ_2 (ns)
2PACz	Solution (bulk)	Monomial	67.1	1080.9	-	-
	Solution (mono.)	Binomial	556.9	371.9	1980.0	59.9
	Evaporated (mono.)	Monomial	52.9	277.6	-	-
MeO-2PACz	Solution (bulk)	Binomial	3412.1	104.9	6032.4	27.9
	Solution (mono.)	Monomial	100.4	268.7	-	-
	Evaporated (mono.)	Binomial	3501.6	129.1	6085.2	35.5
Me-4PACz	Solution (bulk)	Monomial	43.0	1585.8	-	-
	Solution (mono.)	Binomial	959.5	216.9	9268.7	23.4
	Evaporated (mono.)	Monomial	116.2	121.6	-	-

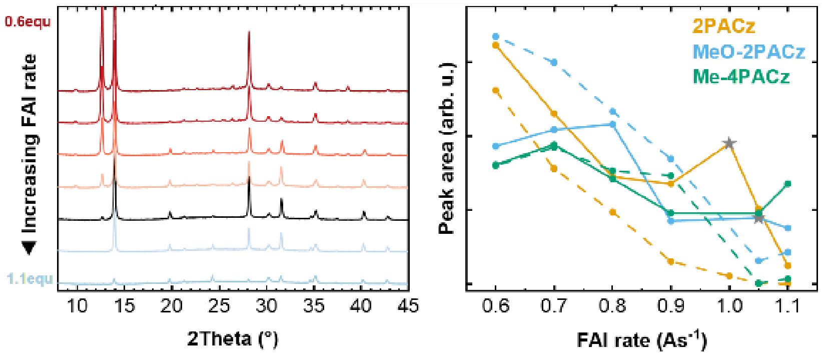

Figure S6-12 Sets of XRD spectra for co-evaporated perovskites deposited onto 2 nm evaporated 2PACz. (*Right*) peak areas for (0 0 1) perovskite (solid) and PbI_2 (dashed) from this graph, plus data from MeO-2PACz and Me-4PACz. The perovskite with the highest performance is marked with a star.

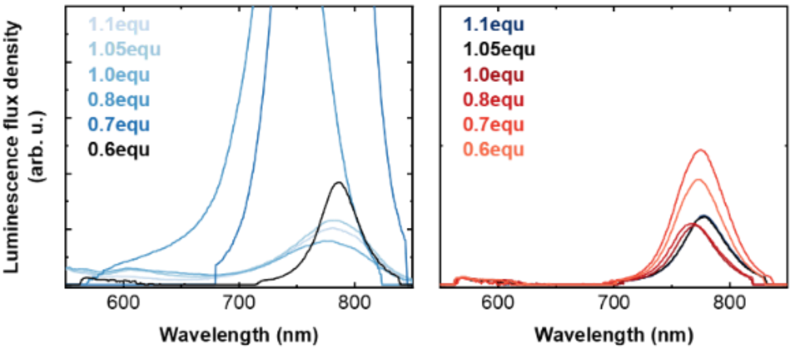

Figure S6-13 Raw PLQY spectra for perovskite half stacks deposited on evaporated 2PACz as a bulk layer (*left*) or as a washed monolayer (*right*) showing a change in bandgap that is not mirrored in EQE.

9.4 Appendix for Chapter 7

Table S7-1 – Deposition conditions, including champion PCE with corresponding compositions and bandgaps, of various organic-inorganic co-evaporated perovskites. Data with known deposition rates, or rates extracted from ref.[51] are specified as exact. Data without known deposition rates (dentoed with ~) are estimated by assuming a given PbI_2 to perovskite thickness ratio. To ease readability only $MAPbI_3$ devices with >15 nm.min^{-1} deposition speed and those with >20% PCE are shown. When bandgap is extracted from data, rather than directly stated in the referenced literature, uncertainty is denoted using ~. When approximate rates are determined from author responses, it is denotes using *. Data from this chapter is presented throughout the manuscript and supporting information.

Deposition rate (nm.min^{-1})	PCE (%)	Composition	Bandgap (eV)	Year	Ref.
		MA-BASED			
17.5	15.7	$MAPbI_3$	~1.60	2019	[515]
5	20.6	$MAPbI_3$	~1.60	2020	[73]
4.2	20.6	$MAPbI_3$	~1.60	2021	[548]
20	19.4	$MAPbI_3$	1.60	2023	[74]
26.8	17.5	$MAPbI_3$	1.60	2024	[220]
		MAFA-BASED			
6.2	16.0	$Cs_{0.5}FA_{0.4}MA_{0.1}Pb(I_{0.83}Br_{0.17})_3$	1.70	2018	[51,453]
6.3	20.4	$FA_{0.53}MA_{0.47}PbI_3$	1.53	2021	[54]
		FA-BASED			
3.1	15.8	$FAPbI_3$	1.47	2017	[50]
6.2	8.5	$Cs_{0.5}FA_{0.5}Pb(I_{0.83}Br_{0.17})_3$	1.62	2018	[51,453]
5.1	11.5	$Cs_{0.75}FA_{0.25}Pb_{0.5}Sn_{0.5}(I_{0.83}Br_{0.17})_3$	1.37	2019	[549]
8.2	18.1	$Cs_{0.3}FA_{0.7}Pb(I_{0.9}Br_{0.1})_3$	~1.62	2020	[463]
10.0	16.6	$Cs_{0.1}FA_{0.9}Pb(I_{0.9}Br_{0.1})_3$	1.58	2020	[550]
6.5	15.8	$FAPbI_3$	1.54	2021	[54]
~7	16.8	$FA_{0.65}Cs_{0.35}Pb(I_{0.73}Br_{0.27})_3$	1.75	2021	[172]
~5	20	$FA_{0.7}Cs_{0.3}Pb(I_{0.9}Br_{0.1})_3$	1.62	2022	[39]
6.0	15.6	$Cs_{0.7}FA_{0.3}Pb(I_{0.9}Br_{0.1})_3$	1.63	2022	[75]
3.1	19.3	$Cs_{0.17}FA_{0.83}Pb(I_{0.7}Cl_{0.3})_3$	1.60	2022	[415]
3.2	13.9	$Cs_{0.17}FA_{0.83}PbI_3$	1.56	2023	[464]

4*	20	$Cs_{0.7}FA_{0.3}Pb(I_{0.9}Br_{0.1})_3$	1.62	2023	510
4*	17.6	$Cs_{0.7}FA_{0.3}Pb(I_{0.79}Br_{0.21})_3$	1.68	2023	510
7.1	21	$FA_{0.8}Cs_{0.2}Pb(I_{0.9}Br_{0.1})_3$	1.65	2024	503
~9	15.6	$FA_{0.9}Cs_{0.1}Pb(I_{0.9}Br_{0.1})_3$	1.65	2024	551
~10	17.8	$FA_xCs_{1-x}Pb(I_yBr_{1-y})_3$	1.67	2024	552
4	17	$Cs_{0.13}FA_{0.87}Pb(I_{0.95}Cl_{0.05})_3$	1.57	2024	221
5	16.2	$Cs_{0.17}FA_{0.83}Pb(I_{0.75}Br_{0.25})_3$	1.68	This work	
18	16.8	$Cs_{0.17}FA_{0.83}Pb(I_{0.75}Br_{0.25})_3$	1.68	This work	

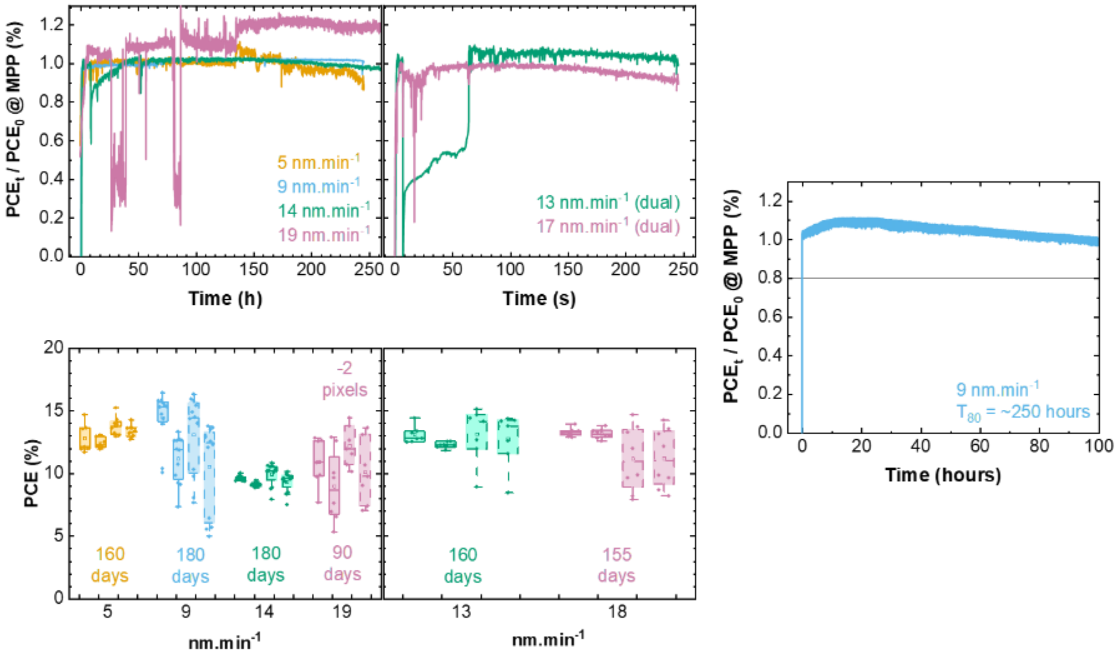

Figure S7-1 Stability of representative samples from each deposition rate under various testing conditions. Samples were deposited using a single FAI source (*left*) and dual FAI sources (*middle*). Shown is light tracking in N_2 @ 25 °C (*top*) and @ 85 °C (*right*). During the measurement of the 19 nm.min^{-1} single source and 13 nm.min^{-1} dual source samples the lamp experienced large fluctuations. Also shown is stability of the champion batch under the quoted timescales, stored in N_2 under dark conditions and 25 °C. Reproduced from Wiley-VCH GmbH ©2025 with permission.[504]

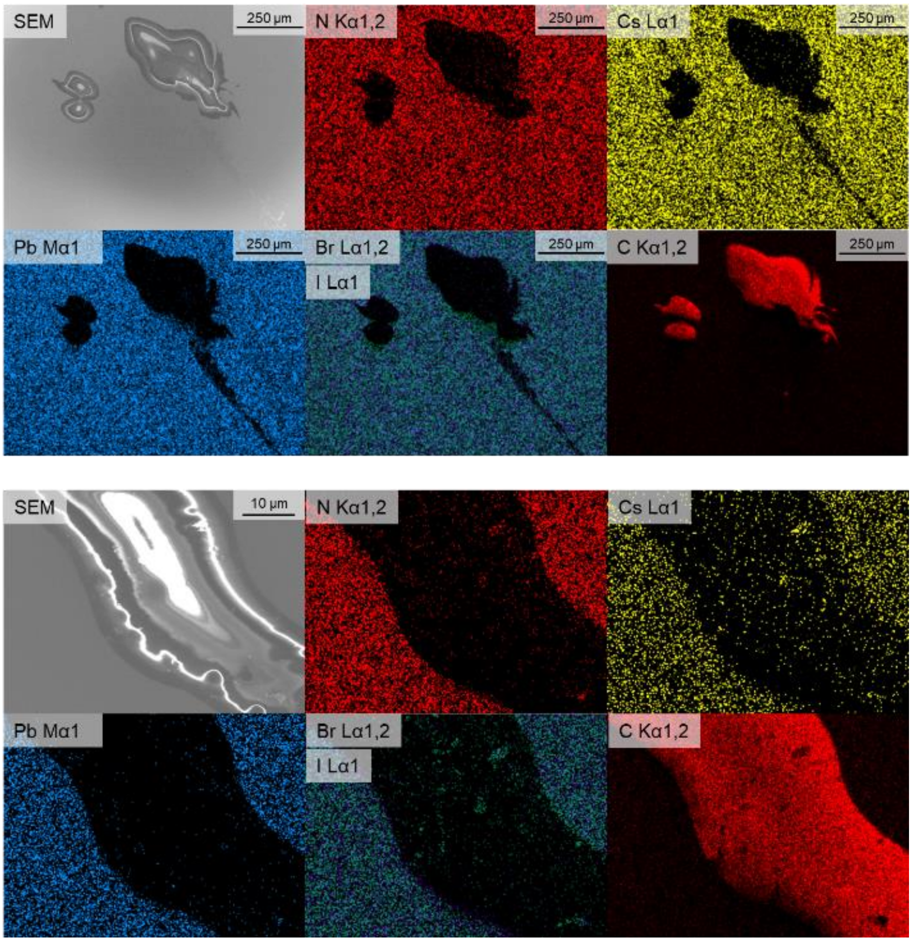

Figure S7-2 Additional SEM images and relevant EDX data of dark spots measured on the 19 nm.min^{-1} sample from **Figure 7-12**. Iodine and bromine components are overlaid. Carbon is always detected outside the carbon-rich region of the EDX spectra, but is not readily apparent due to the high concentration of carbon at the defect. Measurement performed by Aleksandra Miaskiewicz.

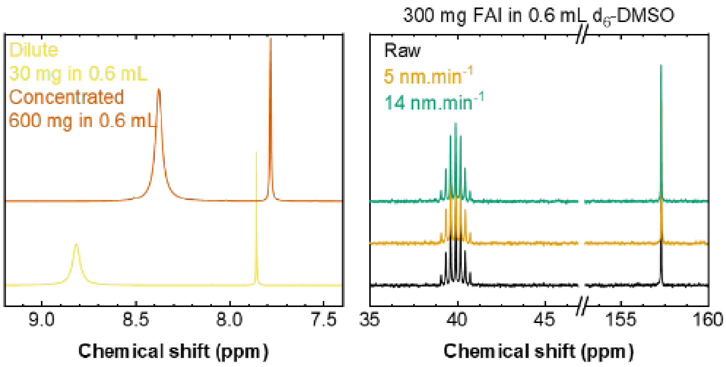

Figure S7-3 Supplemental NMR measurements. (*left*) FAI spectra of a ~5.8 M solution comprised of raw FAI powder dissolved in d$_6$-DMSO and a ~0.29 M dilution from the same spectra to demonstrate that concentration leads to peak shift but not to peak splitting. (*right*) ^{13}C-NMR spectra of raw FAI powder and residual crucible material deposited at stated deposition rates, showing no significant change in spectra or emergence of other peaks. Reproduced from Wiley-VCH GmbH ©2025 with permission.[504]

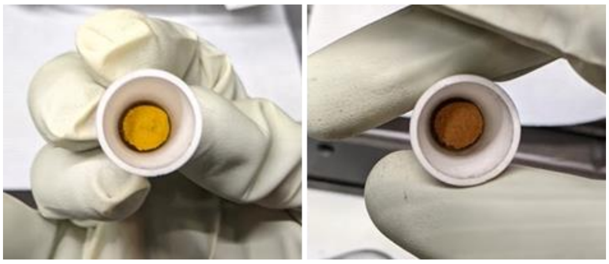

Figure S7-4 Images of PbI_2 residual crucible material before (*left*) and after (*right*) a perovskite deposition with a high degree of organic cation cross-contamination

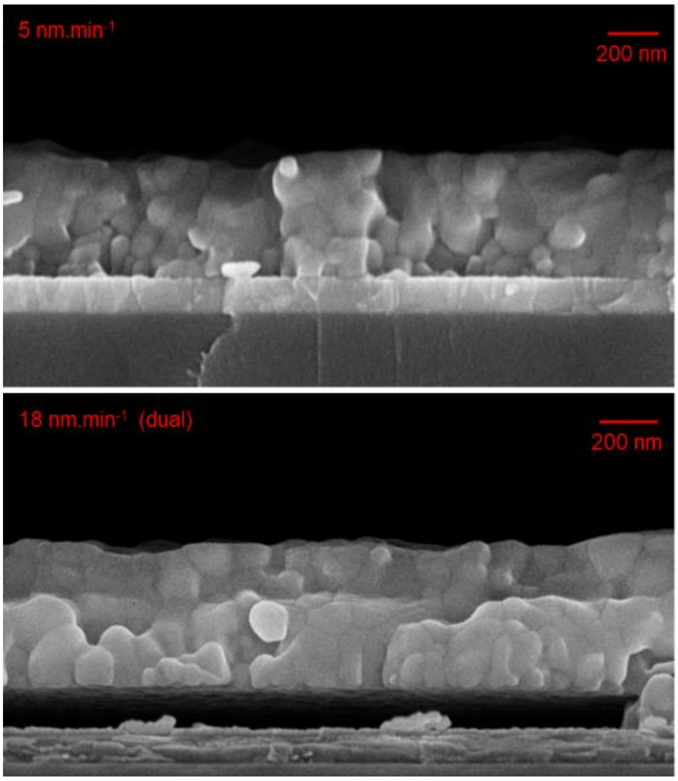

Figure S7-5 Representative cross-sectional SEM images of perovskite films corresponding to 5 nm.min^{-1} single FAI source and 18 nm.min^{-1} dual FAI source processes. Reproduced from Wiley-VCH GmbH ©2025 with permission.[504]

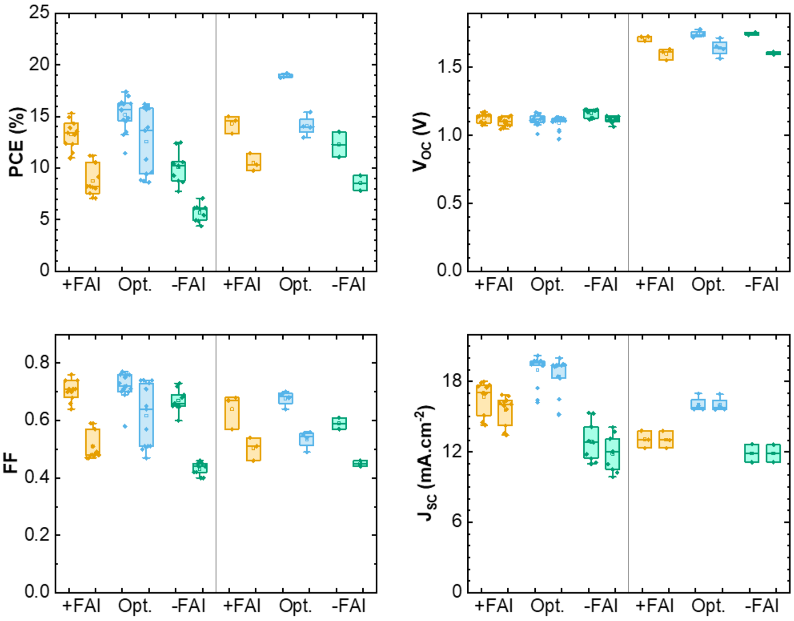

Figure S7-6 Photovoltaic parameter statistics derived from forward and reverse *J-V* scans of single-junction and nanotextured silicon tandem devices deposited at 18 nm.min^{-1} from dual FAI sources. Shown is the impact of increased (+FAI) and decreased (-FAI) cation rate compared to the optimum presented in **Figure 7-33**.

List of figures / Abbildungsverzeichnis

Main text

Appendix

List of Tables / Tabellenverzeichnis

Main text

Appendix

References

1. Core Writing Team, Lee, H. & Romero, J. *Climate Change 2023: Synthesis Report. Contribution of Working Groups I, II and III to the Sixth Assessment Report of the Intergovernmental Panel on Climate Change*. (2023).
2. Hersbach, H. et al. ERA5 hourly data on single levels from 1940 to present. *Copernicus Climate Change Service (C3S) Climate Data Store (CDS)* 10.24381/cds.adbb2d47 (2025) doi:10.24381/cds.adbb2d47.
3. Masson-Delmotte, V. et al. *Global Warming of 1.5°C. An IPCC Special Report on the impacts of global warming of 1.5°C above pre-industrial levels and related global greenhouse gas emission pathways, in the context of strengthening the global response to the threat of climate change,*. https://www.cambridge.org/core/product/identifier/9781009157940%23prf2/type/book_part (2018).
4. Peñuelas, J. & Nogué, S. Catastrophic climate change and the collapse of human societies. *Natl Sci Rev* **10**, 0–2 (2023).
5. Hill, R. & Weeks, J. M. Maya Civilization. *Ethnohistory* **42**, 164 (1995).
6. Pathak, M. et al. *Technical Summary. In: Climate Change 2022: Mitigation of Climate Change. Contribution of Working Group III to the Sixth Assessment Report of the Intergovernmental Panel on Climate Change*. (2022) doi:10.1017/9781009157926.002.
7. Li, X., Lepour, D., Heymann, F. & Maréchal, F. Electrification and digitalization effects on sectoral energy demand and consumption: A prospective study towards 2050. *Energy* **279**, 127992 (2023).
8. IEA. *Tracking Clean Energy Progress 2023*. https://www.iea.org/reports/tracking-clean-energy-progress-2023 (2023).
9. Climate at a Glance: Global Time Series. *NOAA National Centers for Environmental information* https://www.ncei.noaa.gov/access/monitoring/climate-at-a-glance/global/time-series (2025).
10. Ritchie, H., Rosado, P. & Roser, M. CO_2 and Greenhouse Gas Emissions. *OurWorldinData.org* https://ourworldindata.org/co2-and-greenhouse-gas-emissions (2023).
11. World Energy Council. *Energy resources: Solar*. *World Energy Council 2013 World Energy Resources: Solar* (2013).
12. Kost, C. et al. Levelized Cost of Electricity- Renewable Energy Technologies July 2024. 1–35 (2024).
13. Goldschmidt, J. C., Wagner, L., Pietzcker, R. & Friedrich, L. Technological learning for resource efficient terawatt scale photovoltaics. *Energy Environ Sci* **14**, 5147–5160 (2021).
14. Haegel, N. M. et al. Photovoltaics at multi-terawatt scale: Waiting is not an option. *Science (1979)* **380**, 39–42 (2023).
15. Fulghum, N. *Solar power continues to surge in 2024*. (2024).
16. Richter, A., Hermle, M. & Glunz, S. W. Reassessment of the limiting efficiency for crystalline silicon solar cells. *IEEE J Photovolt* **3**, 1184–1191 (2013).
17. Vossier, A., Gualdi, F., Dollet, A., Ares, R. & Aimez, V. Approaching the Shockley-Queisser limit: General assessment of the main limiting mechanisms in photovoltaic cells. *J Appl Phys* **117**, (2015).
18. Philipps, S. & Warmuth, W. *PV report - Fraunhofer Institute for Solar Energy Systems, ISE with support of PSE Projects GmbH*. *Fraunhofer ISE* https://www.ise.fraunhofer.de/en/publications/studies/photovoltaics-report.html (2024).
19. Essig, S. et al. Raising the one-sun conversion efficiency of III–V/Si solar cells to 32.8% for two junctions and 35.9% for three junctions. *Nat Energy* **2**, 17144 (2017).
20. Padture, N. P. The promise of metal-halide-perovskite solar photovoltaics: A brief review. *MRS Bull* **48**, 983–998 (2023).
21. Li, H. & Zhang, W. Perovskite Tandem Solar Cells: From Fundamentals to Commercial Deployment. *Chem Rev* **120**, 9835–9950 (2020).
22. Eperon, G. E., Hörantner, M. T. & Snaith, H. J. Metal halide perovskite tandem and multiple-junction photovoltaics. *Nat Rev Chem* **1**, 0095 (2017).
23. Wolf, S. De et al. Organometallic halide perovskites: Sharp optical absorption edge and its relation to photovoltaic performance. *Journal of Physical Chemistry Letters* **5**, 1035–1039 (2014).

24. Chen, B. et al. Enhanced optical path and electron diffusion length enable high-efficiency perovskite tandems. *Nat Commun* **11**, 1257 (2020).
25. Filip, M. R., Eperon, G. E., Snaith, H. J. & Giustino, F. Steric engineering of metal-halide perovskites with tunable optical band gaps. *Nat Commun* **5**, 5757 (2014).
26. Bailie, C. D. et al. Semi-transparent perovskite solar cells for tandems with silicon and CIGS. *Energy Environ Sci* **8**, 956–963 (2015).
27. Jaysankar, M. et al. Perovskite-silicon tandem solar modules with optimised light harvesting. *Energy Environ Sci* **11**, 1489–1498 (2018).
28. Hou, Y. et al. Efficient tandem solar cells with solution-processed perovskite on textured crystalline silicon. *Science (1979)* **367**, 1135–1140 (2020).
29. Schneider, B. W., Lal, N. N., Baker-Finch, S. & White, T. P. Pyramidal surface textures for light trapping and antireflection in perovskite-on-silicon tandem solar cells. *Opt Express* **22**, A1422 (2014).
30. Hörantner, M. T. & Snaith, H. J. Predicting and optimising the energy yield of perovskite-on-silicon tandem solar cells under real world conditions. *Energy Environ Sci* **10**, 1983–1993 (2017).
31. Sahli, F. et al. Fully textured monolithic perovskite/silicon tandem solar cells with 25.2% power conversion efficiency. *Nat Mater* **17**, 820–826 (2018).
32. Hou, F. et al. Monolithic perovskite/silicon tandem solar cells: A review of the present status and solutions toward commercial application. *Nano Energy* **124**, 109476 (2024).
33. Langenhorst, M. et al. Energy yield of all thin-film perovskite/CIGS tandem solar modules. *Progress in Photovoltaics: Research and Applications* **27**, 290–298 (2019).
34. Gharibzadeh, S. et al. 2D/3D Heterostructure for Semitransparent Perovskite Solar Cells with Engineered Bandgap Enables Efficiencies Exceeding 25% in Four-Terminal Tandems with Silicon and CIGS. *Adv Funct Mater* **30**, 1909919 (2020).
35. Feeney, T. et al. Four-Terminal Perovskite/Copper Indium Gallium Selenide Tandem Solar Cells: Unveiling the Path to 27% in Power Conversion Efficiency. *Solar RRL* **6**, 2200662 (2022).
36. Palmstrom, A. F. et al. Enabling Flexible All-Perovskite Tandem Solar Cells. *Joule* **3**, 2193–2204 (2019).
37. Abdollahi Nejand, B. et al. Scalable two-terminal all-perovskite tandem solar modules with a 19.1% efficiency. *Nat Energy* **7**, 620–630 (2022).
38. Singh, A. & Gagliardi, A. Device simulation of all-perovskite four-terminal tandem solar cells: towards 33% efficiency. *EPJ Photovoltaics* **12**, 4 (2021).
39. Chiang, Y.-H. et al. Efficient all-perovskite tandem solar cells by dual-interface optimisation of vacuum-deposited wide-bandgap perovskite. 1–28 (2022).
40. De Bastiani, M., Larini, V., Montecucco, R. & Grancini, G. The levelized cost of electricity from perovskite photovoltaics. *Energy Environ Sci* **16**, 421–429 (2022).
41. Sofia, S. E. et al. Roadmap for cost-effective, commercially-viable perovskite silicon tandems for the current and future PV market. *Sustain Energy Fuels* **4**, 852–862 (2020).
42. Cordell, J. J., Woodhouse, M. & Warren, E. L. Technoeconomic analysis of perovskite/silicon tandem solar modules. *Joule* 101781 (2024) doi:10.1016/j.joule.2024.10.013.
43. NREL. Best Research-Cell Efficiency Chart | Photovoltaic Research | NREL. https://www.nrel.gov/pv/cell-efficiency.html.
44. Duan, L. et al. Stability challenges for the commercialization of perovskite–silicon tandem solar cells. *Nat Rev Mater* **8**, 261–281 (2023).
45. Li, B. & Zhang, W. Improving the stability of inverted perovskite solar cells towards commercialization. *Commun Mater* **3**, 65 (2022).
46. Meng, L., You, J. & Yang, Y. Addressing the stability issue of perovskite solar cells for commercial applications. *Nat Commun* **9**, 5265 (2018).
47. Kosasih, F. U., Erdenebileg, E., Mathews, N., Mhaisalkar, S. G. & Bruno, A. Thermal evaporation and hybrid deposition of perovskite solar cells and mini-modules. *Joule* **6**, 2692–2734 (2022).
48. Li, J. et al. Highly Efficient Thermally Co-evaporated Perovskite Solar Cells and Mini-modules. *Joule* **4**, 1035–1053 (2020).
49. Ritzer, D. B. et al. Upscaling of perovskite solar modules The synergy of fully evaporated layer fabrication and all-laser-scribed interconnections. *Prog Photovolt* **30**, 360–373 (2021).

50. Borchert, J. et al. Large-Area, Highly Uniform Evaporated Formamidinium Lead Triiodide Thin Films for Solar Cells. *ACS Energy Lett* **2**, 2799–2804 (2017).
51. Abzieher, T. et al. Vapor phase deposition of perovskite photovoltaics: short track to commercialization? *Energy Environ Sci* **17**, 1645–1663 (2024).
52. Howard, I. A. et al. Coated and Printed Perovskites for Photovoltaic Applications. *Advanced Materials* **31**, 1806702 (2019).
53. Guesnay, Q., Sahli, F., Ballif, C. & Jeangros, Q. Vapor deposition of metal halide perovskite thin films: Process control strategies to shape layer properties. *APL Mater* **9**, 100703 (2021).
54. Roß, M. et al. Co-Evaporated Formamidinium Lead Iodide Based Perovskites with 1000 h Constant Stability for Fully Textured Monolithic Perovskite/Silicon Tandem Solar Cells. *Adv Energy Mater* **11**, 2101460 (2021).
55. Dewi, H. A. et al. Excellent Intrinsic Long-Term Thermal Stability of Co-Evaporated MAPbI 3 Solar Cells at 85 °C. *Adv Funct Mater* **31**, 2100557 (2021).
56. Susic, I. et al. Combinatorial Vacuum-Deposition of Wide Bandgap Perovskite Films and Solar Cells. *Adv Mater Interfaces* 202271 (2023) doi:10.1002/admi.202202271.
57. Li, H. et al. Molten Salt Strategy for Reproducible Evaporation of Efficient Perovskite Solar Cells. *Adv Funct Mater* **33**, 2211232 (2023).
58. Choi, Y. et al. Scalable All-Vacuum-Processed Perovskite Solar Cells Enabled by Low Energy-Disorder Hole-Transport Layer. *Adv Energy Mater* 2404797–2404809 (2025) doi:10.1002/aenm.202404797.
59. Zhou, J. et al. Highly efficient and stable perovskite solar cells via a multifunctional hole transporting material. *Joule* **8**, 1691–1706 (2024).
60. Jacobsson, T. J. et al. An open-access database and analysis tool for perovskite solar cells based on the FAIR data principles. *Nat Energy* **7**, 107–115 (2022).
61. Green, M. A. et al. Solar cell efficiency tables (Version 64). *Progress in Photovoltaics: Research and Applications* **32**, 425–441 (2024).
62. Liang, Z. et al. Homogenizing out-of-plane cation composition in perovskite solar cells. *Nature* **624**, 557–563 (2023).
63. Min, H. et al. Perovskite solar cells with atomically coherent interlayers on SnO2 electrodes. *Nature* **598**, 444–450 (2021).
64. Jacobs, D. A. et al. Light Management: A Key Concept in High-Efficiency Perovskite/Silicon Tandem Photovoltaics. *Journal of Physical Chemistry Letters* **10**, 3159–3170 (2019).
65. Kore, B. P. et al. Efficient fully textured perovskite silicon tandems with thermally evaporated hole transporting materials. *Energy Environ Sci* 354–366 (2024) doi:10.1039/d4ee03899a.
66. Zhu, Z. et al. Low-Temperature Atomic Layer Deposition of Hole Transport Layers for Enhanced Performance and Scalability in Textured Perovskite/Silicon Tandem Solar Cells. *Adv Energy Mater* **14**, 2402365 (2024).
67. Chakrabarti, T., Das, S., Lin, Y. H. & Perumal, A. Efficient, Stable, and Reproducible Inverted p-i-n Perovskite Solar Cells with a Dopant-Free Spiro-TTB Hole Transport Layer Modified with a PFN-P1 Interfacial Layer. *ACS Appl Energy Mater* **7**, 6220–6229 (2024).
68. Susic, I. et al. Combinatorial Vacuum-Deposition of Wide Bandgap Perovskite Films and Solar Cells. *Adv Mater Interfaces* **10**, 2202271 (2023).
69. Diercks, A. et al. Sequential Evaporation of Inverted FAPbI3 Perovskite Solar Cells − Impact of Substrate on Crystallization and Film Formation. *ACS Energy Lett* **20**, 1165–1173 (2025).
70. Al-Ashouri, A. et al. Conformal monolayer contacts with lossless interfaces for perovskite single-junction and monolithic tandem solar cells. *Energy Environ Sci* **12**, 3356–3369 (2019).
71. Olthof, S. & Meerholz, K. Substrate-dependent electronic structure and film formation of MAPbI3 perovskites. *Sci Rep* **7**, 40267 (2017).
72. Abzieher, T. et al. From Groundwork to Efficient Solar Cells: On the Importance of the Substrate Material in Co-Evaporated Perovskite Solar Cells. *Adv Funct Mater* **31**, 2104482 (2021).
73. Roß, M. et al. Co-Evaporated p-i-n Perovskite Solar Cells beyond 20% Efficiency: Impact of Substrate Temperature and Hole-Transport Layer. *ACS Appl Mater Interfaces* **12**, 39261–39272 (2020).
74. Piot, M. et al. Fast Coevaporation of 1 µm Thick Perovskite Solar Cells. *ACS Energy Lett* **8**, 4711–4713 (2023).
75. Kroll, M. et al. Insights into the evaporation behaviour of FAI: material degradation and consequences for perovskite solar cells. *Sustain Energy Fuels* **6**, 3230–3239 (2022).
76. Bredas, J. L. Mind the gap! *Mater Horiz* **1**, 17–19 (2014).

77. Green, M. A., Ho-Baillie, A. & Snaith, H. J. The emergence of perovskite solar cells. *Nat Photonics* **8**, 506–514 (2014).
78. Let, D. & Cimpoca, G. V. Study over optical absorption and emission in semiconductors. *Journal of Science and Arts* 326–335 (2017).
79. Usami, A. Theoretical study of application of multiple scattering of light to a dye-sensitized nanocrystalline photoelectrochemical cell. *Chem Phys Lett* **277**, 105–108 (1997).
80. Abou-Ras, D., Kirchartz, T. & Rau, U. *Advanced Characterization Techniques for Thin Film Solar Cells: Second Edition*. *Advanced Characterization Techniques for Thin Film Solar Cells: Second Edition* vols 1–2 (2016).
81. Saba, M., Quochi, F., Mura, A. & Bongiovanni, G. Excited State Properties of Hybrid Perovskites. *Acc Chem Res* **49**, 166–173 (2016).
82. Simbula, A. et al. Exciton dissociation in 2D layered metal-halide perovskites. *Nat Commun* **14**, 1–9 (2023).
83. Savenije, T. J. et al. Thermally activated exciton dissociation and recombination control the carrier dynamics in organometal halide perovskite. *Journal of Physical Chemistry Letters* **5**, 2189–2194 (2014).
84. Lin, G. et al. Novel exciton dissociation behavior in tin-lead organohalide perovskites. *Nano Energy* **27**, 638–646 (2016).
85. Trupke, T., Daub, E. & Würfel, P. Absorptivity of silicon solar cells obtained from luminescence. *Solar Energy Materials and Solar Cells* **53**, 103–114 (1998).
86. Kirchartz, T., Abou-Ras, D. & Rau, U. *Advanced Characterization Techniques for Thin Film Solar Cells: Second Edition*. vols 1–2 (2016).
87. Bisquert, J. *The physics of solar cells: Perovskites, organics, and photovoltaic fundamentals*. *The Physics of Solar Cells: Perovskites, Organics, and Photovoltaic Fundamentals* (2017). doi:10.1201/b22380.
88. Wannier, G. H. The structure of electronic excitation levels in insulating crystals. *Physical Review* **52**, 191–197 (1937).
89. Frenkel, J. On the transformation of light into heat in solids. i. *Physical Review* **37**, 17–44 (1931).
90. Gay, J. G. Screening of Excitons in Semiconductors. *Phys Rev B* **4**, (1972).
91. Elliott, R. J. Intensity of optical absorption by excitons. *Physical Review* **108**, 1384–1389 (1957).
92. Mahan, G. D. Excitons in Metals: Infinite Hole Mass. *Physical R* **163**, (1967).
93. Wu, J. et al. A Comparison of Charge Carrier Dynamics in Organic and Perovskite Solar Cells. *Advanced Materials* **34**, (2022).
94. Fu, Y. et al. Incorporating Large A Cations into Lead Iodide Perovskite Cages: Relaxed Goldschmidt Tolerance Factor and Impact on Exciton-Phonon Interaction. *ACS Cent Sci* **5**, 1377–1386 (2019).
95. Kirchartz, T., Bisquert, J., Mora-Sero, I. & Garcia-Belmonte, G. Classification of solar cells according to mechanisms of charge separation and charge collection. *Physical Chemistry Chemical Physics* **17**, 4007–4014 (2015).
96. Prew, B. A. *Physics of Semiconductor Devices*. *Physics Bulletin* vol. 26 (1975).
97. Wurfel, U., Cuevas, A. & Wurfel, P. Charge carrier separation in solar cells. *IEEE J Photovolt* **5**, 461–469 (2015).
98. Rau, U. & Kirchartz, T. Charge Carrier Collection and Contact Selectivity in Solar Cells. *Adv Mater Interfaces* **6**, (2019).
99. Fonash, S. J. *Solar Cell Device Physics*. (Elsevier, 2010).
100. Würfel, P. & Würfel, U. *Physics of Solar Cells: From Basic Principles to Advanced Concepts*. *Wiley-VCH* (Wiley-VCH Verlag, 2016).
101. Nyman, M. et al. Highly Conductive Charge Transport Layers Impair Charge Extraction Selectivity in Thin-Film Solar Cells. *Advanced Energy and Sustainability Research* **4**, 2300030 (2023).
102. Das, C. et al. Band Bending at Hole Transporting Layer-Perovskite Interfaces in n-i-p and in p-i-n Architecture. *Solar RRL* **6**, 2200348 (2022).
103. Caprioglio, P. et al. On the Relation between the Open-Circuit Voltage and Quasi-Fermi Level Splitting in Efficient Perovskite Solar Cells. *Adv Energy Mater* **9**, (2019).
104. Svanström, S. et al. Direct Measurements of Interfacial Photovoltage and Band Alignment in Perovskite Solar Cells Using Hard X-ray Photoelectron Spectroscopy. *ACS Appl Mater Interfaces* **15**, 12485–12494 (2023).
105. Herterich, J. et al. Decoupling of Implied and External VOC Due to Ionic Movement Explaining Transient VOC Overshoot in Perovskite Solar Cells. *Energy Technology* **10**, 2100868 (2022).
106. Wurfel, P. The chemical potential of radiation. *Journal of Physics C: Solid State Physics* **15**, 3967–3985 (1982).
107. Honsberg, C.B, Bowden, S.G, Impact of Both Series and Shunt Resistance. *PVeducation* https://www.pveducation.org/pvcdrom/solar-cell-operation/impact-of-both-series-and-shunt-resistance.

108. Warby, J. et al. Mismatch of Quasi–Fermi Level Splitting and V oc in Perovskite Solar Cells. *Adv Energy Mater* **13**, 2303135 (2023).
109. Luo, D., Su, R., Zhang, W., Gong, Q. & Zhu, R. Minimizing non-radiative recombination losses in perovskite solar cells. *Nat Rev Mater* **5**, 44–60 (2020).
110. Rau, U. Reciprocity relation between photovoltaic quantum efficiency and electroluminescent emission of solar cells. *Phys Rev B Condens Matter Mater Phys* **76**, 1–8 (2007).
111. Chin, R. L. et al. Surface saturation current densities of perovskite thin films from Suns-photoluminescence quantum yield measurements. *Progress in Photovoltaics: Research and Applications* 1–7 (2024) doi:10.1002/pip.3767.
112. Stolterfoht, M. et al. The impact of energy alignment and interfacial recombination on the internal and external open-circuit voltage of perovskite solar cells. *Energy Environ Sci* **12**, 2778–2788 (2019).
113. Auger, P. Sur l'effet photoélectrique composé. *Journal de Physique et Le Radium* **6**, 205–208 (1925).
114. Dias, A. M. Auger Effect Revisited: An Essay by Inelastic Collision Theory. *Nat Sci (Irvine)* **10**, 59–62 (2018).
115. Meyaard, D. S., Lin, G.-B., Cho, J. & Schubert, E. F. Efficiency droop in gallium indium nitride (GaInN)/gallium nitride (GaN) LEDs. in *Nitride Semiconductor Light-Emitting Diodes (LEDs)* 279–300 (Elsevier, 2014). doi:10.1533/9780857099303.2.279.
116. Wenger, B. et al. Consolidation of the optoelectronic properties of CH3NH3PbBr3 perovskite single crystals. *Nat Commun* **8**, (2017).
117. Singh, S., Laxmi & Kabra, D. Defects in halide perovskite semiconductors: impact on photo-physics and solar cell performance. *J Phys D Appl Phys* **53**, (2020).
118. Ball, J. M. & Petrozza, A. Defects in perovskite-halides and their effects in solar cells. *Nat Energy* **1**, 16149 (2016).
119. SHOCKLEY, W. & READ, W. T. Statistics of the Recombinations of Holes and Electrons. *Semiconductor Devices: Pioneering Papers* 62–69 (1991) doi:10.1142/9789814503464_0002.
120. Cuevas, a. Lifetime studies of multicrystalline silicon. *Proceedings of the 8th Workshop on Crystalline Silicon Solar Cells Materials and Processes, Copper Mountain, 17-19 Aug 1998* 50–59 (1998).
121. Cuevas, A., Stocks, M., Macdonald, D., Kerr, M. & Samundsett, C. Recombination and trapping in multicrystalline silicon. *IEEE Trans Electron Devices* **46**, 2026–2034 (1999).
122. Sherkar, T. S. et al. Recombination in Perovskite Solar Cells: Significance of Grain Boundaries, Interface Traps, and Defect Ions. *ACS Energy Lett* **2**, 1214–1222 (2017).
123. Aydin, E., Bastiani, M. & Wolf, S. Defect and Contact Passivation for Perovskite Solar Cells. *Advanced Materials* **31**, 1900428 (2019).
124. Gharibzadeh, S. et al. Two birds with one stone: Dual grain-boundary and interface passivation enables >22% efficient inverted methylammonium-free perovskite solar cells. *Energy Environ Sci* **14**, 5875–5893 (2021).
125. Yang, J. et al. Precise control of PbI2 excess into grain boundary for efficacious charge extraction in off-stoichiometric perovskite solar cells. *Electrochim Acta* **338**, 135697 (2020).
126. Byeon, J. et al. Charge Transport Layer-Dependent Electronic Band Bending in Perovskite Solar Cells and Its Correlation to Light-Induced Device Degradation. *ACS Energy Lett* **5**, 2580–2589 (2020).
127. Onno, A., Chen, C., Koswatta, P., Boccard, M. & Holman, Z. C. Passivation, conductivity, and selectivity in solar cell contacts: Concepts and simulations based on a unified partial-resistances framework. *J Appl Phys* **126**, (2019).
128. Xu, X. et al. Improving Contact and Passivation of Buried Interface for High-Efficiency and Large-Area. *Adv Funct Mater* **32**, 2109968 (2022).
129. Liu, J. et al. Efficient and stable perovskite-silicon tandem solar cells through contact displacement by MgFx. *Science (1979)* (2022) doi:10.1126/SCIENCE.ABN8910.
130. Kirchartz, T. & Rau, U. What Makes a Good Solar Cell? *Adv Energy Mater* **8**, (2018).
131. Fassl, P. et al. Revealing the internal luminescence quantum efficiency of perovskite films via accurate quantification of photon recycling. *Matter* **4**, 1391–1412 (2021).
132. Stolterfoht, M. et al. How To Quantify the Efficiency Potential of Neat Perovskite Films: Perovskite Semiconductors with an Implied Efficiency Exceeding 28%. *Advanced Materials* **32**, 2000080 (2020).
133. Nelson, C. A., Monahan, N. R. & Zhu, X. Y. Exceeding the Shockley-Queisser limit in solar energy conversion. *Energy Environ Sci* **6**, 3508–3519 (2013).
134. Shockley, W. & Queisser, H. J. Detailed Balance Limit of Efficiency of p-n Junction Solar Cells. *J Appl Phys* **32**, 510–519 (1961).

135. Tiedje, T., Yablonovitch, E., Cody, G. D. & Brooks, B. G. Limiting Efficiency of Silicon Solar Cells. *IEEE Trans Electron Devices* **31**, 711–716 (1984).
136. Chuang, M. Calculation and visualization tools for theoretical solar cell efficiencies based on the Shockley Queisser limit. www.github.com/marcus-cmc/Shockley-Queisser-limit (2019).
137. Rühle, S. Tabulated values of the Shockley–Queisser limit for single-junction solar cells. *Solar Energy* **130**, 139–147 (2016).
138. De Vos, A. Detailed balance limit of the efficiency of tandem solar cells. *J Phys D Appl Phys* **13**, 839–846 (1980).
139. Futscher, M. H. & Ehrler, B. Efficiency Limit of Perovskite/Si Tandem Solar Cells. *ACS Energy Lett* **1**, 863–868 (2016).
140. Eperon, G. E., Hörantner, M. T. & Snaith, H. J. Metal halide perovskite tandem and multiple-junction photovoltaics. *Nature Reviews Chemistry* vol. 1 Preprint at https://doi.org/10.1038/S41570-017-0095 (2017).
141. Kim, B., Kim, J. & Park, N. First-principles identification of the charge-shifting mechanism and ferroelectricity in hybrid halide perovskites. *Sci Rep* **10**, 19635 (2020).
142. Goldschmidt, V. M. Die gesetze der krystallochemie. *Naturwissenschaften* **14**, 477–485 (1926).
143. Turnley, J. W., Agarwal, S. & Agrawal, R. Rethinking tolerance factor analysis for chalcogenide perovskites. *Mater Horiz* 4802–4808 (2024) doi:10.1039/d4mh00689e.
144. Travis, W. et al. On the application of the tolerance factor to inorganic and hybrid halide perovskites: A revised system. *J Mater Chem A Mater* **7**, 4548–4556 (2018).
145. Li, C. et al. Formability of ABX 3 (X = F, Cl, Br, I) halide perovskites. *Acta Crystallogr B* **64**, 702–707 (2008).
146. Ahmad, S. et al. Dion-Jacobson Phase 2D Layered Perovskites for Solar Cells with Ultrahigh Stability. *Joule* **3**, 794–806 (2019).
147. Chen, Y. et al. 2D Ruddlesden–Popper Perovskites for Optoelectronics. *Advanced Materials* **30**, 1–15 (2018).
148. Patel, J. B. et al. Light Absorption and Recycling in Hybrid Metal Halide Perovskite Photovoltaic Devices. *Adv Energy Mater* **10**, (2020).
149. Yue, L., Yan, B., Attridge, M. & Wang, Z. Light absorption in perovskite solar cell: Fundamentals and plasmonic enhancement of infrared band absorption. *Solar Energy* **124**, 143–152 (2016).
150. Baranowski, M. & Plochocka, P. Excitons in Metal-Halide Perovskites. *Adv Energy Mater* **10**, (2020).
151. D'Innocenzo, V. et al. Excitons versus free charges in organo-lead tri-halide perovskites. *Nat Commun* **5**, 1–6 (2014).
152. Leppert, L. Excitons in metal-halide perovskites from first-principles many-body perturbation theory. *Journal of Chemical Physics* **160**, (2024).
153. Leguy, A. M. A. et al. Experimental and theoretical optical properties of methylammonium lead halide perovskites. *Nanoscale* **8**, 6317–6327 (2016).
154. Miyata, A. et al. Direct measurement of the exciton binding energy and effective masses for charge carriers in organic-inorganic tri-halide perovskites. *Nat Phys* **11**, 582–587 (2015).
155. Galkowski, K. et al. Determination of the exciton binding energy and effective masses for methylammonium and formamidinium lead tri-halide perovskite semiconductors. *Energy Environ Sci* **9**, 962–970 (2016).
156. Jha, A. et al. Direct Observation of Ultrafast Exciton Dissociation in Lead Iodide Perovskite by 2D Electronic Spectroscopy. *ACS Photonics* **5**, 852–860 (2018).
157. Blancon, J. C. et al. Extremely efficient internal exciton dissociation through edge states in layered 2D perovskites. *Science (1979)* **355**, 1288–1292 (2017).
158. Lim, J. et al. Elucidating the long-range charge carrier mobility in metal halide perovskite thin films. *Energy Environ Sci* **12**, 169–176 (2019).
159. Herz, L. M. Charge-Carrier Mobilities in Metal Halide Perovskites: Fundamental Mechanisms and Limits. *ACS Energy Lett* **2**, 1539–1548 (2017).
160. Wehrenfennig, C., Eperon, G. E., Johnston, M. B., Snaith, H. J. & Herz, L. M. High charge carrier mobilities and lifetimes in organolead trihalide perovskites. *Advanced Materials* **26**, 1584–1589 (2014).
161. Zhao, J. et al. Charge Carrier Dynamics in Co-evaporated MAPbI3with a Gradient in Composition. *ACS Appl Energy Mater* **5**, 7049–7055 (2022).
162. Yuan, Y., Yan, G., Akel, S., Rau, U. & Kirchartz, T. Deriving mobility-lifetime products in halide perovskite films from spectrally- and time-resolved photoluminescence. 1–24.
163. Davies, C. L. et al. Bimolecular recombination in methylammonium lead triiodide perovskite is an inverse absorption process. *Nat Commun* **9**, 1–9 (2018).

164. DeQuilettes, D. W. et al. Tracking Photoexcited Carriers in Hybrid Perovskite Semiconductors: Trap-Dominated Spatial Heterogeneity and Diffusion. *ACS Nano* **11**, 11488–11496 (2017).

165. Chirvony, V. S. et al. Short Photoluminescence Lifetimes in Vacuum-Deposited CH3NH3PbI3 Perovskite Thin Films as a Result of Fast Diffusion of Photogenerated Charge Carriers. *Journal of Physical Chemistry Letters* **10**, 5167–5172 (2019).

166. Alcocer, M. J. P., Leijtens, T., Herz, L. M., Petrozza, A. & Snaith, H. J. Electron-Hole Diffusion Lengths Exceeding 1 Micrometer in an Organometal Trihalide Perovskite Absorber. *Science (1979)* **342**, 341–344 (2013).

167. Yin, X. et al. Critical roles of potassium in charge-carrier balance and diffusion induced defect passivation for efficient inverted perovskite solar cells. *J Mater Chem A Mater* **7**, 5666–5676 (2019).

168. Ou, Q. et al. Band structure engineering in metal halide perovskite nanostructures for optoelectronic applications. *Nano Materials Science* **1**, 268–287 (2019).

169. Tao, S. et al. Absolute energy level positions in tin- and lead-based halide perovskites. *Nat Commun* **10**, 1–10 (2019).

170. Eperon, G. E. et al. Formamidinium lead trihalide: A broadly tunable perovskite for efficient planar heterojunction solar cells. *Energy Environ Sci* **7**, 982–988 (2014).

171. McMeekin, D. P. et al. A mixed-cation lead mixed-halide perovskite absorber for tandem solar cells. *Science (1979)* **351**, 151–155 (2016).

172. Gil-Escrig, L. et al. Efficient Wide-Bandgap Mixed-Cation and Mixed-Halide Perovskite Solar Cells by Vacuum Deposition. *ACS Energy Lett* **6**, 827–836 (2021).

173. Pareja-Rivera, C., Solís-Cambero, A. L., Sánchez-Torres, M., Lima, E. & Solis-Ibarra, D. On the True Composition of Mixed-Cation Perovskite Films. *ACS Energy Lett* **3**, 2366–2367 (2018).

174. Yi, C. et al. Entropic stabilization of mixed A-cation ABX3 metal halide perovskites for high performance perovskite solar cells. *Energy Environ Sci* **9**, 656–662 (2016).

175. Ghosh, D., Smith, A. R., Walker, A. B. & Islam, M. S. Mixed A-Cation Perovskites for Solar Cells: Atomic-Scale Insights into Structural Distortion, Hydrogen Bonding, and Electronic Properties. *Chemistry of Materials* **30**, 5194–5204 (2018).

176. Li, Z. et al. Stabilizing Perovskite Structures by Tuning Tolerance Factor: Formation of Formamidinium and Cesium Lead Iodide Solid-State Alloys. *Chemistry of Materials* **28**, 284–292 (2016).

177. Becker, M., Klüner, T. & Wark, M. Formation of hybrid ABX 3 perovskite compounds for solar cell application: first-principles calculations of effective ionic radii and determination of tolerance factors. *Dalton Transactions* **46**, 3500–3509 (2017).

178. Li, Y. et al. Lasing from Laminated Quasi-2D 3D Perovskite Planar Heterostructures. *Adv Funct Mater* **32**, 2200772 (2022).

179. Kumawat, N. K., Liu, X. K., Kabra, D. & Gao, F. Blue perovskite light-emitting diodes: Progress, challenges and future directions. *Nanoscale* **11**, 2109–2120 (2019).

180. Li, Y. et al. Enhancement of Amplified Spontaneous Emission by Electric Field in CsPbBr3 Perovskites. *Nano Lett* **23**, 1637–1644 (2023).

181. Zhang, Q., Shang, Q., Su, R., Do, T. T. H. & Xiong, Q. Halide Perovskite Semiconductor Lasers: Materials, Cavity Design, and Low Threshold. *Nano Lett* **21**, 1903–1914 (2021).

182. Park, N. G. Perovskite solar cells: An emerging photovoltaic technology. *Materials Today* **18**, 65–72 (2015).

183. Momblona, C. et al. Efficient vacuum deposited p-i-n and n-i-p perovskite solar cells employing doped charge transport layers. *Energy Environ Sci* **9**, 3456–3463 (2016).

184. Mali, S. S. & Hong, C. K. P-i-n/n-i-p type planar hybrid structure of highly efficient perovskite solar cells towards improved air stability: Synthetic strategies and the role of p-type hole transport layer (HTL) and n-type electron transport layer (ETL) metal oxides. *Nanoscale* **8**, 10528–10540 (2016).

185. Roger, J. et al. Laminated Monolithic Perovskite/Silicon Tandem Photovoltaics. *Adv Energy Mater* **12**, 2200961 (2022).

186. Schmager, R. et al. Laminated Perovskite Photovoltaics: Enabling Novel Layer Combinations and Device Architectures. *Adv Funct Mater* **30**, 1907481 (2020).

187. Park, I. J. et al. A Three-Terminal Monolithic Perovskite/Si Tandem Solar Cell Characterization Platform. *Joule* **3**, 807–818 (2019).

188. Gota, F., Langenhorst, M., Schmager, R., Lehr, J. & Paetzold, U. W. Energy Yield Advantages of Three-Terminal Perovskite-Silicon Tandem Photovoltaics. *Joule* **4**, 2387–2403 (2020).

189. Baker-Finch, S. & McIntosh, K. Reflection of normally incident light from silicon solar cells with pyramidal textures. *Progress in Photovoltaics: Research and Applications* **19**, 406–416 (2011).
190. Farag, A. et al. Efficient Light Harvesting in Thick Perovskite Solar Cells Processed on Industry-Applicable Random Pyramidal Textures. *ACS Appl Energy Mater* **5**, 6700–6708 (2022).
191. Hamada, K. et al. Vacuum deposition of CsPbI3 layers on textured Si for Perovskite/Si tandem solar cells. *Jpn J Appl Phys* **58**, (2019).
192. Gota, F., Schmager, R., Farag, A. & Paetzold, U. Energy Yield Modelling of Textured Perovskite/Silicon Tandem Photovoltaics with Thick Perovskite Top Cells. *Opt Express* **30**, 14172–14188 (2022).
193. Subbiah, A. S. et al. High-performance perovskite single-junction and textured perovskite/silicon tandem solar cells via slot-die-coating. *ACS Energy Lett* **5**, 3034–3040 (2020).
194. Mao, L. et al. Fully Textured, Production-Line Compatible Monolithic Perovskite/Silicon Tandem Solar Cells Approaching 29% Efficiency. *Advanced Materials* **34**, 2206193 (2022).
195. Shrivastav, N., Madan, J. & Pandey, R. Optimizing tandem solar cells efficiency through current matching technique in lead-free perovskite/c-Si and lead-free perovskite/CIGS absorbers. *Indian Journal of Physics* **98**, 4899–4907 (2024).
196. De Bastiani, M. et al. Recombination junctions for efficient monolithic perovskite-based tandem solar cells: Physical principles, properties, processing and prospects. *Mater Horiz* **7**, 2791–2809 (2020).
197. Langenhorst, M. et al. Energy yield of all thin-film perovskite CIGS tandem solar modules. *Progress in Phot* **27**, 290–298 (2019).
198. Gohri, S., Madan, J. & Pandey, R. Spectral management and current matching optimization for high-efficiency perovskite-CIGS-SnS triple junction tandem solar cells. *Solid State Commun* **395**, 115754 (2025).
199. Orooji, S. & Paetzold, U. W. Energy Yield Modeling of Perovskite–Silicon Tandem Photovoltaics: Degradation and Total Lifetime Energy Yield. *Energy Technology* **12**, 2400998 (2024).
200. Lehr, J. et al. Energy yield modelling of perovskite/silicon two-terminal tandem PV modules with flat and textured interfaces. *Sustain Energy Fuels* **2**, 2754–2761 (2018).
201. Neder, V., Tabernig, S. W. & Polman, A. Detailed-balance efficiency limits of two-terminal perovskite/silicon tandem solar cells with planar and Lambertian spectral splitters. *J Photonics Energy* **12**, 1–11 (2022).
202. Schmager, R. et al. Methodology of energy yield modelling of perovskite-based multi-junction photovoltaics. *Opt Express* **27**, A507 (2019).
203. Munir, R. et al. Hybrid Perovskite Thin-Film Photovoltaics In Situ Diagnostics and Importance of the Precursor Solvate Phases. *Advanced Materials* **29**, (2016).
204. Ternes, S. et al. Drying Dynamics of Solution-Processed Perovskite Thin-Film Photovoltaics. *Adv Energy Mater* **9**, (2019).
205. Ternes, S. et al. Drying and Coating of Perovskite Thin Films: How to Control the Thin Film Morphology in Scalable Dynamic Coating Systems. *ACS Appl Mater Interfaces* **14**, 11300–11312 (2022).
206. Küffner, J. et al. One-Step Blade Coating of Inverted Double-Cation Perovskite Solar Cells from a Green Precursor Solvent. *ACS Appl Energy Mater* **4**, 11700–11710 (2021).
207. Cao, X. et al. All green solvent engineering of organic–inorganic hybrid perovskite layer for high-performance solar cells. *Chemical Engineering Journal* **437**, 135458 (2022).
208. Al-Ashouri, A. et al. Wettability Improvement of a Carbazole-Based Hole-Selective Monolayer for Reproducible Perovskite Solar Cells. *ACS Energy Lett* **8**, 898–900 (2023).
209. Longo, G., Gil-Escrig, L., Degen, M. J., Sessolo, M. & Bolink, H. J. Perovskite solar cells prepared by flash evaporation. *Chemical Communications* **51**, 7376–7378 (2015).
210. Leyden, M. R. et al. High performance perovskite solar cells by hybrid chemical vapor deposition. *J Mater Chem A Mater* **2**, 18742–18745 (2014).
211. Rodkey, N. et al. Close-Space Sublimation as a Scalable Method for Perovskite Solar Cells. *ACS Energy Lett* **9**, 927–933 (2024).
212. Paliwal, A., Zanoni, K. P. S., Roldán-Carmona, C., Hernández-Fenollosa, M. A. & Bolink, H. J. Fully vacuum-deposited perovskite solar cells in substrate configuration. *Matter* **6**, 3499–3508 (2023).
213. Li, H. et al. Sequential vacuum-evaporated perovskite solar cells with more than 24% efficiency. *Sci Adv* **8**, eabo7422 (2022).

214. Škorjanc, V. et al. Seed Layers for Wide-Band Gap Coevaporated Perovskite Solar Cells: CsCl Regulates Band Gap and Reduces Process Variability. *ACS Energy Lett* **9**, 5639–5646 (2024).

215. Peng, C. et al. High-Performance Thermally Evaporated Blue Perovskite Light-Emitting Diodes Enabled by Post-Evaporation Passivation. *Chemical Engineering Journal* **499**, 155955 (2024).

216. Han, S., Hyeong, S.-K., Lee, S.-K. & Shin, N. Sequential surface passivation for enhanced stability of vapor-deposited methylammonium lead iodide thin films. *Chemical Engineering Journal* **439**, 135715 (2022).

217. Abzieher, T. et al. Continuous flash sublimation of inorganic halide perovskites: overcoming rate and continuity limitations of vapor deposition. *J Mater Chem A Mater* **12**, 8405–8419 (2024).

218. Tai, M. et al. Laser-Induced Flash-Evaporation Printing CH3NH3PbI3 Thin Films for High-Performance Planar Solar Cells. *ACS Appl Mater Interfaces* **10**, 26206–26212 (2018).

219. Xu, H. et al. Grain growth study of perovskite thin films prepared by flash evaporation and its effect on solar cell performance. *RSC Adv* **6**, 48851–48857 (2016).

220. Dewi, H. A., Erdenebileg, E., De Luca, D., Mhaisalkar, S. G. & Bruno, A. Accelerated MAPbI 3 Co-evaporation: Productivity Gains without Compromising Performance. *ACS Energy Lett* **9**, 4319–4322 (2024).

221. Feeney, T. et al. Understanding and exploiting interfacial interactions between phosphonic acid functional groups and co-evaporated perovskites. *Matter* **7**, 2066–2090 (2024).

222. Yan, S. et al. A Templating Approach to Controlling the Growth of Coevaporated Halide Perovskites. *ACS Energy Lett* **8**, 4008–4015 (2023).

223. Nikita Aleksandrovich, T. Chemistry of high-temperature materials. in *Proceedings of the Second All-Union Conference on the High-Temperature Chemistry of Oxides* (1965).

224. Ritala, M. et al. Atomic layer deposition of oxide thin films with metal alkoxides as oxygen sources. *Science (1979)* **288**, 319–321 (2000).

225. Hughes, K. J. & Engstrom, J. R. Nucleation delay in atomic layer deposition on a thin organic layer and the role of reaction thermochemistry. *Journal of Vacuum Science & Technology A: Vacuum, Surfaces, and Films* **30**, 01A102 (2012).

226. Brinkmann, K. O. et al. Suppressed decomposition of organometal halide perovskites by impermeable electron-extraction layers in inverted solar cells. *Nat Commun* **8**, 1–9 (2017).

227. Gong, B. & Parsons, G. N. Quantitative in situ infrared analysis of reactions between trimethylaluminum and polymers during Al 2O 3 atomic layer deposition. *J Mater Chem* **22**, 15672–15682 (2012).

228. Jur, J. S. et al. Temperature-dependent subsurface growth during atomic layer deposition on polypropylene and cellulose fibers. *Langmuir* **26**, 8239–8244 (2010).

229. Parsons, G. N. et al. Mechanisms and reactions during atomic layer deposition on polymers. *Coord Chem Rev* **257**, 3323–3331 (2013).

230. Mullings, M. N., Hägglund, C. & Bent, S. F. Tin oxide atomic layer deposition from tetrakis(dimethylamino)tin and water. *Journal of Vacuum Science & Technology A: Vacuum, Surfaces, and Films* **31**, (2013).

231. Choi, D. W., Maeng, W. J. & Park, J. S. The conducting tin oxide thin films deposited via atomic layer deposition using Tetrakis-dimethylamino tin and peroxide for transparent flexible electronics. *Appl Surf Sci* **313**, 585–590 (2014).

232. Tanskanen, J. T. & Bent, S. F. Insights into the Surface Chemistry of Tin Oxide Atomic Layer Deposition from Quantum Chemical Calculations. *The Journal of Physical Chemistry C* **117**, 19056–19062 (2013).

233. Kavan, L., Steier, L. & Gratzel, M. Ultrathin buffer layers of SnO2 by atomic layer deposition: Perfect blocking function and thermal stability. *Journal of Physical Chemistry C* **121**, 342–350 (2017).

234. Elam, J. W. et al. Atomic layer deposition of tin oxide films using tetrakis(dimethylamino) tin. *Journal of Vacuum Science & Technology A: Vacuum, Surfaces, and Films* **26**, 244–252 (2008).

235. Zardetto, V. et al. Atomic layer deposition for perovskite solar cells: Research status, opportunities and challenges. *Sustain Energy Fuels* **1**, 30–55 (2017).

236. Hultqvist, A. et al. SnOx Atomic Layer Deposition on Bare Perovskite—An Investigation of Initial Growth Dynamics, Interface Chemistry, and Solar Cell Performance. *ACS Appl Energy Mater* **4**, 510–522 (2021).

237. Palmstrom, A. F. et al. Interfacial Effects of Tin Oxide Atomic Layer Deposition in Metal Halide Perovskite Photovoltaics. *Adv Energy Mater* **8**, 1–10 (2018).

238. Johnson, S. A. et al. Improving the barrier properties of tin oxide in metal halide perovskite solar cells using ozone to enhance nucleation. *Joule* **7**, 2873–2893 (2023).

239. Mallik, N. et al. Interface defect formation for atomic layer deposition of SnO2 on metal halide perovskites. *Nano Energy* **126**, 1–10 (2024).

240. Yu, X., Yan, H. & Peng, Q. Reaction Temperature and Partial Pressure Induced Etching of Methylammonium Lead Iodide Perovskite by Trimethylaluminum. *Langmuir* **35**, 6522–6531 (2019).

241. Aune, R. E. & Seetharaman, S. Thermodynamic aspects of metals processing. *Fundamentals of Metallurgy* 38–81 (2005) doi:10.1533/9781845690946.1.38.

242. Frey, H. & Khan, H. R. *Handbook of Thin-Film Technology*.

243. Harsha, K. S. *Principles of Vapor Deposition of Thin Films*. *Principles of Vapor Deposition of Thin Films* (2006). doi:10.1016/B978-0-08-044699-8.X5000-1.

244. Koffman, L. D., Plesset, M. S. & Lees, L. Theory of evaporation and condensation. *Physics of Fluids* **27**, 876–880 (1984).

245. Gmbh, S. B. H. *Epitaxy: physical principles and technical implementation*. *Choice Reviews Online* vol. 42 (2004).

246. Shannon, R. D. Revised effective ionic radii and systematic studies of interatomic distances in halides and chalcogenides. *Acta Crystallographica Section A* **32**, 751–767 (1976).

247. Freidburg, J. *Plasma Physics and Fusion Energy*. (Cambridge University Press, 2007).

248. Fan, C., Do, D. D. & Nicholson, D. The concept of mean free path in the kinetic Monte Carlo description of bulk fluid behaviour, vapour–liquid equilibria and surface adsorption of argon. *Mol Simul* **38**, 1001–1009 (2012).

249. Kieslich, G., Sun, S. & Cheetham, A. K. Solid-state principles applied to organic–inorganic perovskites: new tricks for an old dog. *Chem. Sci.* **5**, 4712–4715 (2014).

250. Podolesheva, I., Gushterova, P., Platikanova, V. & Konstantinov, I. Determination of the emission characteristics of evaporation sources and of the thickness and composition of mixed layers. *Journal of Vacuum Science & Technology A: Vacuum, Surfaces, and Films* **16**, 674–678 (1998).

251. Venables, J. A., Spiller, G. D. T. & Hanbucken, M. Nucleation and growth of thin films. *Reports on Progress in Physics* **47**, 399–459 (1984).

252. Dhanaraj, G., Byrappa, K., Prasad, V. & Dudley, M. *Springer Handbook of Crystal Growth*. *Springer* (2010). doi:0.1007/978-3-540-74761-1.

253. Volmer, M. & Weber, A. Keimbildung in übersättigten Gebilden. *Zeitschrift für Physikalische Chemie* **119U**, 277–301 (1926).

254. Stranski, I. N. & Krastanow, L. Berichtigung zur Arbeit - 'Zur Theorie der orientierten Ausscheidung von Ionenkristallen aufeinander'. *Monatsh Chem* **72**, 76 (1939).

255. Grabow, M. H. & Gilmer, G. H. Thin film growth modes, wetting and cluster nucleation. *Surf Sci* **194**, 333–346 (1988).

256. Huse, D. A. Incomplete wetting by adsorbed solid films. *Phys Rev B* **29**, 6985–6987 (1984).

257. Frank, F. C. & van der Merwe, J. H. One-dimensional dislocations. I. Static theory. *Proceedings of the Royal Society of London* **198**, 205–216 (1949).

258. Frank, F. C. & van der Merwe, J. H. One-dimensional dislocations . II . Misfitting. *Proceedings of the Royal Society of London* 216–225 (1947).

259. Madras, G. & McCoy, B. J. Temperature effects during Ostwald ripening. *J Chem Phys* **119**, 1683–1693 (2003).

260. Kirchartz, T., Marquez, J. A., Stolterfoht, M. & Unold, T. Photoluminescence-Based Characterization of Halide Perovskites for Photovoltaics. *Adv Energy Mater* **10**, 1904134 (2020).

261. Farag, A. et al. Evaporated Self-Assembled Monolayer Hole Transport Layers: Lossless Interfaces in p-i-n Perovskite Solar Cells. *Adv Energy Mater* **13**, 2203982 (2023).

262. Dang, M. T., Lefebvre, J. & Wuest, J. D. Recycling Indium Tin Oxide (ITO) Electrodes Used in Thin-Film Devices with Adjacent Hole-Transport Layers of Metal Oxides. *ACS Sustain Chem Eng* **3**, 3373–3381 (2015).

263. Blum, M. et al. Solid and liquid spectroscopic analysis (SALSA)–a soft x-ray spectroscopy endstation with a novel flow-through liquid cell. *Review of Scientific Instruments* **80**, 123102 (2009).

264. Fuchs, O. et al. High-resolution, high-transmission soft x-ray spectrometer for the study of biological samples. *Review of Scientific Instruments* **80**, (2009).

265. Weinhardt, L. et al. Sulfate Speciation Analysis Using Soft X-ray Emission Spectroscopy. *Anal Chem* **93**, 8300–8308 (2021).

266. Kwok, D. Y. & Neumann, A. W. Contact angle measurement and contact angle interpretation. *Adv Colloid Interface Sci* **81**, 167–249 (1999).

267. Owens, D. K. & Wendt, R. C. Estimation of the Surface Free Energy of Polymers. *J Appl Polym Sci* **13**, 1741–1747 (1969).

268. Saliba, M. & Etgar, L. Current density mismatch in Perovskite solar cells. *ACS Energy Lett* **5**, 2886–2888 (2020).

269. Bliss, M. et al. Spectral Response Measurements of Perovskite Solar Cells. *IEEE J Photovolt* **9**, 220–226 (2019).

270. Eames, C. et al. Ionic transport in hybrid lead iodide perovskite solar cells. *Nat Commun* **6**, 2–9 (2015).

271. Tang, Z. & Minemoto, T. Experimental demonstration of ions induced electric field in perovskite solar cells. *ArXiv* **47**, 124–134 (2021).

272. ’Schmager, R., ’Paetzold, U. W. ’, ’Langenhorst, M., ’Gota, F. & ’Lehr, J. EYcalc - Energy yield calculator for multi-junction solar modules with realistic irradiance data and textured interfaces. doi.org/10.5281/zenodo.4696257 (2021) doi:10.5281/zenodo.4696257.

273. Byrnes, S. J. Multilayer optical calculations. *ArXiv* 1–20 (2016).

274. Grimme, S., Antony, J., Ehrlich, S. & Krieg, H. A consistent and accurate ab initio parametrization of density functional dispersion correction (DFT-D) for the 94 elements H-Pu. *Journal of Chemical Physics* **132**, (2010).

275. Giannozzi, P. et al. QUANTUM ESPRESSO: A modular and open-source software project for quantum simulations of materials. *Journal of Physics Condensed Matter* vol. 21 Preprint at https://doi.org/10.1088/0953-8984/21/39/395502 (2009).

276. Marín-Villa, P., Arauzo, A., Drużbicki, K. & Fernandez-Alonso, F. Unraveling the Ordered Phase of the Quintessential Hybrid Perovskite MAPbI 3 –Thermophysics to the Rescue. *J Phys Chem Lett* **13**, 8422–8428 (2022).

277. Feeney, T., Abzieher, T., Ritzer, D. B., Diercks, A. & Paetzold, U. W. All-evaporated perovskites: challenges and opportunities for tandem photovoltaic devices. in *PVSEC-31* (2020).

278. Xu, Y., Gong, T. & Munday, J. N. The generalized Shockley-Queisser limit for nanostructured solar cells. *Sci Rep* **5**, 1–9 (2015).

279. Vossier, A., Gualdi, F., Dollet, A., Ares, R. & Aimez, V. Approaching the Shockley-Queisser limit: General assessment of the main limiting mechanisms in photovoltaic cells. *J Appl Phys* **117**, 15102 (2015).

280. Liu, X. et al. Over 28% efficiency perovskite/Cu(InGa)Se2 tandem solar cells: highly efficient sub-cells and their bandgap matching. *Energy Environ Sci* **16**, 5029–5042 (2023).

281. De Bastiani, M. et al. Efficient bifacial monolithic perovskite/silicon tandem solar cells via bandgap engineering. *Nat Energy* **6**, 167–175 (2021).

282. Duong, T. et al. Rubidium Multication Perovskite with Optimized Bandgap for Perovskite-Silicon Tandem with over 26% Efficiency. *Adv Energy Mater* **7**, 1700228 (2017).

283. Hosseinian Ahangharnejhad, R. et al. Irradiance and temperature considerations in the design and deployment of high annual energy yield perovskite/CIGS tandems. *Sustain Energy Fuels* **3**, 1841–1851 (2019).

284. Kim, D. H. et al. Bimolecular Additives Improve Wide-Band-Gap Perovskites for Efficient Tandem Solar Cells with CIGS. *Joule* **3**, 1734–1745 (2019).

285. Yang, D. et al. Nano Energy transparent electrode for high efficient semitransparent top cell. *Nano Energy* **84**, 105934 (2021).

286. Sheng, R. et al. Four-Terminal Tandem Solar Cells Using CH3NH3PbBr3 by Spectrum Splitting. *Journal of Physical Chemistry Letters* **6**, 3931–3934 (2015).

287. Fu, F. et al. Low-temperature-processed efficient semi-transparent planar perovskite solar cells for bifacial and tandem applications. *Nat Commun* **6**, 1–9 (2015).

288. Werner, J. et al. Efficient Near-Infrared-Transparent Perovskite Solar Cells Enabling Direct Comparison of 4-Terminal and Monolithic Perovskite/Silicon Tandem Cells. *ACS Energy Lett* **1**, 474–480 (2016).

289. Duong, T. et al. Rubidium Multication Perovskite with Optimized Bandgap for Perovskite-Silicon Tandem with over 26% Efficiency. *Advanced Energy Materials* vol. 7 Preprint at https://doi.org/10.1002/aenm.201700228 (2017).

290. Fu, F. et al. High-efficiency inverted semi-transparent planar perovskite solar cells in substrate configuration. *Nature Energy* vol. 2 Preprint at https://doi.org/10.1038/nenergy.2016.190 (2017).

291. Shen, H. et al. Mechanically-stacked perovskite/CIGS tandem solar cells with efficiency of 23.9% and reduced oxygen sensitivity. *Energy Environ Sci* **11**, 394–406 (2018).

292. Jaysankar, M. et al. Minimizing Voltage Loss in Wide-Bandgap Perovskites for Tandem Solar Cells. *ACS Energy Lett* **4**, 259–264 (2019).

293. Al-Ashouri, A. et al. Monolithic perovskite/silicon tandem solar cell with >29% efficiency by enhanced hole extraction. *Science (1979)* **370**, 1300–1309 (2020).

294. Huang, Y. C. et al. A comprehensive optimization of highly efficient MA-Free wide-bandgap perovskites for 4-T Perovskite/Silicon tandem solar cells. *Chemical Engineering Journal* **503**, 158272 (2025).
295. Zhang, C. et al. CNT-based bifacial perovskite solar cells toward highly efficient 4-terminal tandem photovoltaics. *Energy Environ Sci* **15**, 1536–1544 (2022).
296. Belghachi, A. & Limam, N. Effect of the absorber layer band-gap on CIGS solar cell. *Chinese Journal of Physics* **55**, 1127–1134 (2017).
297. Lang, F. et al. Proton Radiation Hardness of Perovskite Tandem Photovoltaics. *Joule* **4**, 1054–1069 (2020).
298. Jiang, Y. & Qi, Y. Metal halide perovskite-based flexible tandem solar cells: Next-generation flexible photovoltaic technology. *Mater Chem Front* **5**, 4833–4850 (2021).
299. Schultes, M. et al. Sputtered Transparent Electrodes (IO H and IZO) with Low Parasitic Near-Infrared Absorption for Perovskite–Cu(In,Ga)Se2 Tandem Solar Cells Enhanced Reader.pdf. *Applied Energy Materials* **2**, 7823–7831 (2019).
300. Duong, T. et al. Semitransparent Perovskite Solar Cell With Sputtered Front and Rear Electrodes for a Four-Terminal Tandem. *IEEE J Photovolt* **6**, 679–687 (2016).
301. Schultes, M. Four-Terminal Perovskite-CIGS Tandem Solar Cells with Improved Near-Infrared Response. (2020). doi:10.5445/IR/1000118573.
302. Hossain, I. M. et al. Nanostructured front electrodes for perovskite/c-Si tandem photovoltaics. *Opt Express* **28**, 8878 (2020).
303. Goul, R. et al. Electron tunneling properties of Al 2 O 3 tunnel barrier made using atomic layer deposition in multilayer devices. *AIP Adv* **9**, (2019).
304. Jiang, Y. et al. High-Mobility In2O3:H Electrodes for Four-Terminal Perovskite/CuInSe2Tandem Solar Cells. *ACS Nano* **14**, 7502–7512 (2020).
305. Koida, T. et al. Hydrogen-doped In2O3 transparent conducting oxide films prepared by solid-phase crystallization method. *J Appl Phys* **107**, 33514 (2010).
306. Moghadamzadeh, S. et al. In2O3:H-Based Hole-Transport-Layer-Free Tin/Lead Perovskite Solar Cells for Efficient Four-Terminal All-Perovskite Tandem Solar Cells. *ACS Appl Mater Interfaces* **13**, 46488–46498 (2021).
307. Gupta, D. C. Non-Destructive Concentration Determination Reflection of Carrier in Epitaxial Silicon Using a Total. *Solid State Electron* **13**, 543–552 (1970).
308. Egbo, K. O., Adesina, A. E., Ezeh, C. V., Liu, C. P. & Yu, K. M. Effects of free carriers on the optical properties of high mobility transition metal doped In2 O3 transparent conductors. *Phys Rev Mater* **5**, 1–12 (2021).
309. Jiang, H., Wang, S., Xu, Y. & Yang, S. Preparation of a-IZO thin films by RF magnetron sputtering for Cu (In, Ga) Se2 solar cells. *J Phys Conf Ser* **1549**, (2020).
310. Brewer, S. H. & Franzen, S. Indium tin oxide plasma frequency dependence on sheet resistance and surface adlayers determined by reflectance FTIR spectroscopy. *Journal of Physical Chemistry B* **106**, 12986–12992 (2002).
311. Sathiaraj, T. S. Effect of annealing on the structural, optical and electrical properties of ITO films by RF sputtering under low vacuum level. *Microelectronics J* **39**, 1444–1451 (2008).
312. Tohsophon, T., Dabirian, A., De Wolf, S., Morales-Masis, M. & Ballif, C. Environmental stability of high-mobility indium-oxide based transparent electrodes. *APL Mater* **3**, (2015).
313. Hu, T. et al. Effect of UV-ozone treatment on ITO and post-annealing on the performance of organic solar cells. *Synth Met* **159**, 754–756 (2009).
314. Dodge, M. J. Refractive properties of magnesium fluoride. *Appl Opt* **23**, 1980 (1984).
315. Liu, X. et al. Triple cathode buffer layers composed of PCBM, C60, and LiF for high-performance planar perovskite solar cells. *ACS Appl Mater Interfaces* **7**, 6230–6237 (2015).
316. Langenhorst, M. et al. Energy yield of all thin-film perovskite/CIGS tandem solar modules. *Prog Photovolt* **27**, 290–298 (2018).
317. Domanski, K. et al. Migration of cations induces reversible performance losses over day/night cycling in perovskite solar cells. *Energy Environ Sci* **10**, 604–613 (2017).
318. Kamat, P. V. & Kuno, M. Halide Ion Migration in Perovskite Nanocrystals and Nanostructures. *Acc Chem Res* **54**, 520–531 (2021).
319. Luo, Y. et al. Direct Observation of Halide Migration and its Effect on the Photoluminescence of Methylammonium Lead Bromide Perovskite Single Crystals. *Advanced Materials* **29**, 1–7 (2017).
320. Podraza, N. J. et al. Urbach energy and open-circuit voltage deficit for mixed anion− cation perovskite solar cells. *ACS Appl Mater Interfaces* **14**, 7796–7804 (2022).

321. Chen, B. et al. Enhanced optical path and electron diffusion length enable high-efficiency perovskite tandems. *Nat Commun* **11**, (2020).
322. Herguth, A. et al. Influence of spectral mismatch, cell reflection properties and IQE on the efficiency measurement. in *EU-PVSEC 26th* 1555–1557 (2011). doi:10.4229/26thEUPVSEC2011-2BV.2.47.
323. De Carvalho Neto, J. T. Performance Analysis of Silicon Technologies Photovoltaic Cells Using Artificial Light Source in Different Spectra. *IEEE Sens J* **23**, 9972–9980 (2023).
324. ’Schmager, R., ’Paetzold, U. W. ’, ’Langenhorst, M., ’Gota, F. & ’Lehr, J. EYcalc - Energy yield calculator for multi-junction solar modules with realistic irradiance data and textured interfaces. (2021).
325. Chen, J. et al. High-Performance Thickness Insensitive Perovskite Solar Cells with Enhanced Moisture Stability. *Advanced Energy Materials* vol. 8 Preprint at https://doi.org/10.1002/aenm.201800438 (2018).
326. Zhu, L. et al. Investigation on the role of Lewis bases in the ripening process of perovskite films for highly efficient perovskite solar cells. *J Mater Chem A Mater* **5**, 20874–20881 (2017).
327. Deinega, A., Valuev, I., Potapkin, B. & Lozovik, Y. Minimizing light reflection from dielectric textured surfaces. *Journal of the Optical Society of America A* **28**, 770 (2011).
328. Schmager, R. et al. Texture of the Viola Flower for Light Harvesting in Photovoltaics. *ACS Photonics* **4**, 2687–2692 (2017).
329. Dottermusch, S. et al. Micro-cone textures for improved light in-coupling and retroreflection-inspired light trapping at the front surface of solr modules. *Prog Photovolt* **27**, 593–602 (2019).
330. Jošt, M. et al. Textured interfaces in monolithic perovskite/silicon tandem solar cells: Advanced light management for improved efficiency and energy yield. *Energy Environ Sci* **11**, 3511–3523 (2018).
331. Esiner, S., Bus, T., Wienk, M. M., Hermans, K. & Janssen, R. A. J. J. Quantification and validation of the efficiency enhancement reached by application of a retroreflective light trapping texture on a polymer solar cell. *Adv Energy Mater* **3**, 1013–1017 (2013).
332. Lipovšek, B. et al. Detailed optical modelling and light-management of thin-film organic solar cells with consideration of small-area effects. *Opt Express* **25**, A176 (2017).
333. Myers, J. D. et al. A universal optical approach to enhancing efficiency of organic-based photovoltaic devices. *Energy Environ Sci* **5**, 6900–6904 (2012).
334. Ulbrich, C., Gerber, A., Hermans, K., Lambertz, A. & Rau, U. Analysis of short circuit current gains by an anti-reflective textured cover on silicon thin film solar cells. *Prog Photovolt* **21**, 1672–1681 (2013).
335. Lipovsek, B., Krc, J. & Topic, M. *Microtextured Light-Management Foils and Their Optimization for Planar Organic and Perovskite Solar Cells*. *IEEE Journal of Photovoltaics* vol. 8 783–792 (IEEE Electron Devices Society, 2018).
336. Lipovsek, B., Krc, J. & Topic, M. *Optimization of microtextured light-management films for enhanced light trapping in organic solar cells under perpendicular and oblique illumination conditions*. *IEEE Journal of Photovoltaics* vol. 4 639–646 (2014).
337. Kuo, S.-Y. et al. Flexible-textured polydimethylsiloxane antireflection structure for enhancing omnidirectional photovoltaic performance of Cu(In,Ga)Se_2 solar cells. *Opt Express* **22**, 2860 (2014).
338. Ruiz-Preciado, M. A. et al. Monolithic Two-Terminal Perovskite/CIS Tandem Solar Cells with Efficiency Approaching 25%. *ACS Energy Lett* **7**, 2273–2281 (2022).
339. Uzagare, S. & Chavan, K. B. Design and numerical optimisation of a CH3NH3SnI3−xBrx/CI(G)S tandem solar cell with over 50% PCE. *Phys Scr* **99**, (2024).
340. Moradbeigi, M. & Razaghi, M. Opto-electrical study of 4T perovskite-chalcogenide tandem solar cell with the addition of quasi-2D perovskite as capping layer of 3D perovskite layer. *Energy Convers Manag* **320**, 118991 (2024).
341. Zein, W., Alanazi, T. I., Saeed, A., Salah, M. M. & Mousa, M. Proposal and design of organic/CIGS tandem solar cell: Unveiling optoelectronic approaches for enhanced photovoltaic performance. *Optik (Stuttg)* **302**, 171719 (2024).
342. Wu, S. et al. Modulation of Defects and Interfaces through Alkylammonium Interlayer for Efficient Inverted Perovskite Solar Cells. *Joule* **4**, 1248–1262 (2020).
343. Yang, G. et al. Stable and low-photovoltage-loss perovskite solar cells by multifunctional passivation. *Nat Photonics* **15**, 681–689 (2021).
344. Wu, S. et al. 2D metal–organic framework for stable perovskite solar cells with minimized lead leakage. *Nat Nanotechnol* **15**, 934–940 (2020).
345. Mei, A. et al. Stabilizing Perovskite Solar Cells to IEC61215:2016 Standards with over 9,000-h Operational Tracking. *Joule* **4**, 2646–2660 (2020).

346. Kang, Y. et al. *Thermal Shock Fabrication of Ion-Stabilized Perovskite and Solar Cells*. *Advanced Materials* vol. 34 2203166 (John Wiley and Sons Inc, 2022).
347. Jošt, M. et al. Perovskite/CIGS Tandem Solar Cells: From Certified 24.2% toward 30% and beyond. *ACS Energy Lett* **7**, 1298–1307 (2022).
348. Jošt, M. et al. Efficient Monolithic Perovskite/Cu(In,Ga)Se2 Tandem Solar Cells with Thin Conformal Hole Transport Layers for Integration on Rough Bottom Cell Surfaces Enhanced Reader. *ACS Energy Lett* **4**, 583–590 (2019).
349. Meng, L., You, J. & Yang, Y. Addressing the stability issue of perovskite solar cells for commercial applications. *Nature Communications* vol. 9 1–4 Preprint at https://doi.org/10.1038/s41467-018-07255-1 (2018).
350. Rong, Y. et al. Challenges for commercializing perovskite solar cells. *Science* vol. 361 Preprint at https://doi.org/10.1126/science.aat8235 (2018).
351. Boyd, C. C. et al. Overcoming Redox Reactions at Perovskite-Nickel Oxide Interfaces to Boost Voltages in Perovskite Solar Cells. *Joule* **4**, 1759–1775 (2020).
352. Park, I. J. et al. Highly Efficient and Uniform 1 cm2 Perovskite Solar Cells with an Electrochemically Deposited NiOx Hole-Extraction Layer. *ChemSusChem* vol. 10 2660–2667 Preprint at https://doi.org/10.1002/cssc.201700612 (2017).
353. Michalska, M. et al. Microfluidic Processing of Ligand-Engineered NiO Nanoparticles for Low-Temperature Hole-Transporting Layers in Perovskite Solar Cells. *Solar RRL* vol. 5 Preprint at https://doi.org/10.1002/solr.202100342 (2021).
354. Di Girolamo, D. et al. Progress, highlights and perspectives on NiO in perovskite photovoltaics. *Chem Sci* **11**, 7746–7759 (2020).
355. Abzieher, T. et al. *Electron-Beam-Evaporated Nickel Oxide Hole Transport Layers for Perovskite-Based Photovoltaics*. *Advanced Energy Materials* vol. 9 1802995 (John Wiley & Sons, Ltd, 2019).
356. Yang, G. et al. Defect engineering in wide-bandgap perovskites for efficient perovskite–silicon tandem solar cells. *Nat Photonics* **16**, 588–594 (2022).
357. Rombach, F. M., Haque, S. A. & Macdonald, T. J. Lessons learned from spiro-OMeTAD and PTAA in perovskite solar cells. *Energy Environ Sci* **14**, 5161–5190 (2021).
358. Xu, X. et al. Improving Contact and Passivation of Buried Interface for High-Efficiency and Large-Area Inverted Perovskite Solar Cells. *Adv Funct Mater* **32**, 2109968 (2022).
359. Chen, K. et al. Facile Physical Modifications of Polymer Hole Transporting Layers for Efficient and Reproducible Perovskite Solar Cells with Fill Factor Exceeding 80%. *Solar RRL* **2000365**, 1–9 (2020).
360. Li, B. et al. Reduced bilateral recombination by functional molecular interface engineering for efficient inverted perovskite solar cells. *Nano Energy* **78**, 105249 (2020).
361. You, J. et al. The fabrication of homogeneous perovskite films on non-wetting interfaces enabled by physical modification. *Journal of Energy Chemistry* **38**, 192–198 (2019).
362. Thampy, S., Xu, W. & Hsu, J. W. P. Metal Oxide-Induced Instability and Its Mitigation in Halide Perovskite Solar Cells. *Journal of Physical Chemistry Letters* **12**, 8495–8506 (2021).
363. Di Girolamo, D. et al. From Bulk to Surface: Sodium Treatment Reduces Recombination at the Nickel Oxide/Perovskite Interface. *Adv Mater Interfaces* **6**, 1900789 (2019).
364. Hu, Y. et al. Construction of Charge Transport Channels at the NiOx/Perovskite Interface through Moderate Dipoles toward Highly Efficient Inverted Solar Cells. *ACS Appl Mater Interfaces* **14**, 13431–13439 (2022).
365. Farag, A. et al. Mitigation of Open-Circuit Voltage Losses in Perovskite Solar Cells Processed over Micrometer-Sized-Textured Si Substrates. *Adv Funct Mater* **33**, 2210758 (2023).
366. Pylnev, M., Barbisan, A. M. & Wei, T.-C. Effect of wettability of substrate on metal halide perovskite growth. *Appl Surf Sci* **541**, 148559 (2021).
367. Hu, H. et al. Triple-junction perovskite–perovskite–silicon solar cells with power conversion efficiency of 24.4%. *Energy Environ Sci* **17**, 2800–2814 (2024).
368. Magomedov, A. et al. Self-Assembled Hole Transporting Monolayer for Highly Efficient Perovskite Solar Cells. *Adv Energy Mater* **8**, 1801892 (2018).
369. Yalcin, E. et al. Semiconductor self-assembled monolayers as selective contacts for efficient PiN perovskite solar cells. *Energy Environ Sci* **12**, 230–237 (2019).
370. Gu, Z. et al. Interfacial engineering of self-assembled monolayer modified semi-roll-to-roll planar heterojunction perovskite solar cells on flexible substrates. *J Mater Chem A Mater* **3**, 24254–24260 (2015).

371. Liu, L. et al. Fully printable mesoscopic perovskite solar cells with organic silane self-assembled monolayer. *J Am Chem Soc* **137**, 1790–1793 (2015).
372. Zuo, L. et al. Enhanced photovoltaic performance of CH3NH3PbI3 perovskite solar cells through interfacial engineering using self-assembling monolayer. *J Am Chem Soc* **137**, 2674–2679 (2015).
373. Schreiber, F. Structure and growth of self-assembling monolayers. *Progress in Surface Science* vol. 65 151–257 Preprint at https://doi.org/10.1016/S0079-6816(00)00024-1 (2000).
374. Halik, M. & Hirsch, A. The Potential of Molecular Self-Assembled Monolayers in Organic Electronic Devices. *Advanced Materials* **23**, 2689–2695 (2011).
375. Hoegl, H. On photoelectric effects in polymers and their sensitization by dopants. *Journal of Physical Chemistry* **69**, 755–766 (1965).
376. Kang, M. S. et al. Novel Carbazole-Based Hole-Transporting Materials with Star-Shaped Chemical Structures for Perovskite-Sensitized Solar Cells. *ACS Appl Mater Interfaces* **7**, 22213–22217 (2015).
377. Paniagua, S. A. et al. Phosphonic Acids for Interfacial Engineering of Transparent Conductive Oxides. *Chem Rev* **116**, 7117–7158 (2016).
378. Hoegl, H. On photoelectric effects in polymers and their sensitization by dopants. in *Journal of Physical Chemistry* vol. 69 755–766 (American Chemical Society, 1965).
379. Hou, Y. et al. A generic interface to reduce the efficiency-stability-cost gap of perovskite solar cells. *Science (1979)* **358**, 1192–1197 (2017).
380. Tockhorn, P. et al. Nano-optical designs for high-efficiency monolithic perovskite–silicon tandem solar cells. *Nature Nanotechnology 2022 17:11* **17**, 1214–1221 (2022).
381. Liu, J. et al. Efficient and stable perovskite-silicon tandem solar cells through contact displacement by MgF x. *Science (1979)* **377**, 302–306 (2022).
382. Aktas, E. et al. Understanding the perovskite/self-assembled selective contact interface for ultra-stable and highly efficient p-i-n perovskite solar cells. *Energy Environ Sci* **14**, 3976–3985 (2021).
383. Yeo, D., Shin, J., Kim, D., Jaung, J. Y. & Jung, I. H. Self-Assembled Monolayer-Based Hole-Transporting Materials for Perovskite Solar Cells. (2024).
384. Qu, G. et al. Conjugated linker-boosted self-assembled monolayer molecule for inverted perovskite solar cells. *Joule* **8**, 2123–2134 (2024).
385. Cassella, E. J. et al. Gas-Assisted Spray Coating of Perovskite Solar Cells Incorporating Sprayed Self-Assembled Monolayers. *Advanced Science* **9**, 2104848 (2022).
386. Kore, B. P. et al. Efficient fully textured perovskite silicon tandems with thermally evaporated hole transporting materials. *Energy Environ Sci* (2024) doi:10.1039/d4ee03899a.
387. Levine, I. et al. Charge transfer rates and electron trapping at buried interfaces of perovskite solar cells. *Joule* **5**, 2915–2933 (2021).
388. Biesinger, M. C. Accessing the robustness of adventitious carbon for charge referencing (correction) purposes in XPS analysis: Insights from a multi-user facility data review. *Appl Surf Sci* **597**, 153681 (2022).
389. Larrude, D. G., Maia Da Costa, M. E. H., Monteiro, F. H., Pinto, A. L. & Freire, F. L. Characterization of phosphorus-doped multiwalled carbon nanotubes. *J Appl Phys* **111**, (2012).
390. Furlan, A. et al. Synthesis of phosphorus-carbide thin films by magnetron sputtering. *Physica Status Solidi - Rapid Research Letters* vol. 2 191–193 Preprint at https://doi.org/10.1002/pssr.200802077 (2008).
391. Bulusheva, L. G. et al. Electronic structure of nitrogen-and phosphorus-doped graphenes grown by chemical vapor deposition method. *Materials* **13**, (2020).
392. Puziy, A. M., Poddubnaya, O. I., Socha, R. P., Gurgul, J. & Wisniewski, M. XPS and NMR studies of phosphoric acid activated carbons. *Carbon N Y* **46**, 2113–2123 (2008).
393. Fuggle, J. C. & Menzel, D. Coverage dependent shifts of XPS peaks during chemisorption on metals. *Surf Sci* **53**, 21–34 (1975).
394. Baer, D. R. et al. XPS guide: Charge neutralization and binding energy referencing for insulating samples. *Journal of Vacuum Science & Technology A: Vacuum, Surfaces, and Films* **38**, (2020).
395. NIST. NIST Electron Inelastic-Mean-Free-Path Database. http://dx.doi.org/10.18434/T48C78 (2021) doi:10.18434/T48C78.
396. Tan, Z. et al. Electron stopping power and mean free path in organic compounds over the energy range of 20-10,000 eV. *Nucl Instrum Methods Phys Res B* **222**, 27–43 (2004).

397. Alghamdi, A. R. M., Yanagida, M., Shirai, Y., Andersson, G. G. & Miyano, K. Surface Passivation of Sputtered NiOxUsing a SAM Interface Layer to Enhance the Performance of Perovskite Solar Cells. *ACS Omega* **7**, 12147–12157 (2022).

398. Guo, R. et al. Refining the Substrate Surface Morphology for Achieving Efficient Inverted Perovskite Solar Cells. *Adv Energy Mater* **13**, 1–9 (2023).

399. Wu, M. et al. Reconstruction of the Indium Tin Oxide Surface Enhances the Adsorption of High-Density Self-Assembled Monolayer for Perovskite/Silicon Tandem Solar Cells. *Adv Funct Mater* **33**, 2304708 (2023).

400. Kralj, S. et al. Impact of the TCO Microstructure on the Electronic Properties of Carbazole-Based Self-Assembled Monolayers. *ACS Mater Lett* **6**, 366–374 (2024).

401. Menzel, D. et al. *Field Effect Passivation in Perovskite Solar Cells by a LiF Interlayer*. *Advanced Energy Materials* vol. 12 2201109 (John Wiley and Sons Inc, 2022).

402. Qiu, W., Li, Y. & Lin, C. Scalable post-treatment for improved self-assembled monolayer coverage in perovskite solar cells. *Sustain Energy Fuels* **8**, 5399–5406 (2024).

403. Song, W., So, S. K. & Cao, L. Angular-dependent photoemission studies of indium tin oxide surfaces. *Appl Phys A Mater Sci Process* **72**, 361–365 (2001).

404. Kim, S. Y., Lee, J. L., Kim, K. B. & Tak, Y. H. Effect of ultraviolet-ozone treatment of indium-tin-oxide on electrical properties of organic light emitting diodes. *J Appl Phys* **95**, 2560–2563 (2004).

405. Hashimoto, Y., Osato, Y., Tanaka, M., Hamagaki, M. & Sakakibara, T. Effect of oxygen plasma treatment of indium tin oxide for organic light-emitting devices with iodogallium phthalocyanine layer. *Japanese Journal of Applied Physics, Part 1: Regular Papers and Short Notes and Review Papers* **41**, 2249–2251 (2002).

406. Kong, G. D., Kim, M. & Yoon, H. J. EGaIn Microelectrode for Electrical Characterization of ITO-Based van der Waals Interface and Airborne Molecular Contamination of ITO Surface. *J Electrochem Soc* **162**, H703–H712 (2015).

407. Breen, T. L., Fryer, P. M., Nunes, R. W. & Rothwell, M. E. Patterning indium tin oxide and indium zinc oxide using microcontact printing and wet etching. *Langmuir* **18**, 194–197 (2002).

408. Carmichael, T. B., Vella, S. J. & Afzali, A. Selective electroless metal deposition using microcontact printing of phosphine-phosphonic acid inks. *Langmuir* **20**, 5595–5598 (2004).

409. Hubert Mutin, P., Guerrero, G. & Vioux, A. Hybrid materials from organophosphorous coupling molecules. *J Mater Chem* **15**, 3761–3768 (2005).

410. Li, H., Paramonov, P. & Bredas, J.-L. Theoretical study of the surface modification of indium tin oxide with trifluorophenyl phosphonic acid molecules: impact of coverage density and binding geometry. *J Mater Chem* **20**, 2630–2637 (2010).

411. Bermudez, V. M., Berry, A. D., Kim, H. & Piqué, A. Functionalization of indium tin oxide. *Langmuir* **22**, 11113–11125 (2006).

412. Chockalingam, M., Darwish, N., Le Saux, G. & Gooding, J. J. Importance of the Indium Tin Oxide Substrate on the Quality of Self-Assembled Monolayers Formed from Organophopsphonic Acids. *Langmuir* **27**, 2545–2552 (2011).

413. Stolterfoht, M. et al. Approaching the fill factor Shockley-Queisser limit in stable, dopant-free triple cation perovskite solar cells. *Energy and Environmental Science* vol. 10 1530–1539 Preprint at https://doi.org/10.1039/c7ee00899f (2017).

414. Phung, N. et al. Enhanced Self-Assembled Monolayer Surface Coverage by ALD NiO in p-i-n Perovskite Solar Cells. *ACS Appl Mater Interfaces* **14**, 2166–2176 (2022).

415. Lohmann, K. B. et al. Solvent-Free Method for Defect Reduction and Improved Performance of p-i-n Vapor-Deposited Perovskite Solar Cells. *ACS Energy Lett* **7**, 1903–1911 (2022).

416. Xu, K. et al. Slot-Die Coated Triple-Halide Perovskites for Efficient and Scalable Perovskite/Silicon Tandem Solar Cells. *ACS Energy Lett* **7**, 3600–3611 (2022).

417. Staub, F. et al. Beyond Bulk Lifetimes: Insights into Lead Halide Perovskite Films from Time-Resolved Photoluminescence. *Phys Rev Appl* **6**, 1–13 (2016).

418. Wu, J. et al. Using hysteresis to predict the charge recombination properties of perovskite solar cells. *Journal of Materials Chemistry A* vol. 9 6382–6392 Preprint at https://doi.org/10.1039/d0ta12046d (2021).

419. Kim, G. Y. et al. Large tunable photoeffect on ion conduction in halide perovskites and implications for photodecomposition. *Nature Materials* vol. 17 445–449 Preprint at https://doi.org/10.1038/s41563-018-0038-0 (2018).

420. Wang, Z. S., Ebadi, F., Carlsen, B., Choy, W. C. H. & Tress, W. Transient Photovoltage Measurements on Perovskite Solar Cells with Varied Defect Concentrations and Inhomogeneous Recombination Rates. *Small Methods* **4**, (2020).

421. Wang, Y. et al. Patterned Wettability Surface for Competition-Driving Large-Grained Perovskite Solar Cells. *Adv Energy Mater* **9**, 1900838 (2019).

422. Bi, C. et al. Non-wetting surface-driven high-aspect-ratio crystalline grain growth for efficient hybrid perovskite solar cells. *Nat Commun* **6**, 7747 (2015).

423. Taddei, M. et al. Ethylenediamine Addition Improves Performance and Suppresses Phase Instabilities in Mixed-Halide Perovskites. *ACS Energy Lett* **7**, 4265–4273 (2022).

424. Bi, C. et al. Non-wetting surface-driven high-aspect-ratio crystalline grain growth for efficient hybrid perovskite solar cells. *Nat Commun* **6**, 1–7 (2015).

425. Kim, S., Can Quy, H., Wook Choi, H. & Wung Bark, C. Effect of UV-Light Treatment on Efficiency of Perovskite Solar Cells (PSCs). *Energies (Basel)* **13**, 1069 (2020).

426. Chen, J. et al. Solvent effect on the hole-conductor-free fully printable perovskite solar cells. *Nano Energy* **27**, 130–137 (2016).

427. Zhang, N., Wei, B. X., Ma, T., Tian, Y. & Wang, G. A carbazole-grafted covalent organic framework as turn-on fluorescence chemosensor for recognition and detection of Pb2+ ions with high selectivity and sensitivity. *J Mater Sci* **56**, 11789–11800 (2021).

428. Mangrulkar, M. & Stevenson, K. J. The progress of additive engineering for ch3nh3pbi3 photo-active layer in the context of perovskite solar cells. *Crystals (Basel)* **11**, (2021).

429. Zhang, S. et al. Conjugated Self-Assembled Monolayer as Stable Hole-Selective Contact for Inverted Perovskite Solar Cells. *ACS Mater Lett* **4**, 1976–1983 (2022).

430. Kawahara, S., Tsuzuki, S. & Uchimaru, T. Lewis Acidity Basicity of pi-Electron Systems Theoretical Study of a Molecular Interaction between a pi System and a Lewis Acid/Base. *Chemistry (Easton)* **11**, 4458–4464 (2005).

431. Fournier, O. et al. Chemical Passivation with Phosphonic Acid Derivatives of ZnO Deposited by Atomic Layer Deposition and Its Influence on the Halide Perovskite Interface. *ACS Appl Energy Mater* **4**, 5787–5797 (2021).

432. Guo, Y. et al. Efficient Inverted Perovskite Solar Cells With Low-Temperature Processed NiOx/SAM Hole Transport Layer. *J Mater Chem C Mater* 1507–1515 (2024) doi:10.1039/d3tc03575a.

433. Abzieher, T. et al. Additive-Assisted Crystallization Dynamics in Two-Step Fabrication of Perovskite Solar Cells. *Physica Status Solidi - Rapid Research Letters* **214**, 1700509 (2017).

434. Xue, J., Wang, R. & Yang, Y. The surface of halide perovskites from nano to bulk. *Nature Reviews Materials* vol. 5 809–827 Preprint at https://doi.org/10.1038/s41578-020-0221-1 (2020).

435. Zhang, B. et al. Alkyl phosphonic acids deliver CsPbBr3 Nanocrystals with high photoluminescence quantum yield and truncated octahedron shape. *Chemistry of Materials* **31**, 9140–9147 (2019).

436. Mishra, J. K. et al. Defect Passivation Using a Phosphonic Acid Surface Modifier for Efficient RP Perovskite Blue-Light-Emitting Diodes. *ACS Appl Mater Interfaces* **14**, 34238–34246 (2022).

437. Cheng, C. et al. A Novel Organic Phosphonate Additive Induced Stable and Efficient Perovskite Solar Cells with Efficiency over 24% Enabled by Synergetic Crystallization Promotion and Defect Passivation. *Nano Lett* **23**, 8850–8859 (2023).

438. Akman, E., Esmail Shalan, A., Sadegh, F. & Akin, S. Moisture-Resistant FAPbI3 Perovskite Solar Cell with 22.25% Power Conversion Efficiency through Pentaflrorobenzyl Phosphonic Acid Passivation. *ChemSusChem* **14**, 1176–1183 (2020).

439. Lin, Y. et al. pi-Conjugated Lewis Base Efficient Trap-Passivation and Charge-Extraction for Hybrid Perovskite Solar Cells. *Advanced Materials* **29**, 1604545 (2016).

440. Gidey, A. T., Assayehegn, E. & Kim, J. Y. Hydrophilic Surface-Driven Crystalline Grain Growth of Perovskites on Metal Oxides. *ACS Appl Energy Mater* **4**, 6923–6932 (2021).

441. Zhao, D. et al. Improved Efficiency and Stability of Perovskite Solar Cells Using a Difluorobenzothiadiazole-Based Interfacial Material. *ACS Appl Energy Mater* **4**, 10646–10655 (2021).

442. Wang, Y. et al. Patterned Wettability Surface for Competition-Driving Large-Grained Perovskite Solar Cells. *Advanced Energy Materials* vol. 9 Preprint at https://doi.org/10.1002/aenm.201900838 (2019).

443. Wu, G. et al. Enlarging grain sizes for efficient perovskite solar cells by methylamine chloride assisted recrystallization. *Journal of Energy Chemistry* **65**, 55–61 (2022).

444. Cai, Q. et al. High-performance perovskite solar cells resulting from large perovskite grain size enabled by the urea additive. *Sustain Energy Fuels* **6**, 2955–2961 (2022).

445. Gil-Escrig, L. et al. Fully Vacuum-Processed Perovskite Solar Cells on Pyramidal Microtextures. *Solar RRL* **5**, 2000553 (2021).

446. Mariotti, S. et al. Unraveling the Morphological and Energetic Properties of 2PACz Self-Assembled Monolayers Fabricated With Upscaling Deposition Methods. *Energy and Environmental Materials* 1–14 (2024) doi:10.1002/eem2.12825.

447. Geistert, K., Ternes, S., Ritzer, D. B. & Paetzold, U. W. Controlling Thin Film Morphology Formation during Gas Quenching of Slot-Die Coated Perovskite Solar Modules. *ACS Appl Mater Interfaces* **15**, 52519–52529 (2023).

448. Li, J. et al. An Energy Level Alignment Study of 2PACz Molecule on Perovskite Device-Related Interfaces by Vacuum Deposition. *Advanced Energy and Sustainability Research* **2400336**, 1–12 (2025).

449. Huang, S., Liang, C. & Lin, Z. Application of PACz-Based Self-Assembled Monolayer Materials in Efficient Perovskite Solar Cells. *ACS Appl Mater Interfaces* (2024) doi:10.1021/acsami.4c13977.

450. Aydin, E. et al. Enhanced optoelectronic coupling for perovskite/silicon tandem solar cells. *Nature* **623**, 732–738 (2023).

451. Longo, G. et al. Fully Vacuum-Processed Wide Band Gap Mixed-Halide Perovskite Solar Cells. *ACS Energy Lett* **3**, 214–219 (2018).

452. Gil-Escrig, L. et al. Efficient vacuum-deposited perovskite solar cells with stable cubic FA1- xMAxPbI3. *ACS Energy Lett* **5**, 3053–3061 (2020).

453. Gil-Escrig, L. et al. Vacuum Deposited Triple-Cation Mixed-Halide Perovskite Solar Cells. *Adv Energy Mater* **8**, 1703506 (2018).

454. Shallcross, R. C., Olthof, S., Meerholz, K. & Armstrong, N. R. Impact of Titanium Dioxide Surface Defects on the Interfacial Composition and Energetics of Evaporated Perovskite Active Layers. *ACS Appl Mater Interfaces* **11**, 32500–32508 (2019).

455. Klipfel, N. et al. Crystallographically Oriented Hybrid Perovskites via Thermal Vacuum Codeposition. *Solar RRL* **5**, 2100191 (2021).

456. Gallet, T. et al. Co-evaporation of CH 3 NH 3 PbI 3 : How Growth Conditions Impact Phase Purity, Photostriction, and Intrinsic Stability. *ACS Appl Mater Interfaces* **13**, 2642–2653 (2021).

457. Zhang, Z. et al. Robust heterojunction to strengthen the performances of FAPbI3 perovskite solar cells. *Chemical Engineering Journal* **432**, 134311 (2022).

458. Xie, H. et al. Decoupling the effects of defects on efficiency and stability through phosphonates in stable halide perovskite solar cells. *Joule* **5**, 1246–1266 (2021).

459. Castro-Méndez, A. F. et al. Tailoring Interface Energies via Phosphonic Acids to Grow and Stabilize Cubic FAPbI3 Deposited by Thermal Evaporation. J Am Chem Soc 146, 18459–18469 (2024).

460. Pitaro, M. et al. Tuning the Surface Energy of Hole Transport Layers Based on Carbazole Self-Assembled Monolayers for Highly Efficient Sn/Pb Perovskite Solar Cells. *Adv Funct Mater* 2306571 (2023) doi:10.1002/ADFM.202306571.

461. Sinnokrot, M. O. & Sherrill, C. D. Substituent Effects in π−π Interactions: Sandwich and T-Shaped Configurations. *J Am Chem Soc* **126**, 7690–7697 (2004).

462. Aliakbar Tehrani, Z. & Kim, K. S. Functional molecules and materials by π-Interaction based quantum theoretical design. *Int J Quantum Chem* **116**, 622–633 (2016).

463. Chiang, Y. H., Anaya, M. & Stranks, S. D. Multisource Vacuum Deposition of Methylammonium-Free Perovskite Solar Cells. ACS Energy Lett 5, 2498–2504 (2020).

464. Yuan, Q. et al. Thermally Stable Perovskite Solar Cells by All-Vacuum Deposition. ACS Appl Mater Interfaces 15, 772–781 (2023).

465. Lohmann, K. B. et al. Control over Crystal Size in Vapor Deposited Metal-Halide Perovskite Films. *ACS Energy Lett* **5**, 710–717 (2020).

466. Wang, Q. et al. Qualifying composition dependent p and n self-doping in CH3NH3PbI3. *Appl Phys Lett* **105**, 163508 (2014).

467. Fassl, P. et al. Fractional deviations in precursor stoichiometry dictate the properties, performance and stability of perovskite photovoltaic devices. Energy Environ Sci 11, 3380–3391 (2018).

468. Castro-Méndez, A. F. et al. Formation of a Secondary Phase in Thermally Evaporated MAPbI3and Its Effects on Solar Cell Performance. *ACS Appl Mater Interfaces* **14**, 34269–34280 (2022).

469. Hauschild, D. et al. Impact of n-Butylammonium Bromide on the Chemical and Electronic Structure of Double-Cation Perovskite Thin Films. *ACS Appl Mater Interfaces* **13**, 53202–53210 (2021).

470. Kamal, C. et al. Coupling Methylammonium and Formamidinium Cations with Halide Anions: Hybrid Orbitals, Hydrogen Bonding, and the Role of Dynamics. *Journal of Physical Chemistry C* **125**, 25917–25926 (2021).

471. Zhou, N. et al. CsI Pre-Intercalation in the Inorganic Framework for Efficient and Stable FA1 x CsxPbI3 Cl .pdf. *Small* **13**, 1700484 (2017).

472. Sun, Y. materials Chemical state of chlorine in perovskite solar cell and its effect on the photovoltaic performance. *J Mater Sci* **53**, 13976–13986 (2018).

473. Hossain, K. et al. Resolving the Hydrophobicity of the Me-4PACz Hole Transport Layer for Inverted Perovskite Solar Cells with Efficiency >20%. *ACS Energy Lett* **8**, 3860–3867 (2023).

474. Liu, M. et al. Compact Hole-selective Self-assembled Monolayers Enabled by Disassembling Micelles in Solution for Efficient Perovskite Solar Cells. *Advanced Materials* 2304415 (2023) doi:10.1002/adma.202304415.

475. Gompel, W. T. M. Van et al. Degradation of the Formamidinium Cation and the Quantification of the Formamidinium-Methylammonium Ratio in Lead Iodide Hybrid Perovskites by Nuclear Magnetic Resonance Spectroscopy. *Journal of Physical Chemistry C* **122**, 4117–4124 (2018).

476. Kuang, C. et al. Critical role of additive-induced molecular interaction on the operational stability of perovskite light-emitting diodes. *Joule* **5**, 618–630 (2021).

477. Charisiadis, P. et al. 1H-NMR as a Structural and Analytical Tool of Intra- and Intermolecular Hydrogen Bonds of Phenol-Containing Natural Products and Model Compounds. Molecules 2014, Vol. 19, Pages 13643-13682 19, 13643–13682 (2014).

478. Fabini, D. H. et al. Reentrant Structural and Optical Properties and Large Positive Thermal Expansion in Perovskite Formamidinium Lead Iodide. *Angewandte Chemie International Edition* **55**, 15392–15396 (2016).

479. Costa, J. C. S., Azevedo, J., Santos, L. M. N. B. F. & Mendes, A. On the Deposition of Lead Halide Perovskite Precursors by Physical Vapor Method. *The Journal of Physical Chemistry C* **121**, 2080–2087 (2017).

480. Ghosh, J. & Giri, P. K. Vacuum deposited PbI 2 film grown at elevated temperatures for improved efficiency of CH 3 NH 3 PbI 3 based planar perovskite solar cells. *Mater Res Bull* **139**, 111255 (2021).

481. Kuba, A. G. et al. Two-step close-space vapor-transport of MAPbI3 solarcells: effects of electron transport layers residual PbI2. *Applied Energy Materials* **5**, 10731–10741 (2022).

482. Evans, H. A. et al. Hydrogen Bonding Controls the Structural Evolution in Perovskite- Related Hybrid Platinum(IV) Iodides. *Inorg Chem* 6–13 (2018) doi:10.1021/acs.inorgchem.8b01597.

483. Li, X. et al. Improved performance and stability of perovskite solar cells by crystal crosslinking with alkylphosphonic acid ω -ammonium chlorides. *Nat Chem* **7**, 703–711 (2015).

484. Sousa, S. F., Fernandes, P. A. & Ramos, M. J. General performance of density functionals. *Journal of Physical Chemistry A* **111**, 10439–10452 (2007).

484. Ehlert, C., Piras, A. & Gryn'ova, G. CO2 on Graphene: Benchmarking Computational Approaches to Noncovalent Interactions. *ACS Omega* **8**, 35768–35778 (2023).

486. Marín-Villa, P., Arauzo, A., Drużbicki, K. & Fernandez-Alonso, F. Unraveling the Ordered Phase of the Quintessential Hybrid Perovskite MAPbI3Thermophysics to the Rescue. *Journal of Physical Chemistry Letters* **13**, 8422–8428 (2022).

487. Vicent-Luna, J. M., Apergi, S. & Tao, S. Efficient Computation of Structural and Electronic Properties of Halide Perovskites Using Density Functional Tight Binding: GFN1-xTB Method. *J Chem Inf Model* **61**, 4415–4424 (2021).

488. Chen, T. et al. Entropy-driven structural transition and kinetic trapping in formamidinium lead iodide perovskite. *Sci Adv* **2**, (2016).

489. Zheng, Z. et al. Development of formamidinium lead iodide-based perovskite solar cells: efficiency and stability. *Chem Sci* **13**, 2167–2183 (2022).

490. Fu, Y. et al. Stabilization of the Metastable Lead Iodide Perovskite Phase via Surface Functionalization. *Nano Lett* **17**, 4405–4414 (2017).

491. Chen, T. et al. Inhibition of defect-induced α-to-δ phase transition for efficient and stable formamidinium perovskite solar cells. *Nat Commun* **14**, 6125 (2023).

492. Ma, F. et al. Stable α/δ phase junction of formamidinium lead iodide perovskites for enhanced near-infrared emission. *Chem Sci* **8**, 800–805 (2017).

493. Thiesbrummel, J. et al. Universal Current Losses in Perovskite Solar Cells Due to Mobile Ions. *Adv Energy Mater* **11**, 2101447 (2021).

494. Xu, W. et al. Impact of Interface Energetic Alignment and Mobile Ions on Charge Carrier Accumulation and Extraction in p-i-n Perovskite Solar Cells. *Adv Energy Mater* **13**, 1–15 (2023).

495. Ye, F. et al. Overcoming C_{60}-induced interfacial recombination in inverted perovskite solar cells by electron-transporting carborane. *Nat Commun* **13**, 7454 (2022).

496. de Quilettes, D. W. et al. Impact of microstructure on local carrier lifetime in perovskite solar cells. *Science (1979)* **348**, 683–686 (2015).

497. Peán, E. V., Dimitrov, S., De Castro, C. S. & Davies, M. L. Interpreting time-resolved photoluminescence of perovskite materials. *Physical Chemistry Chemical Physics* **22**, 28345–28358 (2020).

498. Chiu, K. P. The influence of a trap state on the photoluminescence decay times under single pulse excitation. *Opt Quantum Electron* **55**, 1–11 (2023).

499. Jacobsson, T. J. et al. Unreacted PbI2 as a Double-Edged Sword for Enhancing the Performance of Perovskite Solar Cells. J Am Chem Soc 138, 10331–10343 (2016).

500. Singh, R. et al. Danger in the Dark: Stability of Perovskite Solar Cells with Varied Stoichiometries and Morphologies Stressed at Various Conditions. ACS Appl Mater Interfaces 16, 27450–27462 (2024).

501. Breniaux, E., Dufour, P., Guillemet-Fitsch, S. & Tenailleau, C. Unraveling All-Inorganic CsPbI3 and CsPbI2Br Perovskite Thin Films Formation Black Phase Stabilization by Cs2PbCl2I2 Addition and Flash-Annealing. *Eur J Inorg Chem* 3059–3073 (2021) doi:doi.org/10.1002/ejic.202100304.

502. Ma, Z. et al. Excess PbI2 evolution for triple-cation based perovskite solar cells with 21.9% efficiency. *Journal of Energy Chemistry* **66**, 152–160 (2022).

503. Leyden, M. R. et al. Loading Precursors into Self-Assembling Contacts for Improved Performance and Process Control in Evaporated Perovskite Solar Cells. *Solar RRL* **8**, 2400575 (2024).

504. Feeney, T., Miaskiewicz, A. et al. High-Rate FA-Based Co-Evaporated Perovskites: Understanding Rate Limitations and Practical Considerations to Overcome Their Impact. *Adv Funct Mater*, e17873 (2025).

505. Rühle, S. Tabulated values of the Shockley-Queisser limit for single-junction solar cells. Solar Energy 130, 139–147 (2016).

506. Subhan, F. E. et al. Optical optimization of double-side-textured monolithic perovskite-silicon tandem solar cells for improved light management. *RSC Adv* **10**, 26631–26638 (2020).

507. Chen, B. et al. Blade-Coated Perovskites on Textured Silicon for 26%-Efficient Monolithic Perovskite/Silicon Tandem Solar Cells. *Joule* **4**, 850–864 (2020).

508. Baloch, A. A. B., Albadwawi, O., AlShehhi, B. & Alberts, V. Impact of mixed perovskite composition based silicon tandem PV devices on efficiency limits and global performance. *Energy Reports* **8**, 504–510 (2022).

509. Palazon, F. et al. Coating Evaporated MAPI Thin Films with Organic Molecules: Improved Stability at High Temperature and Implementation in High-Efficiency Solar Cells. *ACS Energy Lett* **3**, 835–839 (2018).

510. Conings, B. et al. Intrinsic Thermal Instability of Methylammonium Lead Trihalide Perovskite. *Adv Energy Mater* **5**, 1500477 (2015).

511. Chiang, Y. H. et al. Vacuum-Deposited Wide-Bandgap Perovskite for All-Perovskite Tandem Solar Cells. *ACS Energy Lett* **8**, 2728–2737 (2023).

512. Dewi, H. A., Erdenebileg, E., Luca, D. De, Mhaisalkar, S. G. & Bruno, A. Accelerated MAPbI 3 Co-evaporation: Productivity Gains without Compromising Performance. *ACS Energy Lett* **9**, 4319–4322 (2024).

513. Khorasani, A., Mohamadkhani, F., Marandi, M., Luo, H. & Abdi-Jalebi, M. Opportunities, Challenges, and Strategies for Scalable Deposition of Metal Halide Perovskite Solar Cells and Modules. *Advanced Energy and Sustainability Research* **5**, 2300275 (2024).

514. Zhu, P. et al. Toward the Commercialization of Perovskite Solar Modules. *Advanced Materials* **36**, 2307357 (2024).

515. Du, T. et al. Light-intensity and thickness dependent efficiency of planar perovskite solar cells: charge recombinationversusextraction. *J Mater Chem C Mater* **8**, 12648–12655 (2020).

516. Arivazhagan, V. et al. Vacuum co-deposited CH3NH3PbI3 films by controlling vapor pressure for efficient planar perovskite solar cells. *Solar Energy* **181**, 339–344 (2019).

517. Heinze, K. L. et al. Importance of methylammonium iodide partial pressure and evaporation onset for the growth of co-evaporated methylammonium lead iodide absorbers. *Sci Rep* **11**, 15299 (2021).

518. Thampy, S., Zhang, B., Park, J. G., Hong, K. H. & Hsu, J. W. P. Bulk and interfacial decomposition of formamidinium iodide (HC(NH2)2I) in contact with metal oxide. *Mater Adv* **1**, 3349–3357 (2020).

519. Ma, L. et al. Temperature-dependent thermal decomposition pathway of organic-inorganic halide perovskite materials. *Chemistry of Materials* **31**, 8515–8522 (2019).
520. Juarez-Perez, E. J., Ono, L. K. & Qi, Y. Thermal degradation of formamidinium based lead halide perovskites into: Sym -triazine and hydrogen cyanide observed by coupled thermogravimetry-mass spectrometry analysis. *J Mater Chem A Mater* **7**, 16912–16919 (2019).
521. J. Petry, V. Skorjanc, A. Diercks, T. Feeney, A. Morsa, S. Kimmig, J. Baumann, F. Löffker, S. Auschill, J. Damm, D. Baumann, F. Laufer, J. Kurpiers, M. Müller, L. Korte, S. Albrecht, M. Roß, U. W. Paetzold and P. Fassl, Industrialization of perovskite solar cell fabrication: strategies to achieve high-throughput vapour deposition processes*, EES Solar*, 1, 404 – 418 (2025)
522. A. Diercks, J. Petry, T. Feeney, R. Thelen, P. Fassl and U. W. Paetzold, Particle Size Matters – Impact of Particle Size and Crucible Geometry on Sublimation Behavior of Formamidinium Iodide, Adv. Mat. Tech, e01549 (2025)
523. Saliba, M., Unger, E., Etgar, L., Luo, J. & Jacobsson, T. J. A systematic discrepancy between the short circuit current and the integrated quantum efficiency in perovskite solar cells. *Nat Commun* **14**, 1–6 (2023).
524. Tumen-Ulzii, G. et al. Detrimental Effect of Unreacted PbI2 on the Long-Term Stability of Perovskite.pdf. *Advanced Materials* **32**, 1905035 (2020).
525. Baumann, D. O. et al. Repeatable Perovskite Solar Cells through Fully Automated Spin-Coating and Quenching. *ACS Appl Mater Interfaces* **16**, 54007–54016 (2024).
526. Plesser, H. E. Reproducibility vs. Replicability: A Brief History of a Confused Terminology. *Front Neuroinform* **11**, 1–4 (2018).
527. Er-Raji, O., Rustam, L., Kore, B. P., Glunz, S. W. & Schulze, P. S. C. Insights into Perovskite Film Formation Using the Hybrid Evaporation/Spin-Coating Route: An In Situ XRD Study. *ACS Appl Energy Mater* **6**, 6183–6193 (2023).
528. Tan, W. L. & McNeill, C. R. X-ray diffraction of photovoltaic perovskites: Principles and applications. *Appl Phys Rev* **9**, 021310 (2022) (2022).
529. Van Gompel, W. T. M. et al. Degradation of the Formamidinium Cation and the Quantification of the Formamidinium-Methylammonium Ratio in Lead Iodide Hybrid Perovskites by Nuclear Magnetic Resonance Spectroscopy. *Journal of Physical Chemistry C* **122**, 4117–4124 (2018).
530. Tupikina, E. Y., Denisov, G. S., Antonov, A. S. & Tolstoy, P. M. Unusual behaviour of the spin-spin coupling constant 1: J CH upon formation of CH···X hydrogen bond. *Physical Chemistry Chemical Physics* **22**, 1994–2000 (2020).
531. Del Bene, J. E., Alkorta, I. & Elguero, J. Ab initio study of ternary complexes X:(HCNH) +:Z with X, Z = NCH, CNH, FH, ClH, and FCl: Diminutive cooperative effects on structures, binding energies, and spin-spin coupling constants across hydrogen bonds. *Journal of Physical Chemistry A* **115**, 12677–12687 (2011).
532. Del Bene, J. E. & Elguero, J. One-Bond Spin−Spin Coupling Constants of X− 1 H Proton Donors in Complexes with X−H−Y Hydrogen Bonds, for X = 13 C, 15 N, 17 O, and 19 F: Predictions, Comparisons, and Relationships among 1 J X-H , 1 K X-H , and X−H Distances. *J Am Chem Soc* **126**, 15624–15631 (2004).
533. Gmbh, C. W. V. et al. NMR solvent impurities. 200–203.
534. Qiu, L. et al. Vapor Deposition of FAI on SnO 2 Provides Interface Modification and Crystallization Control for High-Performance and Stable Perovskite Solar Cells. (2023) doi:10.1021/acsanm.3c01867.
535. Wang, S. et al. Ion-Dipole Interaction for Self-Assembled Monolayers: A New Strategy for Buried Interface in Inverted Perovskite Solar Cells. *Adv Funct Mater* **34**, 2316202 (2024).
536. Das Adhikari, R., Baishya, H., Patel, M. J., Yadav, D. & Iyer, P. K. Bi-Directional Modification to Quench Detrimental Redox Reactions and Minimize Interfacial Energy Offset for NiOX/Perovskite-Based Solar Cells. *Small* **20**, 2404588 (2024).
537. Jackson, S. Determining hybridization differences for amorphous carbon from the XPS C 1s envelope. *Appl Surf Sci* **90**, 195–203 (1995).
538. Vaynzof, Y. The Future of Perovskite Photovoltaics—Thermal Evaporation or Solution Processing? *Adv Energy Mater* **10**, 2003073 (2020).
539. Du, P. et al. Thermal Evaporation for Halide Perovskite Optoelectronics: Fundamentals, Progress, and Outlook. *Adv Opt Mater* **10**, 2101770 (2022).
540. Bae, S.-R., Heo, D. Y. & Kim, S. Y. Recent progress of perovskite devices fabricated using thermal evaporation method: Perspective and outlook. *Mater Today Adv* **14**, 100232 (2022).
541. Li, J. et al. Potassium Acetate-Based Treatment for Thermally Co-Evaporated Perovskite Solar Cells. *Coatings* **10**, 1163 (2020).

542. Holmlin, R. E. et al. Electron transport through thin organic films in metal-insulator-metal junctions based on self-assembled monolayers. *J Am Chem Soc* **123**, 5075–5085 (2001).

543. Li, H. et al. 2D/3D heterojunction engineering at the buried interface towards high-performance inverted methylammonium-free perovskite solar cells. *Nat Energy* **8**, 946–955 (2023).

544. Leung, T. L. et al. Stability of 2D and quasi-2D perovskite materials and devices. *Commun Mater* **3**, 63 (2022).

545. Lin, L. et al. Hydrogen bonding in perovskite solar cells. *Matter* **7**, 38–58 (2024).

546. Chowdhury, S. et al. Investigation on the formation of two dimensional perovskite nanostructures at the water surface through self initiated reaction. *Sci Rep* **15**, 6216 (2025).

547. Cho, S. H. et al. *Fabrication Strategies for 2D Halide Perovskite Towards Next-Generation Optoelectronic Applications*. *International Journal of Precision Engineering and Manufacturing - Green Technology* vol. 12 (Korean Society for Precision Engineering, 2024).

548. Dong, B. et al. Self-assembled bilayer for perovskite solar cells with improved tolerance against thermal stresses. *Nat Energy* (2025) doi:10.1038/s41560-024-01689-2.

549. Li, J. et al. Co-Evaporated $MAPbI_3$ with Graded Fermi Levels Enables Highly Performing, Scalable, and Flexible p-i-n Perovskite Solar Cells. *Adv Funct Mater* **31**, 2103252 (2021).

550. Ball, J. M. et al. Dual-Source Coevaporation of Low-Bandgap FA1-xCsxSn1-yPbyI3 Perovskites for Photovoltaics. *ACS Energy Lett* **4**, 2748–2756 (2019).

551. Ji, R. et al. Thermally evaporated methylammonium-free perovskite solar cells. *J Mater Chem C Mater* **8**, 7725–7733 (2020).

552. Shih, C.-J. et al. Exploring buried interface in all-vapor-deposited perovskite photovoltaics. *Solar Energy* **280**, 112872 (2024).

553. Xu, Y.-Y. et al. Octahedral Tilt Enables Efficient and Stable Fully Vapor-Deposited Perovskite/Silicon Tandem Cells. *Adv Funct Mater* **34**, 2312037 (2024).

List of contributions

First author (published)

T. Feeney, I. M. Hossain, S. Gharibzadeh, F. Gota, R. Singh, P. Fassl, A. Mertens, A. Farag, J. Becker, S. Paetel, E. Ahlswede, and U. W. Paetzold, *Four-Terminal Perovskite/Copper Indium Gallium Selenide Tandem Solar Cells: Unveiling the Path to >27% in Power Conversion Efficiency*. Sol. RRL 6, 2200662 (2022).

A. Farag, **T. Feeney,** I. M. Hossain, F. Schackmar, P. Fassl, K. Küster, R. Bäuerle, M. A Ruiz-Preciado, M. Hentschel, D. B. Ritzer, A. Diercks, Y. Li, B. A. Nejand, F. Laufer, R. Singh, U. Starke, U. W. Paetzold, *Evaporated Self-Assembled Monolayer Hole Transport Layers: Lossless Interfaces in p-i-n Perovskite Solar Cells*. Adv. Energy Mater. 13, 2203982 (2023).

T. Feeney, J. Petry, A. Torche, D. Hauschild, B. Hacene, C. Wansorra, A. Diercks, M. Ernst, L. Weinhardt, C. Heske, G. Gryn'ova, U. W. Paetzold, and P. Fassl, *Understanding and exploiting interfacial interactions between phosphonic acid functional groups and co-evaporated perovskites.* Matter 7, 2066-2090 (2024).

T. Feeney, A. Miaskiewicz, J. Petry, F. Laufer, R. Singh, S. Severin, V. Škorjanc, A. Diercks, S. Maniyarasu, L. Korte, S. Albrecht, U. W. Paetzold, M. Roß and P. Fassl, *High-rate FA-based co-evaporated perovskites: Understanding rate limitations and practical considerations to overcome their impact.* Advanced Funcitonal Materials, e17873 (2025)

Co-author (published)

T. Abzieher, **T. Feeney**, F. Schackmar, Y. J Donie, I. M. Hossain, J. A. Schwenzer, T. Hellmann, T. Mayer, M. Powalla, U. W. Paetzold, *From Groundwork to Efficient Solar Cells: On the Importance of the Substrate Material in Co-Evaporated Perovskite Solar Cells*. Adv. Funct. Mater. 31, 2104482 (2021).

S. Gharibzadeh, P. Fassl, I. M. Hossain, P. Rohrbeck, M. Frericks, M. Schmidt, T. Duong, M. Rahman Khan, T. Abzieher, B. A. Nejand, F. Schackmar, O. Almora, **T. Feeney**, R. Singh, D. Fuchs, U. Lemmer, J. P. Hofmann, S. A. L. Weberc and U. W. Paetzold., *Two birds with one stone: dual grain-boundary and interface passivation enables >22% efficient inverted methylammonium-free perovskite solar cells*, Energy Environ. Sci. 14, 5875-5893 (2021).

D. B. Ritzer, T. Abzieher, A. Basibüyük, **T. Feeney**, F. Laufer, S. Ternes, B. S. Richards, S. Bergfeld, U. W. Paetzold. *Upscaling of perovskite solar modules: The synergy of fully evaporated layer fabrication and all-laser-scribed interconnections*. Prog Photovolt Res Appl. 30(4), 360-373 (2022).

J. Roger, L. K. Schorn, M. Heydarian, A. Farag, **T. Feeney**, D. Baumann, H. Hu, F. Laufer, W. Duan, K. Ding, A. Lambertz, P. Fassl, M. Worgull, U. W. Paetzold, *Laminated Monolithic Perovskite/Silicon Tandem Photovoltaics*. Adv. Energy Mater. 12, 2200961 (2022).

M. A. Ruiz-Preciado, F. Gota, P. Fassl, I. M. Hossain, R. Singh, F. Laufer, F. Schackmar, **T. Feeney**, A. Farag, I. Allegro, H. Hu, S. Gharibzadeh, B. A. Nejand, V. S. Gevaerts, M. Simor, P. J. Bolt, and U. W. Paetzold, *Monolithic Two-Terminal Perovskite/CIS Tandem Solar Cells with Efficiency Approaching 25%.*, ACS Energy Lett. 7, 2273–2281 (2022).

B. A. Nejand, D. B. Ritzer, H. Hu, F. Schackmar, S. Moghadamzadeh, **T. Feeney**, R. Singh, F. Laufer, R. Schmager, R. Azmi, M. Kaiser, T. Abzieher, S. Gharibzadeh, E. Ahlswede, U. Lemmer, B. S. Richards & U. W. Paetzold. *Scalable two-terminal all-perovskite tandem solar modules with a 19.1% efficiency*. Nat Energy 7, 620–630 (2022).

A. Farag, P. Fassl, H. Hu, **T. Feeney,** A. Quintilla, M. A. Ruiz-Preciado, W. Hempel, D. Bagrowski, P. Noack, B. Wattenberg, T. Dippell, U. W. Paetzold, *Mitigation of Open-Circuit Voltage Losses in Perovskite Solar Cells Processed over Micrometer-Sized-Textured Si Substrates*. Adv. Funct. Mater. 33, 2210758 (2023).

D. B. Ritzer, B. Abdollahi Nejand, M. A. Ruiz-Preciado, S. Gharibzadeh, H. Hu, A. Diercks, **T. Feeney**, B. S. Richards, T. Abzieher and U. W. Paetzold, *Translucent perovskite photovoltaics for building integration*, Energy Environ. Sci. 16, 2212-2225 (2023).

Y. Li, H. Hu, A. Farag, **T. Feeney**, I. Allegro, U. Lemmer, U. W. Paetzold, and I. A. Howard, *Enhancement of Amplified Spontaneous Emission by Electric Field in CsPbBr3 Perovskites*, Nano Lett. 23, 5, 1637–1644 (2023).

B. Hacene, F. Laufer, S. Ternes, A. Farag, R. Pappenberger, P. Fassl, S. Moghadamzadeh, B. A. Nejand, **T. Feeney,** I. Howard, U. W. Paetzold, *Intensity Dependent Photoluminescence Imaging for In-Line Quality Control of Perovskite Thin Film Processing*. Adv. Mater. Technol. 9, 11, 2301279 (2023).

H. Hu, S. X. An, Y. Li, S. Orooji, R. Singh, F. Schackmar, F. Laufer, Q. Jin, **T. Feeney,** A. Diercks, F. Gota, S. Moghadamyadeh, T. Pan, M. Rienäcker, R. Peibst, B. Abdollahi Nejand, U. W. Paetzold, *Triple-junction perovskite–perovskite–silicon solar cells with power conversion efficiency of 24.4%*, Energy Environ. Sci. 17, 2800-2814 (2024).

R. Singh, H. Hu, **T. Feeney**, A. Diercks, F. Laufer, Y. Li, T. Duong, F. Schackmar, B. Abdollahi Nejand, U. W. Paetzold, *Danger in the Dark: Stability of Perovskite Solar Cells with Varied Stoichiometries and Morphologies Stressed at Various Conditions*, ACS Appl. Mater. Interfaces 21, 27450-27462 (2024).

A. Diercks, J. Petry, **T. Feeney**, R. Singh, T. Zhao, H. Hu, Y. Li, U. W. Paetzold and P. Fassl, *Sequential Evaporation of Inverted FAPbI3 Perovskite Solar Cells – Impact of Substrate on Crystallization and Film Formatio*n, ACS Energy Letters 10, 1165 – 1173 (2025).

Y. Li, S. Liu, **T. Feeney**, J. Roger, M. Gholipoor, H. Hu, D. Zhao, I. Howard, F. Deschler, U. Lemmer, and U. W. Paetzold, *Electrically-Switchable Gain in Optically Pumped CsPbBr3 Lasers With Low Threshold at Nanosecond Pumping*, Small 21, 13, 2411935 (2025).

X. Lui, M. Rienäcker, M. Gholipoor, L. Fang, T. Zhao, B. Hacene, J. Peterman, R. Cai, H. Hu, **T. Feeney**, F. Sadegh, P. Fassl, R. Gao, U. Lemmer, R. Peibst and U. W. Paetzold, *Charge carrier management for highly efficient perovskite/Si tandem solar cells with poly-Si based passivating contacts*, Energy Environ. Sci. 18, 5599 – 5609 (2025).

J. Petry, V. Skorjanc, A. Diercks, **T. Feeney**, A. Morsa, S. Kimmig, J. Baumann, F. Löffker, S. Auschill, J. Damm, D. Baumann, F. Laufer, J. Kurpiers, M. Müller, L. Korte, S. Albrecht, M. Roß, U. W. Paetzold and P. Fassl, *Industrialization of perovskite solar cell fabrication: strategies to achieve high-throughput vapour deposition processes*, EES Solar 1, 404 – 418, (2025).

A. Diercks, J. Petry, **T. Feeney**, R. Thelen, P. Fassl and U. W. Paetzold, *Particle Size Matters – Impact of Particle Size and Crucible Geometry on Sublimation Behavior of Formamidinium Iodide*, Adv. Mat. Tech, e01549 (2025).

Conference (presenter)

T. Feeney, H. Hu, T. Abzieher, B. A. Nejand, A. Diercks, F. Gota, D. Ritzer, U. W. Paetzold*, All-evaporated perovskites: challenges and opportunities for tandem photovoltaic devices*, Oral presentation, PVSEC-31, 2021

T. Feeney, A. Farag, I. M. Hossain, F. Schackmar, P. Fassl, K. Küster, R. Bäuerle, M. A Ruiz-Preciado, M. Hentschel, D. B. Ritzer, A. Diercks, Y. Li, B. A. Nejand, F. Laufer, R. Singh, U. Starke, U. W. Paetzold, *Evaporated Self-Assembled Monolayer Hole Transport Layers: Lossless Interfaces in p-i-n Perovskite Solar Cells*. Oral presentation, EMRS Spring, 2023

T. Feeney, J. Petry, A. Farag, A. Diercks, A. Torche, M. Ernst, I. M. Hossain, F. Schackmar, K. Küster, R. Bäuerle, M. Hentschel, Y. Li, R. Singh, U. Starke, G. Gryn'ova, P. Fassl, and U. W. Paetzold, *Understanding and exploiting interfacial interactions between phosphonic acid functional groups and co-evaporated perovskites*, Oral presentation, PVSEC-34, 2023

T. Feeney, J. Petry, A. Torche, D. Hauschild, B. Hacene, C. Wansorra, A. Diercks, M. Ernst, L. Weinhardt, C. Heske, G. Gryn'ova, U. W. Paetzold, and P. Fassl, *Understanding and exploiting interfacial interactions between phosphonic acid functional groups and co-evaporated perovskites.* IEEE-PVSC 52, 2024

Acknowledgements

I would like to take the opportunity to thank everyone who supported me along the journey that was my PhD. Special thanks go to Prof. Dr. Ulrich W. Paetzold for giving me the opportunity to pursue my PhD as part of his research group Next Generation Photovoltaics. I am sincerely grateful for his guidance, patience, empathy and enthusiasm in supervising me during this time.

Moreover, I would like to offer my special thanks to Prof. Dr. Bryce S. Richards for being my original first supervisor and his support at the Institute of Microstructure Technology at KIT. I would also thank Dr. Tobias Abzieher for his guidance and supervision in the initial stages of my PhD and Dr. Paul Fassl for his supervision in the later stages of my PhD. Further thanks go to Prof. Dr. Uli Lemmer for his support during my time at the Light Technology Institute at KIT. Furthermore, I am incredibly grateful to Prof. Dr. Stefan Weber for agreeing to be my second reviewer.

Additional thanks go to the welcoming researchers at Australia National University, especially Dr. The Duong, whom I visited and collaborated with in 2024 for a short time. I would like to thank the support staff at the Institute of Nanotechnology at KIT, which enabled me to develop and apply the ALD process.

I am incredibly grateful for the support of the Next Generation photovoltaics Taskforce at LTI for the fruitful discussions and incredible collaborative atmosphere, which helped elevate the science and enjoyment of my research. I would extend this gratitude to all other former and current group members as well for the support, both scientific and emotional that was fostered in this research group. Especially here are thanks to the colleagues who collaborated with me to produce the presented work and further the endless pursuit of science, including but not limited to: Roja Singh, Dr. Hang Hu, Dr. Bahram Abdollahi, Dr. Tobias Abzieher, Dr. Fabian Schackmar, Felix Laufer, Dr. Li Yang, Dr. Ihteaz M. Hossain, Dr. Ahmed Farag, Dr. Saba Gharibzadeh, Julian Petry, Dr. David B. Ritzer, Benjamin Hacene, Dr. Marco A Ruiz-Preciado, Dr. Sara Moghadamzadeh, Fabrizio Gota, Dr. Jonas Schwenzer, Alexander Diercks and Julie Roger. Also thanks go to Dr. Paul Fassl and Prof. Dr. Ulrich W. Paetzold for supervision and guidance in these publications. I would also like to gratefully acknowledge that Dr. Hang Hu, Julian Petry, Roja Singh, Alexander Diercks, Julie Roger and Paul Fassl gave me many valuable comments on my thesis

I sincerely acknowledge the scientific collaboration with groups outside the institute including: Prof. Dr. Clemens Heske (KIT, UNLV), Dr. Lars Korte(HZB),, Dr. Adrian Mertens (KIT), Dr. Jan Becker (ZSW), Dr. Stefan Paetel (ZSW), Dr. Erik Ahlswede (ZSW), Dr. Constantin Wansorra (KIT), Michelle Ernst (HU), Dr. Lothar Weinhardt (KIT, UNLV), Prof. Dr. Steve Albrecht (HZB),, Stephanie Severin (HZB), Viktor Škorjanc (HZB), Dr. Suresh Maniyarasu(HZB), Kathrin Küster (MPI-FKF), Dr. Rainer Bäuerle (InnovationLab), Dr. Mario Hentschel (SCoPE) and Prof. Dr. Ulrich

Starke (MPI-FKF). Science is a collaborative effort, and it is wonderful to see just how much cross collaboration between research groups and universities is possible.

A special acknowledgement go to Dr. Dirk Hauschild (KIT, UNLV), Dr. Abderrezak Torche (HU), Aleksandra Miaskiewicz (HZB), Dr. Marcel Roß (HZB), and Assoc. Prof. Ganna Grynova (HU), who prompted numerous discussions and refining of the associated works.

A special thanks goes to my friends at the institute, including but not limited to: Julie Rogers, Roja Singh, Isabel Allegro, Simon Ternes, Hang Hu, Kristina Geistert, Alexander Diercks, Julian Petry, Felix Laufer, Joshua Damm, Ihteaz M. Hossain, Saba Gharibzadeh, Sara Moghadamzadeh, and Bahram Abdollahi-Nejand. They were always willing to provide intellectual and emotional support, as well as do what they could to encourage me to improve my work life balance when needed. Without them, the time of my PhD would have been nowhere near as enjoyable as it has proven to be.

I must also mention Matthew Walker and Hamidreza Borghei, who kept in regular contact even from the other side of the world, and provided immeasurable emotional support. Also included in this thanks are Caitlin Bush, Christina Mercuri and MJ Simkiss. An incredibly warm mention belongs to my wonderful girlfriend, Lisa Lainsbury, who loves and accepts me and my sometimes irrational obsession with work. Even in the closing months of this thesis her support has never wavered.

And last but not the least, I would like to thank my family, who were sad to see me leave but happy for my journey. My mum, who missed me terribly and always kept a room for me whenever I went back to Melbourne, my dad, who gave me a love of cooking that helped me make these last years more enjoyable coupled with a spice tolerance that has become a monster in its own right, and my sister, who has always believed in me more than I could ever believe in myself. I would also like to thank my extended family, with a special thanks to my close cousins Alasdair, Andrea, Rhianna, Tristan, Isabel, Jem, Grace, Rose, Oscar, Lily and Vivienne, who were always happy to see me come visit and several of whom made the trip to visit in turn.